Coherent Atom-Light Interaction in an Ultracold Atomic Gas

Experimental Study of Faraday Rotation Imaging and Matter Wave Superradiance

Kaminski, Franziska

Publication date:
2012

Document version
Early version, also known as pre-print

Citation for published version (APA):
Kaminski, F. (2012). *Coherent Atom-Light Interaction in an Ultracold Atomic Gas: Experimental Study of Faraday Rotation Imaging and Matter Wave Superradiance*. QUANTOP: Faculty of Science, University of Copenhagen.

UNIVERSITY OF COPENHAGEN

Coherent Atom-Light Interaction in an Ultracold Atomic Gas
Experimental Study of Faraday Rotation Imaging and Matter-Wave Superradiance

PhD Thesis
Franziska Kaminski

Danish National Research Foundation
Centre for Quantum Optics (QUANTOP)
Niels Bohr Institute
Faculty of Science
University of Copenhagen, Denmark

Academic Supervisors	Eugene S. Polzik
	Jörg H. Müller
Evaluation Committee	
NBI Local Head	Jan W. Thomsen
External Experts	Silke Ospelkaus
	Morgan Mitchell
Thesis Submitted	April 4th 2012
Defense Date	May 10th 2012

Summary – Sammendrag

Summary

Atom-light interfaces for quantum information applications have been mainly realized in room-temperature gases and in laser-cooled atomic ensembles. The interaction strength between atomic ensembles and light can be parametrized with the optical depth, which determines, for example, the fidelity of the storage of a quantum state of light in a quantum memory and the amount of achievable spin squeezing for metrological applications. Evaporatively cooled atomic ensembles have an extraordinarily large optical depth and are therefore candidates for high fidelity multimode quantum memories. For practical implementations it is important to identify and study processes not covered by simplified models and evaluate their impact on the performance of an atom-light quantum interface with evaporatively cooled atoms.

In this thesis the interaction of light with Bose-Einstein condensates and ultracold thermal atomic ensembles is examined. A quantitative study of polarization rotation, also called Faraday rotation, is presented. Rotation angles are predicted from atom numbers determined from absorption imaging after a time of flight and are then compared to rotation angles determined with in-situ dispersive imaging. A mismatch is found and attributed to light-assisted cold-collisions. The in-trap optical depth of a thermal ensemble was determined to be $\mathrm{OD} = 680$ on the strongest transition of the D1 line.

In inhomogeneous atomic ensembles diffraction effects start to play a role as the atomic density is increased. We use a dispersive imaging technique, based on a dual-port polarization-contrast setup, which allows us to obtain spatially-resolved Faraday rotation signals. This imaging system can be used to distinguish between diffraction effects and the polarization rotation signal, which is not possible in standard dispersive imaging techniques. Diffraction effects due to the sample and due to the imaging system are estimated with numerical models and are compared to the experimental data. Faraday rotation experiments with Bose condensed samples were performed as well, but could not be analyzed quantitatively due to their strong diffraction and the limitations of our imaging system.

Light-assisted collisions are also identified to be the cause of a broad atom loss spectrum, which is observed when the atoms are probed close to the atomic resonance. The width of this spectrum depends on the atomic density.

In matter-wave superradiance experiments, the correlations between recoiling atoms and scattered photons were analyzed. The superradiant process follows a parametric gain Hamiltonian and is therefore expected to produce entangled atom-photon pairs. It is shown how correlation measurements are complicated by the presence of an atom-atom collisional halo on the time of flight absorption images. The interactions between recoiling atoms and the zero momentum condensate mode were further studied by observing a velocity reduction of the recoiling atoms during a time of flight.

Sammendrag

Vekselvirkningen mellem atomer og lys med henblik på anvendelse af kvanteinformation er primært blevet realiseret i atomare gasser ved stuetemperatur og i lasernedkølede atomare ensembler. Styrken af vekselvirkningen mellem atomare ensembler og lys kan parametriseres ved den optiske dybde, der for eksempel bestemmer, med hvor stor fidelitet en kvantetilstand i lyset kan lagres i en kvantehukommelse og hvor meget 'spinsqueezing', der kan skabes til brug i metrologiske applikationer. Et atomart ensemble, der er nedkølet ved hjælp af fordampning, har en ekstraordinært høj optisk dybde, og er derfor kandidat til en 'multimode'-kvantehukommelser med høj fidelitet. For den eksperimentelle praksis er det vigtigt at identificere og studere de processer, der ikke er beskrevet ved simple modeller, og at evaluere, hvordan de påvirker vekselvirkningen mellem lys og atomer, der er nedkølede ved fordampning.

I denne afhandling undersøges interaktionen mellem lys og Bose-Einstein kondensater samt termiske atom ensembler. En kvantitativ undersøgelse foretages af rotation af polarizationen, også kaldet Faraday rotation. Vinkler for rotationen forudsiges udfra måling af antallet af atomer, der er bestemt ved absorption afbildning efter en flyvningstid. Disse vinkler er sammenlignet med rotationsvinkler bestemt ved in-situ dispersive afbildninger. Et misforhold findes og forklares ved lys-assisterede kold-kollisioner. Den optiske dybde for et termisk ensemble blev bestemt til OD = 680 ved den stærkeste overgang for D1 linien.

I inhomogene atom ensembler begynder diffraction effekter at spille ind da atomtætheden stiger. Vi benytter en dispersiv afbilningsteknik der er baseret på en dual-port polarization-kontrast opstilling, der tillader en spatialt opløst måling af Faraday rotationsvinkler. Dette afbildningssystem kan skelne mellem diffraktionseffekter og polarizationsrotation signaler, hvilket ikke er muligt i de standard opstillinger der benyttes til dispersive afbildninger. Diffraktionseffekter der skyldes prøven samt skyldes afbildningssystemet, er estimeret ved numeriske modeller og sammenlignet med eksperimentelle data. Faraday rotationseksperimenter med kondenserede Bose prøver blev også udført, men kunne ikke blive kvantitativt analyseret pga. den stærke diffration og begrænsninger ved afbildningssystemet.

Lys-assisterede kollisioner blev også identificeret som årsaget til et bredt atom tabs spektrum, der observeres når atomer probes tæt ved atomets resonansovergang. Bredden af dette spektrum afhænger af atomtætheden.

I materie-bølge superradians eksperimenter blev korrelationerne mellem tilbagestødte atomer og spredte atomer analyseret. Den superradiante process følger en parametrisk forstærknings Hamiltonian og forventes derfor at producere sammenfiltrede atom-foton par. Det vises hvorledes korrelationsmålinger bliver besværliggjort af en atom-atom kollisions halo i flyvningstid absorptions afbildningen. Interaktionen mellem tilbagestødte atomer og nul-momentum kondensater tilstande blev yderligere undersøgt ved at bestemme en hastighedsreduktion af de tilbagestødte atomer under en flyvningstid.

Acknowledgments

The research presented in this thesis was performed in the BEC subgroup of Eugene Polziks quantum optics lab in copenhagen. I am very grateful for receiving the opportunity to work in this group. The BEC subgroup is led by Jörg Helge Müller. He is a source of infinite scientific knowledge. I owe him a lot for his patience in explaining physics to me.

This thesis builds upon work done before i joined the group. The first BEC was achieved in autumn 2006. The setup was built by Andrew Hilliard, who concluded his PhD in 2008 [Hil08] and Christina Olausson, who finished her Master thesis in 2007 [Ola07]. Andrew introduced me to the workings of the lab and to the secret tricks and knobs that make the BEC machine do its job.

There were several people whom i worked with during the PhD studies. They all contributed with insights and help to this thesis. Rodolphe Le Targat joined us as a post doc in late 2007 until the beginning of 2009. In early 2008 Nir Kampel joined as a PhD student and Axel Griesmaier joined us in the beginning of 2010 for one year. During the last year Mads Peter H. Steenstrup joined as a new PhD student. Eva Bookjans arrived shortly before i submitted the thesis. I am grateful to her, Nir, Mads-Peter an Jörg for reading the thesis and helping with improving formulations. Special thanks goes also to Andreas and Jonas who helped with the translation of the summary to danish.

I am especially grateful to Anna Grodecka-Grad and Emil Zeuthen with whom i had an excellent collaboration on the sample diffraction theory presented in this thesis.

I would also like to thank the technical support at NBI. Especially Henrik Bertelsen, who was a great help with all the electronics and Erik Grønbæk Jacobsen, who was a big help with all the smaller and bigger mechanical jobs.

My PhD was largely funded by the european union training network EMALI. I am very grateful to have been allowed to be a part of such a big network. It enabled me to meet a lot of other PhD students working on similar topics. There were plenty of opportunities to present my own work and to meet other researchers. It was a very inspiring experience and i would not have wanted to miss it.

Not least, I would like to thank all the Quantoppies for the coffee breaks with cake and without, for the social events, for the musical performances and in general for just being a great bunch of people.

As well, I would like to thank my mother and father, for without their support this thesis would not have been written. I am most indebted to Stefan who had an endless understanding for my off working hours.

Contents

Part I

Overview

One

Introduction

The basic theory of quantum mechanics has been established during the first half of the last century. It can explain atomic spectra and the wave-particle duality of atoms and photons. With the advent of the laser in the middle of the century it became possible to study atom-light interactions with great precision and the field of quantum optics was born. During the last 20 years information technology became a topic of big interest due to the establishment of new communication methods. Applying quantum mechanics to information technology lead to the new field of quantum information science. The classical bit with its 0 and 1 states becomes a quantum bit, that can still only store one bit of classical information, but has an additional continuous phase that can be used in quantum information protocols. The applications range from secure communication protocols to the concept of a quantum computer that can solve certain problems with unprecedented ease. Of greater practical interest is the reduction of measurement noise below the quantum limit, which is known as spin squeezing. It allows for increased measurement precision in atomic clocks and for the determination of nature constants as compared to the quantum limit.

Long-distance entanglement and the establishment of secure communication channels has been proposed to be feasible with quantum memories [DLCZ01]. Quantum memories have been experimentally demonstrated in various systems [SAA$^+$10]. The first demonstration has been performed in room-temperature vapors [JSC$^+$04].

1.1 Ultracold Gases and Quantum Information Science

The figure of merit of atom-light interaction is the optical depth. In a quantum memory a high efficiency for mapping a quantum state of light into atomic ground state coherences is expected for large optical depths. While room-temperature gases and also laser-cooled gases have typically on-resonant optical depths below one hundred, Bose condensed gases easily reach optical depths of one thousand. It is therefore of interest to investigate Bose condensed gases as candidates for quantum memory applications. A large efficiency makes it also interesting to attempt multimode storage. Several independent light modes could be efficiently stored, increasing the capacity of the memory.

In contrast to room-temperature gases the atomic linewidth is not Doppler-broadened in an ultracold ensemble and the atoms are not moving during the interaction time. This raises the prospect of long memory storage times.

1.2 The Scope of this Thesis

After producing the first condensed sample in late 2006 the experimental efforts were concentrated on the study of matter-wave superradiance. Superradiance is a four-wave mixing process that has conceptually the same Hamiltonian as parametric down conversion of photons. In matter-wave superradiance pairs of photons and atoms are created that are expected to be entangled. In the experimental realization two-body collisions render the proof of such correlations as difficult. The experimental results are presented in Chap. 12.

We then went on to investigate polarization rotation, also called Faraday rotation, with a dual-port polarization-contrast imaging technique. The Faraday measurements give us in-trap access to the interaction strength with a probe beam and the dual-port imaging technique sets the stage for a spatially resolved multimode memory.
The analysis of the Faraday data lead to an extensive study of diffraction effects and the influence thereof on the focusing of the imaging system, which in turn has an effect on the measured angle. As compared to atom number estimates from absorption imaging we found an increased angle from the in-situ measurements. We propose a model including light-assisted collisions to account for the access angle.

The thesis is organized as follows: First an introduction to ultracold gases is given. Then the theoretical models are introduced, followed by the employed experimental techniques. Chapter 11 to 13 present the experimental results. Finally, a summary of the thesis and conclusions are given in Chap. 14. The appendices include detailed information on some of the models and contain a technical documentation. A list of publications is attached at the end.

Two

An Ultracold Gas Of Rubidium 87

The experiment is designed for the trapping and cooling of Rubidium 87 atoms. The first section of this chapter introduces the basic properties of Rubidium 87. The following sections give an introductory overview of Bose gases and their condensation in the experimentally relevant 3D harmonic oscillator trapping potential.

2.1 Rubidium 87

Rubidium 87 is an alkali metal and has therefore only one electron in its outer electronic shell. This means that its electronic level structure is fairly simple and it is possible to find cycling transitions for cooling.

Rubidium 87 was the first element to be Bose condensed in 1995 [AEM$^+$95]. It has a large and positive scattering length leading to repulsive interactions (Sec. 2.3.1), which is necessary for the final cooling steps towards condensation, i.e. radio-frequency evap-

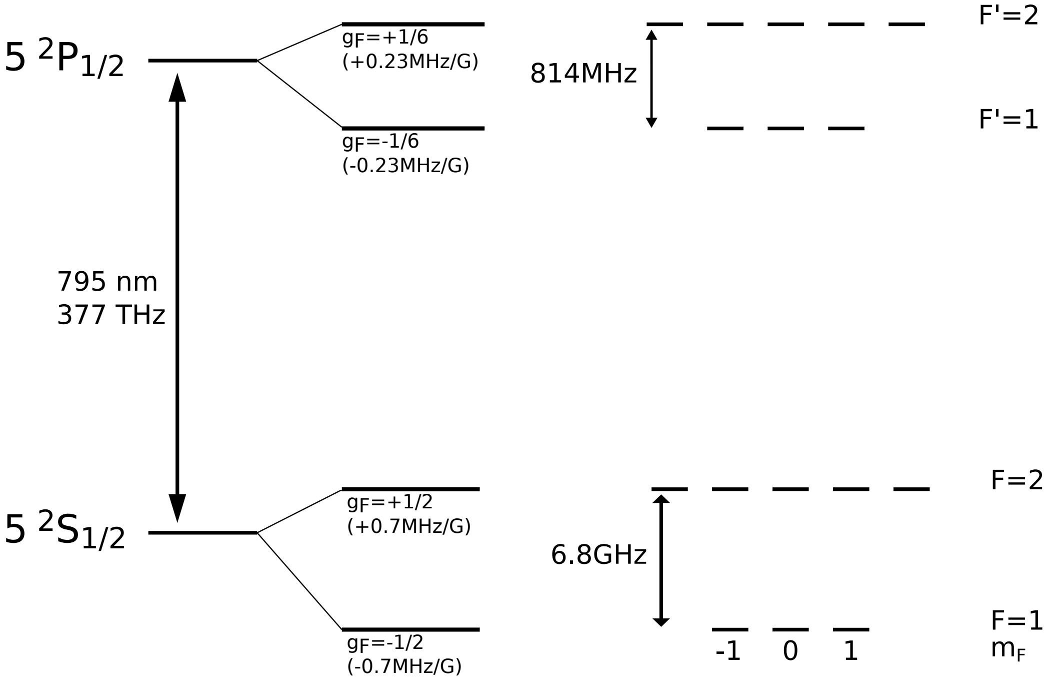

Figure 2.1: Rubidium 87 D1 line level scheme. Indicated are frequency splittings and the transition wavelength as well as the total atomic angular momentum quantum numbers F and their projections onto the quantization axis m_F. Landé factors g_F relevant for the Zeeman effect due to external magnetic fields are indicated together with the resulting frequency shifts.

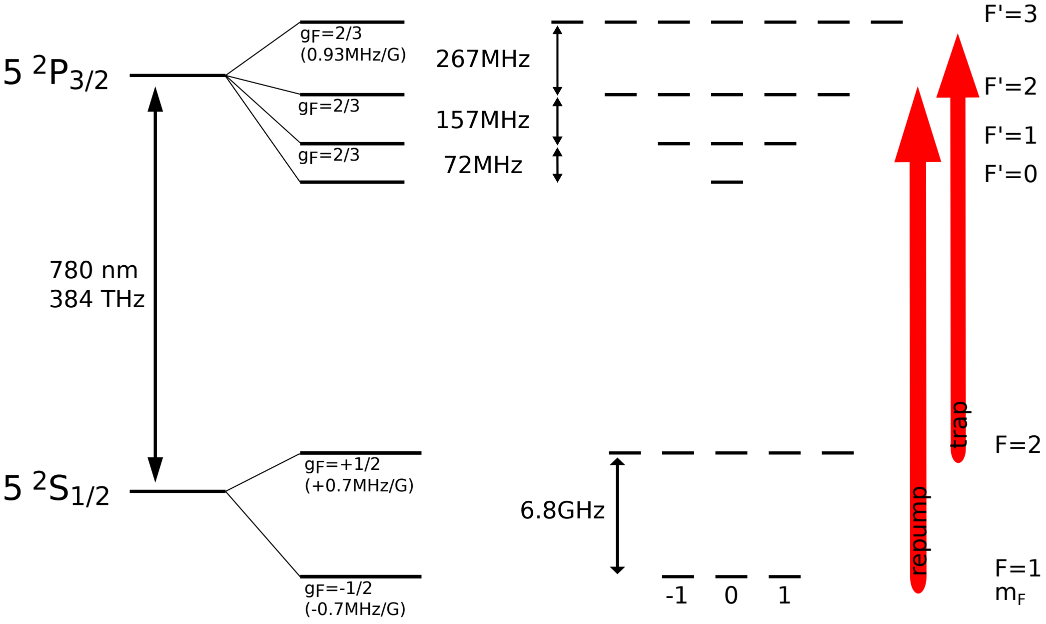

Figure 2.2: Rubidium 87 D2 line level scheme. The red arrows indicate the transitions used for trapping and cooling of the atoms. The repump laser drives the F=1 to F'=2 transition and the trap laser drives the F=2 to F'=3 transition.

oration. For this reason, together with the availability of inexpensive diode lasers at the relevant wavelength for cooling, it is a popular element for condensation. It is accordingly well studied.

The nucleus of Rubidium 87 has a half integer spin of $I = 3/2$. The hyperfine interaction couples the total electron angular momentum **J** of the single outer electron to the nuclear spin, which results in an integer valued total atomic angular momentum of $F = 1$ and $F = 2$ for the ground states. Rubidium 87 is therefore a Boson and consequently follows Bose statistics.

There are two excited states relevant for the work presented in this thesis. That is the $5^2\mathrm{P}_{1/2}$ state and the $5^2\mathrm{P}_{3/2}$ state. The transitions between the ground state $5^2S_{1/2}$ and these excited states are called D1 and D2 line respectively. The energy level schemes of the two lines including the hyperfine interaction are shown in Fig. 2.1 and Fig. 2.2. The total atomic angular momentum is denoted by F and its projection onto the quantization axis is m_F. Landé factors are noted as g_F together with the level shifts due to the Zeeman effect [Ste09].

The D2 line is used for cooling and trapping of the atoms and for absorption imaging. The transitions used for repumping and trapping are indicated by red arrows. The D1 line is used for probing the atoms inside the trap. This choice is due to the simpler level structure, though it comes at the cost of a factor of two smaller dipole moment as compared to the D2 line, decreasing the interaction strength with light.

2.2 The Thermal Bose Gas

2.2.1 Bose Statistics and Thermal Density Distribution

The quantum mechanical Bose distribution function, which is the mean occupation number of a state ν of a potential is

$$f^0(\epsilon) = \frac{1}{\exp\left(\frac{\epsilon_\nu - \mu}{kT}\right) - 1}, \tag{2.1}$$

where ϵ_ν is the energy of the state ν and μ is the chemical potential of the gas. The temperature is denoted as T and the Boltzmann constant is k. In a 3D harmonic oscillator potential (Eq. B.90) the density of the states ν at energy ϵ is given by $g(\epsilon) = \epsilon^2/(2\hbar^3\omega_x\omega_y\omega_z)$, where ω_i are the harmonic oscillator frequencies for each spatial direction and $\hbar$ is Planck's constant. The number of particles in excited states, $\nu > 0$, is then given by [PS01]

$$N_{ex} = \int_0^\infty g(\epsilon) f^0(\epsilon) \mathrm{d}\epsilon. \tag{2.2}$$

The zero momentum state occupation is not taken account in this equation since the energy of this state vanishes and therefore it does not contribute to the integral.

The wavelength of a matter-wave is the de Broglie wavelength

$$\lambda_{dB} = \frac{2\pi\hbar}{p} = \sqrt{\frac{2\pi\hbar^2}{MkT}}, \tag{2.3}$$

where p is the momentum of the particle and M is its mass. If the de Broglie wavelength is small with respect to the length scale over which the confining potential varies, the gas can be assumed to have locally the same properties as a bulk gas. It is then possible to use a semi-classical distribution function $f_{\mathbf{p}}(\mathbf{r}) = (\exp([\epsilon_{\mathbf{p}}(\mathbf{r}) - \mu]/kT) - 1)^{-1}$, with the spatial coordinate denoted as $\mathbf{r}$ and the classical particle energy as $\epsilon_{\mathbf{p}}(\mathbf{r}) = p^2/2M + V(\mathbf{r})$, where $V(\mathbf{r})$ is the potential energy. Integrating the semi-classical distribution function over phase-space and dividing by $(2\pi\hbar)^3$ gives the particle number. The density of non-condensed particles is then $\rho_{ex}(\mathbf{r}) = \mathrm{d}^3\mathbf{p}/((2\pi\hbar)^3) f_{\mathbf{p}}(\mathbf{r})$. This can be rewritten in terms of the function $g_\gamma[z] = \sum_{n=1}^{\infty} z^n/n^\gamma$ as [PS01]

$$\rho_{ex}(\mathbf{r}) = \frac{g_{3/2}\left[z(\mathbf{r})\right]}{\lambda_{dB}^3}, \tag{2.4}$$

where $z(\mathbf{r}) = e^{[\mu - V(\mathbf{r})]/kT} = \zeta e^{-V(\mathbf{r})/kT}$, where $\zeta = \exp(\mu/kT)$ is the fugacity. This density distribution is referred to as the Bose enhanced density distribution, since its peak value is increased compared to the density of a classical gas. Some useful relations of this density distribution are presented in App. A.3.

2.2.2 The Classical Limit

The phase space density ϖ of a uniform gas is the number of particles contained in a cube with edge length equal to the thermal wavelength

$$\varpi = \rho\lambda_{dB}^3. \tag{2.5}$$

If $\varpi \approx 1$ the extend of the matter waves is comparable to the inter-particle distance, the particles begin to overlap and if they are identical they become indistinguishable. This is the onset of the quantum regime. If $\varpi \ll 1$ the extend of the matter waves is small compared to the inter-particle distance and the gas can be treated as classical. This situation appears at large temperatures. The gas then follows Maxwell-Boltzmann statistics, with the distribution function

$$f^0(\epsilon_\nu) = \exp\left(-\frac{\epsilon_\nu - \mu}{kT}\right). \tag{2.6}$$

The resulting density distribution is then

$$\rho_{ex} = \frac{z(\mathbf{r})}{\lambda_{dB}^3}, \tag{2.7}$$

which is the first term in the sum of the Bose enhanced density Eq. 2.4. For a 3D harmonic oscillator potential this yields a simple Gaussian density distribution. This is presented in App. A.2.

2.2.3 Density Distribution after Free Expansion

Information about the properties of an ultracold gas are experimentally obtained by imaging the sample and reconstructing the density distribution. Since ultracold gases are very dense inside the trapping potential imaging is often performed after releasing the atoms from the trap and allowing them to expand in order to reduce the density. This free expansion happens during a time of flight t_{TOF} during which the atoms fall due to gravity. During this time the atoms expand with a velocity that arises from their momentum distribution inside the trap as $\dot{\mathbf{r}} = \mathbf{p}/M$. The momentum stays constant after the potential is turned off: $\dot{\mathbf{p}} = 0$. The time of flight distribution function is therefore $f_\mathbf{p}(\mathbf{r}, t_{TOF}) = f_\mathbf{p}^0(\mathbf{r} - \mathbf{p}t_{TOF}/M)$ and the density is then [KDSK99]

$$\rho(\mathbf{r}, t_{TOF}) = \frac{d\mathbf{r}_0 d\mathbf{p}}{(2\pi\hbar)^3}\delta^3\left(\mathbf{r} - \mathbf{r}_0 - \frac{\mathbf{p}t}{M}\right) f_\mathbf{p}(\mathbf{r}_0, t_{TOF}), \tag{2.8}$$

where $\delta^3(\cdot)$ is the Dirac delta function. In a 3D harmonic oscillator potential this leads to a density in time of flight of

$$\rho(\mathbf{r}, t_{TOF}) = \frac{1}{\lambda_{dB}^3}\prod_{i=1}^{3}\frac{1}{1+\omega_i^2 t_{TOF}^2} g_{3/2}\left(\exp\left(\frac{\mu}{kT} - \sum_{i=1}^{3}\frac{x_i^2}{2x_i(0)^2}\frac{1}{1+\omega_i^2 t_{TOF}^2}\right)\right), \tag{2.9}$$

where $x_i(0) = \sqrt{kT/M\omega_i^2}$ is the in-trap $e^{-1/2}$ Gaussian radius. This shows that the axis evolve during time of flight according to

$$x_i(t_{TOF}) = x_i(0)\sqrt{1+\omega_i^2 t_{TOF}^2}. \tag{2.10}$$

In the classical limit the evolution of the axes is identical to the Bose distribution case. The peak density evolves according to $\rho(0, t_{TOF}) = \rho(0,0)\prod_{i=1}^{3}\left(1+\omega_i^2 t_{TOF}^2\right)^{-1}$, where the in-trap peak density is given in terms of the fugacity ζ as $\rho(0,0) = g_{3/2}(\zeta)/\lambda_{dB}^3$. Appendix A for details on how to derive atomic parameters from time of flight images.

2.2.4 Chemical Potential

The chemical potential is defined by the Maxwell relation $\mu = (\partial A/\partial N)|_{V,T}$, where A is the free energy, N is the particle number, V is the volume of the gas. In the case of an ideal classical gas the chemical potential is then [Hua01]

$$\mu^{MB} = kT \ln\left(\rho\lambda_{dB}^3\right). \tag{2.11}$$

In the quantum mechanical case of Bose statistics the chemical potential needs to be rewritten by using the equation of state $\rho_{ex}\lambda_{dB}^3 = g_{3/2}(z)$ as $\mu = kT\ln(z)$ and can be approximated as [Hua01]

$$\mu^{Bose} = kT\left[\ln\left(\rho\lambda_{dB}^3\right) + \ln\left(1 + \frac{\rho\lambda_{dB}^3}{2^{3/2}} + \ldots\right)\right]. \tag{2.12}$$

In the case of Maxwell-Boltzmann statistics $\mu^{MB} > 0$ for $\varpi < 1$, while for Bose statistics the chemical potential vanishes if no particle interactions are included as the lowest energy state is macroscopically occupied.

$$\begin{array}{lll} \mu^{Bose} < 0 & \text{for } \varpi \ll 1 & \text{(classical regime)} \\ \mu^{Bose} = 0 & \text{for } \varpi < 1 & \text{(quantum regime).} \end{array}$$

2.3 Bose Condensation

2.3.1 S-Wave Scattering

The density distribution of a condensate is not determined by the kinetic energy, but by two-body interactions between the atoms, as will be shown in Sec.2.3.3. These interactions are also relevant in the final steps of the process used to cool the atoms to condensation, i.e. in evaporative cooling.

The interaction potential of collisions between two atoms is due to the static electric dipole-dipole-interaction

$$U_{ed} = \frac{1}{4\pi\epsilon_0 r^3}\left[\mathbf{d}_1 \cdot \mathbf{d}_2 - 3(\mathbf{d}_1 \cdot \hat{\mathbf{r}})(\mathbf{d}_2 \cdot \hat{\mathbf{r}})\right], \tag{2.13}$$

where $\mathbf{d}_i$ refers to the electric dipole moment of the atoms $i = [1,2]$, $\mathbf{r}$ is the vector separation between the atoms and $\hat{\mathbf{r}} = \mathbf{r}/r$ its unit vector. From this expression the C_6 coefficient of the van der Waals interaction potential $U_{vdW}(r) = -\frac{C_6}{r^6}$ can be calculated.

At low temperatures the scattering wavefunction has only s-wave contributions. The wavefunction can then be approximated as

$$\psi = 1 - \frac{a}{r}, \tag{2.14}$$

where a is the scattering length and it is the only parameter necessary to determine an effective interaction energy or pseudopotential

$$U_0 = \frac{4\pi\hbar^2 a}{M}. \tag{2.15}$$

This effective interaction can be used together with a mean-field treatment to determine the condensate density distribution.

The following table shows the scattering lengths of the maximally stretched state (both atoms in $|F=1, m_F=-1\rangle$), the singlet state (opposite spins) and the triplet state (both atoms in the same state $|F=2, m_F=\pm 2\rangle$) in units of a_0, the Bohr radius.

^{87}Rb Scattering Lengths [a_0][PS01]

Triplet	Singlet	Maximally Stretched
106 ± 4	90 ± 1	103 ± 5

2.3.2 Condensation Criterion and Condensation Temperature

The condensation temperature T_c of the gas is reached when the chemical potential vanishes while still none of the particles is in the lowest state of the potential

$$N_{at} = N_{ex}(T_c, \mu = 0) = \int_0^\infty \mathrm{d}\epsilon g(\epsilon) \frac{1}{e^{\epsilon/kT_c} - 1}. \tag{2.16}$$

In a uniform non-interacting gas the condensation condition can be simply stated as $\varpi = \zeta(3/2) \approx 2.61$, where $\zeta(\cdot)$ is the Riemann zeta-function.

For a non-interacting gas in a 3D harmonic oscillator potential the condensation temperature is found to be [PS01]

$$kT_c = \frac{\hbar\bar{\omega} N_{at}^{1/3}}{[\zeta(3)]^{1/3}} \approx 0.94 \hbar\bar{\omega} N_{at}^{1/3}, \tag{2.17}$$

where $\bar{\omega} = (\omega_x \omega_y \omega_z)^{1/3}$. There are two corrections to this result. The first one is the finite particle number correction. The relative change of the transition temperature is [PS01]

$$\left(\frac{\Delta T_c}{T_c}\right)^{(fp)} = -\frac{\zeta(2)}{2[\zeta(3)]^{2/3}} \frac{\omega_m}{\bar{\omega}} N_{at}^{-1/3} \approx -0.73 \frac{\omega_m}{\bar{\omega}} N_{at}^{-1/3}, \tag{2.18}$$

where $\omega_m = (\omega_x + \omega_y + \omega_z)/3$. At infinite particle numbers N_{at} this correction vanishes and it is large for small particle numbers. The effect originates from the zero-point energy of the particles in the harmonic potential $\Delta\epsilon_{min} = 3\hbar\omega_m/2$ which leads to a shift of the chemical potential at the critical temperature of $\Delta\mu = \Delta\epsilon_{min}$. The integral in Eq. 2.16 therefore needs to be evaluated at non-vanishing μ. This effect leads to a T_c correction of -1.1% for 10^6 atoms in our trap geometry.

The second correction takes into account the interactions between particles and is referred to as the mean-field correction [PS01]

$$\left(\frac{\Delta T_c}{T_c}\right)^{(mf)} = -1.33 \frac{a}{\bar{a}} N_{at}^{1/6}, \tag{2.19}$$

where $\bar{a} = \sqrt{\hbar/M\bar{\omega}}$ is the geometric mean of the trap oscillator lengths and a is the scattering length. The correction arises from the shift in energy of the lowest single-particle state due to the van-der-Waals interaction $\epsilon_0 = 2\rho(0)U_0$. The correction is 4.9% for $N_{at} = 10^6$ in our trap.

2.3.3 Density Distribution

Interaction between particles need to be taken into account in determining the condensate density distribution. Interactions can be modeled as a contact interaction of with the potential $U_{eff} = U_0\delta(\mathbf{r}-\mathbf{r}')$. It is then assumed that all the particles are in the ground state of the trap with wavefunction ϕ. In the mean field approximation the N-particle wave function is the product $\prod_{i=1}^{N}\phi(\mathbf{r_i})$. The wavefunction of the condensate is defined by $\psi(\mathbf{r}) = N^{1/2}\phi(\mathbf{r})$, such that the particle density is $\rho(\mathbf{r}) = |\psi(\mathbf{r})|^2$ and the particle number is $N = \int \mathrm{d}\mathbf{r}|\psi(\mathbf{r})|^2$. This wavefunction can be shown to follow a non-linear Schrödinger equation that is called the Gross-Pitaevskii equation

$$-\frac{\hbar^2}{2M}\nabla^2\psi(\mathbf{r}) + V(\mathbf{r})\psi(\mathbf{r}) + U_0|\psi(\mathbf{r})|^2\psi(\mathbf{r}) = \mu\psi(\mathbf{r}), \tag{2.20}$$

where the chemical potential is given by the interaction strength between the particles $\mu = U_0|\psi(\mathbf{r})|^2 = U_0\rho(\mathbf{r})$ and does not vanish, as predicted by Bose statistics of non-interacting particles. It is the energy for adding a particle to the condensate.

In order to find a simple approximate expression for the wavefunction one uses the Thomas-Fermi approximation, which neglects the kinetic energy term in the Gross-Pitaevskii equation and then yields

$$\rho_c(\mathbf{r}) = \frac{\mu - V(\mathbf{r})}{U_0}. \tag{2.21}$$

For a 3D harmonic oscillator potential this results in a density distribution with the shape of an inverted parabola (App. A.1).

The radii of the clouds are found by setting $V(\mathbf{R}) = \mu$. For a 3D harmonic oscillator they are

$$R_i = \sqrt{\frac{2\mu}{M\omega_i^2}} \tag{2.22}$$

and in turn the chemical potential can be expressed in terms of the experimentally accessible radii of the atomic cloud as

$$\mu = \frac{M}{2}\omega_i^2 R_i^2. \tag{2.23}$$

The temperature can be inferred by setting $kT = \mu$. Integrating the density over space gives a relation between the particle number and the chemical potential

$$\mu = \frac{15^{2/5}}{2}\left(\frac{Na}{\bar{a}}\right)^{2/5}\hbar\bar{\omega}, \tag{2.24}$$

which can be used to express the particle number in terms of trap frequencies and radii only

$$N_{at} = \frac{M^2}{15a\hbar^2}\frac{\omega_i^5}{\bar{\omega}^3}R_i^5. \tag{2.25}$$

In the case of a cigar shaped harmonic oscillator potential with the two radial trap frequencies ω_r and the axial frequency ω_z, the axis of the condensate evolve after a free expansion according to [KDSK99]

$$r_0(t_{TOF}) = r_0(0)\sqrt{1+\omega_r^2 t_{TOF}^2} \tag{2.26}$$

$$z_0(t_{TOF}) = z_0(0)\left(1+\left(\frac{\omega_z}{\omega_r}\right)^2\left[\omega_r t_{TOF}\arctan(\omega_r t_{TOF}) - \ln(1+\omega_r^2 t_{TOF}^2)\right]\right) \tag{2.27}$$

where the in-trap radius along the direction of the lower trap frequency is $z_0(0) = r_0(0)\omega_r/\omega_z$. During the expansion process the atomic interaction energy is converted into atomic momentum. For times $t_{TOF} \ll \omega_r^{-1}$ the atoms expand in the radial direction according to $Mv_r^2/2 = \mu$ corresponding to a momentum of $p = \sqrt{2M\mu}$, which is identical to the in-trap momentum. After an expansion of $t_{TOF} > \omega_r/\omega_z^2$ the aspect ratio of the cloud stays fixed at $r_0/z_0 = \pi\omega_r^2/2\omega_z^2$. For our trap frequencies of $\omega_r = 2\pi$ 115.4Hz and $\omega_z = 2\pi$ 11.75Hz this situation is reached after 133ms. The expansion with a fixed velocity is reached after $\omega_r^{-1} = 1.4$ms. We typically use $t_{TOF} = 45$ms. This means that the atoms expand according to their in-trap momentum, but did not yet reach their final aspect ratio.

See App. A.1 for an overview of how to deduce sample parameters from time-of-flight images.

2.3.4 Bimodal Density Distributions

If the condensation process is incomplete there is a mixture of thermal and condensed atoms inside the trap. We approximate this situation by adding the thermal and condensate density distributions and assume that they are not interacting with one another

$$\rho_{bi} = \rho_{ex}(\mathbf{r}) + \rho_c(\mathbf{r}). \tag{2.28}$$

In the fitting routine we use in absorption images the analysis is done by first fitting the more extended thermal cloud by sparing the condensate part, then subtracting the thermal fit from the image and fitting the condensate part.

Part II

Modeling

Three

Light-Matter Interaction

In experiments with atomic ensembles light is used in almost all the steps of the experiment. Light is needed to cool and trap the atoms. It is used to manipulate the momentum of atoms and as a probe for the ensemble properties. Sensitive light detection devices are available, i.e. photodetectors or cameras. The interaction can be tuned to be destructive, for detunings close to resonance, or non-destructive, for detunings far from resonance.
In the first section of this chapter the basic light-atom interaction will be introduced together with an intuitive model for diffraction. In the later sections Maxwell-Bloch equations, that describe the interaction of a multi-level atom with light will be introduced. These equations allow to incorporate also the influence of inhomogeneous magnetic fields and the inhomogeneity of the atomic ensemble density. Many details of the derivation are included in App. B.

3.1 Simple Model: Atomic Ensemble as a Thin Lens

3.1.1 Absorption and Dispersion

Assuming atomic populations and coherences do not change during the interaction time and neglecting any diffraction effects, we can model the ensemble as a simple phase element like a lens. The incoming electric field E_0 will be phase shifted and slightly attenuated such that we can write the resulting field as

$$E^{out} = tE_0 e^{i\phi} = E_0 + \varDelta E, \tag{3.1}$$

where $\varDelta E$ is the scattered light. The transmission coefficient t and phase shift ϕ are

$$t = \exp\left(-\frac{D}{2}\right) \tag{3.2}$$

$$\phi = \int \mathrm{d}z\, kn = -\frac{D}{2}\tilde{\varDelta} \tag{3.3}$$

and $D = \tilde{\rho}\frac{\sigma_0}{1+\tilde{\varDelta}^2+s}$ is the optical depth of the atomic ensemble. The on-resonant scattering cross section is $\sigma_0 = \xi^2 \frac{3\lambda^2}{2\pi}\frac{2J'+1}{2J+1}$, where ξ is defined via the dipole matrix element $d_i = \xi_i \langle J\|d\|J'\rangle$ and J is the fine structure quantum number of the ground state. In a two level system $\xi = 1$. The line-integrated number density, the so called column density, is $\tilde{\rho} = \int \rho \mathrm{d}z$, $\tilde{\varDelta} = \frac{\varDelta}{\varGamma/2}$ is the detuning normalized to the half linewidth $\varGamma/2$ and $s = I/I_s$ is the saturation parameter given by the light intensity I and the saturation intensity $I_s = \frac{\hbar^2\varGamma^2 c\epsilon_0}{4\xi_i^2|\langle J\|d\|J'\rangle|^2}$ [KDSK99, Ste09, SZ97]. The wavevector of light in vacuum is $k = 2\pi/\lambda$ and n is the refractive index.

This model takes so far no polarization effects into account, but we can expand it to contain polarization rotation. This implies an anisotropy of the polarizability of spin-polarized atomic ensembles. If the populations of the atomic ground state are not symmetrical around the $m_F = 0$ state there will be a relative phase shift between the two circular components of the light field, into which any linear polarization can be decomposed. This leads to an incoming linear polarization to be rotated by the Faraday angle θ_F. The incoming linear field polarization is $\vec{e}^{in} = \vec{e}_x = \left(\vec{e}_- - \vec{e}_+\right) / \sqrt{2}$. After the interaction we have

$$\begin{aligned} \vec{E}^{out} &= \frac{\left(\vec{e}_- t_- e^{i\phi_-} - \vec{e}_+ t_+ e^{i\phi_+}\right)}{\sqrt{2}} && (3.4) \\ &= e^{i\Phi}\left(\cos\theta_F \vec{e}_x - \sin\theta_F \vec{e}_y\right), && (t_- = t_+ = 1) \end{aligned}$$

where we have defined the Faraday angle as $\theta_F = (\phi_+ - \phi_-)/2$ and half of the total phase shift $\Phi = (\phi_+ + \phi_-)/2$.

3.1.2 Diffraction

The thin lens model can also be extended to estimate the focus or defocus of light after the interaction. This implies an effective focal length of the ensemble.

The delay distance of the wavefront in the middle of the ensemble relative to the outside is $\Delta z = \frac{\phi\lambda}{2\pi}$ (Fig. 3.1) proportional to the phase shift ϕ inflicted by the atoms onto the light. The angle α is simply $\tan\left(\alpha/2\right) = \frac{2\Delta z}{d}$, where d is the full width of the atomic ensemble and finally

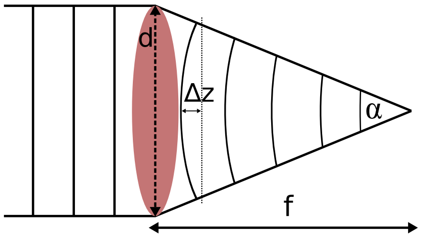

Figure 3.1: Determination of the focal length of the atomic ensemble.

$$\tan\left(\frac{\alpha}{2}\right) = \frac{\phi\lambda}{d\pi} = \frac{d/2}{f}. \tag{3.5}$$

This implies a focal length of the atomic ensemble lens of

$$f = \frac{\pi d^2}{2\phi\lambda} \propto \frac{d^4}{\xi^2\lambda^2 N}\frac{1+\tilde{\Delta}^2}{\tilde{\Delta}}. \tag{3.6}$$

Matching the angle α to the opening angle of a Gaussian beam we can determine a focus spot size of $w_0 = 2\lambda/(\pi\alpha) \approx d/\phi$.

This model works especially well for condensates, because of the sharp edges in the Thomas-Fermi limit. For Gaussian shaped samples it makes less sense to define a point where the density is zero.

3.2 Maxwell-Bloch Equations

In this section the matter-light interaction of multilevel atoms is introduced. The multilevel structure is included in the atomic polarizability. It will be shown that the Hamiltonian can be decomposed into three parts, corresponding to scalar, vector and tensorial parts or correspondingly to diffraction, light polarization rotation and Raman transfers.

3.2.1 Hamiltonian

The coupled light-atom system can be described by a Hamiltonian which is the sum of the Hamiltonians describing the atoms $\hat{\mathcal{H}}_A$, the radiation field $\hat{\mathcal{H}}_R$ and the coupling between the two $\hat{\mathcal{H}}_{AR}$ [Ham06]

$$\hat{\mathcal{H}}^{\mathrm{sys}} = \hat{\mathcal{H}}_A + \hat{\mathcal{H}}_R + \hat{\mathcal{H}}_{AR}. \tag{3.7}$$

The coupling can be described by modeling atoms as dipoles. The interaction energy is then [Jac62]

$$\hat{\mathcal{H}}_{AR} = -\hat{\mathbf{d}} \cdot \hat{\mathbf{E}}, \tag{3.8}$$

where $\hat{\mathbf{E}}$ is the electric field, Eq. B.8, and $\hat{\mathbf{d}}$ is the transition dipole operator, Eq. B.26. After invoking the rotating wave approximation as well as adiabatically eliminating excited states and adding the atomic Hamiltonian we arrive at (App. B.3)

$$\hat{\mathcal{H}}^{\mathrm{eff}}_{\mathrm{AR}} = \hat{\mathbf{E}}^{(-)} \hat{\alpha}(\Delta) \hat{\mathbf{E}}^{(+)} = \sum_{qq'} \hat{E}^{(-)}_q \hat{\alpha}_{qq'}(\Delta) \hat{E}^{(+)}_{q'} \tag{3.9}$$

where we have used the spherical basis (App. B.1) in the last step and introduced the atomic polarizability, Eq. B.36,

$$\hat{\alpha}(\Delta) = - \sum_{F_f F' F_i} \frac{\hat{\mathbf{d}}^{(-)} \hat{\mathbf{d}}^{(+)}}{\hbar \left(\Delta_{F_i F'} + i\gamma\right)}. \tag{3.10}$$

Here $\Delta_{F_i F'}$ is the laser detuning with respect to the excited state with half-width decay rate γ.

3.2.2 Tensor Components

The atomic polarizability $\hat{\alpha}$ can be decomposed into spherical irreducible tensor components [GSM06, Sak94] by rewriting the dyad $\hat{d}_q \hat{d}^{\dagger}_{q'}$ with help of the spherical basis set for polarizations. In general [GSM06, Bay66]

$$\hat{U}^{(\kappa)}_q \hat{V}^{(\kappa')}_{q'} = \sum_{jm} \hat{T}^{(j)}_m \langle \kappa, q; \kappa', q' | j, m \rangle \qquad \text{and} \tag{3.11}$$

$$\hat{T}^{(j)}_m = \sum_{qq'} \hat{U}^{(\kappa)}_q \hat{V}^{(\kappa')}_{q'} \langle \kappa, q; \kappa', q' | j, m \rangle \tag{3.12}$$

where $\hat{T}^{(j)}_m$ is a tensor of rank j and $\hat{U}^{(\kappa)}_q$ and $\hat{V}^{(\kappa')}_{q'}$ are tensors of rank κ and κ'. $\langle \kappa, q; \kappa', q' | j, m \rangle$ is a Clebsch-Gordan Coefficient (App. B.4.2). We can identify $\hat{\mathbf{U}} = \hat{\mathbf{d}}$ and $\hat{\mathbf{V}} = \hat{\mathbf{d}}^{\dagger}$ with $\kappa = \kappa' = 1$, since dipole moments are vectors. This allows the polarizability to be decomposed into three components

$$\begin{aligned}
\hat{\alpha}(\Delta) &= - \sum_{q_f q_i} \hat{d}^{(-)}_{q_f} \hat{d}^{(+)}_{q_i} \vec{e}^{\,*}_{q_f} \vec{e}^{\,*}_{q_i} && (3.13)\\
&= - \sum_{jm} \sum_{q_f q_i} T^{(j)}_m(\Delta) \langle 1, q_f; 1, -q_i | j, m \rangle \vec{e}^{\,*}_{q_f} \vec{e}^{\,*}_{q_i} && (3.14)\\
&= \hat{\alpha}^{(0)} \oplus \hat{\alpha}^{(1)} \oplus \hat{\alpha}^{(2)}. && (3.15)
\end{aligned}$$

See Eq. B.53 to B.55 for explicit notation. Here $j \in [0, 1, 2]$ specifies the rank of the tensor and defines the behavior of the tensor under rotations (as a scalar, vector or tensor). The projection of j on the quantization axis is $m \in [-j, \dots, j-1, +j]$. The $j = 0$ part describes the AC Stark shift, the $j = 1$ part Faraday rotation and the $j = 2$ part Raman transitions. As will become apparent later, m can be interpreted as the atomic angular momentum step size, i.e. $m = 2$ describes a Raman type transition from a Zeeman sublevel $m_F = -1$ to $m_F = 1$.
Using projectors around dipole moments the tensors $\hat{T}^{(j)}_m(\Delta)$ (see Eq. B.57 to B.65 for explicit notation) can be expressed in terms of dipole matrix elements with the help of Clebsch-Gordan Coefficients $\langle JM|j_1, m_1; j_2, m_2\rangle$ (App. B.4.2)

$$\hat{T}^{(j)}_m(\Delta) = \sum_{q_f q_i} \langle 1, q_f; 1, -q_i | j, m\rangle \hat{d}^{(-)}_{q_f} \hat{d}^{(+)}_{q_i} \tag{3.16}$$

$$\hat{d}^{(-)}_{q_f} \hat{d}^{(+)}_{q_i} = \sum_{F_f F' F_i} \mathcal{F}_{F_i F' F_f} \hat{C}^{q_i q_f}_{F_i F' F_f}(\Delta), \tag{3.17}$$

where the new parameters are

$$\mathcal{F}_{F_i F' F_f} = \frac{\langle F_g|\hat{\mathbf{d}}|F'\rangle\langle F_e|\hat{\mathbf{d}}|F'\rangle}{|\langle J_g|\hat{\mathbf{d}}|J'\rangle|^2} \tag{3.18}$$

$$= (-1)^{2(F'+J_g+I)} \cdot (2F'+1)(2J_g+1) \cdot \begin{Bmatrix} 1 & J_g & J' \\ I & F' & F_i \end{Bmatrix} \begin{Bmatrix} 1 & J_g & J' \\ I & F' & F_f \end{Bmatrix} \tag{3.19}$$

and using the relation $\langle e|\hat{d}^{\dagger}_q|g\rangle = (-1)^q \langle g|\hat{d}_{-q}|e\rangle$

$$\hat{C}^{q_i q_f}_{F_f F' F_i}(\Delta) = \sum_{m_f} \hat{\sigma}_{F_i m_i F_f m_f} \cdot \mathcal{D}^{F_i F'}_{m_i m'}(\Delta) \tag{3.20}$$

$$\langle F_f, m_f | 1, -q_f; F', m_f + q_f\rangle \cdot \langle F_i, m_f + q_f - q_i | 1, -q_i, F', m_f + q_f\rangle, \tag{3.21}$$

where the detuning term is

$$\mathcal{D}^{F_i F'}_{m_i m'}(\Delta) = \left(\frac{D_0^2}{\hbar\gamma}\right) \frac{\left(\tilde{\Delta}_{F_i F'} + \tilde{\Delta}^B_{m_i m'}\right) - i}{\left(\tilde{\Delta}_{F_i F'} + \tilde{\Delta}^B_{m_i m'}\right)^2 + 1}. \tag{3.22}$$

The detuning $\tilde{\Delta}_{F_i F'} = \Delta_{F_i F'}/\gamma = \left(\omega_L - \omega_{F'} + \omega_{F_i}\right)/\gamma$ is the relative detuning of the laser from the transition from the initial to the excited hyperfine state normalized to the atomic half linewidth γ. The detuning $\tilde{\Delta}^B_{m_i m'} = \frac{\mu_B}{\hbar\gamma}\left(-g_{Fg} m_i + g_{F'} m'\right) B_z$ is the normalized Zeeman shift of the magnetic substates.
The polarizations $q_f, q_i \in [-1, 0, 1]$ are related by the tensor projection m as $q_f = q_i + m$. The transition strength between ground and excited total electron angular momentum J states [Ste09] is $D_0 = |\langle J_g|\hat{\mathbf{d}}|J_e\rangle|$. The initial and final ground state atomic total angular momentum quantum numbers are F_i and F_f, where $\vec{\mathbf{F}} = \vec{\mathbf{J}} + \vec{\mathbf{I}}$ and I is the nuclear angular momentum quantum number. The quantum number of the projections of $\vec{\mathbf{F}}$ onto the quantization axis are m_f and $m_i = m_f + q_f - q_i$. The atomic density matrix is $\hat{\sigma}_{F_i m_i F_f m_f}$, connecting ground states.
Therefore the matrix representation of $\hat{T}^{(j)}_m$ has $F_i \times F_f$ elements, i.e. the number of

ground states squared. This also explains why an adiabatic elimination of the excited states is useful. The matrices involved are smaller, so there are less equations that need to be solved.
In the case where $F_i = F_f$ and $B_z = 0$ we can write

$$\hat{T}^{(j)}_m(\Delta) = \sum_F \mathcal{D}(\Delta)\hat{T}^{(j)}_m(F). \tag{3.23}$$

The tensors $\hat{T}^{(j)}_m(F)$ are proportional to the spin matrices $\hat{f}_k$ with $(k \in [-1,0,1])$ by the relations [VMK88]

$$\hat{T}^{(0)}_0(F) = \alpha^{(0)}\frac{1}{\sqrt{(2F+1)}}\mathbb{1} \tag{3.24}$$

$$\hat{T}^{(1)}_m(F) = \alpha^{(1)}\sqrt{\frac{3}{F(F+1)(2F+1)}}\hat{f}_m. \tag{3.25}$$

The form of the relations for the rank 2 tensors is more complex [VMK88], but is shown for F=1 in Eq. B.57 to B.65.

3.2.3 Hamiltonian in Tensor and Stokes Language

Now we will rewrite the Hamiltonian using the atomic $\hat{T}^{(j)}_m$ tensors (App. B.4.3) by plugging the polarizability (Eq. 3.14) into the Hamiltonian $\mathcal{H}^{\text{eff}}_{\text{AR}}$ (Eq. 3.9), and the light Stokes operators $\hat{S}_i$ (App. B.5, while we use them here with units $[\hat{S}] = 1$ in discrete variables), which arise from the $\hat{\mathbf{E}}^{(+)}\hat{\mathbf{E}}^{(-)}$ products mapped into the spherical polarization basis (App. B.1). This will allow us to describe atoms and light on equal footing.
After some algebra we arrive at the following Hamiltonian components for a configuration in which only circular polarizations are relevant (light propagation direction along quantization axis):

$$\hat{\mathcal{H}}^{\text{eff}(0)}_{\text{AR}} = -\tfrac{2}{\sqrt{3}}H_0'\hat{S}_0\tilde{T}^{(0)}_0(\tilde{\Delta}) \tag{3.26}$$

$$\hat{\mathcal{H}}^{\text{eff}(1)}_{\text{AR}} = H_0'\sqrt{2}\hat{S}_3\tilde{T}^{(1)}_0(\tilde{\Delta}) \tag{3.27}$$

$$\hat{\mathcal{H}}^{\text{eff}(2)}_{\text{AR}} = H_0'\left[2\left(\hat{S}_1\tilde{T}^{(2)}_{2+}(\tilde{\Delta}) + \hat{S}_2\tilde{T}^{(2)}_{2-}(\tilde{\Delta})\right) + \tfrac{2}{\sqrt{6}}\hat{S}_0\tilde{T}^{(2)}_0(\tilde{\Delta})\right]. \tag{3.28}$$

Here we defined

$$\tilde{T}^{(2)}_{2+}(\tilde{\Delta}) = \frac{1}{2}\left(\tilde{T}^{(2)}_2(\tilde{\Delta}) + \tilde{T}^{(2)}_{-2}(\tilde{\Delta})\right) \tag{3.29}$$

$$\tilde{T}^{(2)}_{2-}(\tilde{\Delta}) = \frac{1}{2i}\left(\tilde{T}^{(2)}_{-2}(\tilde{\Delta}) - \tilde{T}^{(2)}_2(\tilde{\Delta})\right). \tag{3.30}$$

The tilde over tensors indicates normalization with

$$\left(\frac{D_0^2}{\hbar\gamma}\right)^{\text{SI}} = 3\cdot 2\pi\cdot\epsilon_0\cdot\bar{\lambda}^3\cdot\frac{2J'+1}{2J+1} \tag{3.31}$$

and $H_0' = \frac{1}{\hbar}\left(\frac{D_0^2}{\hbar\gamma}\right)\left(\frac{\hbar\omega_0}{2\epsilon_0 V}\right)$ contains all the units. This description is valid for N atoms in a volume V and for light with frequency ω_0.

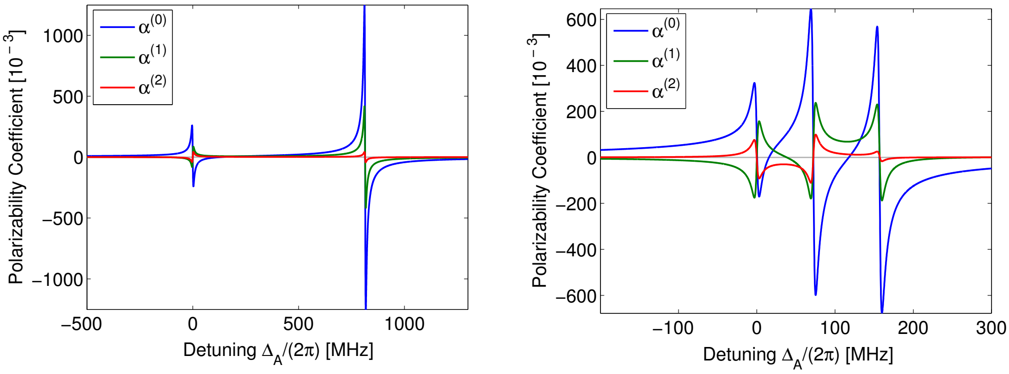

Figure 3.2: D1 line (left) and D2 line (right) polarizability coefficients normalized by $2|\langle J'|d|J\rangle|^2/\hbar\Gamma_A$ for atoms in the F=1 ground state manifold of Rubidium 87.

3.2.4 Hamiltonian in Continuous Variables - 1 Dimensional Propagation Model

We now change to a description where the propagation direction of light is a continuous variable. The transverse modes of the light field are still quantized. This is useful for the description of the propagation of the light field from the beginning to the end of the sample.

As described in App. B.2 the Hamiltonian reads in continuous variables (Eq. B.16)

$$\hat{\mathcal{H}}^{(0)} = \int \rho A \mathrm{d}z \, \frac{2}{\sqrt{3}} H_0 \hat{S}_0(z,t) \, \tilde{T}_0^{(0)}(z,t,\tilde{\Delta}) \tag{3.32}$$

$$\hat{\mathcal{H}}^{(1)} = \int \rho A \mathrm{d}z \, \sqrt{2} H_0 \, \hat{S}_3(z,t) \, \tilde{T}_0^{(1)}(z,t,\tilde{\Delta}) \tag{3.33}$$

$$\hat{\mathcal{H}}^{(2)} = \int \rho A \mathrm{d}z \, H_0 \left[2\left(\hat{S}_1(z,t) \, \tilde{T}_{2+}^{(2)}(z,t,\tilde{\Delta}) + \hat{S}_2(z,t) \, \tilde{T}_{2-}^{(2)}(z,t,\tilde{\Delta}) \right) + \frac{2}{\sqrt{6}} \hat{S}_0 \, \tilde{T}_0^{(2)}(z,t,\tilde{\Delta}) \right]. \tag{3.34}$$

where ρ is the atomic density and A the interaction area.

Now the constant is

$$H_0 = \frac{1}{\hbar} \left(\frac{D_0^2}{\hbar \gamma} \right) \left(\frac{\hbar \omega_0}{2\epsilon_0 A} \right). \tag{3.35}$$

3.2.5 Hamiltonian in Spin Operator Notation

We can rewrite the Hamiltonian using spin operators $\hat{F}_i$ by using the relations B.57 to B.65:

$$\mathcal{H}^{(0)} = \frac{2}{3} C_0 \alpha^{(0)}(\Delta_A) \hat{S}_0 \mathbb{1} \tag{3.36}$$

$$\mathcal{H}^{(1)} = C_0 \alpha^{(1)}(\Delta_A) \hat{S}_3 \hat{F}_z \tag{3.37}$$

$$\mathcal{H}^{(2)} = C_0 \alpha^{(2)}(\Delta_A) \Big[\hat{S}_1 \left(\hat{F}_x^2 - \hat{F}_y^2 \right) + \hat{S}_2 \left(\hat{F}_x \hat{F}_y + \hat{F}_y \hat{F}_x \right) - \hat{S}_0 \left(\hat{F}_z^2 - \tfrac{1}{3} F(F+1) \mathbb{1} \right) \Big], \tag{3.38}$$

where we defined

$$C_0 = \rho A \mathrm{d}z \frac{1}{\hbar}\left(\frac{2|\langle J||d_A||J'\rangle|^2}{\hbar\Gamma_A}\right)\left(\frac{\hbar\omega}{2\epsilon_0 A}\right) \tag{3.39}$$

and omitted the space and time (z,t)-dependence of all operators. A is the interaction area. Figure 3.2 shows the polarizability coefficients $\alpha^{(0)}$, $\alpha^{(1)}$ and $\alpha^{(2)}$ normalized by $2|\langle J'|d|J\rangle|^2/\hbar\Gamma_A$ to be unit free.

3.2.6 Equations of Motion for a 1D Ensemble of Atoms

Using the continuous variable Hamiltonian (Eq. B.16) we can write down the Heisenberg equations of motion.
The time evolution of the atomic density matrix $\hat{\sigma}$ can be decomposed in the three parts of the Hamiltonian

$$\frac{\partial\hat{\sigma}}{\partial t} = -\frac{i}{\hbar}[\hat{\mathcal{H}},\hat{\sigma}] = -\frac{i}{\hbar}[\hat{\mathcal{H}}^{(0)}+\hat{\mathcal{H}}^{(1)}+\hat{\mathcal{H}}^{(2)},\hat{\sigma}] = \frac{\partial\hat{\sigma}^{(0)}}{\partial t}+\frac{\partial\hat{\sigma}^{(1)}}{\partial t}+\frac{\partial\hat{\sigma}^{(2)}}{\partial t}. \tag{3.40}$$

This equation can be solved directly numerically using a matrix representation of the Hamiltonian and the density matrix. For an effective two-level system it is also feasible to write out the commutators, while this is more cumbersome for a spin 1 system. For the spin 1/2 system each component can be written as (leaving out the space-time and detuning dependence of the rank 2 part)

$$\frac{\partial\hat{\sigma}^{(0)}}{\partial t} = 0 \tag{3.41}$$

$$\frac{\partial\hat{\sigma}^{(1)}}{\partial t} = C_A \langle\hat{S}_3(z,t)\rangle \left(\tilde{T}_x^{(1)}(z,t,\tilde{\varDelta}) - \tilde{T}_y^{(1)}(z,t,\tilde{\varDelta})\right) \tag{3.42}$$

$$\frac{\partial\hat{\sigma}^{(2)}}{\partial t} = 2C_A\Big[\sqrt{\frac{3}{2}}\langle\hat{S}_0\rangle\left(\tilde{T}^{(2)}_{1+} - \tilde{T}^{(2)}_{1-}\right) \tag{3.43}$$

$$+\sqrt{3}\left(\langle\hat{S}_1\rangle\tilde{T}^{(2)}_{2-} + \langle\hat{S}_2\rangle\tilde{T}^{(2)}_{2+}\right) \tag{3.44}$$

$$-i\sqrt{\frac{3}{2}}\left(\langle\hat{S}_1\rangle\left(\tilde{T}^{(2)}_{1+}+\tilde{T}^{(2)}_{1-}\right) - \langle\hat{S}_2\rangle\left(\tilde{T}^{(2)}_{1+}-\tilde{T}^{(2)}_{1-}\right)\right)\Big], \tag{3.45}$$

where we introduced the constant $C_A = H_0/\hbar$ and used

$$\hat{T}_x^{(1)} = \frac{1}{\sqrt{2}}\left(\hat{T}_{-1}^{(1)} - \hat{T}_1^1\right) \qquad \hat{T}_y^{(1)} = \frac{i}{\sqrt{2}}\left(\hat{T}_1^{(1)} + \hat{T}_{-1}^1\right) \tag{3.46}$$

$$\hat{T}_{1+}^{(2)} = \frac{1}{2}\left(\hat{T}_1^{(2)} + \hat{T}_{-1}^{(2)}\right) \qquad \hat{T}_{1-}^{(2)} = \frac{1}{2i}\left(\hat{T}_{-1}^{(2)} - \hat{T}_1^{(2)}\right) \tag{3.47}$$

as well as the commutation relations (Eq. B.69) and the density matrix decomposition into spin matrices (Eq. B.70). The expectation value of the Stokes operators is obtained by tracing over the product of the Stokes operator with the second-order coherence matrix of light $\hat{p}$ as defined in App. B.5, which is the light analog of the density matrix

$$\langle\hat{S}_k(z,t)\rangle = \mathrm{tr}(\hat{S}_k(z,t)\hat{p}). \tag{3.48}$$

Analogously we can write for the time evolution of the second-order coherence matrix of the light (Eq. B.24)

$$\frac{\partial \hat{p}}{\partial z} + \frac{1}{c}\frac{\partial \hat{p}}{\partial t} = -\frac{i}{\hbar c}[\hat{\mathcal{H}}, \hat{p}] \tag{3.49}$$

where we will neglect retardation and set $\frac{1}{c}\frac{\partial \hat{p}}{\partial t} \to 0$. By means of the commutation relations for Stokes operators (Eq. B.77) we can get rid of the integrals. The decomposed evolution is then

$$\frac{\partial \hat{p}^{(0)}}{\partial z} = 0 \tag{3.50}$$

$$\frac{\partial \hat{p}^{(1)}}{\partial z} = C_L\ \sqrt{2}\langle \tilde{T}_0^{(1)}(z,t,\tilde{\Delta})\rangle \left(\hat{S}_2(z,t) - \hat{S}_1(z,t)\right) \tag{3.51}$$

$$\frac{\partial \hat{p}^{(2)}}{\partial z} = C_L\, 2\left(\langle \tilde{T}_{2+}^{(2)}(z,t,\tilde{\Delta})\rangle \left(\hat{S}_3(z,t) - \hat{S}_2(z,t)\right) + \langle \tilde{T}_{2-}^{(2)}(z,t,\tilde{\Delta})\rangle \left(\hat{S}_1(z,t) - \hat{S}_2(z,t)\right)\right), \tag{3.52}$$

where we used the expectation value of the atomic tensors

$$\langle \tilde{T}_m^{(j)}(z,t,\tilde{\Delta})\rangle = \mathrm{tr}(\tilde{T}_m^{(j)}(z,t,\tilde{\Delta})\hat{\sigma}) \tag{3.53}$$

and defined the constant $C_L = \frac{H_0}{\hbar c}\rho A$.
The complete set of equations can be solved by making a linear approximation

$$\hat{p}(z+\Delta z) \approx \hat{p}(z) + \frac{\partial \hat{p}}{\partial z}\Delta z \tag{3.54}$$

$$\hat{\sigma}(t+\Delta t) \approx \hat{\sigma}(t) + \frac{\partial \hat{\sigma}}{\partial t}\Delta t \tag{3.55}$$

where Δz and Δt need to be small steps compared to the derivatives. An exact solution can be obtained in some cases analytically by means of Laplace transformations [KMS$^+$05].

3.2.7 Effect of Magnetic Fields

The general Hamiltonian describing the interaction of a magnetic moment $\vec{\mu}$ with a magnetic field $\vec{B}$ is

$$\hat{\mathcal{H}}_B = -\vec{\mu}\cdot\vec{\mathbf{B}} \tag{3.56}$$

with

$$\vec{\mu} = -g_J\mu_B\vec{\mathbf{J}} + g_I\mu_N\vec{\mathbf{I}} \approx -g_J\mu_B\vec{\mathbf{J}}, \tag{3.57}$$

where the last step is an approximation, since μ_N is much smaller than the Bohr magneton μ_B. g is the Landé g-factor.
The Hamiltonian can be mapped onto the total angular momentum $\vec{\mathbf{F}} = (\hat{\mathbf{f}}_x, \hat{\mathbf{f}}_y, \hat{\mathbf{f}}_z)$ (Eq. B.67) if the magnetic field is small, such that F is still a good quantum number:

$$\hat{\mathcal{H}}_B = \frac{g_J\mu_B}{\hbar}\vec{\mathbf{J}}\cdot\vec{\mathbf{B}} = \frac{g_J\mu_B}{\hbar}\frac{\langle\vec{\mathbf{J}}\cdot\vec{\mathbf{F}}\rangle}{F(F+1)}\vec{\mathbf{F}}\cdot\vec{\mathbf{B}} = \frac{g_F\mu_B}{\hbar}\vec{\mathbf{F}}\cdot\vec{\mathbf{B}} \tag{3.58}$$

$$= \frac{g_F\mu_B}{\hbar}(\hat{f}_xB_x + \hat{f}_yB_y + \hat{f}_zB_z) = \omega_x\hat{f}_x + \omega_y\hat{f}_y + \omega_z\hat{f}_z \tag{3.59}$$

$$= \frac{1}{\sqrt{2}}\Big((\omega_x + i\omega_y)\hat{f}_{-1} - (\omega_x - i\omega_y)\hat{f}_{+}\Big) + \omega_z\hat{f}_z \tag{3.60}$$

with the Landé g_F-factor

$$g_F = g_J\frac{F(F+1) + J(J+1) - I(I+1)}{2F(F+1)} \tag{3.61}$$

and ω_i the Larmor frequency for each spatial direction. From relation 3.25 it is evident that it is a type (1), vector-like, interaction.
The equations of motion in a $F = 1/2$ system are given for collective continuous variables as

$$\frac{\partial\hat{\sigma}^B}{\partial t} = -\frac{i}{\hbar}\left[\hat{\mathcal{H}}_B, \hat{\sigma}^B\right] = \frac{1}{2\hbar}\frac{1}{\rho A}\Big(\left(\omega_y - \omega_z\right)\hat{f}_x + \left(\omega_z - \omega_x\right)\hat{f}_y + \left(\omega_x - \omega_y\right)\hat{f}_z\Big). \tag{3.62}$$

For the $F = 1$ system the equation gets considerably more complicated since one now needs to calculate the time evolution of all the components of the density matrix, Eq. B.71. This is done in App. B.4.3.
The evolution of the total angular momentum vector is generally given as

$$\frac{\partial\vec{\mathbf{F}}}{\partial t} = \frac{g_F\mu_B}{\hbar}\vec{\mathbf{F}}\times\vec{\mathbf{B}} \tag{3.63}$$

explicitly showing the vector-like rotations.

3.3 Faraday Rotation

In Faraday rotation linearly polarized light is rotated by an angle θ_F by interacting with matter. This happens if the interaction strength for right hand and left hand polarizations is different. In terms of the decomposed Hamiltonian, Faraday rotation appears if the evolution of the light field due to the $\hat{\alpha}^{(1)}$ term is non-vanishing and ideally the rank 2 part is vanishing.
In a simple model considering only phase-shifts ϕ, the Faraday angle is the rotation angle of the electric field vector which is identical to half of the phase-shift difference between the two circular polarizations ϕ_R and ϕ_L:

$$\theta_F = \frac{1}{2}\left(\phi_R - \phi_L\right). \tag{3.64}$$

This implies the proportionality to the refractive index difference, since $\phi_R - \phi_L = \int \frac{2\pi}{\lambda}(n_R - n_L)\mathrm{d}z$.
In terms of Stokes vectors the equations of motion are

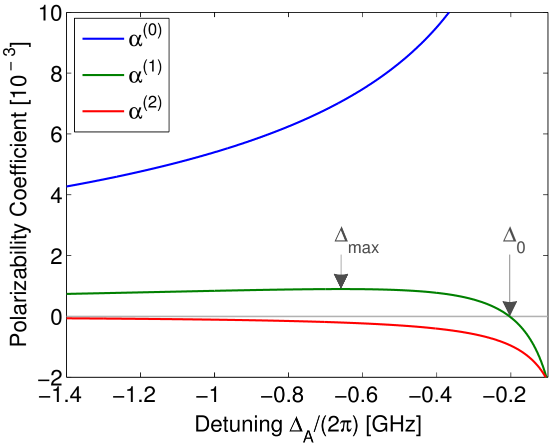

Figure 3.3: D1 line polarizability coefficients for red detunings. The coefficients are normalized by $2|\langle J'|d|J\rangle|^2/\hbar\Gamma_A$. Marked are the point where Faraday rotation ($\alpha^{(1)}$) vanishes and the point with a local maximum in the rotation.

$$\frac{\partial \hat{S}_1}{\partial z} = C_L\left(\sqrt{2}\langle \hat{T}_0^{(1)}\rangle \hat{S}_2 - 2\langle \hat{T}_{2-}^{(2)}\rangle \hat{S}_3\right) \tag{3.65}$$

$$\frac{\partial \hat{S}_2}{\partial z} = C_L\left(-\sqrt{2}\langle \hat{T}_0^{(1)}\rangle \hat{S}_1 + 2\langle \hat{T}_{2+}^{(2)}\rangle \hat{S}_3\right) \tag{3.66}$$

$$\frac{\partial \hat{S}_3}{\partial z} = C_L\left(\hat{S}_1\langle \hat{T}_{2-}^{(2)}\rangle - \hat{S}_2\langle \hat{T}_{2+}^{(2)}\rangle\right). \tag{3.67}$$

Assuming the light enters the ensemble in a linear polarization ($\hat{S}_1$, $\hat{S}_2$) and the expectation values of the Raman terms are negligible ($\langle \hat{T}_{2+}^{(2)}\rangle = \langle \hat{T}_{2-}^{(2)}\rangle = 0$) as well as the influence of a magnetic field, the Faraday angle is

$$\theta_F = \frac{1}{2}\left(\arctan\left(\frac{\langle S_2^{end}\rangle}{\langle S_1^{end}\rangle}\right) - \arctan\left(\frac{\langle S_2^{in}\rangle}{\langle S_1^{in}\rangle}\right)\right). \tag{3.68}$$

The zero crossing of the Faraday angle close to the D1 line is at $\Delta_0 = \Delta_{hfs}/4 = -203.6\text{MHz}$ and a local maximum occurs at $\Delta_{max} = \Delta_{hfs}\frac{1\pm\sqrt{5}}{4} = -658.9/+251.7\text{MHz}$ (see Fig. 3.3).

3.4 Raman Type Multimode Memory

A Raman type memory stores information encoded in the polarization of the light in groundstate atomic coherences. This facilitates the rank (2) part of the Hamiltonian and ideally the influence of the rank (1) part and therefore the Faraday rotation signal, should vanish, since it adds an unwanted phase to the atomic coherences. This happens for a detuning of $\Delta_0 = \Delta_{hfs}/4 = -203.6\text{MHz}$, red of the D1 line of ^{87}Rb. At this detuning the multilevel system closely resembles a three-level system. The write-in stage of the memory can be described by a beam-splitter type interaction with a Hamiltonian of the form $\mathcal{H}_{write} \sim \hat{a}_A^\dagger \hat{a}_L + H.C.$, while the read-out stage can be described by a parametric gain type interaction with a Hamiltonian $\mathcal{H}_{read} \sim \hat{a}_A \hat{a}_L^\dagger + H.C.$. Figure 3.4 shows the write-in stage. The atoms are initially in the F=1, $m_F = -1$ state. The quantum light mode $\hat{a}_L$ is shown in blue and a classical drive field in red. The atomic collective excitation $\hat{a}_A$ is stored in the coherence between the F=1, $m_F = -1$ and the F=1, $m_F = 1$ state. During

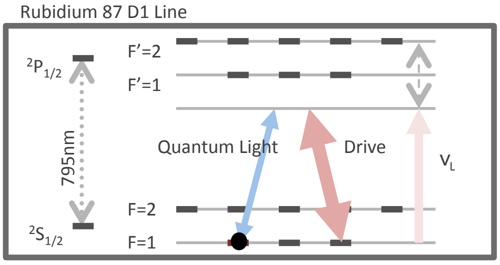

Figure 3.4: Memory scheme showing the drive light and the quantum light, which is to be stored. The protocol is a Raman type memory, which can be described by a beamsplitter Hamiltonian.

the read-out stage only the drive light is applied in order to retrieve the quantum state of light.

In a spatially-multimode memory several quantum states of light can be stored either in various spatial mode-profiles, as for example the Bessel-modes or by using different input angles for the quantum state with respect to the drive field.

Four

Diffraction

Introduction To be able to reconstruct the shape and physical properties of an imaging object, it is relevant to estimate possible distortions of the image. The change in shape of an electric field due to propagation and obstacles in the propagation path is called diffraction. In the first part of the chapter distortions due to the imaging apparatus itself are investigated: the effect of apertures, the resolution limit and aberrations. In the second part diffraction due to the imaging object and the resulting difficulty in deducing physical parameters is discussed. The last section discusses high density corrections to the refractive index.

General Diffraction Theory The propagation of an electric field can be described by the Helmholtz equation. The field after an obstacle can be seen as the superposition of many spherical waves according to the Huygens-Fresnel principal [BW05]. These concepts are combined in the Fresnel-Kirchhoff diffraction formula. The resulting integral can be further simplified for near-field scattering as the Fresnel integral and for far-field scattering as the Fraunhofer integral.
If we know the field distribution on a plane with transverse cylindrical coordinates (r, ϕ) at position $z = 0$, which we call $E(r, \phi)$, then the Fresnel integral will give us the field distribution $E(r', \theta)$ at a position z

$$E(r', \theta, z) = \frac{\exp(ikz)}{i\lambda z} \exp\left(i\frac{k}{2z}r'^2\right) \int_0^\infty \left\{E(r,\phi)\exp\left(i\frac{k}{2z}r^2\right)\right\} J_0\left(\frac{krr'}{z}\right) 2\pi r \mathrm{d}r. \quad (4.1)$$

The cylindrical coordinates allow us to rewrite the angular integral in terms of a zeroth order Bessel function of the first kind, $J_0(\cdot)$. The properties of the light field are the wave vector $k = 2\pi/\lambda$ and the wavelength λ. In the Fraunhofer approximation one is interested in the field at a large distance compared to the radial extend of the initial field $z >> kr_{max}^2/2$ and it allows us to neglect the phase factor inside the curly brackets. The resulting integral is then proportional to a Hankel transform (a Fourier transform using Bessel functions). One can therefore obtain the field distribution on the final plane by Fourier transforming the initial field distribution.

4.1 Imaging System Modeling

This section presents the modeling of an image formation process by optical elements. An ideal imaging system, with ideal lenses, could be fully described by its magnification. A real imaging system contains many apertures, that limit the amount of light and spatial frequency spectrum passing from the object plane to the image plane. This process limits the quality or focus of an image and is parametrized by the resolution.
An imaging system can be completely described by the size and position of its entrance

and exit pupils. These pupils are images of the most restricting aperture within the system viewed from the entrance or exit side of the system.
If we call the exit pupil in real space $P(x,y)$ and its distance to the image plane z_{ep}, the optical transfer function in Fourier space (f_X, f_Y) is given by [Goo06]

$$H(f_X, f_Y) = (A\lambda z_{ep})P(-\lambda z_{ep} f_X, -\lambda z_{ep} f_Y), \tag{4.2}$$

where the prefactor can be set to 1. In this relation A is an amplitude. The most common pupil functions are the ones for round and rectangular apertures:

$$P_{round}(r) = \begin{cases} 1 & \text{if } \sqrt{x^2+y^2} < 1 \\ 0.5 & \text{if } \sqrt{x^2+y^2} = 1 \\ 0 & \text{otherwise} \end{cases} \tag{4.3}$$

$$P_{rect}(x) = \begin{cases} 1 & \text{if } |x| < 0.5 \\ 0.5 & \text{if } |x| = 0.5 \\ 0 & \text{otherwise} \end{cases} . \tag{4.4}$$

Once the optical transfer function is found we can easily multiply it with the Fourier transform of the ideal field strength distribution on the image plane, $U_g(u,v)$,

$$G_g(f_X, f_Y) = \int\int_{-\infty}^{+\infty} U_g(u,v) \exp\left(-i2\pi(f_X u + f_Y v)\right) \mathrm{d}u\mathrm{d}v, \tag{4.5}$$

where

$$U_g(u,v) = \frac{1}{|M_i|} U_0\left(\frac{u}{M_i}, \frac{v}{M_i}\right), \tag{4.6}$$

$U_0\left(\frac{u}{M_i}, \frac{v}{M_i}\right)$ is the electric field distribution in the object plane and M_i the magnification, to obtain:

$$G_i(f_X, f_Y) = H(f_X, f_Y) G_g(f_X, f_Y). \tag{4.7}$$

The function $G_i(f_X, f_Y)$ is the Fourier transform of the observed field distribution in the image plane and includes the finite resolution of the imaging system. The optical transfer function is an impulse response function, i.e. giving the response of the system to a point source. It defines the size of the smallest object that can be imaged, the resolution of the system. The optical transfer function in real-space is called the point-spread function $h(u,v)$ and is obtained by a backward Fourier transform of $H(f_X, f_Y)$.
The point-spread function of round apertures in the Fraunhofer approximation [Goo06, BW05] are Bessel functions of the first kind of first order:

$$h(x) = \frac{\pi w^2}{i\lambda z_{ep}} \exp\left(ikz_{ep}\right) \exp\left(\frac{ikx^2}{2z_{ep}}\right) \frac{2z_{ep}}{kw} J_1\left(\frac{kwx}{\lambda z_{ep}}\right), \tag{4.8}$$

and this results in an Airy intensity pattern. For rectangular apertures the point-spread function is proportional to a sinc function:

$$h(x) = \frac{D^2}{i\lambda z_{ep}} \exp\left(ikz_{ep}\right) \exp\left(\frac{ikx^2}{2z_{ep}}\right) \operatorname{sinc}\left(\frac{Dx}{\lambda z_{ep}}\right). \tag{4.9}$$

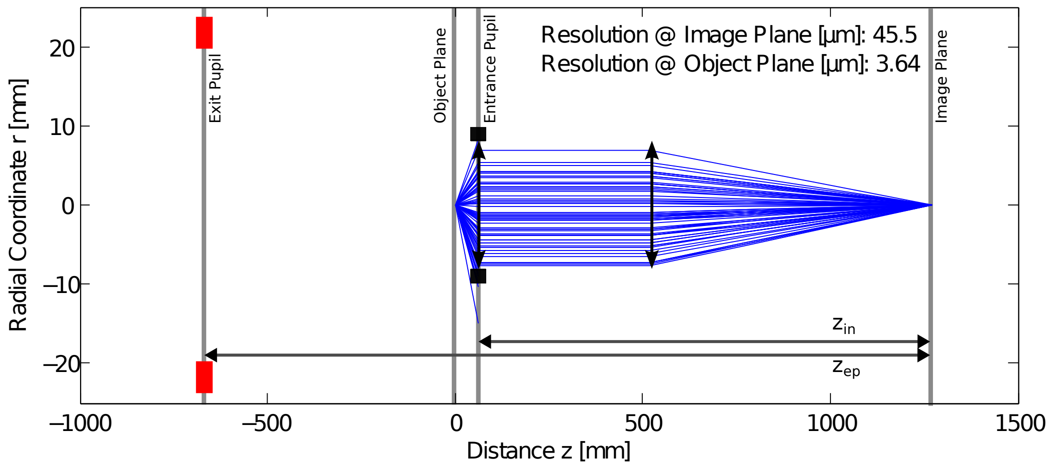

Figure 4.1: Ray tracing through the experimental Faraday imaging system. The object is a point source and is placed at z=0. The first lens is situated at z=60mm and the second lens at z=520mm. The image plane is situated at z=1270mm, at the right end of the graph. In blue are shown the light rays, red is the determined exit pupil and black the entrance pupil. The determined resolution in the object plane is $\delta = 3.64\mu\text{m}$.

A common criterion for resolution is the two-point or Rayleigh criterion. It says that in an imaging system with round apertures, two point sources can be distinguished, if the first zero of one Airy pattern falls onto the peak of the other. This criterion is valid for an incoherent imaging system. For coherent imaging systems the resolvability of two points depends on their relative phase and can be better or worse than for an incoherent system. The Rayleigh resolution criterion for round aperture systems is:

$$\delta_{round} = 0.61 \frac{\lambda z_{ep}}{w} \tag{4.10}$$

where λ is the wavelength, z_{ep} is the distance of the exit pupil to the image plane and w is the radius of the pupil. The numerical aperture is found by using the entrance pupil of radius w_{in} and the distance z_{in} to the object plane. It is $\text{NA} = \sin\theta = w_{in}/z_{in}$, where θ is the half opening angle of the imaging system.
In the case of a 1D rectangular aperture of width D the Rayleigh resolution criterion is

$$\delta_{rect} = \frac{\lambda z_{ep}}{D}. \tag{4.11}$$

The resolution on the object plane δ^{object} can be obtained by scaling with the magnification: $\delta^{object} = \delta/M$.

4.1.1 Ray Tracing

To find the entrance and exit pupil and therefore the resolution of the an imaging system one needs to employ a ray tracing algorithm. We apply this to the Faraday imaging system, as shown in Fig. 10.5. In Fig. 4.1 the resulting beam of rays is presented. The object (left) is assumed to be a point source. Rays emerge from this point with random angle towards the imaging plane on the right end. The outer rays are already lost at the first lens (z=60mm). This lens is found to be the most restricting aperture of this system. The second lens is at z=520mm. There are several apertures (beam-splitter, mirrors, lenses) in the system that do not introduce further diffraction.
The entrance and exit pupils are found by imaging the aperture defined by the first lens towards the beginning/end of the imaging system. The entrance pupil is therefore identical to the determined most restricting aperture, which is not always the case. The exit pupil

Faraday Imaging System Parameters		
Name	Symbol	Value
Wavelength	λ	795nm
Lens 1 focal length	f_1	60mm
Lens 1 position	z_{L1}	60mm
Lens 1 radius	w_{L1}	8mm
Lens 2 focal length	f_2	750mm
Lens 2 position	z_{L2}	520mm
Lens 2 radius	w_{L2}	10mm
Magnification	M_i	12.5
Exit pupil distance to image plane	z_{ep}	1939.7mm
Exit pupil radius	w	20.69mm
Entrance pupil distance to image plane	z_{in}	60mm
Entrance pupil radius	w_{in}	8mm

Table 4.1: Parameters of our Faraday imaging setup, which are used in the ray-tracing algorithm.

is found by using the second lens (of focal length f) to create a geometric optics image at z_{IM}, relative to the lens, of the aperture at z_O:

$$\frac{1}{z_O} + \frac{1}{z_{\mathrm{IM}}} = \frac{1}{f}. \tag{4.12}$$

The exit pupil comes to lie on the left end at a distance $z_{ep} = 1939.7\mathrm{mm}$ to the imaging plane with a radius of $w = 20.69\mathrm{mm}$, resulting in a resolution of $\delta = 45\mu\mathrm{m}$ on the image plane and $\delta^{object} = 3.64\mu\mathrm{m}$. The exit pupil does not lie on the imaging plane in our setup, since $z_O < f$, the distance between the two lenses is smaller than the sum of their focal lengths. The entrance pupil is found to correspond to the first lens of the system at a distance $z_{in} = 60\mathrm{mm}$ from the object plane and with a radius of $w_{in} = 8\mathrm{mm}$. This results in a numerical aperture of $\mathrm{NA} = 0.13$ and a full opening angle of $2\theta = 15°$.
The resulting point-spread function in spatial coordinates on the camera plane is shown in Fig. 4.2.

4.1.2 Image Propagation

Ray-tracing is simple geometric optics applied to a point source in order to characterize the imaging system. This section will show how to propagate an arbitrary object field distribution through an imaging system including lenses, apertures and free space propagation. This was done in order to study the influence of lens positioning on the final image.
The apertures can be treated by the formalism shown above, using the exit pupil to find the Fourier transform of the point-spread function and applying it to the ideal image U_g. Lenses introduce a phase profile onto the field distribution [Goo06] having the form:

$$Q[f]\{E(r)\} = \exp\left(-i\frac{\pi r^2}{\lambda f}\right)E(r). \tag{4.13}$$

Field propagation through free space is described by the Fresnel diffraction integral and can be written in the form of a propagator. The field distribution on the input plane at z_{in} is $E(r)$ and on the observation plane at z_o is $E(\rho)$:

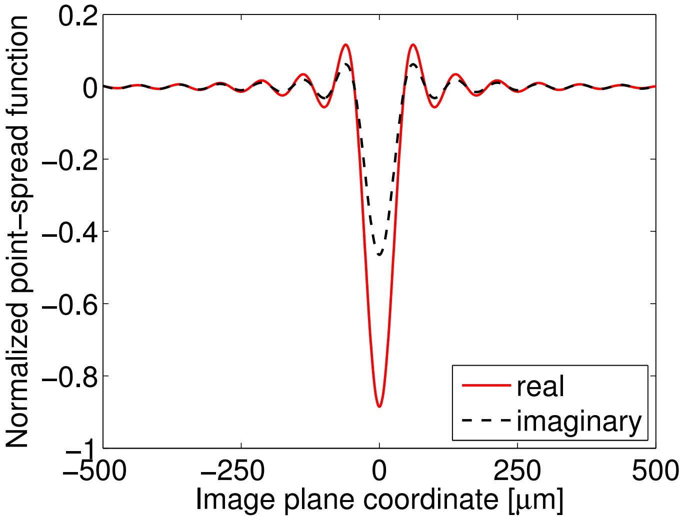

Figure 4.2: Real and imaginary parts of the point-spread function normalized to the absolute value in the center. Parameters are the ones for the Faraday imaging system as presented in Table ??. The abscissa gives the coordinate on the camera plane.

$$\mathcal{R}[z_o - z_{in}]\{E(r)\} = \int \mathrm{d}r E(r) r \frac{2\pi}{i\lambda(z_o - z_{in})} J_0\left(\frac{kr\rho}{z_o - z_{in}}\right) \times \\ \exp\left(ik(z_o - z_{in})\right) \exp\left(ik\frac{r^2+\rho^2}{2(z_o - z_{in})}\right). \tag{4.14}$$

The propagator is written in cylindrical coordinates.

These operators can be conveniently concatenated. As an example: if we have a system, which contains a lens with focal length 60mm and then 200mm of free space, we can obtain the final field distribution $E_f(\rho)$ from the known input field $E_i(r)$ by first calculating the field after the lens $E_1(\rho_1) = \mathcal{Q}[60\text{mm}]\{E_i(r)\}$ and then $E_f(\rho) = \mathcal{R}[200\text{mm}]\{E_1(\rho_1)\}$. In this way we can obtain the resulting electric field distribution on the camera of an arbitrary imaging system.

4.1.3 Aberrations

Aberrations of a lens are deviations of the wave-front after the lens from a perfect spherical wavefront, resulting in distortions of the image. These distortions become important in a spatial multimode memory, when one wants to reproduce an arbitrary mode function. Aberrations are not considered in the data analysis of this theses, but are included at this point for completeness.

Aberrations can be treated within the concept of the point-spread function by introducing a generalized pupil function

$$\mathcal{P}(x,y) = P(x,y)\exp\left(ikW(x,y)\right), \tag{4.15}$$

where $W(x,y)$ is the phase-front path difference due to lens aberrations, which has the same effect as a phase plate. The optical transfer function is then [Goo06]

$$\mathcal{H}(f_X, f_Y) = P(\lambda z_{ep} f_X, \lambda z_{ep} f_Y)\exp\left(ikW(\lambda z_{ep} f_X, \lambda z_{ep} f_Y)\right). \tag{4.16}$$

The aberration function $W(x,y)$ can be calculated in terms of Zernike polynomials using Seidel coefficients [BW05].

4.1.4 Vector Field Diffraction

The electromagnetic field is vectorial. In the scalar approximation of diffraction, which we used so far, the three vector components are assumed to be independent. The diffraction process is assumed not to mix the components. This is said to be a fair approximation for imaging systems with low numerical apertures, which is the case in our experiment. If this still holds for diffraction by the atomic cloud, which we discuss in the next section, is difficult to estimate and depends on the strength of the inhomogeneity of the density distribution.

4.2 Atomic Ensemble Diffraction

The last sections were concerned with diffraction within the imaging system. This introduces distortions on an otherwise ideal image. This section treats diffraction and refraction, also called lensing, of our imaging object, the atomic ensemble itself. The goal of imaging an atomic cloud is notoriously to reconstruct the density distribution of the cloud, finding the radii and peak densities. An atomic ensemble, trapped in an inhomogeneous trap, though, has also an inhomogeneous density profile. This will make the ensemble behave similar to a lens. A column integrated density distribution is then no longer an appropriate model.

I already introduced a simple model for diffraction in Sec. 3.1.2. In this section i want to elaborate on this topic.

4.2.1 Diffraction Mode Shape Without Propagation

For this model [MPO$^+$05], the atoms are assumed as independent dipole scatterers, that are driven by the electric field at their specific position in the atomic ensemble. Their radiated fields are then integrated over the whole sample to give the total field after the sample. The model disregards multiple scattering (first-order Born approximation) and the variation of the drive field along the propagation direction.

Propagation of a light field $\mathbf{E}(\mathbf{r},\omega)$ is described by Maxwell's wave equation for inhomogeneous media

$$\nabla^2\mathbf{E}(\mathbf{r},\omega) + k^2\epsilon(\mathbf{r},\omega)\mathbf{E}(\mathbf{r},\omega) + \mathrm{grad}\left[\mathbf{E}(\mathbf{r},\omega)\mathrm{grad}\left(\ln\epsilon(\mathbf{r},\omega)\right)\right] = 0. \tag{4.17}$$

The scattering properties of the medium are described by the dielectric constant $\epsilon(\mathbf{r},\omega)$, which is related to the refractive index by the Maxwell formula $\epsilon(\mathbf{r},\omega) = n^2(\mathbf{r},\omega)$, where ω is the frequency of the light field, $k = 2\pi/\lambda$ is the wavenumber and λ is the wavelength. The gradient part of the equation makes it very difficult to solve. Assuming that the refractive index is approximately constant over a wavelength we can simplify it to get

$$\nabla^2\mathbf{E}(\mathbf{r},\omega) + k^2 n^2(\mathbf{r},\omega)\mathbf{E}(\mathbf{r},\omega) = 0. \tag{4.18}$$

Further we assume scalar fields, such that each vector component can be solved independently. After introducing a free-space Green's function and volume integrating [BW05] we can rewrite the equation in integral form

$$E_{sc}(r) = \int r\mathrm{d}r\mathrm{d}z\mathrm{d}\theta F(r,\Delta)E_{in}(r)K(|r-r'|), \tag{4.19}$$

where $F(r,\Delta)$ is the scattering potential and $K(|r-r'|)$ is the field propagator. The scattering potential $F(r,\Delta)$ includes the electronic properties of the atoms and the density $\rho(r)$ of the whole ensemble. It can be written in terms of the refractive index, the susceptibility $\chi(r,\Delta)$ or explicit as a sum over transitions i:

$$\begin{aligned} F(r,\Delta) &= \frac{1}{4\pi}k^2(n(r,\Delta)^2-1) = \frac{\pi}{\lambda}\chi(r,\Delta) \\ &= (-\lambda)\frac{3}{4\pi}\rho(\mathbf{r})\sum_i \xi_i^2 \frac{2\Delta_i/\Gamma - i}{1+(2\Delta_i/\Gamma)^2}\frac{2J'+1}{2J+1}. \end{aligned} \tag{4.20}$$

The sum over transitions includes the detuning Δ_i. The interaction strength parameters ξ_i are defined by the dipole moment of the i'th transition as $d_i = \xi_i|\langle J|d|J'\rangle|$, where J is the total electronic angular momentum of the ground state and J' of the excited state. The full linewidth of the transition is Γ. The free-space field propagator in cylindrical coordinates is

$$K(|r-r'|,\phi) = \frac{\exp\left(-ik|z'-z|\right)}{|z'-z|}\exp\left(ikrr'\frac{\cos(\phi-\theta)}{z'-z}\right)\exp\left(-ik\frac{r^2+r'^2}{2(z'-z)}\right). \tag{4.21}$$

Assuming the scattered field amplitude to be much smaller than the probe amplitude we can write the total field as a sum. This is known as the integral equation of potential scattering [BW05]

$$E_{tot}(r,z) = E_{in}(r,z) + E_{sc}(r,z). \tag{4.22}$$

As the input light field we choose a Gaussian beam, matching the experimental conditions:

$$E_{in}(r,z) = E_0\frac{w_0}{w(z)}\exp\left(-\frac{r^2}{w^2(z)}\right)\exp\left(-ikz-ik\frac{r^2}{2R(z)}+i\zeta(z)\right), \tag{4.23}$$

where the $1/e^2$ radius is $w(z) = w_0\sqrt{1+(z/z_R)^2}$, w_0 is the waist and $z_R = \pi w_0^2/\lambda$ is the Rayleigh range. The radius of curvature of the field is $R(z) = z\left(1+(z_R/z)^2\right)$ and $\zeta(z) = \arctan(z/z_R)$ is called the Gouy phase. The atomic density distribution is assumed to be Gaussian (see App. A), even for modeling BECs. This will allow us to solve the transverse integrals analytically. Leaving only the z part of the integral to be solved numerically. The transverse integral has the general form and solution:

$$C\int_0^\infty r\mathrm{d}r\int_0^{2\pi}\mathrm{d}\theta\exp\left(ar^2+br\cos\left(\phi-\theta\right)\right) = -C\frac{\pi}{a}\exp\left(-\frac{b^2}{4a}\right). \tag{4.24}$$

The model can be extended to the case of Faraday rotation by reintroducing polarization channels. The incoming field with polarization $\mathbf{e}_{in}$ needs to be mapped into the atomic system. If we choose the quantization axis along the propagation direction of light, an incoming linear polarization will be mapped into a circular basis $\mathbf{e}_{l/r}$. Each of the two polarization channels has a different transition strength. The resulting scattered fields are then mapped into the detection basis $\mathbf{e}_D$. The polarization mappings can be performed by using the relation $\mathbf{e}_q\cdot\mathbf{e}_{q'}^* = \delta_{qq'}$. Converting the electric fields into intensities we obtain images that can be compared to the experimental results. The diffraction of the imaging

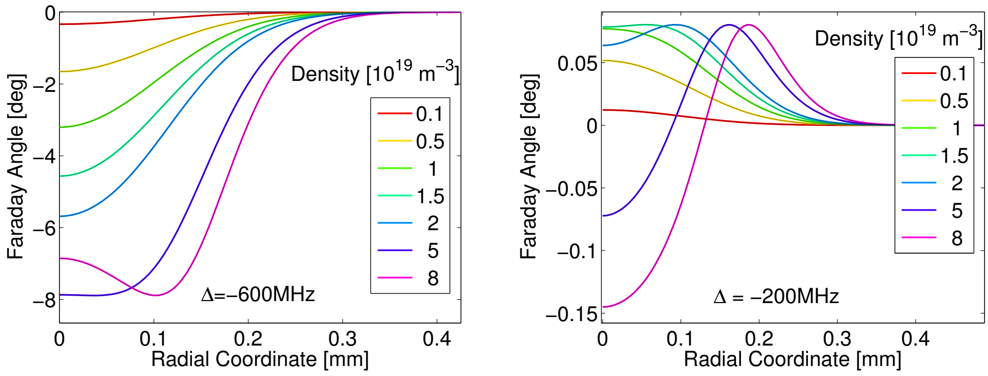

Figure 4.3: Faraday rotation model including diffraction, but no propagation of the field inside the sample. Plotted is the angle as a function of camera plane radial coordinate for various densities. The atomic ensemble Gaussian $e^{-1/2}$ waists are $w_r = 7.7\mu\text{m}$ and $w_Z = 70.5\mu\text{m}$, the beam waist is $w_0 = 140\mu\text{m}$. Left: the detuning is $\varDelta = -600\text{MHz}$ and right panel: $\varDelta = -200\text{MHz}$.

system and the propagation to the camera plane can be performed as discussed in the previous sections.

In Fig. 4.3 Faraday angle profiles on the camera plane are shown for various densities and two detunings, left panel $\varDelta = -600\text{MHz}$ and right panel $\varDelta = -200\text{MHz}$. For both detunings the profiles at low densities are images of the Gaussian density distribution, because diffraction effects are negligible and a simple 1D model would give the same result. For higher densities diffraction effects start to play a role. At the −600MHz detuning diffraction effects are visible for $\rho_0 = 5\ 10^{-19}\text{m}^{-3}$ and $\rho_0 = 8\ 10^{-19}\text{m}^{-3}$. A dip in the middle of the Faraday profile occurs at the largest density. At The −200MHz detuning diffraction effects are even stronger. For large densities the peak Faraday angle at r=0 does not increase as expected from 1D models, but changes sign. An image at this density shows a ring shaped structure.

The simulations show that even for a model that neglects propagation of light through the sample and only models a mode-shape diffraction effects are present as the density is increased.

4.2.2 3D Field Propagation in Cylindrical Coordinates

The following section summarizes the 3D diffraction model developed in [ZGGS11] for a three-level quantum memory. A collaboration with the authors helped us to get a better understanding of the diffraction effects present in our system when light propagation is taken into account. In Sec. 11.3 we compare this model to our Faraday rotation data.

The model assumes a Gaussian density distribution in the transverse coordinate and homogeneous along the propagation direction of the light. The system is therefore described by cylindrical coordinates and Bessel-type mode functions can be employed.

The full equations of motion for the atomic polarization $\mathbf{P}(\tilde{z},\tilde{t})$, the quantum light mode $\mathbf{a}(\tilde{z},\tilde{t})$ and the atomic ground state spin wave $\mathbf{S}(\tilde{z},\tilde{t})$, are after adiabatic elimination and transformation in a co-moving frame, given as

$$\mathbf{P}(\tilde{z},\tilde{t}) = -\frac{\frac{i}{2}\tilde{\Omega}(\tilde{t})}{\frac{1}{2}+i\tilde{\varDelta}}\mathbf{S}(\tilde{z},\tilde{t}) - \frac{\frac{i}{2}\sqrt{\text{OD}_0}}{\frac{1}{2}+i\tilde{\varDelta}}\mathbb{B}\mathbf{a}(\tilde{z},\tilde{t}) \tag{4.25}$$

$$\frac{\partial}{\partial\tilde{z}}\mathbf{a}(\tilde{z},\tilde{t}) = \left(-i\frac{k_\perp^2\sigma_\perp^2}{4\pi F} - \frac{\frac{1}{4}\text{OD}_0}{\frac{1}{2}+i\tilde{\varDelta}}\mathbb{B}^2\right)\mathbf{a}(\tilde{z},\tilde{t}) - \frac{\frac{1}{4}\sqrt{\text{OD}_0}\tilde{\Omega}(\tilde{t})}{\frac{1}{2}+i\tilde{\varDelta}}\mathbb{B}\mathbf{S}(\tilde{z},\tilde{t}) \tag{4.26}$$

$$\frac{\partial}{\partial\tilde{t}}\mathbf{S}(\tilde{z},\tilde{t}) = -\frac{\frac{1}{4}|\tilde{\Omega}(\tilde{t})|^2}{\frac{1}{2}+i\tilde{\varDelta}}\mathbf{S}(\tilde{z},\tilde{t}) - \frac{\frac{1}{4}\sqrt{\text{OD}_0}\tilde{\Omega}^*(\tilde{t})}{\frac{1}{2}+i\tilde{\varDelta}}\mathbb{B}\mathbf{a}(\tilde{z},\tilde{t}). \tag{4.27}$$

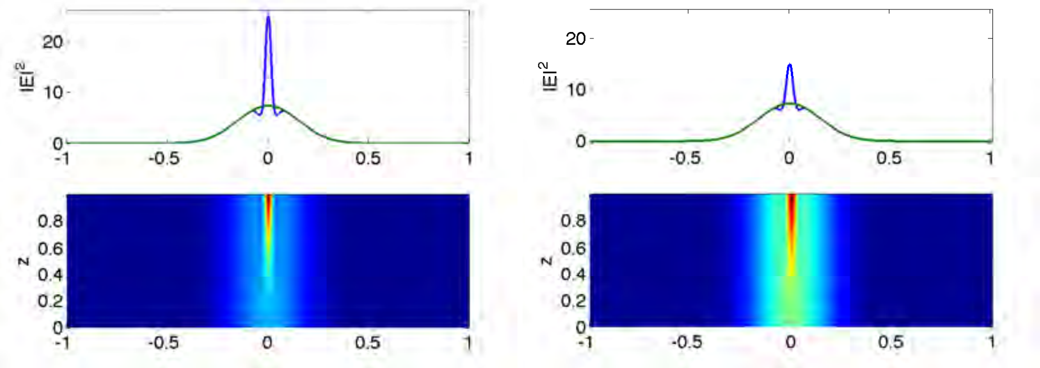

Figure 4.4: The top panel shows the light intensity at the end of the sample (blue) compared to the intensity of the incoming field (green). The lower panel shows the intensity evolution inside the sample. The parameters are characteristic for a typical BEC. The Fresnel number is $F = 0.14$, the optical depth on the σ^- transition is $\mathrm{OD} = 1894$ and the detuning is chosen to be $\Delta_A = -600\mathrm{MHz}$ with respect to the F'=1 excited state. Left: the light field interacting on the σ^- transition. Right: light field interacting on the σ^+ transitions. The simulation was performed by Anna Grodecka-Grad.

The spatial coordinates are $\tilde{z} = z/L$, where L is the sample length, and $\mathbf{r}_\perp$, which is the transverse coordinate. The time variable is $\tilde{t} = \gamma t'$, with γ the full linewidth of the transition, and $t' = t - z/c$ is the time in the co-moving frame, where c is the speed of light. The Rabi frequency in the co-moving frame is $\tilde{\Omega} = \Omega(\tilde{t})/\gamma$, where a homogeneous drive field is assumed. The overlap of the Bessel modes $u_{mn}(r_\perp)$ with the Gaussian density distribution of $e^{-1/2}$ width $\sigma_\perp$ is parametrized by

$$\mathbb{B}_{mm'nn'} = \int \mathrm{d}^2\mathbf{r}_\perp u^*_{mn}(r_\perp) u_{m'n'}(r_\perp) \exp\left(-\frac{\mathbf{r}_\perp^2}{4\sigma_\perp^2}\right). \tag{4.28}$$

An important parameter for diffraction as well as memory performance is the Fresnel number $F = \sigma_\perp^2/(L\lambda)$ and the optical depth $\mathrm{OD}(\mathbf{r}_\perp) = \mathrm{OD}_0 \exp\left(-\mathbf{r}_\perp^2/(2\sigma_\perp^2)\right)$.
In order to compare this model to our Faraday data, we can significantly simplify the equations of motion and assume the drive field to be turned off, such that there is only one light field, the quantum mode, propagating through the medium. After setting $\tilde{\Omega}(\tilde{t}) = 0$ we arrive at

$$\mathbf{P}(\tilde{z},\tilde{t}) = -\frac{\frac{i}{2}\sqrt{\mathrm{OD}_0}}{\frac{1}{2} + i\tilde{\Delta}} \mathbb{B}\mathbf{a}(\tilde{z},\tilde{t}) \tag{4.29}$$

$$\frac{\partial}{\partial \tilde{z}}\mathbf{a}(\tilde{z},\tilde{t}) = \left(-i\frac{k_\perp^2\sigma_\perp^2}{4\pi F} - \frac{\frac{1}{4}\mathrm{OD}_0}{\frac{1}{2} + i\tilde{\Delta}}\mathbb{B}^2\right)\mathbf{a}(\tilde{z},\tilde{t}). \tag{4.30}$$

By choosing an appropriate grid for the numerical simulations one can propagate a light field through the atomic ensemble and one obtains the electric field distribution at the end of the sample. Diffraction is accounted for in this model by including the term $-ik_\perp^2\sigma_\perp^2/(4\pi F)$ in the propagation equation of the light, which contains the Fresnel number F and the perpendicular components of the wave vector $k_\perp$.
For the Faraday rotation case we adjusted the refractive index to appropriately model our multilevel situation (level scheme shown in Fig. 11.1). The model nicely treats transversal diffraction. Since it assumes a homogeneous density distribution along z, it is not obvious how to choose the Fresnel number, in order to come closest to our experimental situation,

Figure 4.5: Illustration of lensing. The path of light rays through the atomic ensemble is bent and therefore diverges from a straight line - 1D model. The accumulated phase along the ray and therefore the resulting Faraday angle is altered.

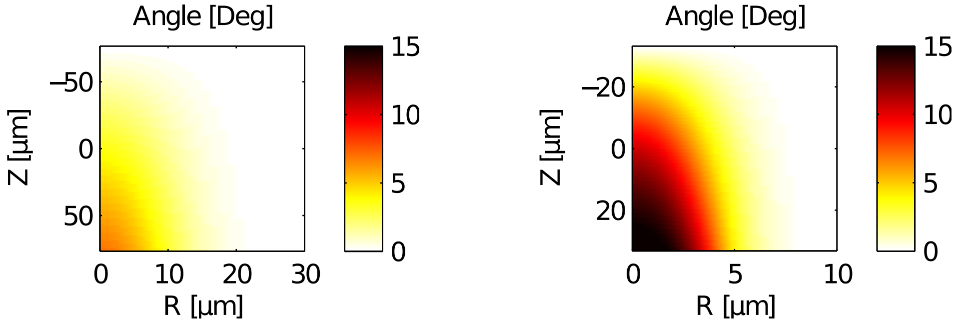

Figure 4.6: Faraday angle evolution through the sample. R denotes the radial coordinate and Z is the coordinate along the propagation direction of light. Left: Parameters corresponding to a typical thermal sample with optical depth OD $= 562$ on the σ^- transition and Fresnel number $F = 0.53$ at a detuning of -600MHz. Right: Parameters corresponding to a typical Bose condensed sample with optical depth D $= 1894$ on the σ^- transition and Fresnel number $F = 0.14$ at a detuning of $\Delta_A = -600$MHz.

with inhomogeneity along z.

Figure 4.4 shows the light intensity distribution for typical parameters of a Bose condensed sample with $\rho_0 = 15\ 10^{19}\text{m}^{-3}$. The left panel shows the intensity of the light driving the stronger, but farther detuned σ^- transition and the right panel the intensity of the σ^+ transitions corresponding to the two circular polarizations involved. The detuning is chosen to be $\Delta_A = -600$MHz with respect to the F'=1 excited state. The plots on the top show the intensity distribution at the end of the sample (blue) compared to the incoming light field (green). The lower plots show the intensity as it evolves through the sample.

The diffraction features are for both light polarizations similar in shape with a large peak appearing in the center as compared to the incoming field and slight reduction of intensity around this peak. The difference in height of the peaks of the two polarizations, signals the presence of Faraday rotation. The evolution of Faraday angles through the sample is shown in Fig. 4.6. The left panel corresponds to typical parameters of a thermal sample (as in Fig. 4.3 with $\rho_0 < 2\ 10^{19}\text{m}^-3$) and the right panel to the BEC parameters. Due to the larger optical depth of the BEC the Faraday rotation angle is larger than for the thermal cloud. There is no strong diffraction visible on the Faraday images. For the BEC with its large density and small spatial extend, this is surprising. The clearly visible diffraction on the intensity profiles at the end of the sample is not visible on the angle plot. The reason for this is the canceling of diffraction when taking the difference of intensities in the analyzing basis as described in the last section. Only for strong diffraction, when the path of a ray of light is significantly bent, is the Faraday angle compromised. This occurs because the Faraday angle is the accumulated phase difference of the two polarizations along the trajectory of the light ray. The accumulated phase along a bent path is different than for a straight trajectory and also the ray exits the atomic cloud at a different radial position. An illustration of this lensing is shown in Fig. 4.5.

4.2.3 Eikonal Equation

It became apparent during the analysis of the data that this model is probably best suited to treat diffraction in an inhomogeneous medium. It addresses the observation of the last section, that the Faraday angle is determined by the accumulated phase along the path of a ray of light through the ensemble of atoms. Due to a lack of time, though, we did not perform any calculations with this model. It is presented here for completeness. There are several publications which use this model for inhomogeneous Gaussian media which diffract Gaussian light beams [BBKS06, BKŻ08].
The electric **E** and magnetic **H** components of a time-dependent electro-magnetic field can be written as

$$\mathbf{E}(\mathbf{r},t) = \mathbf{E}_0(\mathbf{r}) \exp\left(-i\omega t\right), \qquad \mathbf{H}(\mathbf{r},t) = \mathbf{H}_0(\mathbf{r}) \exp\left(-i\omega t\right), \tag{4.31}$$

where the field amplitudes can be further decomposed into an amplitude and a phase:

$$\mathbf{E}_0 = \mathbf{e}(r) \exp\left(ik\mathcal{S}(\mathbf{r})\right), \qquad \mathbf{H}_0 = \mathbf{h}(r) \exp\left(ik\mathcal{S}(\mathbf{r})\right). \tag{4.32}$$

This equation defines $\mathcal{S}(\mathbf{r})$ as the optical path or eikonal. In geometric optics it is then possible to write the evolution of the optical path in terms of the refractive index as the eikonal equation (basic equation of geometrical optics):

$$\left(\mathrm{grad}\mathcal{S}\right)^2 = n^2(x,y,z). \tag{4.33}$$

As the path of a beam is bent due to refraction, the accumulated phase varies according to the inhomogeneous density $\rho(x,y,z)$ of the atoms, that enters the refractive index $n(x,y,z)$.

4.3 Refractive Index

The refractive index is a material property and depends on the density of particles. It is related to the local field with which each dipole in a material is driven and therefore depends on all other dipoles and their local fields, complicating the calculation.
This section will introduce the concept of a refractive index by the Lorentz-Lorenz formula and show low density approximations and high density extensions of it. Then the connections to the Maxwell-Bloch model and diffraction models will be established.

Atomistic Approach: Two-Level System The susceptibility of a two-level atom in SI units is $\chi_{2L} = \chi'_{2L} + i\chi''_{2L}$ [SZ97]

$$\chi'_{2L} = \frac{d^2\rho}{\epsilon_0\hbar}\frac{\Delta}{\gamma^2+\Delta^2}[\sigma^0_{ee} - \sigma^0_{gg}] \tag{4.34}$$

$$\chi''_{2L} = -\frac{d^2\rho}{\epsilon_0\hbar}\frac{\gamma}{\gamma^2+\Delta^2}[\sigma^0_{ee} - \sigma^0_{gg}], \tag{4.35}$$

where σ_{gg} and σ_{ee} are the populations in the ground and excited state, respectively, and we will assume here $\sigma_{gg} = 1$ and $\sigma_{ee} = 0$. The detuning to the excited state is Δ and the half line width is $\gamma = \Gamma/2$.
By using Maxwell's relation one can connect the susceptibility to the refractive index and the electric permittivity ϵ (in SI and cgs units)

$$n = \sqrt{\epsilon} = \sqrt{1+\chi^{SI}} \approx 1 + \frac{1}{2}\chi^{SI} \tag{4.36}$$

$$= \sqrt{1+4\pi\chi^{cgs}} \approx 1 + 2\pi\chi^{cgs}, \tag{4.37}$$

where the approximated form is valid for small susceptibilities (densities). It is used in most models, i.e. the Maxwell-Bloch model of Sec. 3 and all the diffraction models of Sec. 4.2.

The susceptibility and polarizability are connected by the approximate relation $\chi^{SI} = \alpha^{SI}\rho_0/\epsilon_0$ (see next section). For a two-level system they are then explicitly given by

$$\chi_{2L}^{SI} = 3 \cdot 2\pi \cdot \rho_0 \cdot \bar{\lambda}^3 \cdot \frac{2J'+1}{2J+1}\left(\frac{\tilde{\Delta} - i}{\tilde{\Delta}^2 + 1}\right)\xi^2 \tag{4.38}$$

$$\alpha_{2L}^{SI} \approx 3 \cdot 2\pi \cdot \epsilon_0 \cdot \bar{\lambda}^3 \cdot \frac{2J'+1}{2J+1}\left(\frac{\tilde{\Delta} - i}{\tilde{\Delta}^2 + 1}\right)\xi^2, \tag{4.39}$$

where $\bar{\lambda} = \lambda/2\pi$, $\tilde{\Delta} = 2\Delta/\Gamma$ is the detuning normalized to the half linewidth $\Gamma/2$, J and J' are the electronic total angular momentum numbers of the ground and excited states respectively and the dipole moment of the specific transition is $d = \xi|\langle J|d|J'\rangle|$, where ξ is proportional to the Clebsch-Gordan coefficient.

Lorentz-Lorenz Formula The Lorentz-Lorenz formula [BW05] establishes a link between the macroscopic refractive index n and the single atom polarizability α via the local number density ρ_0 of the medium:

$$\alpha_{LL}^{cgs} = \frac{3}{4\pi\rho_0}\frac{n^2-1}{n^2+2} \qquad n = \sqrt{\frac{1 + 2\frac{4\pi}{3}\rho_0\alpha_{LL}^{cgs}}{1 - \frac{4\pi}{3}\rho_0\alpha_{LL}^{cgs}}}. \tag{4.40}$$

Using again Maxwell's relation one finds the connections between χ, α and ϵ. This is done for SI and cgs units in the following overview, where also the approximation between χ and α is indicated:

$$\chi_{LL}^{SI} = \frac{\frac{1}{\epsilon_0}\rho_0\alpha_{LL}^{SI}}{1 - \frac{1}{\epsilon_0}\frac{1}{3}\rho_0\alpha_{LL}^{SI}} \approx \frac{1}{\epsilon_0}\rho_0\alpha_{LL}^{SI} \qquad \chi_{LL}^{cgs} = \frac{\rho_0\alpha_{LL}^{cgs}}{1 - 4\pi\frac{1}{3}\rho_0\alpha_{LL}^{cgs}} \approx \rho_0\alpha_{LL}^{cgs} \tag{4.41}$$

$$\epsilon^{SI} = 1 + \chi^{SI} \qquad \epsilon^{cgs} = 1 + 4\pi\chi^{cgs} \tag{4.42}$$

$$\epsilon_{LL}^{SI} = \frac{1 - B_{LL}^{SI}}{1 + B_{LL}^{SI}/2} \qquad \epsilon_{LL}^{cgs} = \frac{1 - B_{LL}^{cgs}}{1 + B_{LL}^{cgs}/2} \tag{4.43}$$

$$B_{LL}^{SI} = -\frac{1}{\epsilon_0}\frac{2}{3}\rho_0\alpha_{LL}^{SI} \qquad B_{LL}^{cgs} = -4\pi\frac{2}{3}\rho_0\alpha_{LL}^{cgs}. \tag{4.44}$$

Additionally we have $B_{LL}^{SI}/B_{LL}^{cgs} = 1/4\pi\epsilon_0$ and the units of the polarizability in SI units and cgs units are $[\alpha^{SI}] = \mathrm{Jm}^2/\mathrm{V}^2$ and $[\alpha^{cgs}] = \mathrm{cm}^3$. A good reference for cgs to SI conversion is [CK77].

Self-Consistent Approach We are now introducing an extension of the Lorentz-Lorenz formula, that becomes relevant for high densities, when $\bar{\lambda} \approx 1$. At high density the linewidth of a transition becomes proportional to the electric permittivity $\epsilon(\omega)$ [SKKH09]. The complete expression for the permittivity is then dependent on itself and needs to be

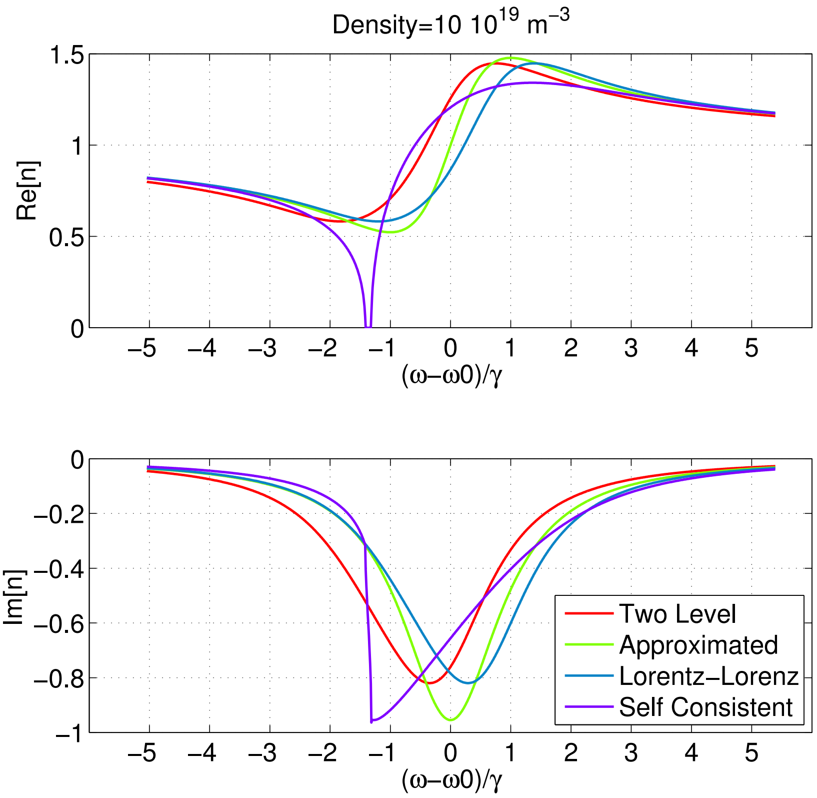

Figure 4.7: Comparison of refractive index models for the superradiance configuration, where only one level is relevant. The detuning is given relative to the F'=2 manifold of the D1 line and is normalized by half line widths. Top panel: real part, bottom panel: imaginary part.

solved self-consistently. We therefore set the value B_{sc}^{SI}, that enters the permittivity expression Eq 4.43 to

$$B_{sc}^{SI} = -4\pi \cdot \rho_0 \bar{\lambda}^3 \cdot \frac{2J'+1}{2J+1} \left(\frac{\tilde{\Delta} - i\sqrt{\epsilon(\omega)}}{\tilde{\Delta}^2 + \epsilon(\omega)} \right) \xi^2. \tag{4.45}$$

and get

$$\begin{aligned} n^2 = \epsilon(\omega) = & \left[1 + 4\pi \cdot \rho_0 \bar{\lambda}^3 \cdot \frac{2J'+1}{2J+1} \left(\frac{1}{\tilde{\Delta} + i\sqrt{\epsilon(\omega)}} \right) \xi^2 \right] \times \\ & \left[1 - \frac{1}{2} 4\pi \cdot \rho_0 \bar{\lambda}^3 \cdot \frac{2J'+1}{2J+1} \left(\frac{1}{\tilde{\Delta} + i\sqrt{\epsilon(\omega)}} \right) \xi^2 \right]^{-1}. \end{aligned} \tag{4.46}$$

Comparison In Fig. 4.7 all the refractive index models are plotted for a density of $\rho_0 = 10 \cdot 10^{19} m^{-3}$. The interaction configuration is chosen to match the later presented superradiance experiments, where only one transition is driven, which is the $|F = 1, m_F = -1\rangle$ ground state to the D1 line $|F' = 2, m_{F'} = -2\rangle$ excited state. While the approximated index is symmetric around the line center, none of the other models is. The self-consistent approach has a very different shape at this density than the other models and even has a region where the index is zero, where light is not allowed to enter the gas.

For absorption imaging in time-of-flight the atomic density is very low and the density corrections are irrelevant.

Comparing the Lorentz-Lorenz and self-consistent models to the approximated index for a density of $\rho_0 = 7 \cdot 10^{19}\mathrm{m}^{-3}$ for the Faraday rotation configuration, where three D1 line levels are relevant (level scheme of Fig. 11.1), we find relative values for the index ratio $(\mathrm{Re}(n_{LL/sc}) - 1)/(\mathrm{Re}(n_A) - 1)$ and the absorption ratio $(\mathrm{Im}(n_{LL/sc}))/(\mathrm{Im}(n_A))$ of less than 1% for detunings farther than -50MHz from resonance.

Note on the Relation between Refractive Index, Scattering Cross-Section and Optical Potential In this section a short overview of interdependencies of macroscopic properties, like the optical scattering potential, and microscopic properties, like atomic transition strengths, are summarized. Classical diffraction calculations tend to use only macroscopic properties and it was very useful to find the relations to two-level atom transition strengths as commonly used in quantum optics.

The optical theorem [BW05] gives a relation between the scattering and absorption cross sections, $\sigma^{(s)}$ and $\sigma^{(a)}$, and the scattering amplitude in the forward direction $f(\omega, \mathbf{s}_0, \mathbf{s}_0)$

$$\sigma_{tot} = \sigma_{tot}^{(s)} + \sigma_{tot}^{(a)} = \frac{4\pi}{k}\mathrm{Im}\left(f(\omega, \mathbf{s}_0, \mathbf{s}_0)\right), \tag{4.47}$$

where ω is the frequency of light and $\mathbf{s}_0$ is the direction of the incoming light. The scattering amplitude is related to the optical scattering potential F by

$$f(\omega, \mathbf{s}, \mathbf{s}_0) = \int_V F(\mathbf{r}', \omega) e^{ik(\mathbf{s}-\mathbf{s}_0)\mathbf{r}'} \mathrm{d}^3\mathbf{r}', \tag{4.48}$$

where $\mathbf{s}$ is the direction of the scattered light. The integration is over the whole sample. The scattering potential is related to the refractive index, as already seen in Sec. 4.2.1:

$$F(\mathbf{r}) = \frac{k^2}{4\pi}\left(n(\mathbf{r})^2 - 1\right) = \frac{\pi}{\lambda^2}\chi(\mathbf{r}). \tag{4.49}$$

The scattering cross section can be directly calculated by integrating the scattering amplitude over the solid angle

$$\sigma^{(s)} = \int_{4\pi} \mathrm{d}\Omega \left|f(\mathbf{s}, \mathbf{s}_0, \omega)\right|^2. \tag{4.50}$$

Five

Imaging Methods

Imaging techniques rely on the interaction of the atomic dipoles with the light field. The interaction can be altered by varying the detuning of the probe light with respect to the atomic transition. The susceptibility of the atoms has a real and an imaginary part. The absorptive, imaginary, part scales with Δ^{-2} and is strongest on resonance, while the dispersive, real, part scales with Δ^{-1} and vanishes on resonance. This allows to distinguish between absorptive and dispersive interactions for imaging. In absorption imaging one records the shadow image of the atoms that scattered the probe light into the 4π solid angle. In fluorescence imaging the camera is placed outside the path of the probe light and it records part of the scattered photons. In dispersive imaging the light is scattered only in the forward direction, but accumulates an extra phase shift due to the atoms.

The first section of this chapter describes absorption imaging and effects that limit its accuracy and precision in determining atom numbers. The second section describes dispersive imaging techniques and which information can be gained from the available techniques. The last section shortly describes fluorescence imaging.

5.1 Absorptive Imaging

Absorption imaging is performed on-resonant. This maximizes the absorptive part of the susceptibility and the dispersive part vanishes. Lensing by the atomic cloud can then be neglected.

The light reaching the camera in an experimental situation is not only composed of resonant light I_0^{res}, but contains also non-resonant components I_0^{nr}. Additionally there is stray light I^{stray} present that reaches the camera from other sources than the probe beam. Resonant light will be absorbed by the atoms. The bigger the optical depth of the sample the more light is absorbed. Non-resonant light will not be absorbed. It originates for example from the wide spectrum of diode lasers.

5.1.1 Lambert-Beer Law

The absorption of the probe light intensity I along the light propagation direction z is described by Lambert-Beer's law

$$\frac{\partial I}{\partial z} = -\sigma(I)\rho I \tag{5.1}$$

where $\sigma(I) = \sigma_0/(1 + I/I_s + (2\Delta_A/\Gamma)^2)$ is the scattering cross section including the saturation intensity I_s, the on-resonant cross-section is $\sigma_0 = 3\lambda^2/2\pi$ for the D2 line cycling transition, the detuning Δ_A and the atomic full linewidth Γ_A. The atomic density is

ρ. If we solve equation 5.1 for a single camera pixel and call the intensity at the beginning of the sample I_{BG}^{pix} and the intensity after the interaction with the atoms I_{IM}^{pix} we get

$$\left(1+\left(\frac{2\Delta_A}{\Gamma_A}\right)^2\right)\ln\left(\frac{I_{BG}^{pix}}{I_{IM}^{pix}}\right)+\frac{I_{BG}^{pix}-I_{IM}^{pix}}{I_s}=\sigma_0 N_{at}^{pix}, \tag{5.2}$$

where we have introduced the number of atoms per pixel N_{at}^{pix}. The saturation correction is valid for small optical depths. The number of atoms is obtained by integrating the atomic density over the area of a pixel A_{pix}, scaled by the magnification M_i of the imaging system

$$N_{\mathrm{at}}^{\mathrm{pix}}=\iint_{A_{\mathrm{pix}}/M_i^2}\int_{-\infty}^{\infty}\rho(\vec{r})\mathrm{d}x\mathrm{d}y\mathrm{d}z. \tag{5.3}$$

The optical depth is $\mathrm{OD}=\sigma_0\tilde{\rho}=\sigma_0\int_{-\infty}^{\infty}\rho(\vec{r})\mathrm{d}z$, where $\tilde{\rho}$ is the column density. We can therefore set the right side of Eq. 5.2 to

$$\sigma_0 N_{\mathrm{at}}^{\mathrm{pix}}=\frac{A_{\mathrm{pix}}}{M_i^2}\mathrm{OD}^{\mathrm{pix}}. \tag{5.4}$$

Using our experimental absorption imaging magnification for 45ms time of flight, the factor between atom number per pixel and optical depth is

$$\frac{A_{\mathrm{pix}}}{M_i^2\sigma_0}=\left\{\ 64 \quad \text{if } M_i=1.577.\right. \tag{5.5}$$

5.1.2 Experimental Determination of Optical Depth

Our absorption imaging setup is described in Sec. 10.1.1. In this section the influence of the non-resonant and stray light components of the light on the measured optical depth

$$\mathrm{OD}^{\mathrm{meas}}=\frac{A_{\mathrm{pix}}}{M_i^2}\mathrm{OD}^{\mathrm{pix}}=\sigma_0 N_{\mathrm{at},m}^{\mathrm{pix}} \tag{5.6}$$

is established. We will assume that the atoms have a 'real' or 'physical' optical depth

$$\mathrm{OD}=\sigma(I)N_{at,p}^{pix}. \tag{5.7}$$

The deviation of the mean value of $\mathrm{OD}^{\mathrm{meas}}$ from OD is the accuracy of the measurement, while the precision is related to the variance of the optical depth.

The camera acquires on each pixel a count $C=G\eta N_{\mathrm{ph}}$, where G is the camera gain, η the quantum efficiency and $N_{\mathrm{ph}}=\bar{I}_{pix}A_{\mathrm{pix}}T_p/(\hbar\omega)$ is the number of photons incident per pixel during the pulse length T_p. In our experimental sequence three images are taken. Each of these images has different light contributions. The resonant light leads to camera counts C^{res}. The non-resonant light leads to camera counts C^{nr} and the stray light gives camera counts of C^{stray}. The first image taken is an absorption image, for which the imaging beam is on and the atoms are present:

$$\mathrm{IM}=C^{\mathrm{res}}e^{-\mathrm{OD}}+C^{\mathrm{nr}}+C^{\mathrm{stray}}. \tag{5.8}$$

The second image is a background image, for which the imaging beam is on but no atoms are present:

$$\mathrm{BG} = C^{\mathrm{res}} + C^{\mathrm{nr}} + C^{\mathrm{stray}}. \tag{5.9}$$

The third image is a stray light image, for which the imaging beam is off and no atoms are present:

$$\mathrm{S} = C^{\mathrm{stray}}. \tag{5.10}$$

From these images we deduce a measured optical depth $\mathrm{OD}^{\mathrm{meas}}$ that is not necessarily identical to the 'real' atomic optical depth OD. The stray light image is used as a correction to the absorption and background images. The optical depth is then determined according to Eq. 5.1 with $\varDelta_A = 0$:

$$\begin{aligned}\mathrm{OD}^{\mathrm{meas}} &= -\ln\left(\frac{\mathrm{IM}-\mathrm{S}}{\mathrm{BG}-\mathrm{S}}\right) + \frac{\mathrm{BG}-\mathrm{IM}}{\mathrm{SAT}} &(5.11)\\ &= -\ln\left(\frac{e^{-\mathrm{OD}} + C^{\mathrm{nr}}/C^{\mathrm{res}}}{1 + C^{\mathrm{nr}}/C^{\mathrm{res}}}\right) + \frac{C^{\mathrm{res}}(1-e^{-\mathrm{OD}})}{C_{sat}}. &(5.12)\end{aligned}$$

If the non-resonant counts C^{nr} vanish, we obtain $\mathrm{OD}^{\mathrm{meas}} = \mathrm{OD}(1 + I/I_s) = \sigma_0 N_{at,p}^{pix}$, when approximating the exponential in the second term with $(1-\mathrm{OD})$. In this way one recovers the 'real' atom number per pixel $N_{at,p}^{pix}$ from the measured optical depth.

5.1.3 Accuracy and Precision of Optical Depth Measurement

There are two processes that limit the accuracy of the optical depth measurement. The non-resonant light is not absorbed by the atoms and it will therefore always reach the camera, even if the atomic optical depth is very large. This will give an upper limit for the detectable optical depth. The second process is a limit imposed by the camera noise. When the intensity of the light transmitted through the atoms is not large enough to overcome the camera noise, the optical depth measurement is limited to an upper value. Also a lower limit for the optical depth measurement arises from the camera noise.
The optical depth variance is in general determined by the sum of the variances of each noise source, weighed by the square of its sensitivity

$$\delta\mathrm{OD}^2 = \left(\frac{\partial\mathrm{OD}}{\partial\mathrm{IM}}\right)^2 \delta\mathrm{IM}^2 + \left(\frac{\partial\mathrm{OD}}{\partial\mathrm{BG}}\right)^2 \delta\mathrm{BG}^2 + \left(\frac{\partial\mathrm{OD}}{\partial\mathrm{S}}\right)^2 \delta\mathrm{S}^2. \tag{5.13}$$

The variance of each image is a sum of the camera noise contribution (read-out noise and dark noise, see Sec. 10.2) and the shot noise of the probe light: $\delta\mathrm{IM}^2 = \delta^2_{\mathrm{read-out}} + \delta^2_{\mathrm{dark}} + \delta^2_{\mathrm{shot}}$ and analogously for the other images. The sensitivities are given by

$$\begin{aligned}\left(\frac{\partial\mathrm{OD}}{\partial\mathrm{IM}}\right) &= -\frac{1}{\mathrm{IM}-\mathrm{S}} - \frac{1}{\mathrm{SAT}} = -\frac{1}{C^{\mathrm{res}}e^{-\mathrm{OD}} + C^{\mathrm{nr}}} - \frac{1}{C_{sat}} &(5.14)\\ \left(\frac{\partial\mathrm{OD}}{\partial\mathrm{BG}}\right) &= \frac{1}{\mathrm{BG}-\mathrm{S}} + \frac{1}{\mathrm{SAT}} = \frac{1}{C^{\mathrm{res}} + C^{\mathrm{nr}}} + \frac{1}{C_{sat}} &(5.15)\\ \left(\frac{\partial\mathrm{OD}}{\partial\mathrm{S}}\right) &= \left(\frac{1}{\mathrm{IM}-\mathrm{S}} - \frac{1}{\mathrm{BG}-\mathrm{S}}\right) = \left(\frac{1}{C^{\mathrm{res}}e^{-\mathrm{OD}} + C^{\mathrm{nr}}} - \frac{1}{C^{\mathrm{res}} + C^{\mathrm{nr}}}\right). &(5.16)\end{aligned}$$

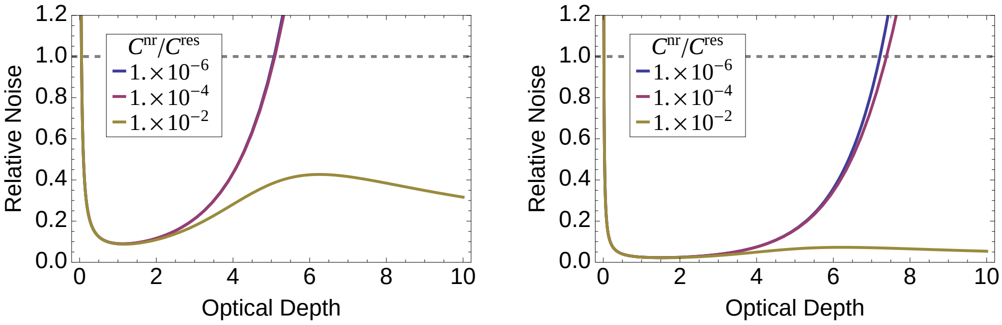

Figure 5.1: Plot of relative optical depth noise $\sqrt{\delta \text{OD}^2}/OD$ for several ratios of non-resonant to resonant light. The left panel is a plot for $C^{\text{res}} = 1000$ and the right panel for $C^{\text{res}} = 6000$.

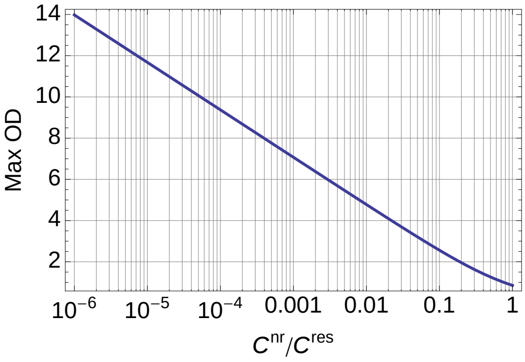

Figure 5.2: Optical depth clipping due to non-resonant light. Plotted is the maximal optical depth vs. the ratio of non-resonant to resonant light.

The mean value of the optical depth can be deduced from images as long as the relative noise per pixel is smaller than 1: $\sqrt{\delta \text{OD}^2}/\text{OD} < 1$. In Fig. 5.1 the relative noise is plotted as a function of the OD of the atomic ensemble for three ratios of non-resonant to resonant counts $C^{\text{nr}}/C^{\text{res}}$. For a resonant count of $C^{\text{res}} = 6000$, which is a typical experimental setting, we find the smallest detectable optical depth to be $\text{OD}^{\text{min}} \approx 0.02$ and for a count of $C^{\text{res}} = 1000$ we get $\text{OD}^{\text{min}} \approx 0.05$. The minimum optical depth is fairly insensitive to the amount of stray light and non-resonant light. A maximal determinable optical depth occurs for lower ratios of non-resonant to resonant light. If there is a lot of non-resonant light present the relative noise stays at a low value for high optical depths. The relative noise is lowest around an optical depth of approximately one, which makes it an optimal value for low noise measurements.

The clipping of the mean value of the measured optical depth occurs for

$$\text{OD}^{\text{meas,max}} = \ln\left(1 + C^{\text{res}}/C^{\text{nr}}\right) + \frac{C^{\text{res}}}{C_{sat}}, \tag{5.17}$$

which is obtained from setting $\text{OD} \to \infty$ in Eq. 5.12 and is shown in Fig. 5.2 on a semi-logarithmic plot.

The maximal observable optical depth for a given non-resonant to resonant count ratio is the smaller of the two presented upper limits, the clipping of the mean value and the maximal optical depth due to relative noise.

The left panel of Fig. 5.3 shows the measured optical depth divided by the saturation correction $\left(1 + C^{nr}/C^{res}\right)$ vs. the 'real' atomic optical depth. The saturation correction is necessary because the 'real' optical depth uses the intensity corrected scattering cross-section $\sigma(I)$ and the measured optical depth is proportional to σ_0. The figure allows to

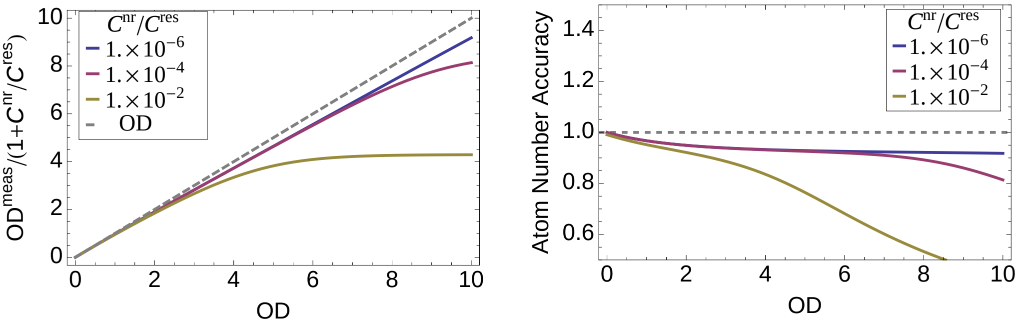

Figure 5.3: Left panel: measured optical depth divided by the saturation correction $(1+C^{nr}/C^{res})$ vs. the 'real' optical depth of the ensemble. Errors on the determined atom number can be estimated in this way (see text). The resonant light count is $C^{\text{res}} = 6000$, corresponding to $C^{nr}/C^{res} = 0.1$. Right panel: The accuracy of the atom number measurement $N_{at,m}/N_{at,p}$ for the same conditions. The dashed lines are the limit of $N_{at,m} = N_{at,p}$. Deviations from that line are errors in accuracy.

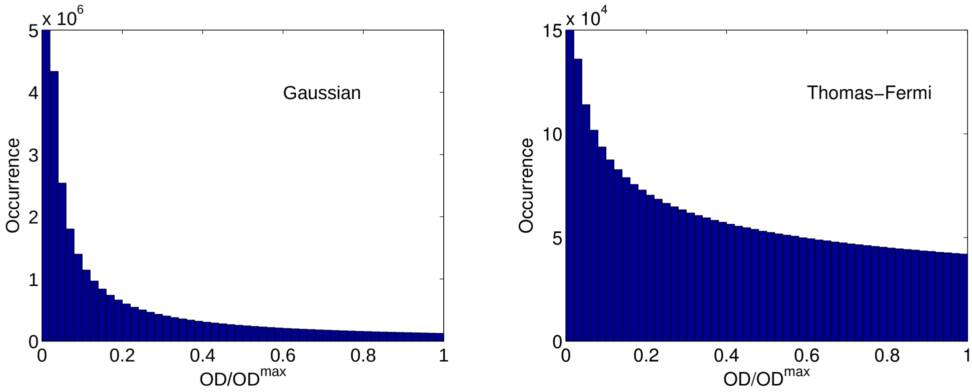

Figure 5.4: Histograms of optical depth occurrences on a pixelated image for a Gaussian (left) and a Thomas-Fermi (right) density distribution. The pixel size was adjusted to give a smooth histogram.

directly compare the measurement result for the atom number with the 'real' atom number. The right panel of the same figure shows the ratio $\text{OD}^{\text{meas}}/(\text{OD}(1+C^{nr}/C^{res}))$, which gives directly the accuracy of the atom number measurement. Both plots use a resonant light count of $C^{\text{res}} = 6000$ which corresponds to a saturation parameter of $C^{nr}/C^{res} = 0.1$. The almost 10% error for small amounts of non-resonant light at large optical depths is caused by the effects of saturation. The saturation correction applied in Eq. 5.2 only works at very small optical depths. For larger amounts of non-resonant light the atom number counting error becomes even larger. This means that under typical experimental conditions the determined atom number is underestimated by approximately 10%, assuming the amount of non-resonant light is small.

The error estimates of the last paragraphs are given for single pixels. An absorption image contains a distribution of pixels with various optical depths. Figure 5.4 shows an optical depth histogram, the number of pixels with a certain optical depth, for a Gaussian and a Thomas-Fermi atomic density distribution. The pixel size was adjusted to give a smooth histogram. From the histogram we can read that there are more pixels with low optical depths on an image than with high optical depths. The low optical depth pixels contain only a small amount of atoms and therefore only add a small amount of noise to the total atom number. It is thus more interesting to look at the distribution of atom numbers with respect to a given optical depth value. For example large errors in the determination of large optical depths might contribute only a small amount of atoms

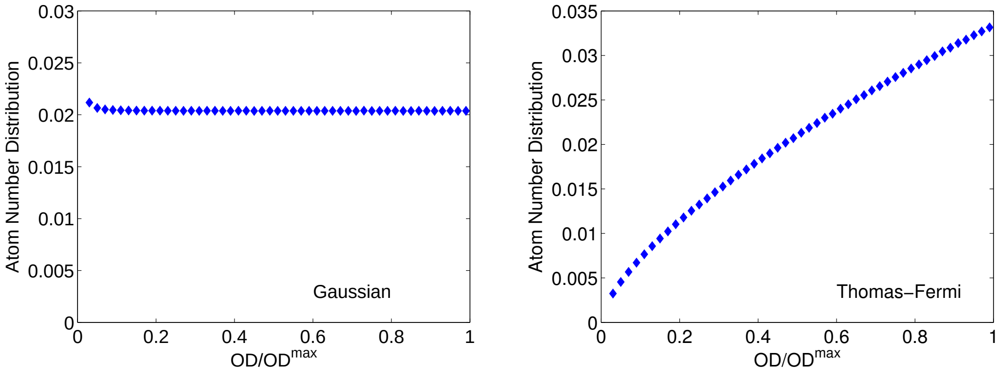

Figure 5.5: Atom number distribution over a pixelated image for a Gaussian atomic density distribution (left) and a Thomas-Fermi atomic density distribution plotted against the optical depth per pixel normalized to the peak optical depth of the atomic density.

to the total atom number. In this way the large error per pixel would not add a lot of noise to the total atom number. In Fig. 5.5 we therefore plot atom number distributions as a function of optical depth normalized to the peak optical depth of the atomic density distribution. The distribution is obtained by multiplying the histogram counts of Fig. 5.4 with the corresponding optical depths and normalizing with the total atom number. While a Gaussian distribution weighs all optical depths with the same factor, the Thomas-Fermi distribution has a larger contribution at high optical depths, making it more susceptible to high optical depth errors.

5.1.4 Scattering Cross Section Estimation

In the last section the scattering cross section σ_0 was assumed to be constant and well known. In an experimental situation it is often difficult to know the scattering cross section precisely. In an ideal situation one uses a cycling transition, i.e. from the ground state $|F = 2, m_F = -2\rangle$ to the D2 line excited state $|F' = 3, m_{F'} = -3\rangle$. As soon as the polarization of the probe light is not clean or there are stray magnetic fields with components perpendicular to the quantization axis, the scattering cross section will be altered and the atom number determination inaccurate. For stray magnetic fields the introduced error is small if optical pumping appears on a faster time-scale than the Larmor frequency. A non-clean polarization does not only change the interaction strength but also alters the population distribution by optical pumping.

5.1.5 High Saturation Imaging

Samples with especially large optical depths, even after long time of flight, are hard to accurately image, due to the clipping of optical depth. This can be overcome by effectively reducing the OD by using high probe light intensities [RLWGO07], which reduce the scattering cross section. In order to not saturate the camera the imaging duration needs to be shortened accordingly. As can be seen from Eq. 5.2, with increasing probe intensity the saturation term on the left becomes more relevant compared to the logarithmic term, which contains the detuning. In this way deviations from the zero detuning become less relevant. The method does not correct for unclean polarization or stray magnetic fields, which influence the on-resonant scattering cross section σ_0.

5.2 Dispersive Imaging

In this section available dispersive imaging techniques are presented in order to contrast them to the dual-port polarization contrast imaging technique, which we use in our exper-

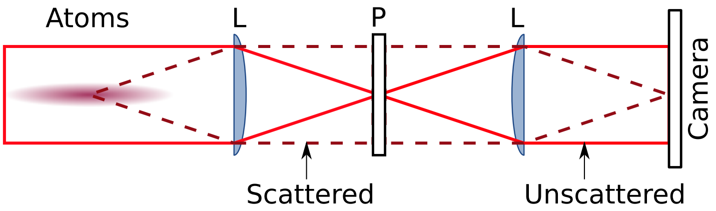

Figure 5.6: General setup used for dispersive imaging. The unscattered light will be focused onto the Fourier plane between the two lenses (L) while the scattered light is not. An optical element P is used in the Fourier plane to modify the unscattered light. A camera captures the image. P can be a phase-plate, a polarizer, a light block or a polarizing beam-splitter.

iments and which is presented in the last paragraph of this section. The analysis is based on the simple model presented in Sec. 3.1.

5.2.1 Dispersive Imaging Techniques Overview

Phase-Contrast Imaging In this technique [MRK+10, HSI+05] the element P which sits in the Fourier plane of the imaging system (Fig. 5.6), is a transparent plate with a phase dimple in the middle, which shifts only the unscattered light by a phase of $\pm\pi/2$. Phase-contrast imaging is similar to homodyne detection.

Following the simple model presented in Sec. 3.1, the field after the interaction including polarization rotation is $\vec{E}^{out} = E_0 e^{i\Phi}\left(\cos\theta_F \vec{e}_x - \sin\theta_F \vec{e}_y\right)$ with $\vec{E}^{in} = E_0\vec{e}_x$. After phase shifting the unscattered light, the intensity reaching the camera is

$$\begin{aligned} I^{cam}_{pha-c} &= \frac{c\epsilon_0}{2}\left|\vec{E}^{in} e^{\pm i\pi/2} + \left(\vec{E}^{out} - \vec{E}^{in}\right)\right|^2 = I_0\left(3 \pm 2\sqrt{2}\cos\theta_F \sin\left(\Phi \mp \frac{\pi}{4}\right)\right) && (5.18)\\ &= I_0\left(3 \pm 2\cos\left(\theta_F\right)\left(\sin\left(\Phi\right) \mp \cos\left(\Phi\right)\right)\right) && (5.19)\\ &\approx I_0\left(1 \pm 2\sin\Phi\right). && (\Phi \text{ and } \theta_F \text{ small}) \end{aligned}$$

This shows that one is mainly sensitive to the total phase shift Φ which corresponds to the scalar part of the polarizability.

In Stokes language this corresponds to measuring $S_0 = \sqrt{S_1^2 + S_2^2 + S_3^2}$. Since the Stokes parameters describe the intensity of light instead of fields, they are not very helpful in describing the total phase shift, which is necessary in this technique.

Dark Ground Imaging In this technique [AMvD+96] the element P in fig. 5.6 is a transparent plate with a small absorptive element in the middle, filtering out the unscattered light, such that only the scattered light reaches the camera:

$$\begin{aligned} I^{cam}_{dg} &= \frac{c\epsilon_0}{2}\left|\vec{E}^{out} - \vec{E}^{in}\right|^2 && (5.20)\\ &= I_0\left|\left(e^{i\Phi}\cos\theta_F - 1\right)\vec{e}_x - e^{i\Phi}\sin\theta_F\vec{e}_y\right|^2 && (5.21)\\ &= 2I_0\left(1 - \cos\theta_F\cos\Phi\right) && (5.22)\\ &= 2I_0\left(\sin\left(\frac{\theta_F - \Phi}{2}\right)^2 + \sin\left(\frac{\theta_F + \Phi}{2}\right)^2\right) && (5.23)\\ &= 4I_0\sin\left(\frac{\Phi}{2}\right)^2. && (\theta_F = 0) \end{aligned}$$

There is no favoring of one of the angles due to sensitivity. One measures the total phase shift and the rotation angle simultaneously. One only recovers the formula of [KDSK99] if one sets the Faraday angle to zero, which occurs only for distinct detunings.

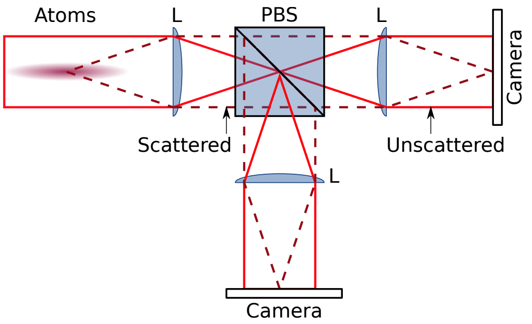

Figure 5.7: In Faraday imaging the main element is a polarizing beam splitter. A camera captures both output ports.

Single-Port Polarization-Contrast Imaging The element P in fig. 5.6 is now a linear polarizer [BSH97]. If the polarizer is oriented perpendicular to the polarization of the probe light one gets a dark-ground image of the Faraday angle. If the polarizer is oriented at 45° relative to the incoming polarization the Faraday angle is accessible from a bright image.

Mapping into the polarizer basis we get the intensity on the camera

$$I^{cam}_{pol-c} = \frac{c\epsilon_0}{2}\left|\vec{E}^{out}\cdot\vec{e}_{pol}\right|^2 = \begin{cases} I_0\left(\sin\theta_F\right)^2 & \text{if } \vec{e}_{pol} = \vec{e}_y \\ \frac{1}{2}I_0\left(1-\sin 2\theta_F\right) & \text{if } \vec{e}_{pol} = \vec{e}_{+45} \end{cases}. \tag{5.24}$$

Since Stokes vectors are well suited to describe polarization we can rephrase this result using the Stokes formalism. For an input polarization along +45°, we have $S^{in}_1 = S^{in}_3 = 0$. If we neglect terms proportional to Raman coherences $T^{(2)}_{2-}$ and $T^{(2)}_{2+}$ in Eq. 3.65 to 3.67 we obtain after the interaction

$$\hat{S}^{out}_1 = \hat{S}^{in}_2 \sin\left(2\theta_F\right) \tag{5.25}$$

$$\hat{S}^{out}_2 = \hat{S}^{in}_2 \cos\left(2\theta_F\right) \tag{5.26}$$

$$\hat{S}^{out}_3 = 0, \tag{5.27}$$

with the definition

$$\theta_F = \frac{1}{\sqrt{2}}C_L\langle\tilde{T}^{(1)}_0\rangle = \frac{1}{2}C_L\alpha^{(1)}\langle\hat{F}_z\rangle. \tag{5.28}$$

Here we assumed that the atomic state populations, parametrized in $\langle\tilde{T}^{(1)}_0\rangle$, do not change during the interaction.

Depending on the orientation of the polarizer we can measure either of the quadratures $\hat{S}^{out}_1$, $\hat{S}^{out}_2$ or a combination of both.

The accessible physical quantity is the phase difference or the vector part of the polarizability, $\alpha^{(1)}$, at least if we assume the effect of $\alpha^{(2)}$ to be negligible.

5.2.2 Faraday Imaging - Dual-Port Polarization Contrast Imaging

This technique is very similar to polarization contrast imaging, but instead of using a polarizer (single port) we use a polarizing beam splitter (dual-port). This enables us to have access to the total amount of scattered light.

For a x polarized probe field the field after the interaction is again $\vec{E}^{out} = E_0 e^{i\Phi}\left(\cos\theta_F\vec{e}_x - \sin\theta_F\vec{e}_y\right)$

after the interaction. Since we probe with 45° polarization in our experimental setup, let's write this case down as well.
In the circular basis a $+45°$ linear polarization reads $\vec{e}_{+45} = \vec{e}_{-}(1+i)/2 + \vec{e}_{+}(-1+i)/2$ and the field after the interaction is

$$\vec{E}^{out} = E_0 \frac{1}{2}\left((1+i)e^{i\phi_-}\vec{e}_- + (-1+i)e^{i\phi_+}\vec{e}_+\right) \tag{5.29}$$

The analyzing beam splitter P/PBS will map into both bases $\vec{e}_H = \cos(\gamma)\vec{e}_x - \sin(\gamma)\vec{e}_y$ and $\vec{e}_V = \sin(\gamma)\vec{e}_x + \cos(\gamma)\vec{e}_y$, the two arms after the cube, where γ gives the orientation of the detection basis such that $\gamma = 0$ is the x-y basis:

$$I_H = \frac{c\epsilon_0}{2}\left|\vec{E}^{out}\cdot\vec{e}_H\right|^2 = \frac{1}{2}I_0\left(1+\sin\left(2\gamma+\phi_+-\phi_-\right)\right) \tag{5.30}$$

$$I_V = \frac{c\epsilon_0}{2}\left|\vec{E}^{out}\cdot\vec{e}_V\right|^2 = \frac{1}{2}I_0\left(1-\sin\left(2\gamma+\phi_+-\phi_-\right)\right). \tag{5.31}$$

The sum and difference of the intensities are

$$I_H + I_V = I_0 \tag{5.32}$$

$$I_H - I_V = I_0 \sin\left(2\gamma+\phi_+-\phi_-\right) \tag{5.33}$$

and therefore we can deduce the Faraday angle to be

$$\theta_F = \frac{1}{2}\left[\operatorname{asin}\left(\frac{I_H-I_V}{I_H+I_V}\right) - 2\gamma\right]. \tag{5.34}$$

This shows us the experimental strategy to use in order to deduce the Faraday angle. It is also apparent that we will be most sensitive to small Faraday angles, where the derivative of the sine is largest, i.e. at $\gamma = 0$.

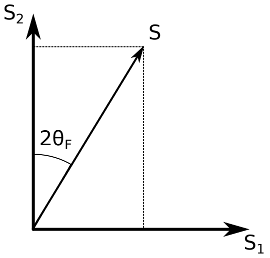

Figure 5.8: The definition of the Faraday angle in terms of Stokes parameters.

In Stokes parameters the x-y measurement basis is represented by S_1 and the probe light is prepared in the 45° basis, i.e. $S_2 = S_0^{in}$. From the definition of the Stokes parameters, Eq. B.78 to B.80, we see that $S_1 = I_H - I_V$ and as described earlier the Faraday angle is

$$\theta_F = \frac{1}{2}\left[\operatorname{atan}\left(\frac{S_1^{out}}{S_2^{out}}\right) - \operatorname{atan}\left(\frac{S_1^{in}}{S_2^{in}}\right)\right], \tag{5.35}$$

where the second term is equivalent to the 2γ term in Eq. 5.34 and corrects the detection imbalance. An illustration of the Faraday angle in the Poincaré sphere (S_1,S_2) plane is shown in Fig. 5.2.2. Equally we can write

$$\theta_F = \frac{1}{2}\left[\operatorname{asin}\left(\frac{S_1^{out}}{S_0^{out}}\right) - \operatorname{asin}\left(\frac{S_1^{in}}{S_0^{in}}\right)\right]. \tag{5.36}$$

Note that if there is any circular polarization after the interaction, we need to use a modified S_0, namely the projection into the S_1-S_2 plane. Experimentally this is not easily accessible. Therefore it is only possible to deduce meaningful Faraday angles if we can neglect contributions of S_3 or equivalently the $\alpha^{(2)}$ part of the polarizability.

5.3 Fluorescence Imaging

In fluorescence imaging spontaneously scattered photons are detected with a photodetector or camera. Since atoms scatter spontaneously emitted photons into an arbitrary spatial direction one can only detect a small fraction of the total number of scattered photons. Therefore this is a rather inaccurate method. It is still useful as a rough estimate or as a triggering signal, to start an experimental run. We use it in our science MOT to decide when to start the evaporation sequence.

Six

Light-Assisted Cold Collisions

In chapter 3 the theory of light-atom interaction under the assumption of non-interacting atoms was presented. This chapter will introduce atom-atom interactions under the influence of probe light and discuss the effect on dispersive measurements. While the theory of light-assisted cold collisions is well established [WBZJ99, JTLJ06], the application to dispersive measurements became crucial in the interpretation of the Faraday rotation experiments presented in chapter 11.

The section closely follows [1].

6.1 Introduction

Section 2.3.1 described the interaction of two atoms in their ground states. At very low temperatures only s-waves contribute to the wavefunction and a collision is said to be cold. In a light-assisted collision one of the two atoms is in an electronic excited state and the typical potentials are $V \propto c_3/R^3$ and extend to far bigger relative atomic distances than the c_6 ground state collisional potentials. For the relatively small detunings (less than 10GHz) used in all our experiments, only the long-range Movre-Pichler potentials [MP77] are of interest (App. C.1). They are plotted in Fig. 6.1 for the D1 and D2 line of Rubidium 87. These potentials can be well approximated with $V = c_n/R^n$ potentials at large enough

---

[1] F. Kaminski, N. Kampel, A. Griesmaier, E. Polzik, and Jörg H. Müller, to be published

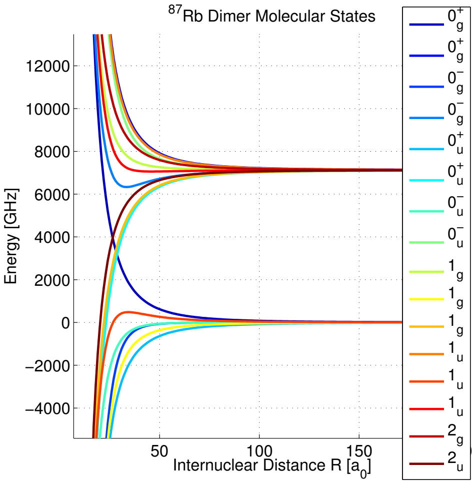

Figure 6.1: Movre-Pichler long-range potentials of the interaction energy of a Rubidium 87 ground/excited-state dimer. Shown are both D1 and D2 line potentials. The labels reflect the symmetry properties of the dimer wavefunction [JTLJ06].

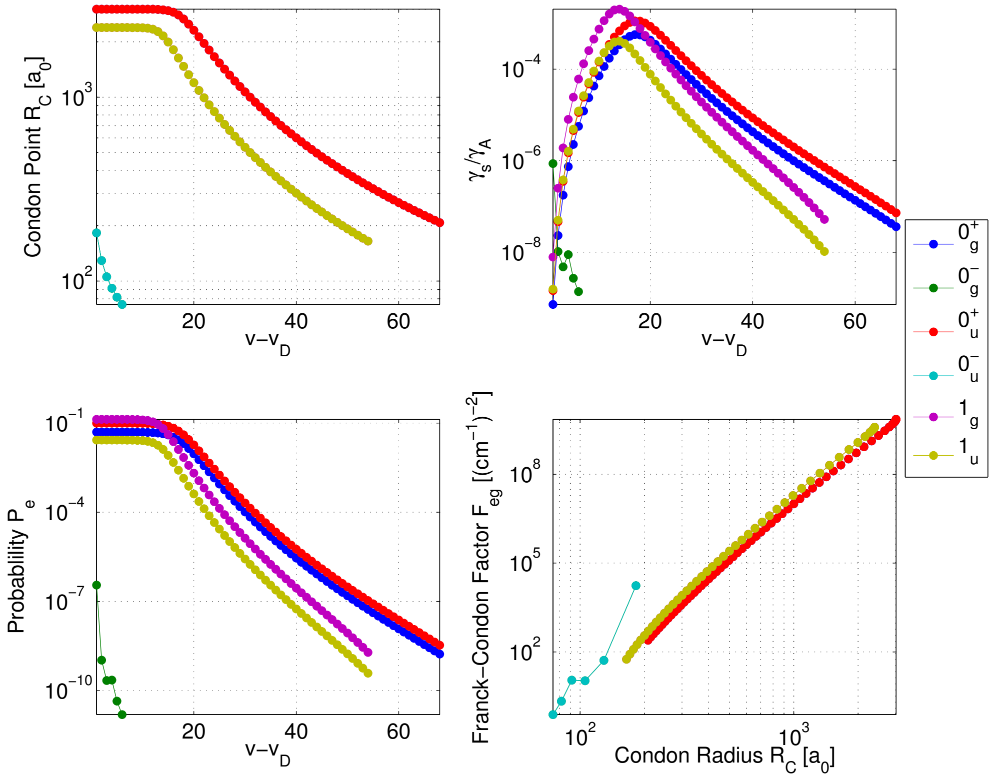

Figure 6.2: Condon radii, stimulated emission rates, excitation probabilities and Franck-Condon factors for D1 line molecular potentials of ^{87}Rb. The hyperfine splitting of the D1 line is not taken into account.

internuclear distances (App. C.1.2), where only $n = 3$ and $n = 6$ are relevant. The interaction is repulsive for detunings on the blue side of an atomic resonance. Attractive potentials lead to vibrational resonances and lie on the red side of the atomic resonance.

The main interest of the field of light-assisted collisions has been the study of trap loss rates. Hence mainly absorption features have been studied. The extension to dispersive interactions will require the calculation of off-resonance contributions of attractive and repulsive potentials. This is easy for attractive potentials but less obvious for repulsive. For our specific experimental situation of probing red detuned from the D1 line an easy approximate calculation is possible.

6.2 Trap Loss Rates

A collision rate coefficient is given by averaging the collision probability P_e over collision energies E for a given atomic detuning Δ_A [Jul96]

$$K_e = \left\langle \frac{\pi\hbar}{\mu k_g} P_e(E, \Delta_A) \right\rangle_E , \tag{6.1}$$

where $\mu = M/2$ is the reduced mass of the dimer and M the mass of a single atom, $k_g = 2\pi/\lambda_{dB}$ is the ground state wave vector relating to the de Broglie wavelength λ_{dB}. The probability for a light-assisted collision is related to the collision S-matrix elements

$$P_e(E, \Delta_A) = |S_{eg}(E, \Delta_A)|^2 \tag{6.2}$$

and for small radiative coupling the radiative distorted wave approximation allows to rewrite it as a Fermi golden rule type transition strength using the coupling strength V_{eg} and the ground and excited state wave functions $\Psi_{g/e}$

$$S_{eg}(E,\Delta_A) = -2\pi i\langle\Psi_e(E+\hbar\Delta_A)|V_{eg}(R)|\Psi_g(E)\rangle. \tag{6.3}$$

Approximating the coupling strength as constant or slowly varying with atomic distance R, it can be taken out of the integral

$$P_e(E,\Delta_A) = 4\pi^2 V_C^2 F_{eg}(E,\Delta_A), \tag{6.4}$$

where the overlap of the excited and ground state wave functions is defined as the Franck-Condon factor

$$F_{eg}(E,\Delta_A) = |\langle\Psi_e(E+\hbar\Delta_A)|\Psi_g(E)\rangle|^2 \approx \frac{1}{D_C}|\Psi_g(R_C,E)|^2. \tag{6.5}$$

The reflection approximation was used in the second step to further simplify. It approximates the excited state wavefunction with the help of the slope of the excited state D_C evaluated at the Condon point, $D_C = \frac{\mathrm{d}}{\mathrm{d}R}|V_e(R) - V_g(R)|_{R=R_C}$.
The Condon radii are given by the resonance condition $\hbar\Delta_A = c_n/R_C^n$. We introduce absorption by setting $\Delta_A \to \Delta_A - i\gamma_A/2$ to limit the interaction strength close to atomic resonances. The Condon radius is then defined by

$$|R_C| \to \left(\frac{c_n}{\hbar\sqrt{\Delta_A^2 + (\gamma_A/2)^2}}\right)^{1/n} \tag{6.6}$$

and shown in Fig. 6.2. There occurs a maximum Condon radius $R_\infty = (2c_n/\hbar\gamma)^{1/n} \approx 2000a_0 = 0.13\lambda$, with a_0 being the Bohr radius. The Condon radii are continuous for repulsive but discrete for attractive potentials, due to the vibrational resonances. An atomic density of $\rho = 3\ 10^{19}\mathrm{m}^{-3}$ corresponds to an inter-particle distance of $6500\mathrm{a}_0$. Most atoms are therefore independent, only if they approach closer than the maximum Condon-radius do they interact.
The ground state wave function of the dimer for intermediate range atomic distances R can be approximately derived from the Milne equation [Jul96],

$$\Psi_g(R,E) = e^{i\eta_g}\left(\frac{2\mu}{\pi\hbar^2 k_\infty}\right)^{1/2} a(R)\sin(k_\infty \Upsilon(R)). \tag{6.7}$$

Intermediate range is defined by $R >> R_B = (\mu C_6/\pi\hbar^2)^{1/4}$ and $R_B = 77a_0$ for Rubidium. C_6 is the ground state potential $E_g = C_6/R^6$ interaction strength. The temperature T defines the wave vector $k_\infty = (2\mu k_B T/\hbar^2)^{1/2}$, $a(R) = 1 - (R_B/R)^4$ and $\Upsilon(R) = R[1 - A_s/R - (R_B/R)2/3]$, with the scattering length A_s and the phase η_g.

The approximate form of the collision rate coefficient is then found by combining the above approximations. Assuming that the atoms are cold enough to disregard the thermal averaging one arrives at

$$K_e = \left(\frac{2-x}{2}\right)\frac{4\pi^3\hbar}{\mu k_g}\frac{V_C^2}{D_C}|\Psi_g(R_C,E)|^2 \approx \left(\frac{2-x}{2}\right)\frac{16\pi^3 V_C^2}{hD_C}a_C^2\Upsilon_C^2. \tag{6.8}$$

Additionally the effect of quantum statistics for the condensate was introduced via the correlation function $g^{(2)}(0) = (2-x)/2$, where x is the condensate fraction (see App. C.3 for a discussion).
The explicit expression for the slope is $D_C(\varDelta_A) \approx -nc_n|R_C|^{-(n+1)}$, for the coupling strength it is $V_C = \hbar b_C \varOmega_A$, where $\varOmega_A = (2I/\epsilon_0 c)^{1/2} d_A/2\hbar$ is the atomic Rabi frequency with I the light intensity and d_A the atomic dipole moment and $b_C = \varOmega(R_C)/\varOmega_A = f_{osc}^{mol}/f_{osc}^{D1}$, the ratio between the molecular and atomic Rabi frequencies or oscillator strengths (see App. C.1.1). The atomic scattering rate is $\varGamma_A(\varDelta_A) = \gamma_A \varOmega_A^2/(\varDelta_A^2 + (\gamma_A/2)^2)$ and γ_A is the full atomic linewidth.
An alternative way of writing K_e using nicely scaled variables is ([BJS96, Jul96]):

$$K_e(\varDelta_A) = \left(\frac{2-x}{2}\right)\frac{8\pi^2 b_C^2 f_n'}{3}\lambdabar^3 g_C \varGamma_A. \tag{6.9}$$

We defined $g_C(\varDelta_A) = a_C^2 \varUpsilon_C^2/R_C^2$, $f_n' = -(3/n)(c_n/\lambdabar^3\hbar\gamma_A)|R_C|^{3-n}$ and used $\lambdabar = \lambda/2\pi$. The two definitions were used to cross-check our numerical results.

To obtain the trap loss rate the collision rate coefficient needs to be multiplied with the atomic density and a factor of two, accounting for the loss of 2 atoms on a scattering event. For repulsive potentials, which have continuous resonances, one obtains [BJS96, Jul96]

$$\gamma_{binary}^{(blue)} = 2K_e(\varDelta_A)\rho(r). \tag{6.10}$$

For attractive potentials the Condon points are determined by the position of the vibrational levels v, which are determined with the LeRoy-Bernstein Formula (App. C.2). The binary rate is then ([BJS96, Jul96])

$$\gamma_{binary}^{(red)} = 2\sum_{v} K_e(\mathrm{v})\frac{\nu_\mathrm{v}\gamma_\mathrm{v}}{\varDelta_\mathrm{v}^2 + (\gamma_\mathrm{v}/2)^2}\rho(r). \tag{6.11}$$

The rate coefficient $K_e(\mathrm{v})$ is discrete for attractive potentials because of the resonance condition $\varDelta_A = E_{LeRoy}(\mathrm{v})/\hbar$ for the Condon points. The laser detuning relative to the resonance v is $\varDelta_\mathrm{v}(\mathrm{v}, \varDelta_A) = \varDelta_A - E_{LeRoy}(\mathrm{v})/\hbar$, the linewidth of a dimer resonance is $\gamma_\mathrm{v} = \gamma_p + \gamma_s$, where $\gamma_p = b_C^2\gamma_A$ is the decay rate back to the initial state and $\gamma_s = P_{eg}\nu_\mathrm{v}$ is the stimulated decay rate, which is much smaller than γ_p. The frequency spacing of LeRoy resonances is $\nu_\mathrm{v}(\mathrm{v}) = \partial E_{LeRoy}/\partial\mathrm{v}/h = \left(\frac{2n}{n-2}\right)\frac{E_n}{h}(\mathrm{v}_D - \mathrm{v})^{\frac{2n}{n-2}-1}$, where v_D is the dissociation limit and can be approximated to zero, since the vibrational levels are very dense at the dissociation limit (see Fig. C.2).
In Fig. 6.2 we plot Condon-radii, stimulated emission rates γ_s, excitation probabilities P_{eg} and Franck-Condon factors F_{eg} for all D1 line molecular potentials of ^{87}Rb. The hyperfine splitting of the excited state is not yet accounted for.

Off-Resonant Contributions of Repulsive Potentials Dispersive line profiles have significant contribution to the interaction strength for much larger detunings than absorptive profiles. For attractive potentials it is obvious how to treat off resonant contributions, since each LeRoy resonance has a Lorentz frequency profile. The wings of the Lorentz profiles also extend towards blue detunings, where the repulsive potentials are.
On the other hand, the repulsive potentials have a fixed resonance condition $\hbar(\varDelta_A^2 + (\gamma_A/2)^2)^{1/2} = c_n/R^n$, such that there is no contribution of those potentials on the red detuning side. This does not appear to make sense. The issue can be addressed by a procedure, that only works for the specific situation of red detunings. In that case all repulsive potentials are far off-resonant and we can introduce an approximation, that introduces artificial resonances and Lorentz profiles.
The repulsive potentials can then be treated by assigning LeRoy resonances and Lorentz

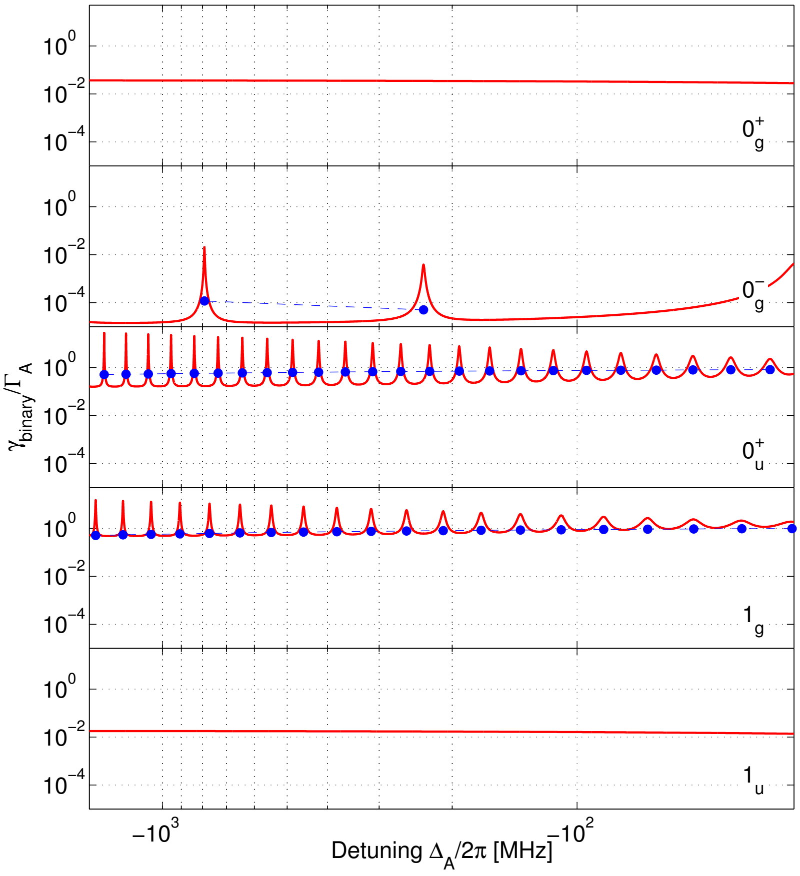

Figure 6.3: Normalized molecular binary rates for the detunings relevant in our experiment and $\rho = 2.64\,10^{19}\mathrm{m}^{-1}$. The off resonant contributions of repulsive potentials 0_g^+ and 1_u is taken into account. The blue dots on red potentials indicate the rate coefficient K_e at the vibrational LeRoy resonances. There is no hyperfine structure included.

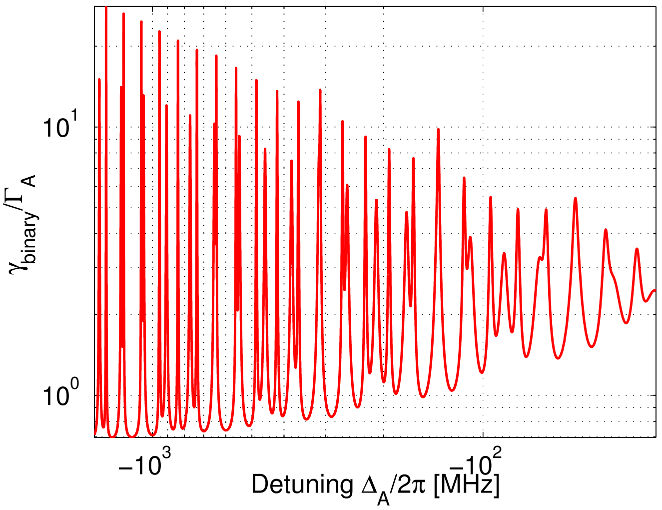

Figure 6.4: Normalized binary rates as in Fig. 6.3 but summed over all potentials.

profiles to them, using the C_n coefficients of the repulsive potentials. This is permissible if the total interaction strength is conserved (shown in App. C.4). If the detuning is far away from the repulsive potentials, the artificially introduced discrete resonances average out.

In Fig. 6.3 the normalized binary trap loss rates for the relevant potentials of the D1 line are plotted. The blue dots indicate the loss coefficient K_e at the Condon points. Attractive potentials (0_g^-, 0_u^+ and 1_g) show in the plotted red detuning range the vibrational resonance lines. The repulsive potentials (0_g^+ and 1_u) have non-vanishing off-resonant contributions. Figure 6.4 shows the sum of these rates, which is the resulting total binary rate. For detunings that hit a vibrational resonance the enhancement can be larger than 10.

6.3 Dispersive Interactions

The trap loss rates can be reformulated into susceptibilities via the scattering cross section. The susceptibility can then be used to calculate the phase shift due to light-assisted collisions.

The scattering cross section [BW05] is given by the scattered photon flux Φ^{scat} and the incident light intensity I^{inc} as $\sigma_{scat} = \hbar\omega\Phi^{scat}/I^{inc}$, where

$$\Phi^{scat} = \frac{I^{scat}\mathrm{d}A}{\hbar\omega} = \frac{N_{ph}}{T_p} = \Gamma_A \tag{6.12}$$

is identical to the number of scattered photons, N_{ph}, per pulse length T_p and therefore to the scattering rate Γ_A.

The molecular scattering rate is $\Gamma_A^{pa} = \gamma_{binary}/2$, where the factor of a half results from the fact that while 2 atoms are lost only one photon is scattered. The molecular scattering cross section can then be noted as

$$\sigma_{pa} = \frac{\gamma_{binary}}{2}\frac{\hbar\omega}{I^{inc}} \tag{6.13}$$

and depends on density.

The atomic scattering cross section of a two-level system can be extended to a multilevel system by introducing the interaction strength scaling ξ that scales the dipole moment d_A with the fine structure transition strength $\langle J||d||J'\rangle$: $d_A = \xi\langle J||d||J'\rangle$. The scattering cross section is then

$$\sigma_A(\Delta_A) = \xi^2\frac{3\lambda^2}{2\pi}\frac{2J'+1}{2J+1}\frac{1}{1+\tilde{\Delta}_A^2}, \tag{6.14}$$

where the normalized detuning $\tilde{\Delta}_A = 2\Delta_A/\gamma_A$ was introduced. The phase shift of the light acquired by passing through the sample is $\phi = \int kn\mathrm{d}z$. In a two-level system the refractive index n is defined through the susceptibility $\chi = \chi' + i\chi''$ [SZ97] and can be approximated for small absorption as $n \approx 1 + \chi'/2$, while

$$\chi = 3\cdot 2\pi\cdot\rho\lambda\!\!\!^-{}^3\xi^2\frac{2J'+1}{2J+1}\left(\frac{\tilde{\Delta}-i}{1+\tilde{\Delta}^2}\right) \tag{6.15}$$

$$= \rho\lambda\!\!\!^-\cdot\sigma(\Delta)\cdot(\tilde{\Delta}-i). \tag{6.16}$$

Finally the refractive index is obtained as

$$n \approx 1 + \frac{1}{2}\rho\lambda\!\!\!^-\cdot\sigma(\Delta)\cdot\tilde{\Delta} \tag{6.17}$$

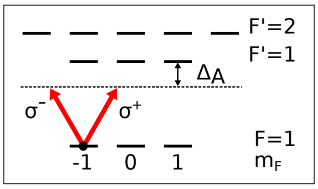

Figure 6.5: Level scheme of the D1 line of ^{87}Rb. Atoms are prepared in $|F=1,m_F=-1\rangle$ and we probe with linear light which translates to equal amounts of circular polarizations in the quantization axis.

and the optical depth is

$$D=\int\sigma(\varDelta)\rho(\vec{r})\mathrm{d}r. \tag{6.18}$$

In the molecular scattering cross section, the transition dipole moments are scaled by b_C, such that the two atomic dipole moments are spread out over the molecular potentials. They are also scaled via the relative transition strength ξ to account for hyperfine structure and Zeeman sublevels.

6.4 Extension to Faraday Rotation in a Multilevel System

In this section the model is completed by applying it to our specific experimental situation 6.5, measuring the polarization rotation of light.

The atomic ensemble is assumed to have a Gaussian density distribution $\rho(r,z)=\rho_0\exp\left(-\frac{r^2}{2w_r^2}-\frac{z^2}{2w_z^2}\right)$, with waists w_r and w_z. The sample is spin polarized in the $|F=1,m_F=-1\rangle$ state in the quantization axis defined by the magnetic field, which is aligned with the propagation direction of the probe light. The probe light is linearly polarized and is mapped into the atomic reference frame as equal amounts of circular left and right hand polarizations, driving the atomic σ^+ and σ^- transitions. A polarization rotation is observed if there is a difference in the phase shift of the two light polarizations. The Faraday angle is then half of the phase shift difference of the circular polarizations:

$$\theta_F=\frac{1}{2}\left(\phi_L-\phi_R\right). \tag{6.19}$$

Here $\phi_{L/R}$ are the sums of the phase shift of all involved excited state levels for the left or right hand circularly polarized light. We can then write the Faraday angle for independent atoms as

$$\theta_F^A(\varDelta_A)=\frac{1}{4}\sum_i p^{(i)}\tilde{\varDelta}_A\sigma_A^{(i)}(\varDelta_A)\int\rho(r)\mathrm{d}z, \tag{6.20}$$

where $p^{(i)}$ is $+1$ for σ^+ transitions and -1 for σ^-, $\tilde{\rho}(r)=\rho_0 w_z\sqrt{2\pi}\exp\left(-r^2/2w_r^2\right)$ is the column density.

Analogously, the molecular Faraday angle is

$$\theta_F^{pa}(\varDelta_A)=\frac{1}{4}\sum_{i,\mathrm{v}} p^{(i)}\tilde{\varDelta}_{\mathrm{v}}\int\sigma_{pa}^{(i)}(\mathrm{v},\varDelta_A,r,z)\rho(r)\mathrm{d}z, \tag{6.21}$$

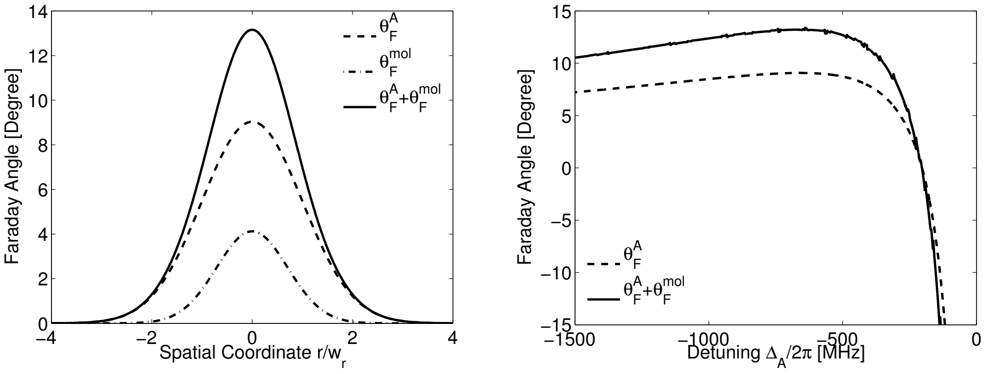

Figure 6.6: Left: Spatially resolved Faraday angle for a Gaussian density distribution at the $\Delta_A = -600$MHz detuning for a peak density of $\rho_0 = 2.64\ 10^{19}$m^{-3}. The molecular Faraday angle has a $\sqrt{2}$ reduced waist compared to the atomic angle. Right: Peak Faraday angle of non-interacting atoms and total angle including interactions as a function of detuning for a peak density of $\rho_0 = 2.64\ 10^{19}$m^{-3}.

where the normalized detuning $\tilde{\Delta}_\mathrm{v} = 2\frac{\Delta_\mathrm{v}}{\gamma_\mathrm{v}}$ was introduced.
In the expression for the angle, only the density is dependent on the position z along the light path. The density appears squared in the molecular expression, such that

$$\int_{-\infty}^{\infty} \rho(r,z)^2 \mathrm{d}z = \rho_0^2 w_z \sqrt{\pi} \exp\left(-\frac{r^2}{w_r^2}\right), \tag{6.22}$$

and the radial shape of the molecular Faraday angle has Gaussian shape with a $\sqrt{2}$ reduced waist compared to the atomic density distribution (Fig. 6.6 left panel). This means that the total angle $\theta_F = \theta_F^A + \theta_F^{pa}$ is spatially a sum of two Gaussians with different widths. While the atomic Faraday angle increases linearly with density, the molecular increases quadratic (Fig. 6.7 left panel) leading to an enhancement $(\theta_F^A + \theta_F^{pa})/\theta_F^A$ (Fig. 6.7 right panel) that is linear in density.

The detuning dependence of the atomic and total angles is plotted in the right panel of Fig. 6.6. The vibrational resonances appear as small spikes on top of the total angle. The enhancement is due to the inclusion of the off-resonant effect of the repulsive potentials. The refractive index deviation from the vacuum value, (n-1), is shown in Fig. 6.8, as well as the enhancement due to light-assisted collisions. The typical dispersive line shapes of the two hyperfine states is recovered and the enhancement plot shows again the vibrational resonance spikes. Finally, Fig. 6.9 shows in the top panel the enhancement of absorptivity by comparing the total optical depth to the atomic optical depth, which is shown in the inset. The bottom panel shows the enhancement of the Faraday angle for a peak density of $\rho_0 = 2.64\ 10^{19}$m^{-3}. The absorptivity is increased by 25% in between resonances and up to a factor of 10 on resonances. The Faraday angle enhancement is almost constant with detuning with a factor 1.46 and small corrections due to vibrational resonance features. The bigger features around the -200MHz detuning appear since the Faraday angle vanishes at this point.

All the presented figures in this chapter use the following parameters. The atomic ensemble has widths $w_r = 7.71\mu$m and $w_z = 70.52\mu$m, the peak density is $\rho_0 = 2.64 \cdot 10^{19}$m^{-3} and the incident light intensity is $I^{inc} = 3.3 \cdot 10^{-3}$W/m^2.

6.5 Limitations

The presented model is to my knowledge the only model that predicts an increase of a dispersive signal. Similar models were devised for absorptive signals [RYG$^+$10], but show

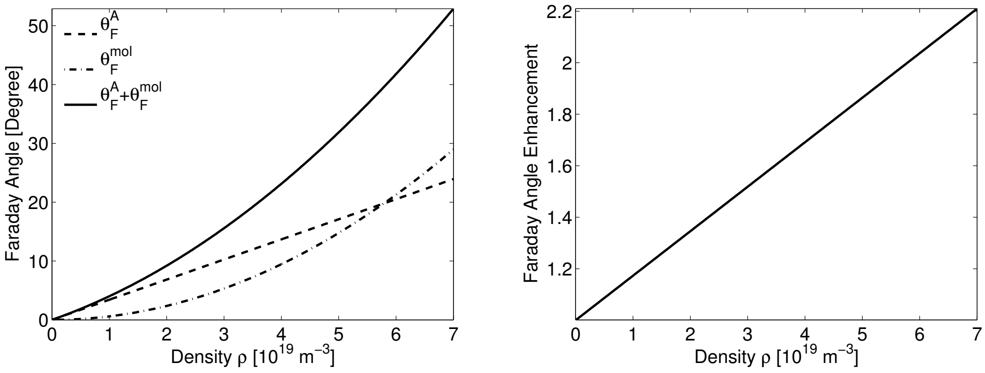

Figure 6.7: Left: Faraday angle as a function of density at a detuning of $\varDelta_A = -600$MHz. The atomic Faraday angle θ_F^A increases linearly while the molecular θ_F^{pa} scales as density squared. Right: Resulting Faraday angle enhancement factor $(\theta_F^A + \theta_F^{pa})/\theta_F^A$ due to interactions between two atoms at the -600MHz detuning.

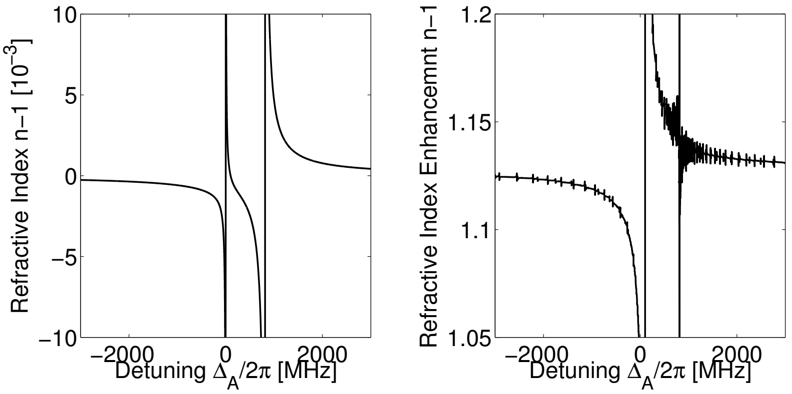

Figure 6.8: Refractive index deviation (n-1) due to non-interacting atoms (left) and the enhancement of (n-1) due to interactions. The peak density is $\rho_0 = 2.64\ 10^{19}\mathrm{m}^{-3}$

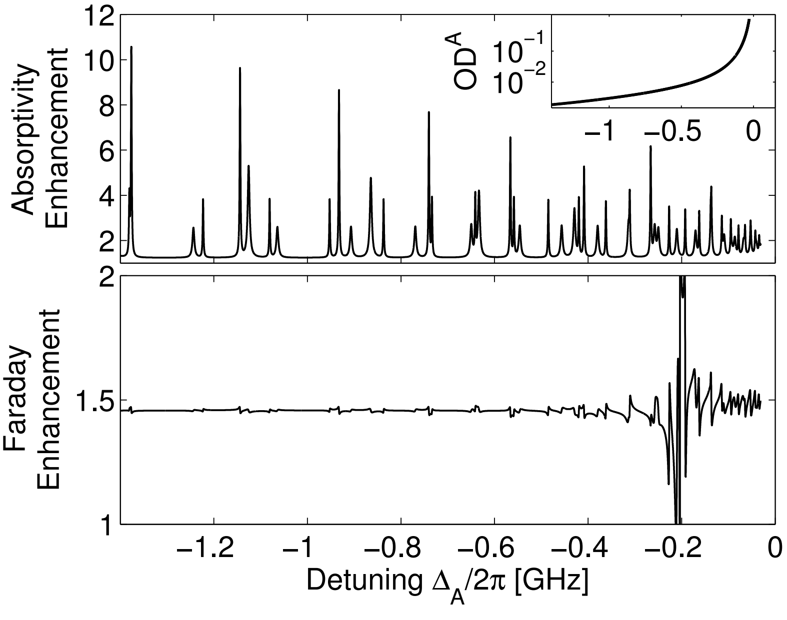

Figure 6.9: Top: Enhancement of absorptivity, the ratio between the total optical depth to the atomic optical depth, which is also plotted in the inset. Bottom: Enhancement of Faraday rotation signal due to light-assisted collisions. The peak density is $\rho_0 = 2.64\ 10^{19}\mathrm{m}^{-3}$.

a signal reduction. This implies that the oscillator strength is redistributed from the line center into the wings.

The light-assisted collision model uses many approximations. The reflection approximation requires the vibrational resonance lines to be treated as non-overlapping. This requirement breaks down for the resonances closest to the atomic line. Even though they are not addressed resonantly they do contribute off-resonantly. The introduced atomic decay rate into the Condon radii limits, on the other hand, the influence of resonances close to the dissociation limit (see Fig. 6.2). The usual picture is that the Condon radii are very large close to the dissociation limit. The assumption of having only dimers is then incorrect and atoms form larger clusters.

The model does not include the effect of hyperfine structure on the molecular potentials. The hyperfine structure is only accounted for in the assignment of detunings to the relevant Zeeman sublevels.

A more fundamental limitation might be the assumption that the light-assisted collision signals are a small perturbation to the independent atom result and may therefore be summed. A more realistic treatment should, pictorially, have a weighting function for the two terms, since an atom that contributes to the independent atom result can not at the same time contribute to the dimer term. This problem could be addressed by an appropriate normalization of the involved wavefunction.

Overall the model hints towards a mechanism that allows for increased Faraday rotation angles as compared to the independent atom assumption.

Seven

Superradiant Rayleigh Scattering

7.1 Introduction

Superradiance is a four-wave mixing process. Coherent emission by the atomic ensemble is generated as a collective process. It was first studied in electronically inverted systems [Dic54] and works in a similar way as a laser. A fully inverted system will start to emit a photon spontaneously, which populates a first photonic mode. After this first event stimulated emission sets in and the system is said to become superradiant as all excitations are released phase-coherent into the same mode. This phenomenon is also referred to as superfluorescence. Since there is a limited number of excitations in the inverted system, the light is emitted in a short pulse with characteristic time τ_{sp}/N, where τ_{sp} is the excited state lifetime and N is the number of emitters present. This is illustrated in Fig. 7.1. If the sample is elongated, two so called endfire modes can appear. Since the emission direction is given by the interference of all dipoles in the sample, scattering occurs predominantly

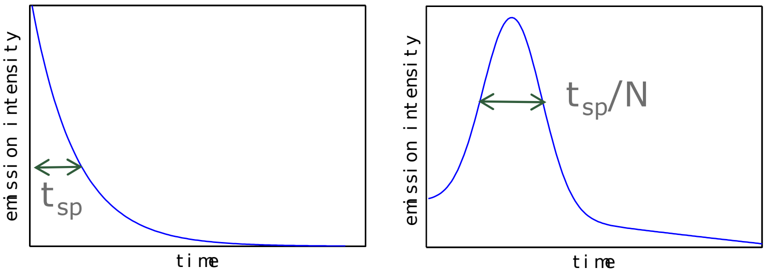

Figure 7.1: Illustration of typical averaged signals obtained from single atom emission (left) and superradiant emission from N atoms (right). The superradiant emission occurs on a timescale which is N times smaller than the spontaneous emission time τ_{sp}.

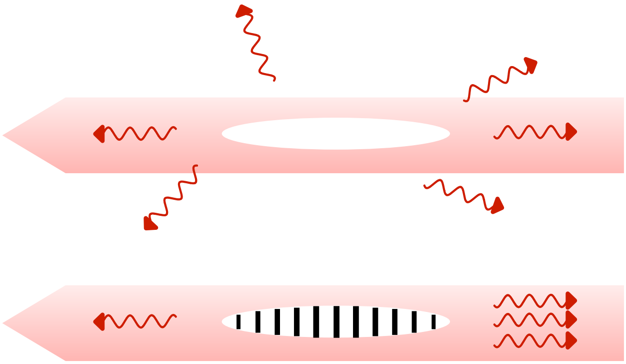

Figure 7.2: After the first spontaneous emission events (top), a density grating forms (bottom) and coherent emission into the backward endfire mode occurs.

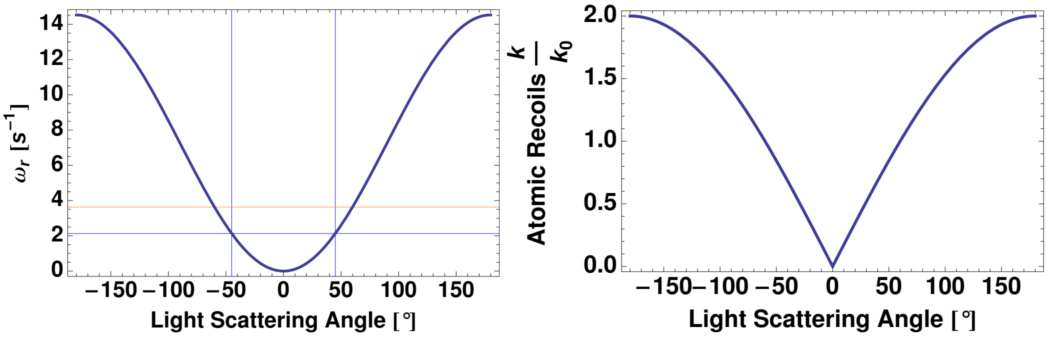

Figure 7.3: Left panel: Recoil frequency of a Rubidium 87 atom as a function of scattering angle between incident and scattered light. The blue lines correspond to the energy of a typical chemical potential and signify the range of small angle scattering, where Bogoliubov excitations occur and the Rayleigh scattering rate is reduced. The orange line is the recoil energy of a single D1 line photon. Right: The number of photon recoils transferred to an atom.

along the long axis of the sample, as is illustrated in Fig. 7.2.

Superradiance has been first observed in a BEC in 1999 [ICSK$^+$99]. When a probe beam with sufficient intensity interacts with an ultracold ensemble of atoms momentum is transferred to the atoms, which can be resolved on absorption images after a time of flight. The process does not involve an electronic inversion, but can be understood as an inversion in momentum space. Initially all atoms are in the zero momentum mode. As the light interacts with the atoms higher order momentum modes can be populated. This process is accompanied by coherent emission of light into the endfire modes. The initial experiments [ICSK$^+$99], where performed in a side-pumped geometry. The light is applied perpendicular to the cigar-shaped sample. The endfire modes then exit the sample perpendicular to the incoming light and atomic higher momentum modes are ejected in a fan shaped pattern. In our experimental geometry the probe light is applied along the long axis of the condensate, which leads to ejection of atoms along a line shaped pattern.

Recoil Momentum and Density Grating The momentum of the recoiling atoms $\mathbf{K}_r$ is defined by the wave vector of the probe light $\mathbf{k}_{in}$ and the wave vector of the endfire mode $\mathbf{k}_{out}$ as $\mathbf{K}_r = \mathbf{k}_{in} - \mathbf{k}_{out}$. The recoil energy is $\hbar\omega_r = \hbar^2|\mathbf{K}_r|^2/2M$ and is plotted in the left panel of Fig. 7.3 as a function of the angle $\alpha = \arccos(\mathbf{k}_{in} \cdot \mathbf{k}_{out}/(|\mathbf{k}_{in}||\mathbf{k}_{out}|))$ between the incident light and the scattered light. The right hand side of Fig. 7.3 shows the atomic recoil momenta normalized to the photon recoil of $k_0 = 2\pi/\lambda$. In a geometry where the sample is probed along its long axis, there is a forward and a backward mode, corresponding to $\alpha = 0$ and $\alpha = 180°$ respectively. There is no momentum transferred to atoms if light is forward scattered, but two photon recoils are transferred for backward scattering.

As momentum is transferred to some of the atoms their wave function Ψ acquires an extra phase $\exp(iK_r x)$ and interferes with the atoms inside the condensate mode to form a density grating $|\Psi_{tot}|^2 = |(1-\epsilon)\Psi_0 + \epsilon\Psi_0\exp(-iK_r x)|^2$ which becomes $\Psi_{tot}|^2 = |\Psi_0^2|\cos^2(K_r x/2)$ for maximal contrast, $\epsilon = 0.5$. Once a grating is established, the probe light is scattered from this grating, coherently building up the endfire modes.

Rayleigh Versus Raman Superradiance In Rayleigh superradiance the electronic state of the atoms is not changed. In Raman superradiance the final electronic state is different from the initial state and Stokes or Anti-Stokes light can become the superradiant mode. The earlier discussed density grating does then not appear, but rather a polarization grating. In this thesis only Rayleigh superradiance is discussed.

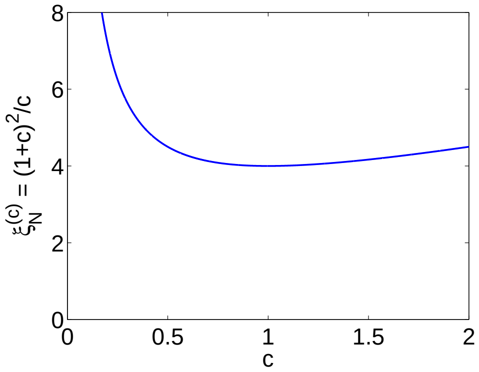

Figure 7.4: Number squeezing parameter assuming two independent coherent states. The variable c is the ratio between atom and photon counts, the asymmetry. $\xi_N^{(c)}$ is minimal for identical atom and photon numbers with a value of 4. In contrast, the two-mode squeezed state achieves $\xi_N = 0$.

Kapitza-Dirac Scattering The backfire-mode-photons can in turn interact with the atoms. The photons scattered in this way are emitted back into the probe light. This results in atoms that are ejected into the backwards direction, against the propagation direction of the probe beam. This process is energetically forbidden, since the scattered photons have a smaller energy than the probe photons. This barrier can be overcome for short pulse durations, for which the photon energy has a bigger spread due to the Heisenberg uncertainty principle or for high light intensities [STB$^+$03].

7.2 Parametric Gain and Two-Mode Squeezing

Superradiance is a four-wave mixing process. The Hamiltonian can be reduced to a parametric down-conversion Hamiltonian when the light probe mode and the atomic zero momentum mode are not significantly depleted:

$$\mathcal{H} = \left(g\hat{a}^\dagger\hat{b}^\dagger + g^*\hat{a}\hat{b}\right). \tag{7.1}$$

Atoms and photons are created or annihilated in pairs. This Hamiltonian generates two-mode squeezed states [GK05]

$$|\xi\rangle_2 = \frac{1}{\cosh r}\sum_{n-0}^{\infty}(-1)^n e^{in\theta}\left(\tanh r\right)^n |n,n\rangle, \tag{7.2}$$

where $|n,n\rangle$ is the Fock basis, r is the squeezing parameter and θ is a phase. The atom and photon pairs created in this way are entangled. The state $|\xi\rangle_2$ is an eigenstate of the number difference operator $\hat{n}_A - \hat{n}_P$ with vanishing eigenvalue and therefore

$$\mathrm{Var}\left(\hat{n}_A - \hat{n}_P\right) = 0. \tag{7.3}$$

The number operator mean values are $\langle\hat{n}_A\rangle = \langle\hat{n}_P\rangle = \sinh^2 r$ and the variances are $\mathrm{Var}(\hat{n}_A) = \mathrm{Var}(\hat{n}_P) = \sinh^2 r \cosh^2 r$. Since $\mathrm{Var}(\hat{n}_A)/\langle\hat{n}_A\rangle > 1$ the atom and photon statistics are super-Poissonian.

A criterion for number squeezing is [EGW$^+$08]

$$\xi_N = N \frac{\mathrm{Var}\,(\hat{n}_A - \hat{n}_P)}{\langle \hat{n}_A \rangle \langle \hat{n}_P \rangle}, \tag{7.4}$$

where $N = \langle \hat{n}_A \rangle + \langle \hat{n}_P \rangle$, the total number of atoms and photons. For the two-mode squeezed state $\xi_N = 0$, since the variance of the number difference vanishes. If atoms and photons in independent coherent states $\xi_N = N^2 / (\langle \hat{n}_A \rangle \langle \hat{n}_P \rangle)$ and this can be simplified by assuming that $\langle \hat{n}_P \rangle = c \langle \hat{n}_A \rangle$, such that $\xi_N = (1 + c^2)/c$ for independent coherent states. This is plotted in Fig. 7.4.

The relevant squeezing parameter for metrology is $\xi_S = \xi_N / \cos\phi$ [WBIH94] and a measurement precision below the quantum noise limit is achieved for $\xi_S < 1$. Since $|\cos\phi| < 1$ two independent coherent states can not reach this limit. Only if $\xi_N < \cos\phi < 1$ is achieved can metrologically relevant squeezing be present.

Part III

Experimental Techniques

Eight

Atom Trapping and Cooling

The experimental setup is described in great detail in Andrew Hilliard's [Hil08] and Christina Olausson's [Ola07] theses and their figures of the experimental apparatus are reproduced here. This chapter emphasizes the parts of the apparatus that are of greatest relevance to the experiments described in this thesis.

At the heart of the experimental setup is a two chamber vacuum system. We use two different magneto-optical traps (MOT) for atom trapping and cooling. The final cooling step is performed by evaporative cooling in a purely magnetic trap. The following sections will describe the different parts in detail.

8.1 Vacuum System

The vacuum system is shown in Fig. 8.1. There are two chambers, the loading MOT chamber and the science MOT chamber. They are connected by a tube (graphite, 5mm inner diameter, 85mm length), which acts as a differential pumping stage. Attached to the loading MOT chamber are the Rubidium dispensers, which we use in continuous

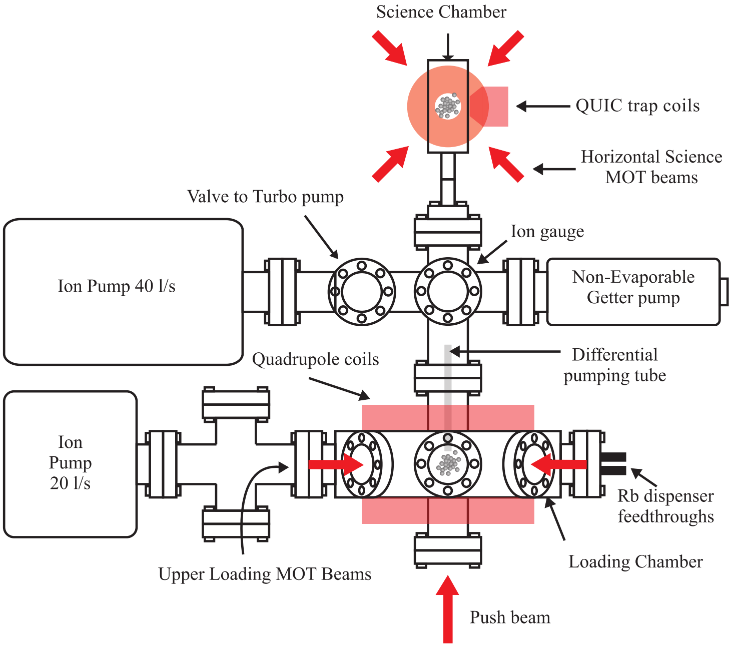

Figure 8.1: Top view of the two chamber vacuum system with ion pumps, dispensers, the differential pumping stage, and the coils for MOTs and magnetic trap. Indicated are also the laser beams for the MOT operation.

operation, and a 20 l/s ion pump. We estimate the pressure to be 10^{-9}mbar. On the science MOT side of the differential pumping stage there is a 20 l/s ion pump and a non-evaporable getter pump. An ion gauge determines the pressure in the science MOT part of the system. The pressure there is about 10^{-11}mbar. The science MOT is obtained in a glass cell (science chamber) which is AR coated on the outer walls.

8.2 Magneto-Optical Traps

Magneto-optical traps (MOTs) are formed by combining a magnetic quadrupole field, which gives linear field gradients, with slightly detuned laser beams. A pair of counter-propagating beams is needed for each spatial direction with the same circular polarization (for a σ^+-σ^- configuration). The detuning of the laser beams is responsible for the slow-down and hence cooling of the atoms. The magnetic field gradients shift the atomic resonances, and therefore regulate which of the excited states interact strongest. The magnetic field is consequently responsible for trapping the atoms at a fixed point in space.

Loading MOT Our loading MOT is in fact an 'open' MOT, since it is missing one beam, which allows the atoms to be transferred to the science MOT. We use two large retro-reflected beams and a push beam, that transfers the atoms to the science MOT through the differential pumping stage. The configuration of the beams and the quadrupole coils can be seen in Fig. 8.1. The light is detuned by -24.4MHz with respect to the F=2 to F'=3 D2 line transition. We mix a repump beam into the MOT beams to pump atoms from the F=1 ground state back into the F=2 state using the F'=2 excited state.

Science MOT The science MOT has six independent beams originating from one laser. The main MOT beam is mixed with a repump beam and then split into the six individual beams, which are then enlarged by lenses in a telescope configuration. Four of the beams enter in a plane parallel to the optical table as indicated in Fig. 8.1. The other two beams come from the top and bottom. The light is detuned by -12.2MHz from the F=2 to F'=3 D2 line transition. The quadrupole field is provided by coils sitting above and below the glass cell with a gradient of about 17G/cm.

The loading of the science MOT is one of the most critical parts of the experimental procedure. It takes about 30 seconds if optimized well, but degrades during the day to much longer times.

8.3 The Laser System

We need light close to the D2 line of Rubidium 87 for trapping, cooling and absorption imaging. Light closely resonant to the D1 line is needed for probing (Faraday imaging and superradiance). We use various saturated absorption locking techniques on the setup in combination with room temperature gas cells filled with Rubidium of natural abundance. The lasers are locked to the lines of the more abundant Rubidium 85. This has the advantage that there is no danger of creating any unwanted stray light which is resonant to the pure Rubidium 87 of the fragile condensate. We only use home-built lasers essentially following the Hänsch design [RWE+95], in a Littrow configuration.

Trapping, Cooling and Absorption Imaging The D2 line laser setup is shown in Fig. 8.2. It comprises one laser for all the repump light needed at the different places and during various stages of the experimental cycle, a master laser that injects four slave lasers, of which two can be frequency shifted by an AOM in double pass configuration, relatively to the master laser.

The repumper is locked by current modulation to the F=1 to F'=1/2 cross-over peak, -78.5MHz to the red of the Rubidium 87 F=1 to F'=2 transition and hereafter frequency

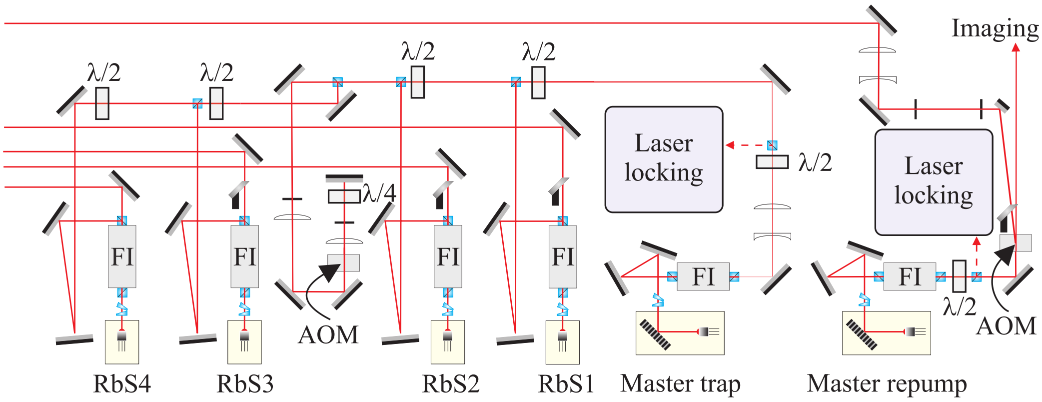

Figure 8.2: Setup of the lasers operating on the D2 line used for trapping and cooling the atoms as well as absorption imaging. Each laser is protected from back-reflected light by Faraday isolators (FI). There is one repump laser and a master laser which injects four slave lasers.

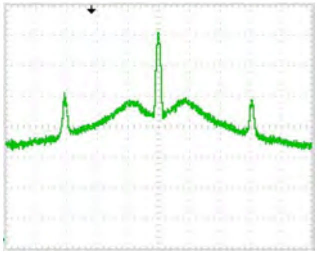

Figure 8.3: Beatnote signal between the two D1 line lasers. The sharper side peaks are 1.3MHz away from the center, the smoother side bumps are 770kHz away. The full width of the main peak is about 2kHz (limited by the resolution bandwidth) and the noise reduction around the peak is -30dBm.

shifted to resonance by AOMs. The AOMs are used in combination with mechanical shutters to switch between the beams for either the loading and science MOT or for absorption imaging.

The master laser, injecting the slaves, is locked to the Rubidium 85 F=1 to F'=2/3 crossover peak by frequency modulating the saturating beam of a saturated absorption setup with an AOM. This results in a detuning of -133.3MHz, towards the red of the Rubidium 87 F=2 to F'=3 transition. The light is then distributed to the four slave lasers. RbS1 and RbS2 generate the light for the loading MOT. RbS3 is used for the science MOT light and RbS4 for absorption imaging and the loading MOT push beam. There are various AOMs involved in getting to the final frequencies.

Light For Probing and Faraday Rotation Imaging To generate the D1 line probe light we use two lasers. The first one is locked by standard saturated absorption spectroscopy to the Rubidium 85 F=2 to F'=3 transition by means of current modulating the laser at 10MHz. The second laser is then locked to the first by a beatnote setup in combination with a digital phase-lock [Al09]. This allows us to lock the two lasers up to about 10GHz apart from one another and gives us the ability to probe the atoms at a wide range of detunings.

A typical beatnote signal is shown in Fig. 8.3 (from the video output of the spectrum analyzer, therefore no scales).

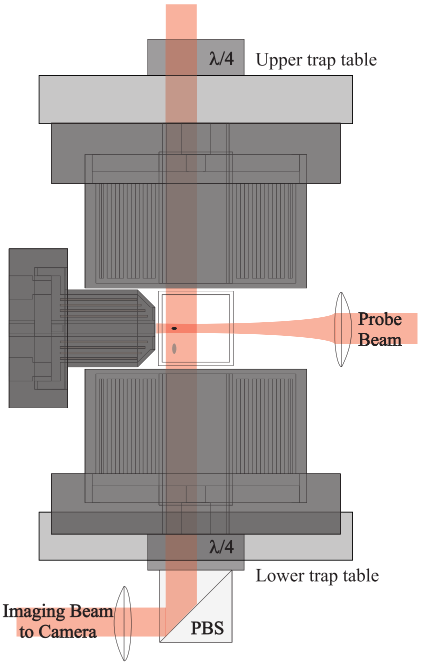

Figure 8.4: QUIC trap setup. The quadrupole coils sit above and below the rectangular glass cell, which contains the atoms. The Ioffe coil is on its left side. The atoms are indicated at their QUIC trap position, 8mm horizontally offset from their quadrupole position. Shown in light grey is the position of the atoms during absorption imaging. The quarter wave plates of the MOT are above and below the quadrupole coils. Also shown is the probe beam coming from the right, which is the configuration for the superradiance experiments.

ω_r	$2\pi \cdot 115.4 \pm 0.5\mathrm{s}^{-1}$
ω_z	$2\pi \cdot 11.75 \pm 0.25\mathrm{s}^{-1}$
B_0	880mG
x_{sag}	18µm

Table 8.1: Parameters of our QUIC trap. The radial and axial trap frequencies ω_r and ω_z are experimentally determined as well as the trap bottom B_0. The sag x_{sag} is calculated.

8.4 Magnetic Trap

Our magnetic trap has a Ioffe-Pritchard type field geometry realized by a Quadrupole-Ioffe configuration (QUIC) [EBH98]. Consequently our setup consists of two coils in an anti-Helmholtz configuration, which produce a quadrupole field, and a smaller Ioffe coil, which is perpendicular to the symmetry axis of the quadrupole coils. This is shown in Fig. 8.4. The extra coil introduces a non-zero magnetic field minimum and therefore avoids atom losses due to Majorana spin-flops. The field geometry is a harmonic field with an offset B_0 and has a symmetry axis which is aligned with the Ioffe coil axis (z). It is further described in App. B.6. The atoms, however, do not sit at the minimum position of the magnetic field. They are dragged by gravity to a lower position by the amount $x_{sag} = -g/\omega^2$, where g is the gravitational constant and ω the trap frequency. The trap parameters are listed in table 8.1.

In the experimental sequence we start by transferring the atoms from the science MOT via a molasses phase into a pure quadrupole magnetic field. This is necessary, since the additional Ioffe coil moves the center position by about 8mm towards the coil, making a direct transfer impossible. The Ioffe coil is slowly switched on in order to avoid any sloshing caused by transferring the atoms into the Ioffe-Pritchard configuration.

The QUIC trap is run at 25A, dissipating 600W of power. Therefore it requires water cooling. To avoid accidental overheating of the coils, we redesigned our water flow control circuitry (App. D.1). The water cooling is provided by a chiller in combination with a large buffer tank.

The coils are driven by the same supply to avoid movements of the trap minimum due to current noise.

The disadvantage of the QUIC trap is that optical access from the Ioffe coil side is obstructed. We therefore designed the Ioffe coil with a hole of 4mm diameter, giving us the possibility to probe along the long axis of the sample. Since there is hardly any space between the Ioffe coil and the glass cell, the closest distance of a collimation lens to the atoms is restricted to the length of the coil. This limits the focus of the probe beam to a radius of about 20μm at the atoms.

8.4.1 Radio-Frequency Dressing and Evaporative Cooling

The last part of the cooling process of the atoms has to be performed without any light present. This is done by evaporative cooling inside the magnetic trap [KV96]. Cooling is performed by removing the atoms with the highest temperature from the trap and leaving enough time for the remaining atoms to thermalize. By slowly cutting deeper into the thermal distribution of the atoms one reaches colder temperatures while increasing the phase-space density.

The process of cutting into the thermal distribution is realized by radio-frequency (rf) fields, which can be used to dress the atomic resonances inside a magnetic field, effectively opening the magnetic trap according to the resonance condition $\mu|B(r)| = \hbar\omega_{rf}$. Atoms with larger energies can escape.

We have two rf coils. One centered on the position of the quadrupole trap and one centered on the QUIC trap position. They are driven by an rf synthesizer which is computer controlled.

Figure 8.5 shows absorption images taken during an evaporation sequence. The images are taken inside the trap. The imaging system is out of focus at this point, but one can still see how the atomic cloud becomes smaller and more dense during the evaporation process. The first image is taken just after transfer of the cloud into the QUIC trap, where the atoms are in the reach of absorption imaging. The other images after further evaporation steps.

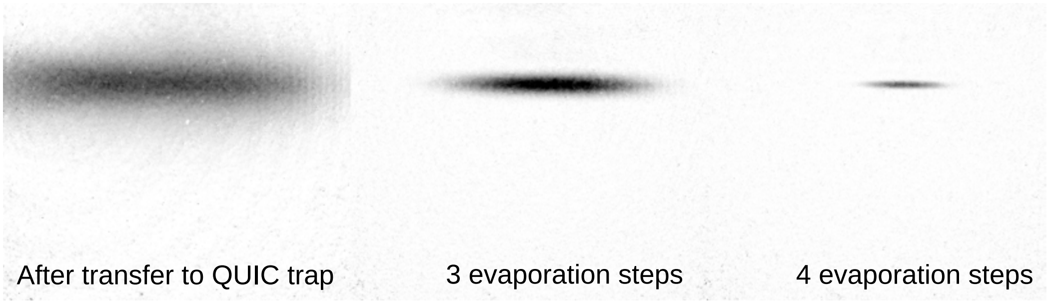

Figure 8.5: Absorption images of the atomic cloud during the evaporation sequence. The images are taken when the atomic cloud is inside the trap (no time of flight).

Nine

Experimental Control

Almost all elements of the experiment are computer controlled for precise timing and automation. A reliable control program is irreplaceable in achieving this.
This chapter will first explain which parts are controlled and in which way and will then go on in explaining the experimental sequence in more detail.

9.1 Experiment-Computer Interface

Our control system (Fig. 9.1) is based on four computers which communicate over the local network by TCP/IP. BECmain is the main control computer, AtomCam and DrMueller host the cameras and Attic is used for data storage and data analysis while acquiring data.
The main control computer, BECmain, hosts our LabView based control program, which has at its heart a time-slice array. This array can be filled with the various time-slice log files, containing all the information on when to switch a device or alter its supplied signal strength. The control program connects to the LabView program that handles the DTA camera (CHROMA C3, KAF3200ME, absorption imaging) on the computer AtomCam, to the rf synthesizer, and the oscilloscope called Robbie. BECmain connects to devices of the experimental setup via two analog boards (National Instruments NI6713 with 8 channels, ±10V, 12bit, 4.9mV amplitude resolution and National Instruments NI6723 with 32 channels, ±10V, 13bit, 2.4mV amplitude resolution - limiting time resolution is 2μs), and a digital board (Viewpoint Systems PCI DIO-64, 64 I/O channels, 20MHz clock - 50ns time resolution). One port of the digital board is defined as an input. This is for the trigger signal which starts the experimental sequence. It is generated by comparing a set-value to a photodiode that monitors the science MOT fluorescence.
Our second camera (ANDOR iKON-M DU934N-BRD) is hosted by the computer called DrMueller and is controlled by the ANDOR acquisition program. The ANDOR and DTA images as well as the oscilloscope traces are stored on the computer named Attic, which is also used for the MATLAB analysis of the data.
Computer controlled are all the shutters, one VCO (voltage controlled oscillator) frequency, several rf attenuators and switches for AOMs, the magnetic field amplitude and switching of the QUIC coils, the amplitude of rf fields for evaporation and the switch between the two available coils, triggers for the scope and the cameras as well as the light pulse for absorption imaging. Controls that are constant throughout any experimental run are not computer controlled. These are the water cooling of the QUIC coils, the laser stabilization locks, the set-point of the beatnote lock of the probe laser, the bias B-fields of the loading MOT, most VCOs for AOMs, any alignment of optical elements, power control of laser beams and the image pulse generator settings.
Most of the mentioned manual tasks are either unnecessary to control by computers or computer control is difficult and even unfeasible. For a real 'controlling-experiment-from-home' experience it would be at least necessary to have online logs of the water cooling

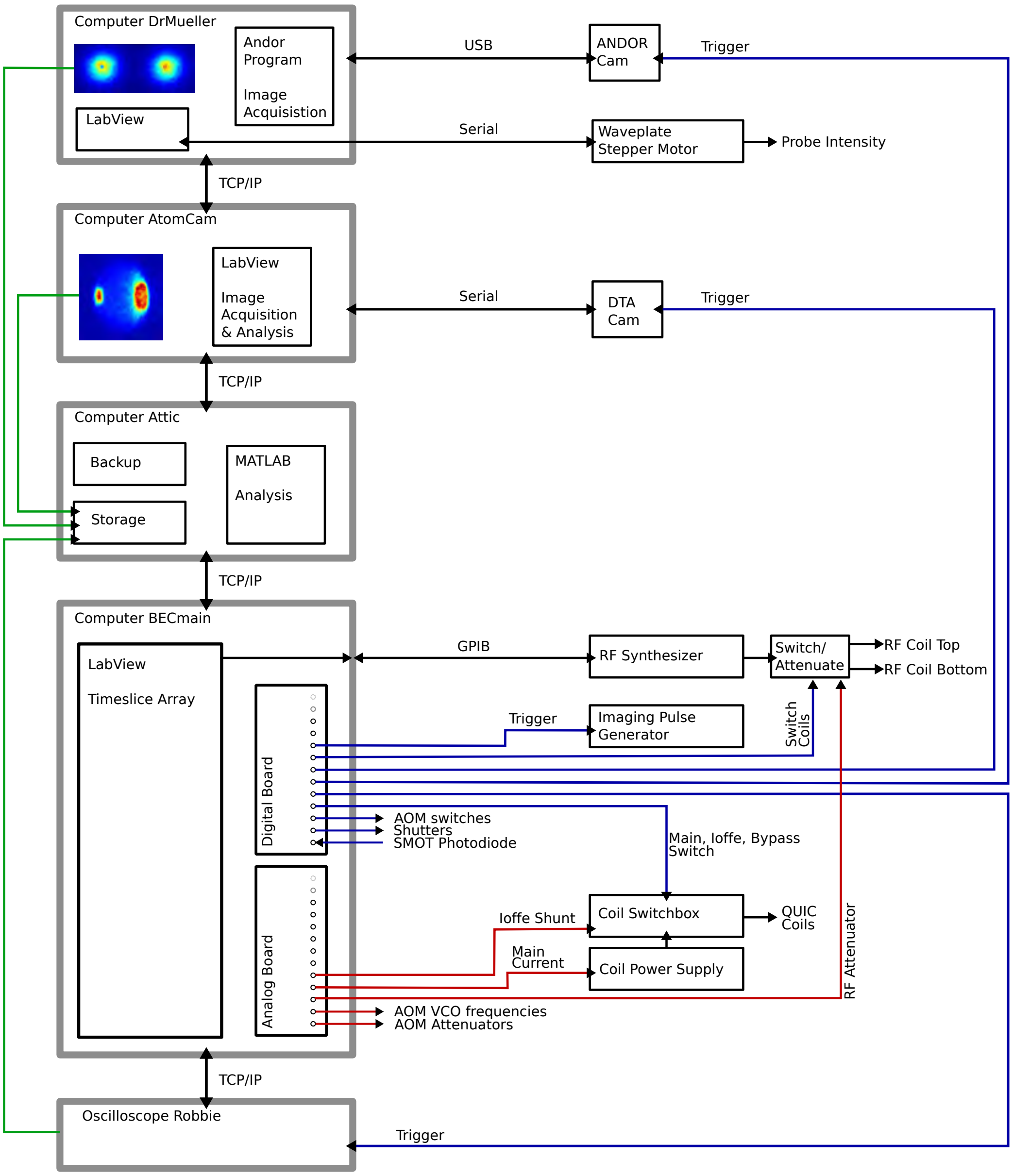

Figure 9.1: Schematic of the computer control of the experiment. Four computers (left) control the devices used in the experiment (right). Digital controls are blue, analog controls red and data storage is green.

and of the laser powers. In practice the laser locks limit the time the experiment can run independently.

9.2 Experimental Sequence

A standard experimental sequence comprises of a MOT loading phase, which is followed by a compression, an optical molasses phase and optical pumping. Then the quadrupole magnetic trap is turned on and the evaporation begins. Then the atoms are transferred to the QUIC trap, where the evaporation continues until a condensate forms. The sequence is finished by probing and imaging the atomic ensemble.

Initially the loading MOT and the science MOT are running, while the push beam connects the two. The sequence starts when the fluorescence of the science MOT reaches the trigger level. What happens next is shown in the left panel of Fig. 9.3: the MOT is expanded by reducing the current in the quadrupole coils during 50ms (see Fig. 9.2 for a schematic drawing of the switching and current control of the coils). Then the main

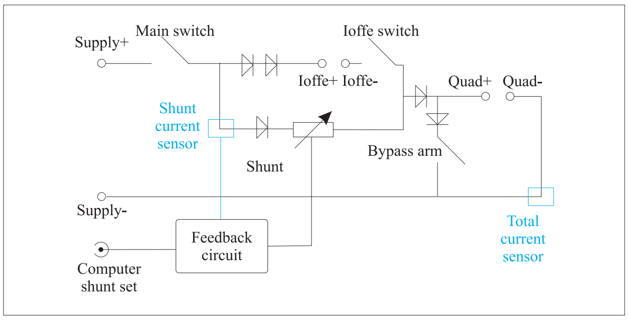

Figure 9.2: Schematic drawing of the QUIC coil switchbox.

current is stepped to zero and held for 20ms. The response of the coils to a current step has a time constant of 60ms. This means the magnetic field strength slowly reduces. Simultaneously the VCO controlling the frequency of the science MOT beams is ramped to larger detunings (from -12MHz to -46MHz) and the repumper intensity is reduced. This leads to a compression and further cooling of the MOT (CMOT stage). Next the magnetic field is switched off completely. The coil response to this is a 200µs linear ramp. This leaves the atoms for 2ms in an optical molasses. After this the repumper is turned off for 3ms, such that the atoms are optically pumped by the science MOT beams into the F=1 ground state.

Now the quadrupole coils are turned on for pure magnetic trapping. This phase is illustrated in the right panel of Fig. 9.3. There is a short coil switching phase that is not shown, then the QUIC trap main switch is turned back on and the current is ramped to its maximal value. The Ioffe switch remains off and the Ioffe shunt is completely open, shunting any current from the coils. The atoms are therefore trapped in a quadrupole magnetic field. At the same time the rf evaporation begins using the top rf coil. During 10s the frequency is linearly decreased from 40MHz down to 20MHz. Then the Ioffe switch is released and the current running through the Ioffe coil increases for 700ms until the shunt is closed and the full current passes through the Ioffe coil. During this period the cloud is transferred from the quadrupole field geometry to the QUIC geometry. The atoms move 8mm in real space towards the Ioffe coil. The evaporation is continued with the lower rf coil down to a rf frequency of about 1MHz. At this point the increased density leads to a significant amount of trap losses via three-body collisions. In order to avoid these losses the QUIC trap current is reduced, decompressing the trap and therefore decreasing the density. The

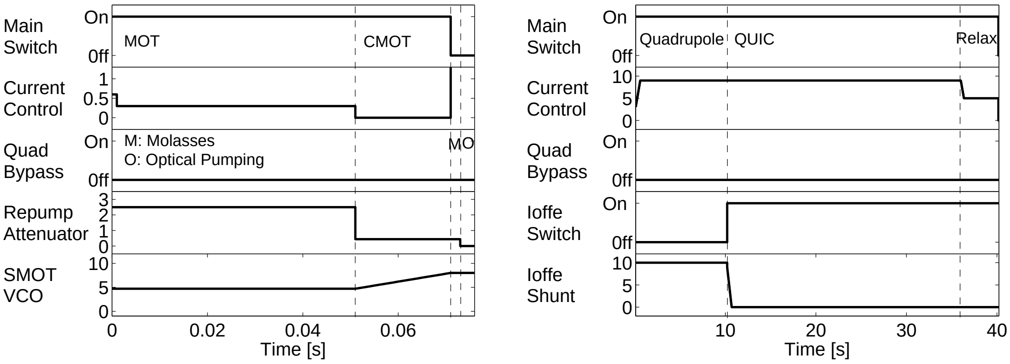

Figure 9.3: Left: Schematic of the beginning of the experimental sequence. Shown are selected digital and analog channels plotted against time as reproduced from our time-slice log files. The channels are the QUIC trap main switch, total current and quadrupole bypass switch, the rf attenuator of the repumper AOM and the VCO regulating the detuning of the science MOT beams. Right: Schematic of the magnetic trapping part of the experimental sequence.

evaporation is continued down to quantum degeneracy (about 570kHz) or slightly above (650kHz or higher). This finalizes the sample preparation and leaves the atoms ready for interrogation.

Depending on the specific experimental aim the atoms are probed inside the magnetic trap or after a time of flight. The probing can be either dispersive imaging or detection with a differential photodiode. The atoms are released from the trap by closing the main switch of the magnetic trap. Consequently the atoms fall freely under the influence of gravity for a time of flight of usually 45ms when we perform absorption imaging (see Sec. 10.1.1).

Ten

Imaging Techniques

This chapter introduces in the first section the experimental imaging setups. The second section describes how the camera calibrations were performed. The chapter rather concentrates on experimental procedures than on theoretical descriptions.

10.1 Imaging Setups

There are two imaging systems on the experimental setup. In each experimental cycle resonant absorption imaging (Sec. 5.1) is employed to gain information on sample parameters. It is performed after a time of flight (TOF) to reduce the interaction strength with the ensemble.
The Faraday rotation experiments are performed with a second imaging system. The atoms are probed inside the trap with a far detuned laser, such that the light-matter interaction is dispersive (Sec. 5.2.1).

10.1.1 Absorption Imaging

Setup

The absorption imaging setup is sketched in Fig. 10.1. The probe beam passes through the same optics as used for the MOT (PBS, wave plates), which is blocked during imaging. The probe beam is prepared in a circular polarization by the first quarter wave plate.

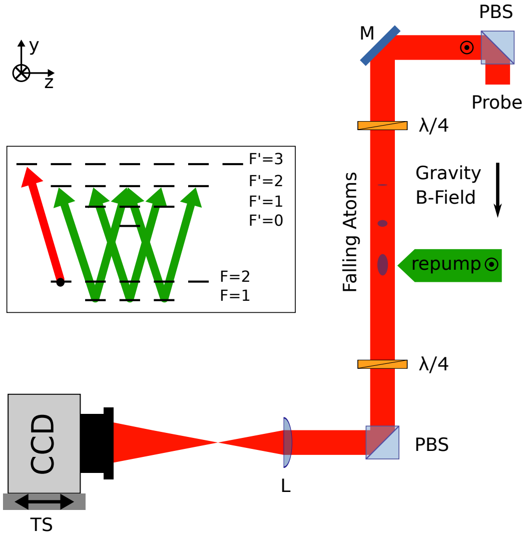

Figure 10.1: Left: Absorption imaging setup and D2 line level scheme. The probe beam is shown in red and the repumper in green.

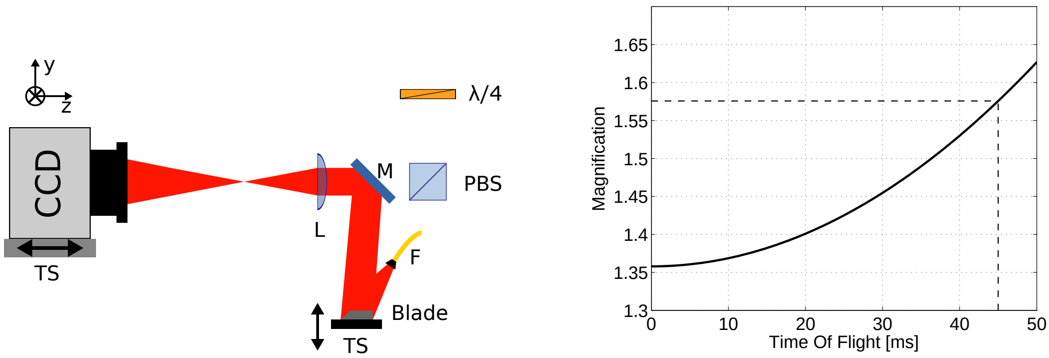

Figure 10.2: Setup for the determination of the magnification of the absorption imaging setup (left) and the magnification as a function of time of flight (right). The lines indicate our standard time of flight setting of 45 ms.

Inside the magnetic trap the atoms reside in the F=1, $m_F = -1$ state in the quantization axis defined by the local magnetic field, which is mainly oriented along the z direction. For imaging, however, we apply a magnetic field oriented along gravity. It is switched on shortly after releasing the atoms from the trap. During time of flight the atoms expand according to their in trap velocities. This reduces the density of the ensemble and therefore also the light absorption. This is crucial for ultracold atoms, since the light signal transmitted by the atoms is otherwise lower than the sensitivity of the camera and cannot be detected.

The atoms fall freely due to gravity after turning off the magnetic trap. We use a 2µs repump pulse on the F=1 to F'=2 D2 line transition which drives simultaneously σ^+ and σ^- transitions and transfers the atoms into the F=2 ground state manifold. The line strength S_{12} from F=1 to F'=2 is $S_{12} = 5/12$, while the line strength from F=2 to F'=2 is $S_{22} = 3/12$. This means that the atoms are more likely to fall back to the F=1 manifold after being excited, but since the light is far detuned once atoms are in F=2, eventually all atoms will end there. After 10 scattering events a single atom will be with nearly 100% probability in the F=2 state. To repump the full ensemble a number of photons which is 10 times the number of atoms is required.

The resonant probe (F=2 to F'=3) is turned on immediately after the repumper for 50µs. It's polarization is circular, driving the σ^- transition. If the sample is fully polarized in the $F = 2$ $m_F = -2$ state, the cycling transition is driven by the probe laser. It has an on-resonant absorption cross section of $\sigma_0 = 3\lambda_{D2}^2/2\pi$, neglecting saturation effects.

We use a gradium lens (L) with a focal length of 100mm to image the atomic cloud onto a CCD camera. The camera is mounted on a translation stage (TS) that allows to keep the atoms in focus for different time of flights.

Diode lasers are known to have a broad background spectrum of incoherent light. The probe light is therefore filtered by a 0.3nm spectral width interference filter to clean part of the non-resonant contributions.

Magnification

In order to determine the magnification, $M_i = s_i/s_o$, we need to image an object of known size s_o and then compare it to the image size s_i on the camera. Since the vacuum cell prevents us from placing an object at the position of the atoms, we redirect the imaging path with a mirror (Fig. 10.2) to perform the calibration. As the imaging object we use a razor blade in order to have a sharp edge that makes it easier to determine if the image is focused. It is crucial to use light at the same wavelength as for imaging, to avoid focal shifts due to chromatic aberrations, which introduce errors in the magnification determination. The blade is mounted on a translation stage (TS), which allows to bring it into focus.

For our standard time of flight of 45ms the magnification is $M_{DTA} = 1.577 \pm 0.0021$ for

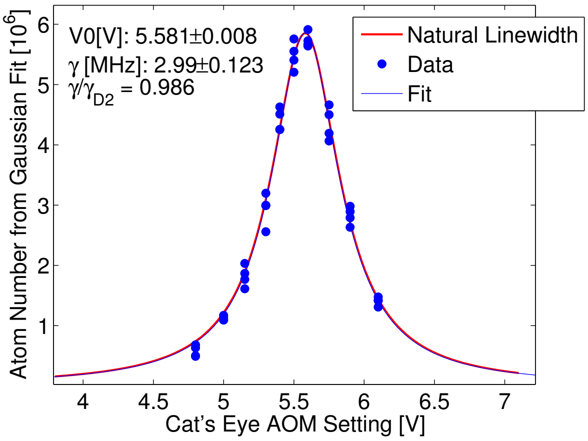

Figure 10.3: Measured (blue dots) and fitted (blue, dashed) absorption imaging line shape compared to natural linewidth of the D2 line (red).

the object being in focus within ±0.1mm.

The right panel of Fig. 10.2 shows the variation of the magnification with time of flight. In order to stay in focus with the falling atoms the camera is moved using a translation stage, which also leads to a change in magnification.

Absorption Imaging Line Shape

We record absorption imaging lineshapes by varying the detuning of the probe beam over the resonance with a double passed AOM and recording the deduced atom number using the saturation corrected on-resonant scattering cross section. This is a good way to account for variations in the resonance frequency and we can use the determined linewidth to check for saturation broadening or other broadening effects. Ideally we recover the natural linewidth of the D2 line.

Fig. 10.3 shows a typical line shape. Plotted is the determined atom number versus the VCO voltage setting (calibration is $2 \cdot 5.1$MHz/V) of the double passed AOM together with a Lorentzian fit (blue) and the natural line shape (red). The determined half linewidth of $\gamma = 2.99 \pm 0.123\mathrm{s}^{-1}$ is identical to the natural linewidth $\gamma_{D2} = 3.03\mathrm{s}^{-1}$ to within the measurement accuracy. The ratio $\gamma/\gamma_{D2} = 0.986$ shows that the determined line shape is less than 2% smaller than the natural linewidth.

High Saturation Imaging

We performed high saturation imaging as a test for the accuracy of atom number determination (see Sec. 5.1.5) on identically prepared Bose condensed samples. Figure 10.4 shows a plot of different atom number estimators as a function of saturation parameter I/I_s, where I is the probe light intensity and I_s the saturation intensity of the transition. Each point is the mean of about 10 realizations.

The first estimator obtains atom numbers by summing over pixels of the optical depth image:

$$N^{(1)} = \sum_{pixel\,(i,j)} \frac{A_{pix}}{M^2\sigma(I)} \mathrm{OD}^{(i,j)} \tag{10.1}$$

and the optical depth is obtained as described in Sec. 5.1.2. The second estimator is obtained from a fit to the Thomas-Fermi optical depth profile. This is done by first summing the image along the x direction and then performing a 1D fit with $\mathrm{OD}^{(1D)} = \mathrm{OD}_0^{(1D)} \max\left(1 - \frac{y^2}{w_y^2}, 0\right)^2$, and we find

$$N^{(2)} = \mathrm{OD}_0^{(1D)} \frac{16}{15} r_0. \tag{10.2}$$

The third estimator makes use of the thermodynamics of the condensate and the fact that the dimensions of the cloud are directly related to the number of atoms, since the mean field energy is in time of flight converted to kinetic energy. This allows for an estimator that is independent of the probe light

$$N^{(3)} = \left(\frac{r_0}{\sqrt{1 + \omega_r t_{TOF}}} \right)^5 \frac{\omega_r^3}{\omega_x} \frac{M^2}{15 a \hbar^2}, \tag{10.3}$$

where a is the scattering length, M the atomic mass, $\hbar$ is Planck's constant, t_{TOF} is the time of flight and ω_i are the trap frequencies.
We find the pixel count $N^{(1)}$ and fit $N^{(2)}$ estimator in good agreement for all employed saturation parameters, strengthening the hypothesis that the density distribution is Thomas-Fermi. For small saturation parameters we find a large discrepancy between $N^{(3)}$ and the other two estimators, while they approach the same atom number estimate for large saturation. The estimator $N^{(3)}$ is constant within measurement accuracy, while the others increase with higher saturation. This might indicate problems with the probe light detuning during imaging.
Note that there is approximately a factor of two difference between the low and high saturation fit result, which we use as our standard method for atom number determination.

10.1.2 Dispersive Imaging

Dual-Port Polarization Contrast Setup

The dispersive imaging setup is shown in Fig. 10.5. We prepare the polarization with a polarizing beam splitter (PBS) rotated by 45° in the S_2 Stokes basis. The light has a beam radius of 140µm at the position of the atoms inside the trap. The scattered light is collimated with a 60mm focal length achromatic lens doublet (L_1) and split with a PBS into the horizontal/vertical Stokes basis S_1. Each arm of the cube has a lens ($L_{2,H}$ and $L_{2,V}$) with a focal length of 750mm which produce images on the CCD camera.
The adjustment of the two arms in the setup, Fig. 10.5, is critical. In order to obtain Faraday angles the two images need to be subtracted and therefore they require the identical magnifications and foci.

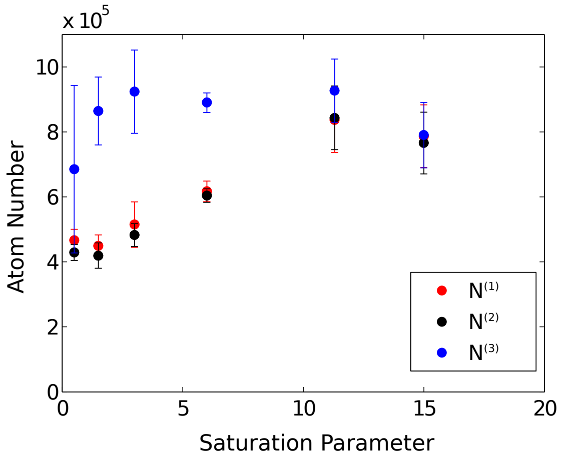

Figure 10.4: High saturation imaging. Deduced atom number for three different estimators vs. saturation parameter.

Magnification Calibration

We perform the magnification calibration with a BEC. The general idea is to image the atoms resonantly on the D1 line F=1, $m_F = -1$ to F'=2, $m_{F'} = -2$, σ^- transition. Then there will be rings due to diffraction close to resonance and due to the misalignment of the imaging system, which we try to correct. First we therefore need to find the resonance point and afterwards we can proceed to minimize the amount of rings due to the imaging. This procedure was inspired by reference [Mar03]. The idea is that by varying the detuning of the light from red to blue the atoms act as a focusing or defocusing lens. Exactly on resonance the light is only absorbed and the diffraction effects are minimized. Changing the focus of the imaging system has a similar effect. The ring structures one observes are different on either side of the lens position for optimal focus.

The two lenses in each arm are chosen to give a magnification of $M_i = f_2/f_1 = 750/60 = 12.5$. In this setup the second lenses L_2 are not critical, while the first lens L_1 is very critical for accurate focusing. We adjust the lenses by first placing the left second lens, $L_{2,L}$, at its nominal position of 750mm away from the camera and proceed with fine tuning the position of the first lens L_1, using a translation stage (TS).

Fig. 10.6 shows the recorded optical depth map. A symmetry center of the ring structures is found in row (r) 2, column (c) 4, corresponding to a detuning of -14MHz and a stage position of 880. This point lies in the center of the identical images r1c1/r7c3 and r3c1/r1c7. The apparent shift in detuning remains unexplained and is probably not a density effect as further discussed in Chap. 13.

For the fine tuning of the lens position we take another set of images around the perceived optimal position, column four on the map. In order to quantify the quality of the focusing we choose the diameter of the first diffraction ring and minimize its size. With this procedure we deduce a lens position of 872.5 (translation stage markings, 10µm graduation) from a fit.

With the first lens fixed we proceed to adjust the lens position in the right arm with the help of another translation stage (TS, $L_{2,R}$) such that the two images on the camera are as similar as possible. This was verified by numerically minimizing the difference of the two images while varying the stage position. The final stage position was at 32.5 turns.

To test how similar the magnifications in the two arms are, we take absorption images of the cloud at various time of flights and fit for the fallen distance, Fig. 10.7. The fallen distance is $d(t_{TOF}) = -\frac{g}{2}t_{TOF}^2$. Since we know the gravitational constant g and the time of flight t_{TOF} we obtain the magnification M_i from the detected fallen distance $d^{cam}(t_{TOF}) = -gM_i/2$ on the camera by a fit.

The resulting magnifications for each arm with 95% confidence bounds are:

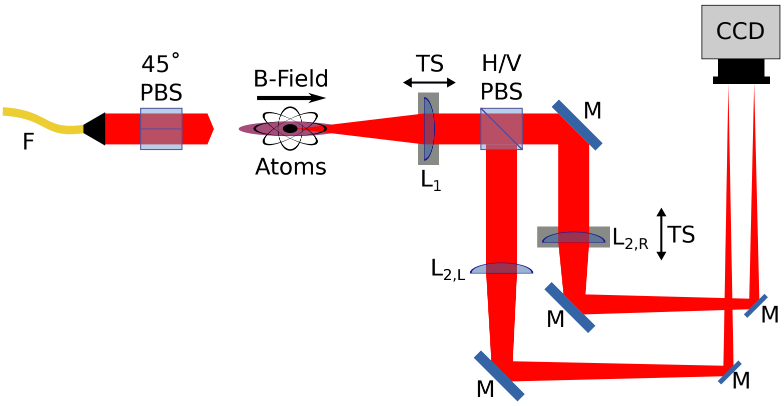

Figure 10.5: Faraday/dual-port polarization contrast imaging setup for dispersive probing inside the magnetic trap. Shown is the 45° PBS preparing the probe light after the Fiber (F), the placement of lenses L_1, $L_{2,R}$ and $L_{2,L}$, mirrors (M) and analyzing cube H/V PBS as well as the CCD camera.

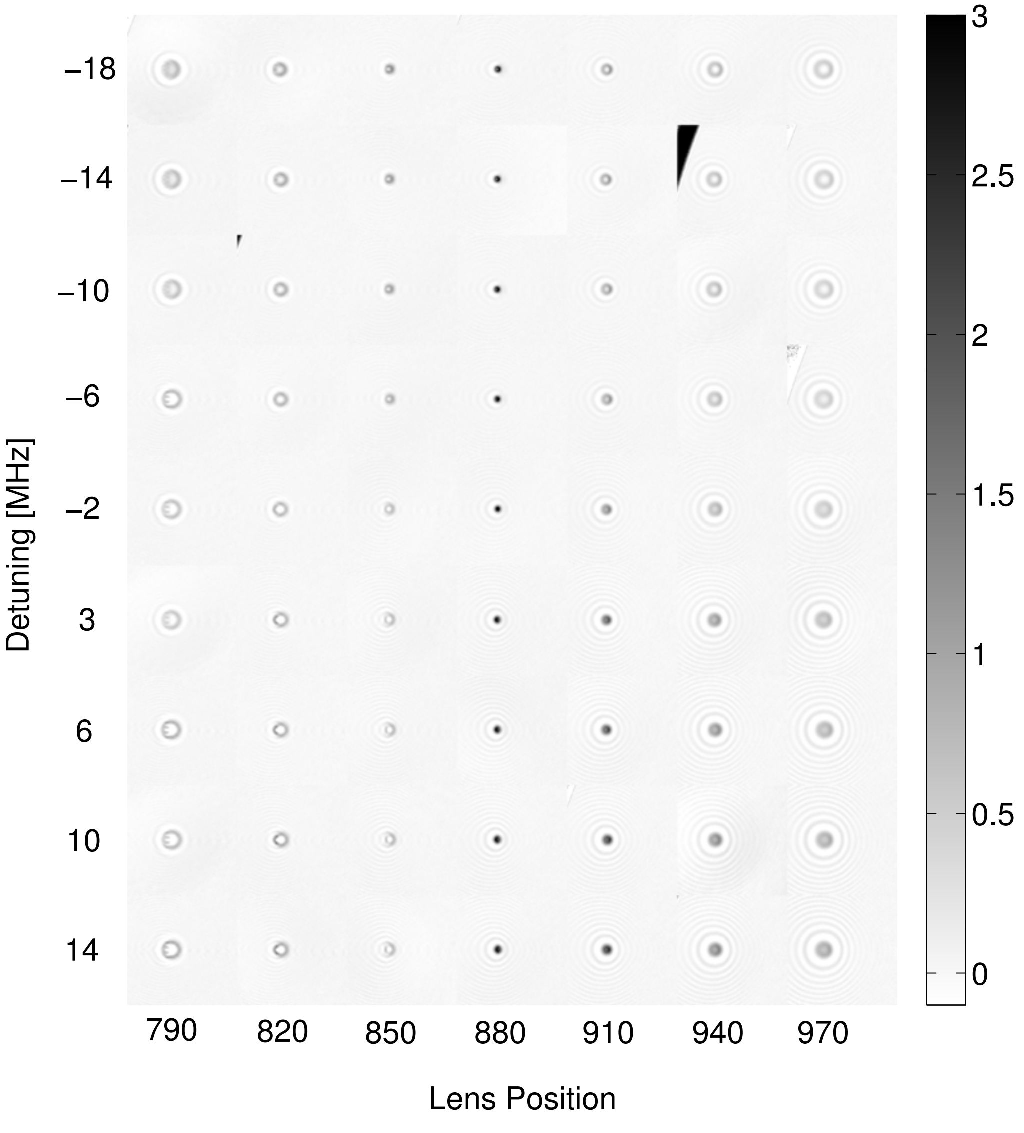

Figure 10.6: Plot of the optical depth for the adjustment of the critical lens L_1. Since the right arm is not yet aligned we plot the images of the left arm only. Along the vertical axis the detuning is varied, along the horizontal axis the position of the lens L_1. The rings are very extended at the extreme positions of the stage, but vary less with detuning. The number of atoms in the BEC is $N_{at} = 6.7\ 10^5$ and the total atom number is $N_{at} = 9.9\ 10^5$, the peak BEC density is $\rho = 1.64\ 10^{20}\mathrm{m}^{-3}$ and the probe light intensity is $I = 1.56\mathrm{W/m}^2$.

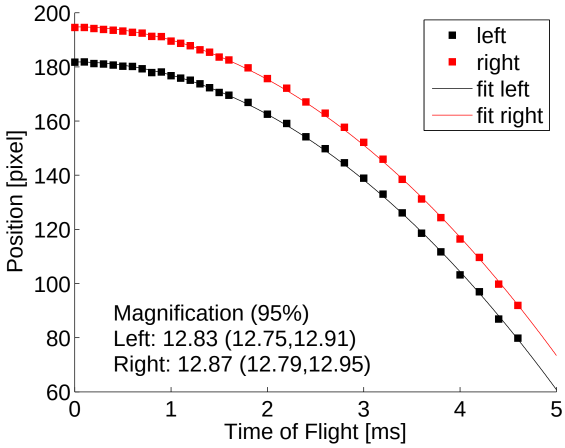

Figure 10.7: Determining the magnification by resonantly imaging of condensates as a function of TOF. The atom number in the BEC is $N_{at} = 6.1\ 10^5$, the total atom number is $N_{at} = 8.9\ 10^5$ the peak density is $\rho = 1.5\ 10^{20}\mathrm{m}^{-3}$ and the probe light intensity is $I = 1.05\mathrm{W/m}^2$ an the detuning is $\Delta = -14\mathrm{MHz}$.

M_i Left	12.83 (12.75,12.91)
M_i Right	12.87 (12.79,12.95)

10.2 Camera Calibrations

This section presents the determination of the camera gain and the quantum efficiency. While the quantum efficiency is based on the photoelectric effect and therefore is an inherently quantum statistical effect, the gain is due to a classical amplification process of the photoelectrons. The amplified signal is then converted to a digital signal with an arbitrary unit of counts.
The number of electrons N_e obtained by the photoelectric effect is related to the impinging photon number N_{ph} by the quantum efficiency η via:

$$N_e = \eta N_{ph} \tag{10.4}$$

and the number of analog-digital (A/D) counts N_c is related to the number of electrons by the gain $G = 1/S$, defined as the inverse of the sensitivity S:

$$N_c = GN_e, \tag{10.5}$$

such that the overall conversion from photons to counts is $N_c = \eta GN_{ph}$.
The quantum efficiency can be inferred from flat field images, i.e. images with a homogeneous illumination.
For this purpose one needs to do a noise analysis of the images. The variance has various contributions:

- Dark noise: thermal noise of the chip that accumulates with time
- Read-out noise: noise that is added on each read-out event
- Signal noise: noise that is related to the impinging photons (i.e shot noise)

If the camera is cooled, dark-noise is negligible. Read-out noise is independent of the illumination and exposure time and therefore adds approximately the same amount of noise on each image. Assuming a coherent state of the light impinging on the camera and

negligible classical noise we can assume the variance of the signal to be proportional to the number of photons. Note that, while the gain enters the count variance quadratically the quantum efficiency enters linearly. This can be illustrated by calculating the effect of beam-splitter type losses (quantum efficiency) on a photo signal ($\hat{a}^\dagger\hat{a}$).
The variance of the camera counts is

$$\mathrm{Var}(N_c) = G^2\mathrm{Var}(N_e) = G^2(\delta^2_{\mathrm{Dark}} + \delta^2_{\mathrm{read-out}} + \delta^2_{\mathrm{signal}}) = G^2\delta^2_{read-out} + \eta G^2\langle N_{ph}\rangle. \tag{10.6}$$

If each pixel sees the same number of photons (flat illumination) we can normalize the variance by the mean value:

$$\frac{\mathrm{Var}(N_c)}{\langle N_c\rangle} = \frac{G^2\delta^2_{read-out} + \eta G^2\langle N_{ph}\rangle}{\eta G\langle N_{ph}\rangle} \approx G \tag{10.7}$$

where the last approximation is valid if the photon shot noise is much bigger than the read-out noise.
There is another important noise term entering this analysis. This is noise due to the inhomogeneity of the camera chip, i.e. response variations from pixel to pixel. These stay fixed from shot to shot, but enter in the analysis of many pixels on a single image. This is referred to as flat field noise and is quadratic in the number of counts

$$\sigma^2_{flat} = k^2\langle N_c\rangle^2. \tag{10.8}$$

This quadratic contribution can spoil the gain determination, but can be avoided by subtracting either two images to cancel this effect or by taking many images and looking at a single pixel [1].
Once the gain is known one can obtain the quantum efficiency by calibrating the total camera counts with respect to a power meter. When N_c is plotted against N_{ph} the slope will be ηG, from which one obtains η.

10.2.1 DTA Camera

Since we do not use the DTA camera for direct photon counting, but only to determine atom numbers using several images, the actual quantum efficiency and gain are not needed. We therefore did not do a full calibration, but used the data sheet values for the noise analysis of Chap. 5.1.

10.2.2 Andor Camera

Photon to Image Count Conversion Calibration

50kHz Read-Out Rate The calibration is used for the superradiance experiments and uses our standard settings of the Andor camera (see Table D.1). The calibration was performed with respect to a photodiode, which was calibrated to a power meter. We take any losses between photodiode and camera into account.

Results with 95% confidence bounds		
Slope [photons/count]	1.0807	± 0.0006
Offset Total [10^6 photons]	1.6	± 0.2
Offset/pixel [photons/pixel]	8	± 1

---

[1] Mirametrics homepage: http://www.mirametrics.com/tech_note_ccdgain.htm

1 MHz Read-Out Rate The calibration is used for all the Faraday experiments and uses our standard settings for the Andor camera (see Table D.2). The calibration was performed with respect to a photodiode, which was calibrated to a power meter. We take any losses between photodiode and camera into account.

Results with 95% confidence bounds		
Slope [photons/count]	1.056	± 0.005
Offset Total [10^7 photons]	1.32	± 0.06
Offset/pixel [photons/pixel]	12.55	± 0.57

Dark Counts – Read-Out Noise

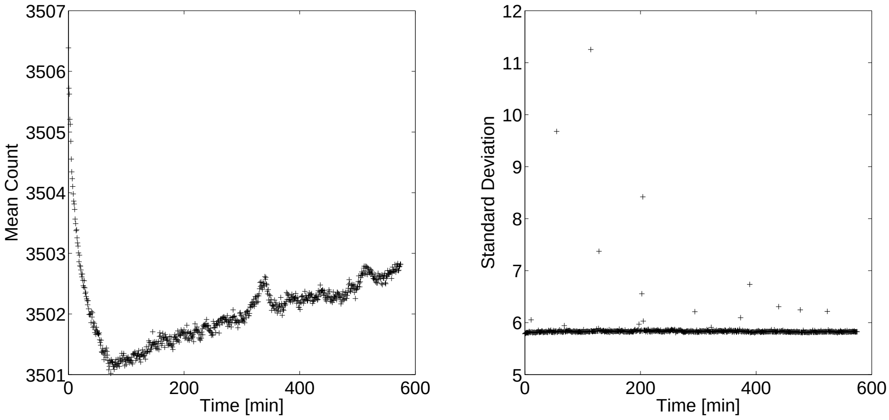

Figure 10.8: Dark-noise of Andor camera. Mean count and standard deviation of full chip images over a time span of almost 10 hours.

We tested the Andor camera for the manufacturer specified dark-noise values. This was done by taking a 12ms exposure picture (our standard setting) with 1MHz read-out rate every 50 seconds for almost 10 hours. The camera was cooled to -60°C. The camera shutter was permanently closed and the camera was completely shielded from any ambient light.
We calculate the mean value and standard deviation f counts for each full chip image (Fig. 10.8). While the mean value drops to a minimum after about an hour (by only 5 counts out of 3500) it then starts to increase steadily. The standard deviation is constant over the whole time span with a mean value of 5.85 counts, which fits to the specified value of 5.4 counts.

Quantum Efficiency and Gain Calibration

We did a flat field analysis for the 2.5MHz A/D read-out rate, with 4x gain, 100ms exposure time, $-60°C$ and 1.575µs shift speed. The measurement was performed by placing a white cardboard directly in front of the camera with an indirect illumination. For the analysis we choose a ROI with as homogeneous intensity as possible. To cancel pixel specific noise sources, we subtract two images and then determine the variance and mean to obtain the gain. With the photon to count conversion we then determine the quantum efficiency.
The experimentally determined values need to be compared to the manufacturer specifications which are $G^{spec} = 0.83$ for the gain and $\eta^{spec} \approx 0.95$ for the quantum efficiency. As can be seen from the following table, the agreement is reasonable.

Results		
Slope @ 2.5MHz [photons/count]	1.241	±0.002
Offset Total @ 2.5MHz [10^7 photons]	0.30	±0.06
Gain G @ 2.5MHz [N_c/N_e]	0.81	±0.01
Quantum Efficiency η [%]	98.2	±0.8

Part IV

Experiments

Eleven

Faraday Rotation Imaging

In this chapter the previously described dual-port polarization contrast imaging setup is used to obtain spatially-resolved Faraday rotation angles. The main difficulty in determining Faraday angles in an inhomogeneous sample is to distinguish between diffraction and Faraday signal. The dual-port imaging setup allows us to distinguish between these effects. There is diffraction associated with the imaging system and diffraction due to the atomic ensemble itself. With the help of numerical simulations these effects can be separated.

The first three sections deal with Faraday rotation in the thermal cloud. The first section closely follows our publication[1]. The second section estimates errors in the determination of Faraday angles due to residual defocusing. The third section compares the data presented in the first section with a diffraction model. Finally, in section four, Faraday rotation data in Bose-condensed samples is presented.

11.1 Faraday Rotation in Ultracold Thermal Atomic Ensembles

Cold thermal ensembles are prepared by evaporative cooling as described in Sec. 9.2. The temperature of the gas is close to, but still above, the condensation temperature. This makes the ensemble optically thick, while diffraction is still small. Under these conditions the numerical aperture of our imaging system is big enough to neglect diffraction due to the imaging system.

11.1.1 Introduction

The storage and retrieval of single photons [DLCZ01] and continuous variable quantum states [JSC$^+$04] in quantum memories [ZGH09, SAA$^+$10] has become a major endeavor for the realization of quantum networks [Kim08]. While single-qubit memories are sufficient to establish a secure communication channel, being able to store more qubits increases the capacity of the channel. It has been shown that not only the fidelity of storage and read-out but also the multimode capacity of an ensemble scales favorably with the on-resonant optical depth (OD) [ZGGS11].

Spatially resolved detection is a requirement for multimode memories [VSP10] that store each polarization qubit in an independent spatial light mode.

Polarization rotation, also called Faraday rotation, is well known as a means to measure the OD of atomic ensembles [KKN$^+$09, THT$^+$99], spin dynamics [SCJ03, LJM$^+$09] and magnetic fields [TBF08].

When applying the Faraday technique to dense, inhomogeneous, high OD samples new

---

[1] Franziska Kaminski, Nir S. Kampel, Mads P. H. Steenstrup, Axel Griesmaier, Eugene S. Polzik, and Jörg H. Müller, to be published in HIDEAS topical issue of EPJ D

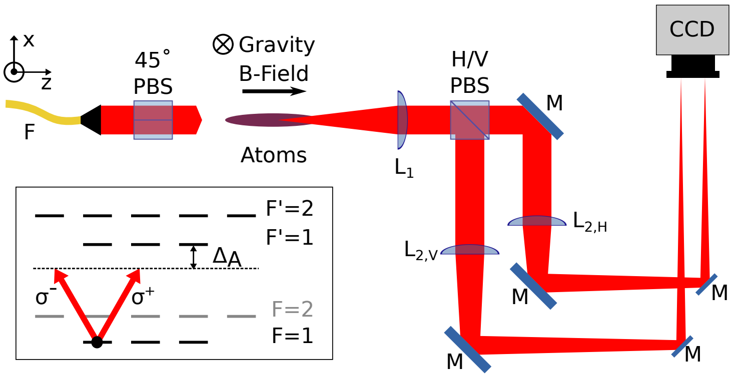

Figure 11.1: Optical setup showing the 45° PBS preparing the probe light after the Fiber (F), the placement of lenses L_1, $L_{2,H}$ and $L_{2,V}$, mirrors (M) and analyzing cube H/V PBS as well as the CCD camera. The B-field direction is mainly along z. The inset shows the ^{87}Rb D1 line level scheme and the linear probe light in the z quantization axis.

challenges arise. A large OD, together with the sample inhomogeneity, leads to stronger refraction or lensing, distorting images. A small transverse size leads to diffraction, posing stringent constraints on the properties of the imaging system. A large density leads to effects beyond the independent atom hypothesis commonly applied in quantum optics [RYG$^+$10].

We present an imaging method that reduces distortions due to refraction and we introduce a model that treats the influence of light assisted cold collisions on dispersive interactions.

There are already several dispersive imaging techniques available (see Sec. 5.2.1). Phase-contrast imaging [MRK$^+$10, HSI$^+$05] uses a spatially selective phase plate and is hardly polarization sensitive. Therefore it mainly measures the scalar part of the polarizability, $\alpha^{(0)}$, or scalar refractive index (Fig. 3.3). Single-port polarization-contrast imaging [BSH97] uses absorptive polarizers and detects the vector part, $\alpha^{(1)}$, or refractive index differences but does not cancel diffraction. Dark-ground imaging [AMvD$^+$96] uses a spatially selective block and is sensitive to both $\alpha^{(0)}$ and $\alpha^{(1)}$. Another technique records directly the diffracted wave of an object and the image is reconstructed numerically [TDS05].

We employ a polarization-contrast imaging method (Sec. 5.2.2 and Sec. 10.1.2) which uses a polarizing beam splitter (PBS) instead of an absorptive polarizer, enabling us to record the full light intensity (dual-port). This gives us access to the scalar and vector components of the polarizability simultaneously and distinguishably. It enables us to cancel diffraction in the same way common-mode noise is canceled on a differential photodiode and leaves us sensitive to the spatial profile of the Faraday rotation signal.

All the described methods are weakly sensitive to the tensor part of the polarizability, $\alpha^{(2)}$, leading to changes in the coherences and populations of the atoms during the interaction. This manifests in an excess ellipticity of the light. A high sensitivity to the tensor components can be obtained in our setup if circular polarizers are introduced.

A Raman/beam splitter-type memory [HSP10] is based on the $\alpha^{(2)}$ part of the polarizability making use of Raman population transfers and coherences. In our specific case of ^{87}Rb it can be realized using the $m_F = \pm 1$ states of the F=1 manifold (Fig. 11.1). To avoid unwanted differential phase imprints it is advantageous to minimize the $\alpha^{(1)}$ part of the polarizability. On the D1 line $\alpha^{(1)}$ is expected to vanish at a detuning $\Delta_0/(2\pi) = -204$MHz (Fig. 3.3). A local maximum of $\alpha^{(1)}$ is expected for red detunings at $\Delta_{max}/(2\pi) = -660$MHz.

Scalar diffraction is due to the $\alpha^{(0)}$ part of the polarizability that is dominant over the whole range of explored detunings. An imaging method that can address these distortions is therefore desirable.

Dual-port polarization contrast imaging, also referred to as Faraday imaging in this thesis, can be more generally employed for spatially resolved detection of the atomic magnetization and the study of quantum coherence in degenerate gases and solid state systems [HSI$^+$05, VGL$^+$10].

11.1.2 Setup

The atoms are spin polarized in the $|F = 1, m_F = -1\rangle$ state in the quantization axis defined by the local magnetic field. The main B-field component is oriented along the propagation direction of light (z). The gravitational sag of 18µm leaves the B-field at an angle between the z and gravity axis (-y) of about 15° in the center of the trap. There is a 5° variation within w_r and a 0.25° variation within w_z.
The first element in the optical assembly, Fig. 11.1 (calibrations are shown in Sec. 10.1.2), is a polarizing beam splitter oriented at 45° to prepare a clean linear polarization. The probe beam enters the ensemble with an $\exp(-2)$ beam radius of 140µm with a flux of 1100 photons/µs/µm^2 which corresponds to a spontaneous emission probability of 0.03 given at a detuning of $\Delta_A/(2\pi) = -200$MHz and with a pulse duration of 10µs. To average over shot-to-shot atom number fluctuations we repeat each experimental run five times under identical conditions.
After the atomic ensemble an achromatic lens doublet (L_1) collimates the scattered light, which is then split into horizontal (H) and vertical (V) polarization components by another PBS and imaged with identical lenses $L_{2,V/H}$ onto a CCD camera (calibrations shown in Sec. 10.2). We take images I_V and I_H with atoms present, images I_V^{ref} and I_H^{ref} without atoms present and bias images to correct for any stray light and electronic offset. We balance the detection in order to split the unscattered light equally into both output arms, $I_V^{\text{ref}} = I_H^{\text{ref}}$. Any small remaining imbalance is corrected for during post-processing. This allows us to detect the difference $I_H - I_V$ and the sum $I_H + I_V$ simultaneously with optimal sensitivity.
The Faraday angle θ_F is the rotation angle of linearly polarized light (Sec. 3.3), which we infer by:

$$\theta_F = \frac{1}{2}\arcsin\left(\frac{I_H - I_V}{I_H + I_V}\right). \tag{11.1}$$

This gives an accurate polarization rotation angle, if the presence of any circular polarizations after the interaction can be neglected. For the accurate determination of Faraday angles it is critical to centering the images on top of each other. Using a fitting algorithm we achieve sub-pixel resolution for the centering. The sensitivity of our method is illustrated by our ability to detect the small rotation angle of 0.038°, produced by the cell windows that are subject to large magnetic fields due to the magnetic trap. The data is corrected for this artifact.
We adjust L_1 to image the plane at the end of the ensemble. The diffraction limited imaging resolution is 3.6µm (Sec. 4.1.1). The magnification with 95% confidence bound in each arm of our imaging system is 12.83 ± 0.08 and 12.87 ± 0.08, respectively, i.e. identical within our measurement accuracy. Images of clouds falling freely under the influence of gravity are used to determine the magnification. The acceptance full opening angle of the system is 15.2°.
For quantitative imaging the opening angle of the imaging system needs to be sufficiently large compared to the diffraction angles of the ensemble. We estimate the full geometric diffraction angle of the ensemble as $\alpha_G \approx \lambda/4d < 1°$, where λ is the wavelength and d the radial extent of the ensemble. The angle due to refraction or lensing can be approximated by comparing the phase shift ϕ in the center to the one at the edge of the sample $\alpha_L = 2(\phi(r=0) - \phi(r=d))\lambda/(\pi d)$ [AMvD$^+$96], which reaches $\alpha_L(\Delta_0) \approx 0.3°$ at a detuning of $\Delta_A/(2\pi) = -200$MHz (Sec. 3.1.2). Both theses angles

are sufficiently small, such that light loss at the apertures of the imaging system can be neglected. We compared these estimates to more elaborate diffraction simulations [MPO$^+$05, ZGGS11] (Sec. 4.2.1 and Sec. 4.2.2) including a model of the full imaging system, which confirmed the conclusions of the simple diffraction estimates.

11.1.3 Absorption Imaging Parameters

As an independent sample characterization we perform standard absorption imaging on the D2 line (Sec. 10.1.1) after a time of flight (TOF) of 45 ms. Using a magnification of 1.577 ± 0.002 (Sec. 10.1.2) and independently measured trap frequencies we can specify the waists of the in-trap density distribution $\rho(r,z) = \rho_0 \exp\left(-\frac{r^2}{2w_r^2} - \frac{z^2}{2w_z^2}\right)$ as $w_r = 7.7\mu\text{m}$ and $w_z = 70.5\mu\text{m}$, leading to a Fresnel number of $F = w_r^2/(2w_z\lambda) = 0.5$. From these parameters we determine the temperature $k_B T_i = M w_i^2 \omega_i^2$ and $T = (T_r^2 T_z)^{1/3} = 300\text{nK}$, where M is the atomic mass.
By using the D2 line scattering cross section for the cycling transition $\sigma_{D2} = 3\lambda_{D2}^2/2\pi$ we determine a peak density of $\rho_0^{\text{abs}} = 1.2 \cdot 10^{19}\text{m}^{-3}$ and an atom number of $N_{\text{at}}^{\text{abs}} = 8.1 \cdot 10^5$ as an average over all data points.
Both absorption imaging and Faraday measurements allows us to deduce the number of atoms using models for the optical cross sections. By comparing the atom numbers deduced by different measurement methods, systematic errors in either method can be identified. While absorption imaging is a standard method, it is well known that it is difficult to estimate the precise effective scattering cross section due to uncertainties in the magnetic field alignment, light polarization quality and repump efficiency[2] [GTR$^+$04]. Since the cycling transition allows for the maximal cross section σ_{D2} our measured $N_{\text{at}}^{\text{abs}}$ and ρ_0^{abs} are hard lower bounds. We estimate a hard upper bound by noting that we do not observe condensed atoms on the absorption images and hence $T/T_c > 1$. The condensation temperature of an ideal gas is $k_B T_c = \hbar\bar{\omega}(N_{at}/\zeta(3))^{1/3}$, with $\bar{\omega} = (\omega_r^2\omega_z)^{1/3}$ and $\zeta(3)$ is the Riemann zeta-function. We correct T_c for the effects of finite size and mean field interactions (Sec. 2.3.2). Both effects reduce T_c for our parameters by maximal 1.2% and 5.5% respectively [GTR$^+$04, DGPS99]. Corrections to the determined ensemble temperature T arise from the use of a Gaussian instead of a Bose distribution in the fit model (see Sec. 2.2.2). We estimate this systematic correction by fitting Gaussian profiles to analytically Bose enhanced densities and find a systematic underestimation of the temperature by about 10%.
Taking all these corrections into account we reach $T/T_c = 1$ for several single-run data points at an atom number scaling factor $f = N_{at}/N_{at}^{\text{abs}}$ of maximal $f_{max} = 2.7$, defining a hard upper bound for the real atom number N_{at}. We will show below that this upper bound is still too low to allow the Faraday rotation data to be fitted with an independent atom model and we conclude that line shape corrections due to light assisted collision become relevant.

11.1.4 Experimental Results

Figure 11.2 shows the detuning dependence of the observed peak Faraday angles (black squares) together with the light assisted cold collision model (red line, Chap. 6) and the coupled Maxwell-Bloch model that assumes independent atoms (grey area, Sec. 3.2). Both use input parameters deduced from absorption imaging, i.e. the sample radii w_r and w_z and the atom number fN_{at}^{abs}, averaged over all detunings. We infer an optimal atom number scaling f, by matching the light assisted cold collision model to the experimental data and obtain $f_{opt} = 2.13$ ([3]). The grey shaded area indicates the atom number scaling range $1 < f < 2.7$, defined in Sec. 11.1.3. Experimental peak angles are determined by

---

[2] In later control experiments we found a systematic undercount of atoms by a factor of two in absorption imaging due to insufficient repumping.

[3] This corresponds to a temperature ratio of $T/T_c = 1.27$.

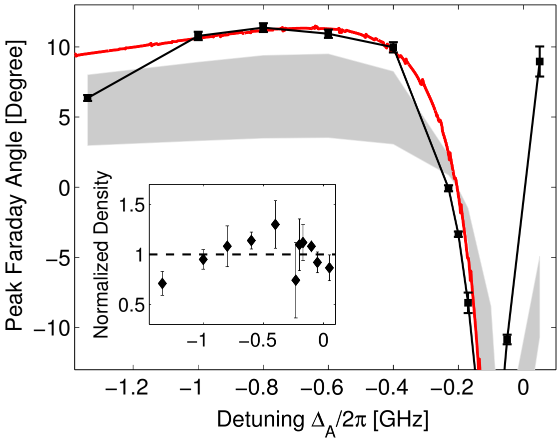

Figure 11.2: Detuning dependence of peak Faraday angle. Experimental data (black squares) is best reproduced by a model including light assisted cold collisions (red solid line). The grey area shows the prediction of a coupled Maxwell-Bloch model assuming independent atoms for the permissible range of the atom number scaling factor f (see text). The inset shows the relative atomic density variation with detuning.

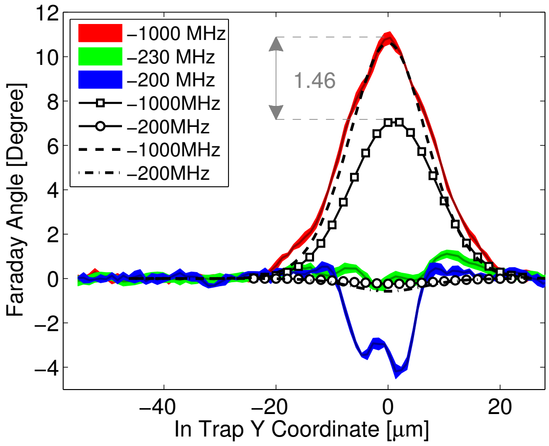

Figure 11.3: Cut through Faraday angle images for various detunings Δ_A. Colored areas represent the standard deviation of 5 experimental realizations. Coupled Maxwell-Bloch simulations assuming independent atoms (squares, circles) underestimate the angle by a factor 1.46, compared to a model including light assisted cold collisions (dashed, dot-dashed).

averaging over 3x3 pixels around the determined center positions of the density distribution and the error bars are the standard deviation of 5 experimental runs. The small structure on the red line is due to vibrational molecular resonances, discussed further below. The figure inset shows the variation of densities for different data points normalized to the averaged density entering the models. The discrepancy between the data point at $\Delta_A/(2\pi) = -1340$MHz and the models might be explained by the low density for this data point.

Figure 11.3 shows the spatially resolved Faraday angle as deduced from the camera images for the detunings $\Delta_A/(2\pi) = -\{1000, 230, 200\}$ MHz averaged over five realizations together with the two model predictions for input atom number $f_{opt}N_{\mathrm{at}}^{\mathrm{abs}} = 1.73 \cdot 10^6$. The good reproducibility of sample preparation is evidenced by the small standard deviation encoded in the colored areas around the averaged profiles. The spatial shape of the Faraday angle profile at $\Delta_A/(2\pi) = -1000$MHz (red) fits the expected shape from the light assisted cold collision model when the finite imaging

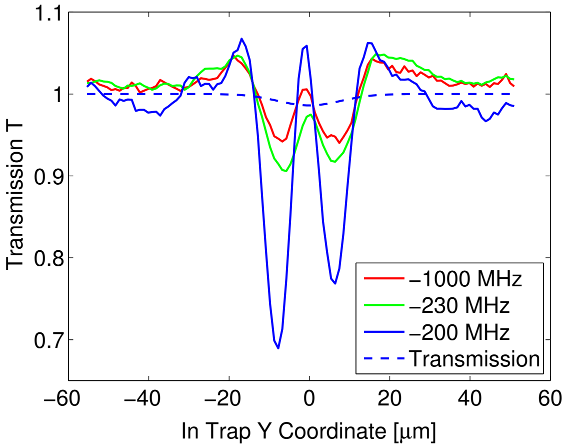

Figure 11.4: Spatially resolved transmission: cut through $T = (I_H + I_V)/(I_H^{\text{ref}} + I_V^{\text{ref}})$ for various detunings compared to the column density approximated transmission profile of the ensemble at $\Delta_A/(2\pi) = -200\text{MHz}$ (dashed). Diffraction dominates over absorption for all detunings.

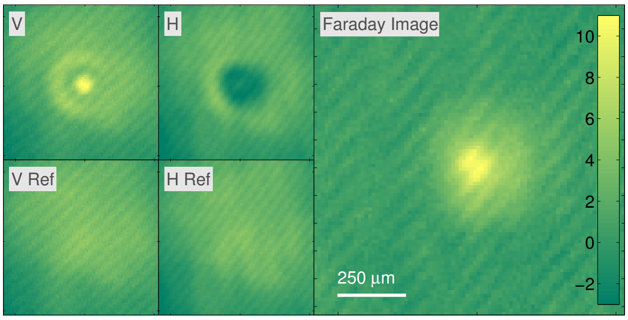

Figure 11.5: Raw images (left panel) and deduced Faraday image (right panel) for a detuning of $\Delta_A/(2\pi) = -400\text{MHz}$. V/H refers to images with atoms present, while V/H Ref to images without atoms. The color scale indicates the Faraday angle in degrees. Diffraction rings in the raw images V/H disappear in the Faraday image.

resolution is taken into account. The experimental profile at $\Delta_A/(2\pi) = -200\text{MHz}$ deviates significantly from the shape of the atomic density distribution. We observe minimal Faraday rotation at $\Delta_A/(2\pi) = -230\text{MHz}$, shifted by about 30MHz from the expected detuning Δ_0. This shift is outside possible systematic errors in the frequency scale.

Figure 11.4 shows a three pixel averaged cut through the transmission $T = (I_H + I_V)/(I_H^{\text{ref}} + I_V^{\text{ref}})$, where we normalize with the reference images. This allows us to visualize the effect of intensity redistribution across the image due to refraction and diffraction. To indicate the expected photon loss we plot an estimated transmission profile for $\Delta_A/(2\pi) = -200\text{MHz}$ using a naive column density model neglecting diffraction effects. The expected photon loss is hardly distinguishable from the detection noise. From the spatial transmission curves it is apparent that data is dominated by refraction rather than absorption for all detuning values shown. We emphasize that due to the dual-port detection the distortion effects of diffraction are largely canceled in Faraday angle profiles.

This compensation of refraction effects is illustrated in Fig. 11.5, where raw images I_H, I_V, I_H^{ref} and I_V^{ref} are shown together with the 2-D reconstruction of Faraday rotation angles measured at a detuning of $\Delta_A/(2\pi) = -400\text{MHz}$.

11.1.5 Models

Our first model accounts for the collective response of all atoms, while treating each atom as an independent scatterer. The model is based on coupled Maxwell-Bloch (MB) equations [KMS$^+$05, GSM06, HSP10] with excited states eliminated adiabatically, using continuous variables and including absorption. The probe light is propagated spatially through the ensemble while simultaneously evolving the ground state F=1 manifold populations and coherences in time. To incorporate the spatial inhomogeneity of sample density, initial atomic state and magnetic field, we extend the 1+1 dimensional geometry to 3+1 dimensions, following [KM09]. In this model, light is assumed to propagate along straight lines and atomic motion is neglected.

The model Hamiltonian $\mathcal{H} = \mathcal{H}_{int}^{(0)} + \mathcal{H}_{int}^{(1)} + \mathcal{H}_{int}^{(2)} + \mathcal{H}_B$ contains the atom-light interaction decomposed into its irreducible tensor components $\mathcal{H}_{int}^{(j)}$ (Sec. 3.2.2) and the effect of the external magnetic field (Sec. 3.2.7) $\mathcal{H}_B = \vec{\Omega}(r) \cdot \vec{F}$. Here $\vec{\Omega}(r)$ is the the vector of Larmor frequencies and $\vec{F}$ is the total atomic angular momentum vector. To compare the simulation results to our image data we plot the Faraday angle, time averaged over the probe pulse duration, at the output end of the atomic sample (Fig. 11.2 and 11.3).

We can use the full MB model to quantify the combined effects of tensor polarizability and B-field inhomogeneity by comparing it to a much simpler, idealized Faraday model, which is also used as the basis for the light-assisted collision model and is discussed in Sec. 6.4. Comparing this simpler model to the full Hamiltonian dynamics we find that the effects of the inhomogeneous magnetic field and the tensor dynamics lead to a reduction of the Faraday angle by a constant factor $\beta_B = 0.86$ for the range of detunings $\Delta_A/(2\pi) = -1340\text{MHz}$ to -400MHz.

Our second model addresses the effect of light assisted cold collisions (Sec. 6). At high atomic densities atoms can no longer be treated as independent scatterers. Electronic energy levels for close pairs of atoms split and shift. The light scattering properties of a pair are modified compared to isolated atoms. This effect of the dipole-dipole interaction can be described by established methods from molecular physics [MP80, MP77]. We consider repulsive and attractive molecular potentials for ground-excited state Rb_2^* atom pairs, neglecting hyperfine recoupling [KMN$^+$04], and calculate the allowed energy levels. For the attractive molecular potentials the position of photoassociation resonances are calculated using the LeRoy-Bernstein formula [LeR70]. For repulsive potentials atom pairs can be excited to a continuum of states. We are interested in the dispersive effects of all these shifted optical resonances.

We calculate the total Faraday rotation angle by using equations 6.20 and 6.21. To correct for magnetic field inhomogeneities and tensor evolution we multiply the result by the above defined β_B, such that

$$\theta_F = \beta_B(\theta_F^A + \theta_F^{pa}). \tag{11.2}$$

The total optical depth $OD(\Delta_A)$, defined via the intensity attenuation $I/I_0 = \exp\left(-OD(\Delta_A)\right)$ is given by the product of the atomic density and the scattering cross section integrated along the propagation direction of the light:

$$\begin{aligned} OD(\vec{r}_\perp, \Delta_A) &= \int \rho(\vec{r}) \sum_{i,v} \left(\sigma_A^{(i)}(\vec{r}, \Delta_A) + \sigma_{pa}^{(i,\text{v})}(\vec{r}, \Delta_A)\right) \mathrm{d}z \\ &= OD^A(\vec{r}_\perp, \Delta_A) + OD^{\text{pa}}(\vec{r}_\perp, \Delta_A). \end{aligned} \tag{11.3}$$

From the determined atom number $f_{opt} N_{\text{at}}^{\text{abs}}$ and ensemble size w_z we calculate the independent atom on-resonant OD for the $|1,-1\rangle$ to $|2,-2\rangle$ D1 transition with $\xi_i^2 = 1/2$. We find a peak optical depth $OD^A = \xi_i^2 (3\lambda_{D1}^2/2\pi)\rho_0 \sqrt{2\pi} w_z = 680$.

11.1.6 Discussion

The data presented in Fig. 11.3, 11.4 and 11.5 show that the influence of diffraction on the Faraday images is reduced. Common-mode diffraction on both images, I_V and I_H, is canceled when calculating the difference $I_H - I_V$. The common-mode diffraction stems from the scalar polarizability $\alpha^{(0)}$, which is the largest contribution to the polarizability as shown in Fig. 3.3. This compensation is, however, not perfect and we discuss in the following the effect of uncompensated diffraction and refraction on the detected Faraday angle. In geometric optics, the trajectories of light rays are curved due to the inhomogeneous density of the sample. Strong refraction leads to a breakdown of the column density approximation, which implicitly assumes a straight line ray path. Eventually this leads to noticeable differences between the column density and the spatial profile of the Faraday angle. For red detunings the extended atomic cloud acts as a thick collimating lens, such that ray trajectories are bent towards the center of the cloud, leading to a reduced Faraday angle in the center.

Differential diffraction and lensing is associated with the $\alpha^{(1)}$ part of the polarizability. It leads to a mismatch in the wavefronts of the left- and right-handed circular polarization modes at the exit plane of the atomic ensemble. This introduces locally ellipticity to the initially pure linear polarization. Since detection in the H/V basis is insensitive to circular polarization this lowers the Faraday angle by a second order correction.

While residual diffraction and refraction reduces the Faraday angle, Fig. 11.2 shows measured peak Faraday angles significantly above the prediction given by the Maxwell-Bloch simulation, which assumes the atoms to be independent scatterers and does not include diffraction. We match our light assisted collision model to the data by choosing $f_{opt} = 2.13 < f_{max}$, scaling our inferred atom number from absorption imaging to $f_{opt}N_{\text{at}}^{\text{abs}} = 1.73\,10^6$. Comparing the cold collision model for this input atom number to the corresponding Maxwell-Bloch simulation we find an increase of the Faraday angle of 1.46 as indicated in Fig. 11.3. Trying to fit the data directly with the Maxwell-Bloch model would require an atom number scaling of $1.46 f_{opt} = 3.1$. This lies 15% above the conservative upper bound of $f_{max} = 2.7$, discussed at the end of Sec. 11.1.3 and strongly suggests that the independent scatterer assumption breaks down.

Our strategy to correct the optical response of the gas by considering atom-atom interactions of molecular potentials and the corresponding redistribution of oscillator strength in frequency space can be contrasted to other approaches that describe the optical properties of a dense gas. Instead of calculating the collective response by a systematic expansion in terms of the atomic density [MCD95] or by a configuration average over many randomly placed interacting point dipoles [SKKH09], we focus on the contribution of close pairs for which big resonance shifts occur which in turn lead to significant modifications in the wing of the atomic line. The number of close pairs is determined by using the quantum mechanical scattering wave function for atom pairs interacting in the ground state molecular potential, hence particle correlations are accounted for. Very close to the unperturbed atomic resonance we expect our approach to fail, because the internuclear distances of the pairs become large and therefore the pairs can no longer be considered isolated and the collective response of ever bigger clusters of atoms should be calculated instead. Our model predicts a surprisingly large modification of the Faraday rotation angle even for the modest particle density $\rho_0^{abs} f_{opt} \lambda\!\!\!^{-3} = 0.05$ used in our experiment. The model neglects hyperfine recoupling on molecular potentials and does not explain the observed shift in the position of Δ_0.

Interestingly, in a recent experiment, which employs resonant absorption imaging as a detection method for high density 2-D quantum gases [RYG$^+$10], a decrease of absorptivity with increasing density has been observed. This is consistent with our simple picture of the redistribution of the oscillator strength from the line center into the wings due to the resonant dipole-dipole interaction.

We now turn to the suitability of our atomic samples for multimode quantum memories.

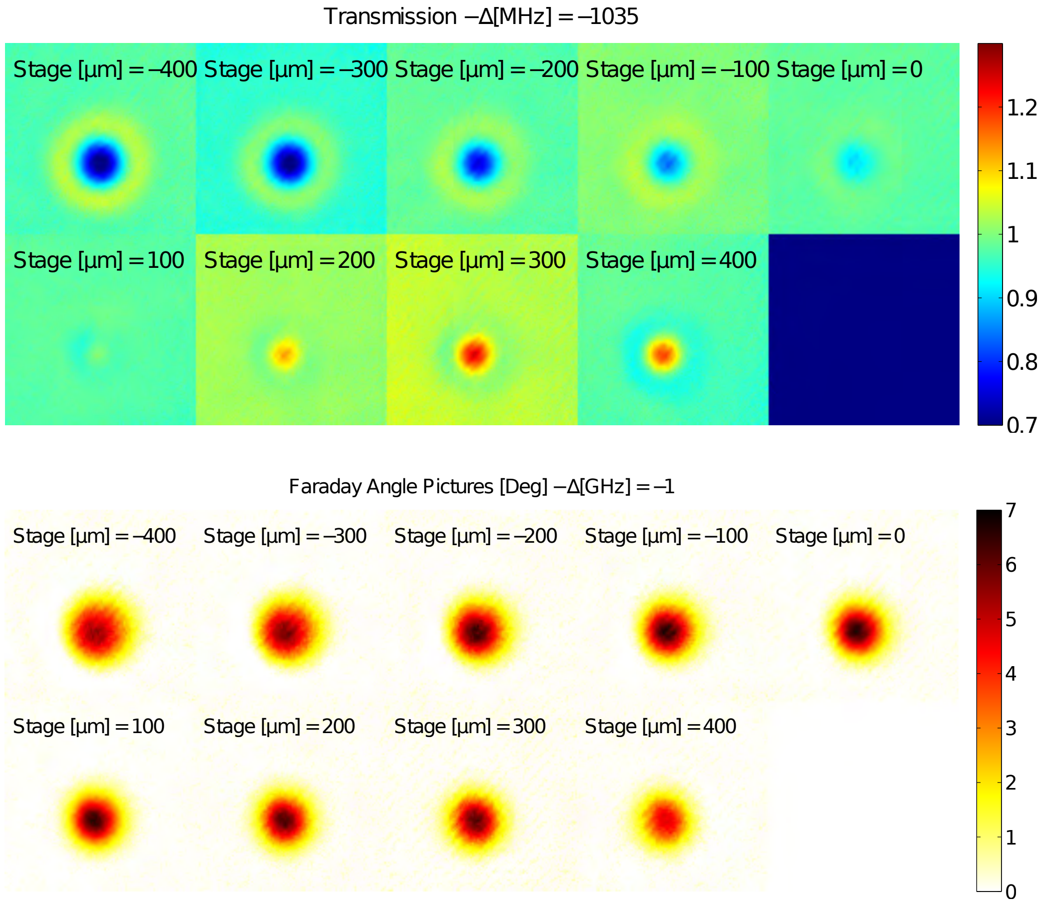

Figure 11.6: Transmission images (top) and Faraday images (bottom) of a thermal sample for various positions of the first imaging lens (L_1), effectively changing the object plane relative to the sample position. The data was taken at a detuning of $\Delta_A = -1\text{GHz}$ for a sample with a Fresnel number $F = 0.61$.

With the favorable optical depth and Fresnel number a mode capacity in the hundreds is predicted in forward read-out [GGZS11]. In experimental implementations this number will likely be limited by the finite resolution of the imaging system.

While the increased Faraday angle signals a higher coupling between atoms and light future experiments are necessary to determine the extend of which the decoherence is increased by the resonant dipole-dipole interaction. For this, the presented weakly destructive dual-port detection method will be an invaluable tool since details of the radial spin density distribution can be examined repeatedly despite of strong refraction and diffraction effects.

11.2 Estimation of Imaging System Misalignment On Thermal Cloud Faraday Rotation Angles

The focusing of the dual-port imaging system was done using a BEC, as presented in Sec. 10.1.2. The BEC acts as a lens with a focal length of about 300μm. This suggests that when the focus position was determined a 300μm misalignment could have been introduced. In the preceding section results for thermal samples were presented together with a model that explains an increase of the Faraday angle. In this section errors in the determination of Faraday angles due to any remaining defocusing are estimated.

Defocusing occurs if the object plane of the imaging system is offset from an optimal position. Ideally one should image the plane at the end of the atomic ensemble, such that the imaged light field corresponds to the field after the interaction with the whole ensemble. The object plane position can be altered by changing the position of the lens

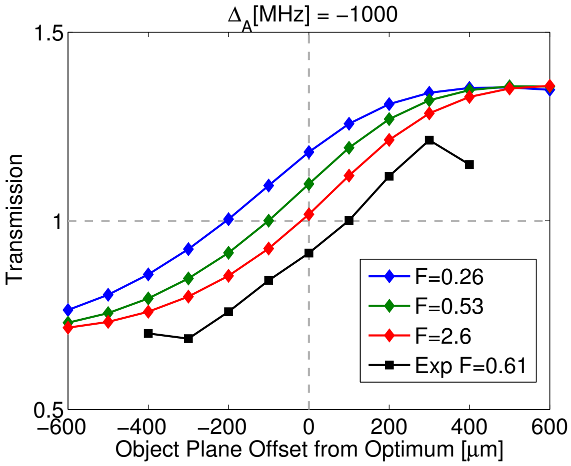

Figure 11.7: Comparison of the measured peak transmission of Fig. 11.6 to a numerical simulation for three Fresnel numbers as a function of the object plane offset. The numerical simulation uses an optical depth of $D = 562$ on the σ^- transition, which is approximately equal to our experimental optical depth.

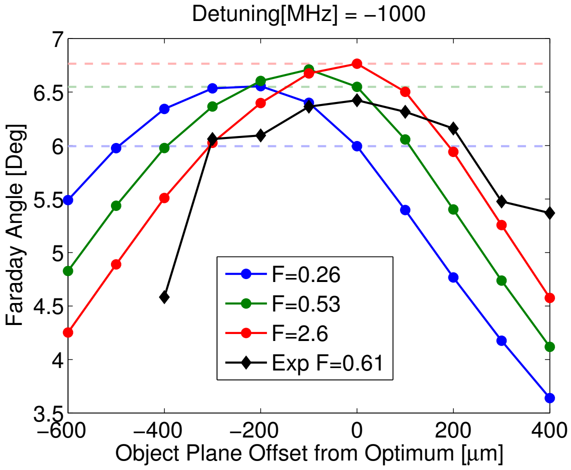

Figure 11.8: Comparison of measured peak Faraday angles of Fig. 11.6 to a numerical simulation for three Fresnel numbers as a function of the object plane offset. The numerical simulation uses an optical depth of $D = 562$ on the σ^- transition, which is approximately equal to our experimental optical depth.

L_1 in Fig. 11.1, the first lens after the atoms.

In order to estimate the effect of object plane misalignment we take a series of images of thermal clouds for several positions of the lens L_1 and compare the results to numerical simulations. The position of the lens is adjusted with a micrometer precision translation stage.

In the top panel of Figure 11.6 the transmission $T = (I_H + I_V)/(I_H^{ref} + I_V^{ref})$ is shown, i.e. the sum of the horizontal and vertical images with the atoms present, I_H and I_V, normalized to the sum of the corresponding images without atoms present, I_H^{ref} and I_V^{ref}. These images directly show the effect of diffraction. The images were taken at a detuning of −1GHz. The associated focal length of the thermal cloud is larger than 5mm. The stage position is given relative to the experimentally determined optimal position, as determined in Sec. 10.1.2. The lower panel of Fig. 11.6 presents the corresponding Faraday rotation images.

One naturally assumes that the image with the smallest amount of visible diffraction corresponds to the optimal lens position. This turns out to be a bad criterion. A benchmark test for our imaging system is to deduce the same Faraday angle from images on the camera plane, as the Faraday angle that occurs at the end of the sample, after the interaction.

Figure 11.7 shows the 3x3 pixel averaged peak transmission (black diamonds) together with a numerical simulation. The simulation uses the 3D field propagation model described in Sec. 4.2.2 for the propagation within the sample and the model of Sec. 4.1.2 to propagate the field from the end of the sample to the camera including all lenses and apertures. It is important to keep in mind that the propagation inside the sample models the atomic density distribution as Gaussian in the transverse direction and as homogeneous along the propagation direction of the probe light. We then determine the Fresnel number, $F = w_r^2/\lambda L$, where w_r is the Gaussian radius of the sample, λ is the wavelength of light and L is the homogeneous length of the sample, with the length to be chosen as twice the Gaussian sample radius along the propagation of light, $L = 2w_z$. It is not obvious if this is a good choice or if the inhomogeneity of the sample along z changes the Fresnel number. For this reason we plot the resulting peak Faraday angles as deduced from the simulation for three different Fresnel numbers. The Fresnel number of the experimental results is $F = 0.61$. The simulation is run for $F = \{0.26, 0.53, 2.6\}$ at a detuning of $\Delta_A = -1\text{GHz}$.

The simulation results indicate that the smallest amount of diffraction, corresponding to a transmission of $T = 1$, occurs only for large Fresnel numbers at the optimal object plane position. For smaller Fresnel numbers a shift occurs. For example for $F = 0.53$ (green) this shift is $\Delta z = -100\mu\text{m}$. The experimental data (black squares) does not match any of the curves given by the simulation. If we assume $F = 0.53$ to match the experimental Fresnel number this indicates an experimental object plane shift of $\Delta z^{exp} = 200\mu\text{m}$.

Figure 11.8 shows the 3x3 pixel averaged peak Faraday angles (black diamonds) together with the simulation results. The colored, dashed horizontal lines indicate the angle at the end of the sample. They are reproduced on the camera plane at the optimal position of the first lens $\Delta z = 0$. The largest observable angle coincides with the object plane position for minimal diffraction. Only for $F = 2.6$ does the largest angle on the camera coincide with the peak angle at the end of the sample.

The experimental data (black diamonds) is peaked at the independently determined optimal stage position. As Fig. 11.7 indicated, we expect an offset of 200µm to the simulation results. The increase of the Faraday angle measured on the camera for an object plane offset of $\Delta z = -100\mu\text{m}$ for the $F = 0.53$ result relative to the angle at the end of the sample is then 2.5%, which is significantly smaller than the observed 15% increase relative to the maximally permitted atom number scaling. We can therefore trust our imaging system to be able to determine Faraday angles of thermal ensembles faithfully.

11.3 Effect of Diffraction On Faraday Rotation Angles

We will complete the thermal cloud analysis by comparing the data presented in Sec. 11.1.4 to the diffraction simulations.

The experimentally obtained Faraday angle trace at the detuning of $\Delta_A = -1\text{GHz}$ is shown in Fig. 11.9 (replotted from Fig. 11.3) together with simulation results for two different optical depths (left panel $D = 562$, right panel $D = 1026$) at a Fresnel number of F=0.53 for two different object plane positions. The experimentally determined optical depth was $D = 680$. The effect of light-assisted collisions was to increase the angle by a factor of 1.46. This would correspond to an optical depth of $D = 993$ if a model without light-assisted collisions is assumed. It is clear from the two figures that the Faraday traces do change in height for the two ODs but their shape remains the same, even if the object plane is slightly misaligned. In this regard the cold collision model appears plausible.

The same simulations are compared in Fig. 11.10 with the experimental transmission data, as in Fig. 11.4, but for a detuning of $\Delta_A = -400\text{MHz}$. The experimental

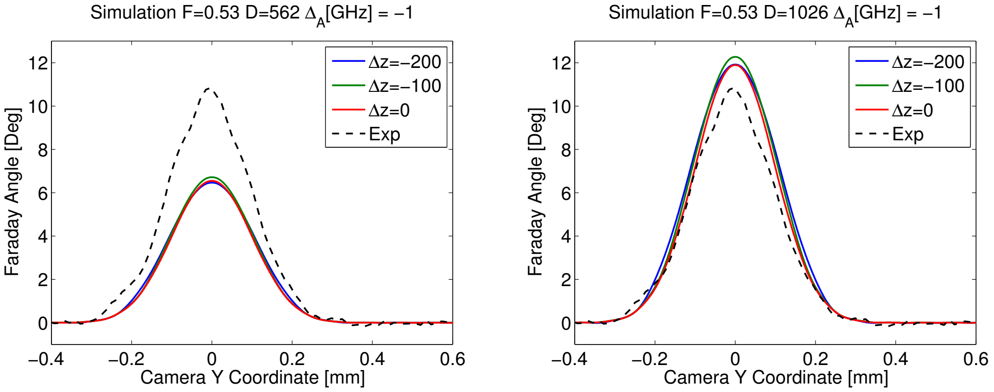

Figure 11.9: Comparison of experimentally obtained thermal cloud Faraday angle traces (black, dashed) to simulations. The left panel shows numerical simulations with an OD of $D = 562$ and the right panel for $D = 1026$. Each curve represents a different object plane offset.

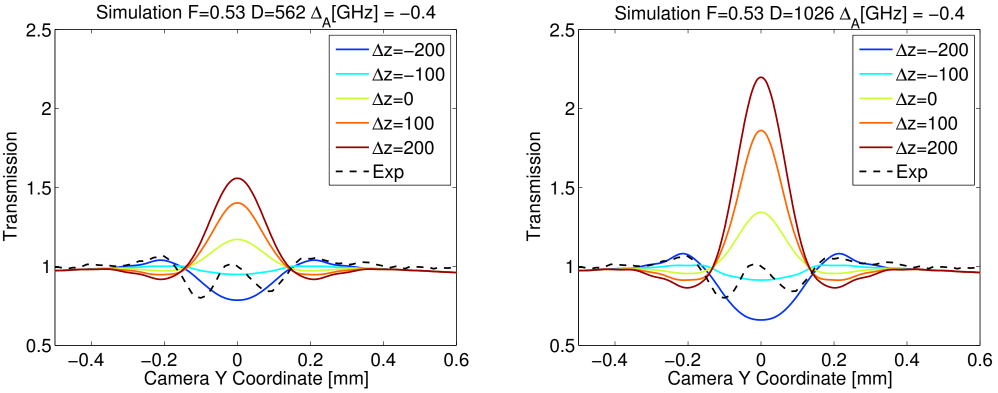

Figure 11.10: Comparison of experimentally obtained thermal cloud transmission traces (black, dashed) to numerical simulations. The detuning is $\Delta_A = -400\text{MHz}$. The left panel shows numerical simulations with an OD of $D = 562$ and the right panel for $D = 1026$. Each curve represents a different object plane offset.

transmission data (black, dashed) has a quite different shape from the simulation results. According to the last section the most plausible offset of the imaging plane would be $\Delta z = -100\mu\text{m}$, for which at least the experimental transmission matches the simulation results, even if the shape does not. The reason for this mismatch might be the homogeneity of the density distribution along the propagation direction of light in the simulation. An eikonal model, as mentioned in Sec. 4.2.3, can include the additional inhomogeneity.

11.4 Faraday Rotation in Bose-Einstein Condensates

11.4.1 Introduction

In a BEC all atoms occupy the lowest energy state in the trapping potential and the phase space density is therefore larger than for a thermal sample. This implies that the condensates are dense and their de Broglie wavelength is large. The geometrical size of the clouds is smaller compared to a thermal sample and the Thomas-Fermi density distribution has contrary to the Gaussian distribution a well-defined edge. For these reasons in-trap imaging is especially challenging.

In our experimental setup the Faraday imaging is performed along the long axis of the condensate, additionally increasing lensing effects.

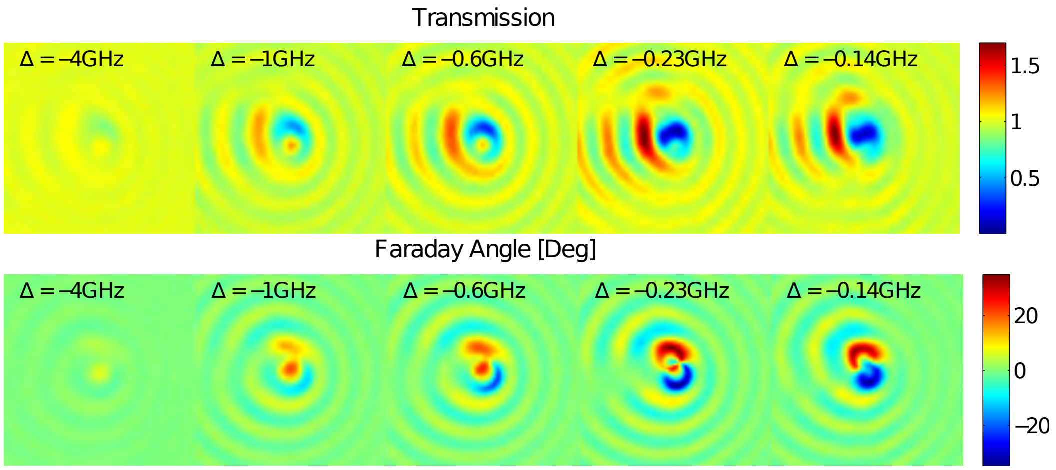

Figure 11.11: Top panel: BEC in-trap transmission images for several detunings. Lower panel: corresponding Faraday rotation images.

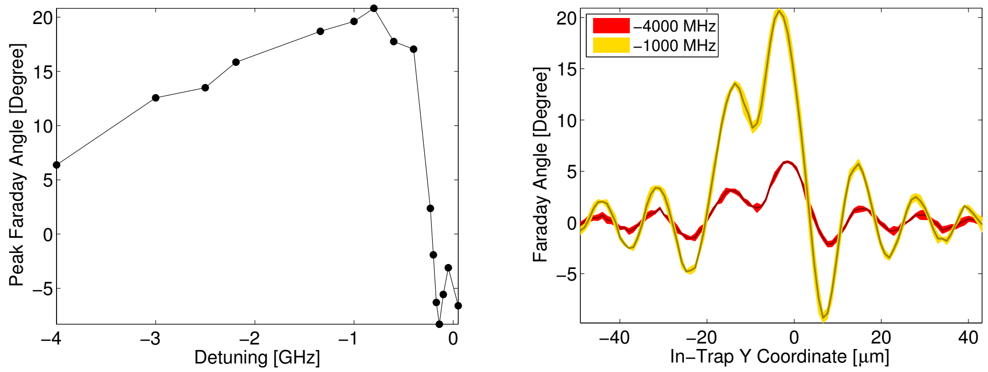

Figure 11.12: Left panel: peak Faraday angle determined from the BEC in-trap images presented in Fig. 11.11. Right panel: spatially resolved Faraday angle for two detunings $\Delta_A = -4$GHz and $\Delta_A = -1$GHz. The width of the curves represents one standard deviation.

11.4.2 Experimental Data

We determine the following sample parameters from absorption imaging. The Thomas-Fermi radii are $r_0 = 6.2\mu$m and $z_0 = 60.7\mu$m. The atom number in the condensate as estimated from a Thomas-Fermi fit is $N_{at}^{BEC} = 2.9 \cdot 10^5$, while the atom number estimated by using the radii is $N_{at} = 1 \cdot 10^6$. The density as estimated from the fit is $\rho_0 = 7.4 \cdot 10^{19}\mathrm{m}^{-3}$ and the temperature is $T = 105$nK. The condensation temperature is $T_c = 160$nK, giving $T/T_c = 0.66$ and there is no discernible thermal fraction on the absorption images. The light intensity is $I = 1.7\mathrm{W/m}^2$. The resulting optical depth $D = \xi_i^2(3\lambda^2/2\pi)\rho_0 z_0 4/3$ is $D = 904$ on the σ^- transition with $\xi_i = 1/2$ and the Fresnel number can be estimated by approximating the Thomas-Fermi atomic density with a Gaussian ($w_r/r_0 = w_z/z_0 = 0.435$) which gives $F = 0.17$.

Figure 11.11 shows the in-trap transmission and Faraday angle images as recorded with the dual-port imaging system for several detunings. Both Faraday and transmission images are strongly distorted due to refraction. Even at a detuning of −4GHz the diffraction rings are comparable in magnitude to the central peak. Additionally the central peak changes position as the detuning is varied, which makes it difficult to determine the peak angles. In the left panel of Fig. 11.12 the 3x3 pixel averaged peak angle is plotted. Despite the strong diffraction the angles follow roughly a typical D1 line Faraday curve, though we will see in the next section that the determined peak angles are

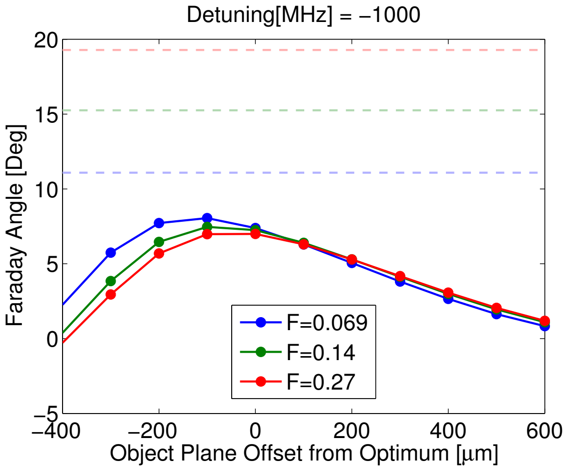

Figure 11.13: Simulation of the peak Faraday angle on the camera plane for an optical depth of $D = 1894$ as a function of object plane offset. Plotted are curves for three Fresnel numbers. The horizontal lines indicate the Faraday angle at the end of the sample.

too small. The right panel of the Figure shows the spatial Faraday angle trace. The width of the curve represents the standard deviation of about 5 experimental runs.

11.4.3 Comparison with Diffraction Models

The simple diffraction model of Sec. 3.1.2 that treats the sample as a thin lens predicts a fairly small diffraction angle of less than 5° for detunings that are farther than $\Delta_A = -200$MHz away from the atomic resonance. Considering the full opening angle of the imaging system of 15.2° perfect imaging should be possible. This model neglects the propagation of the field inside the sample. Using again the propagation model of Sec. 4.2.2 with an input optical depth of $D = 1894$ which roughly corresponds to the experimental OD multiplied by $f_{opt} = 2.13$, the correction for absorption imaging errors, as determined for the thermal cloud. Figure 11.13 shows the peak Faraday angle as a function of the object plane position for the Fresnel numbers $F = \{0.069, 0.14, 0.27\}$, with $F = 0.14$ roughly fitting the experimental conditions. The detuning is $\Delta_A = -1$GHz. The colored horizontal lines correspond to the peak Faraday angle at the end of the sample, before the light is propagated through the imaging system. It is obvious that these values are never reached on the camera plane and that the imaging system therefore introduces significant distortion to the Faraday profiles. The simulation results do not reproduce the experimental peak value of 18°.

11.4.4 Conclusion

In order to be able to reproduce the Faraday angle on the camera plane an imaging system with larger numerical aperture is necessary. This can be achieved by using a large NA objective [BPM$^+$09] and decreasing the working distance of the objective [KFC$^+$09, NLW07] or even by using a lens inside the vacuum system [BGP$^+$09]. In this way a resolution of only hundreds of nanometers can be achieved.

11.5 Faraday Rotation Experiments Conclusions

We presented experimental Faraday rotation and transmission data of ultracold thermal ensembles and Bose condensed ensembles. Thermal ensembles show moderate diffraction, such that their Faraday rotation profiles can be quantitatively analyzed. Bose condensed samples strongly diffract light and we have seen that our current imaging setup is not sufficient to faithfully image these samples.

In the analysis of our absorption images we used the thermal properties of Bose gases to infer a solid upper bound for any errors in determined atom numbers. This allowed us to estimate a maximal 15% increase of the determined in-situ Faraday angle with respect to a Maxwell-Bloch simulation. The increased angle was attributed to the presence of light-assisted cold-collisions and a model that estimates the dispersive properties of these collisions has been introduced in an earlier chapter.

Calibrating two imaging systems with respect to one another is a delicate task, since either method can be subject to flaws. We have estimated errors for both methods. The estimated defocusing errors of the dispersive imaging system proved to be small. We are therefore able to do faithful imaging of the thermal ensembles. The accurate determination of Faraday angles does only depend on the proper focusing of the imaging system and the overlap of the images obtained in the two arms of the imaging system. The determination of atom numbers from absorption images requires the knowledge of the atomic scattering cross section and efficient repumping of atoms, which can easily lead to errors in atom number determination.

The presented diffraction simulation is a model for a cylindrical atomic density distribution, of which the radial distribution is Gaussian and the axial distribution homogeneous. We found a discrepancy between the shape of experimentally determined transmission profiles and the simulation results. This discrepancy might be explained by the inhomogeneity of our samples along the axial direction.

To further investigate the light-assisted collision model presented in this thesis a density dependent measurement of this effect should be done. In our setup it is not possible to change the density independent of the shape of the atomic ensemble, which would be the optimal configuration for such an experiment.

Our imaging method has to our knowledge not been used in this way in other experiments. While the alignment of the system is somewhat harder than for an imaging system with just a single arm, there are many advantages to the method. It is possible to distinguish between diffraction and Faraday rotation signal, since we can always analyze the sum and the difference of the two ports of the beamsplitter simultaneously. The imaging system can also be used for spatial homodyne detection, which is of interest for the realization of a multimode memory.
A general rule of thumb for the calibration of an imaging system with inhomogeneous atomic ensembles and Faraday rotation signals, is to increase the Fresnel number to a large value. This suggests to use short ensembles with large radial extend, effectively bringing the ensemble closer to a homogeneous density distribution. Once the centering of the two images is established, such that meaningful difference images can be obtained, one can adjust the focusing of the imaging system by finding a maximum in the Faraday rotation angle.

Twelve

Superradiance

While in Faraday rotation measurements forward scattered light is investigated, in our superradiance experiments light is scattered into the backward direction in our experimental configuration. We have investigated the timing statistics of the endfire modes as documented in [Hil08]. We also studied the backscattered photon flux as a function of detuning [HKLT$^+$08] and the effect of light-assisted collisions on the superradiance threshold [**?**]. In this chapter i will present our efforts on resolving correlations between the backscattered photons and the simultaneously ejected atoms. In a further extension of our superradiance experimental series we looked at the slow down of the ejected atoms due to interactions with the zero momentum condensate mode.

12.1 Atom-Photon Correlations

Superradiance can be described with a parametric gain Hamiltonian that produces two-mode squeezed states if the depletion of the probe light and of the condensate mode can be neglected. Atoms and photon are created in pairs and therefore in a measurement the variance of the number difference operator to found to vanish.
We probe condensed samples along their long axis. The measurement setup is shown in Fig. 12.1. The probe light is detuned by $\Delta_A = -2.73$GHz with respect to the F=1 $m_F = -1$ to F'=2 $m_{F'} = -2$ D1 line transition, with a probe pulse duration of 100µs.

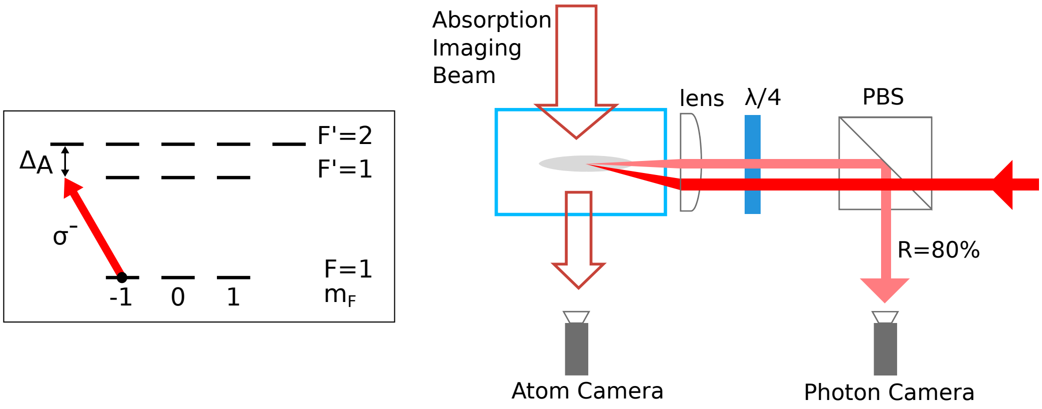

Figure 12.1: Experimental Setup for Atom-Photon correlation measurements. The probe light enters through a polarizing beam splitter (PBS) and is then prepared by a quarter wave plate ($\lambda/4$) in the polarization that drives the σ^- transition on the D1 line. A lens focuses the light onto the atoms. Backward scattered light is again collected by the lens and is then reflected from the cube onto the photon counting camera. Absorption images of the atoms are obtained after a time of flight of 15ms.

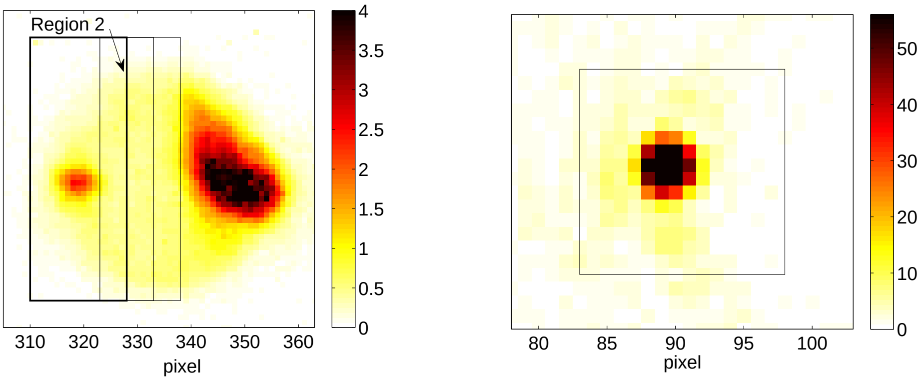

Figure 12.2: Single shot superradiance realizations of camera images. Left: absorption image of the atoms after 15ms TOF showing the optical depth. Right: Image of the superradiant endfire mode. The black areas on both images indicate the regions used for atom/photon counting.

The light enters through a beam splitter (PBS) and a quarter wave plate ($\lambda/4$) prepares a circular polarization. The light is then focused onto the atoms by a $f = 60$mm focal length achromatic doublet lens to a waist of 13µm. The photons that are backwards scattered into the endfire mode are collected by the lens and are then reflected by the cube onto our Andor camera for photon counting. The probe beam enters the atoms at a small angle with respect to the cell window that ensures that the endfire mode and stray reflections of the probe beam do not overlap on the camera. The reflectivity of the cube for the endfire mode is $R = 80\%$. The endfire mode is spread over only a few pixels in order to leave the signal well above the camera noise even for small photon numbers. The camera was set to use its slowest read-out rate of 50kHz. A count of seven photons per pixel corresponds at this setting to the shot-noise limit. We take absorption images after a time of flight of 15ms. This time was chosen such that the atomic recoil mode has an optical depth close to a value of one on a typical superradiance picture. The noise in atom counting is lowest at this optical depth. The total number of atoms in the condensate is $N_{at} = 9 \cdot 10^4$ with a normalized standard deviation of $\sigma_N = 0.15$ and $T/T_c = 0.65$. The condensate axes are $z_0 = 49$µm and $r_0 = 5$µm.

Typical images are shown in Fig. 12.2. On the left an absorption image showing the optical depth in a single realization of superradiance scattering is presented. The superradiance probe light entered from the right and the scattered atoms are the smaller feature on the left side of the image. Since the superradiant process is started spontaneously there is a large variation in the scattered atom and photon images from shot to shot. The image shows a realization with a rather large number of recoiled atoms. The atoms are surrounded by a halo of atoms. A halo can occur either for spontaneously scattered photons or for atom-atom scattering. Spontaneous scattering is small at the chosen detuning. The second process is therefore more probable. The recoiling atoms with momentum $2\hbar k_0$, where k_0 is the wave vector of the light, collide with the condensate atoms that populate the zero momentum mode. In this way a halo of radius $\hbar k_0$ is created. This halo is problematic for the determination of atom numbers in the recoil mode. About half the atoms in the halo originally populated the recoil mode and should therefore be accounted for. The image shows four regions used for atom counting. The right image of Fig. 12.2 shows the endfire mode and the region used to determine photon numbers.

A correlation plot of the atoms counted in region 2 against the number of endfire mode photons is presented in Fig. 12.3. The determined slope with 95% confidence bounds is $1.08\ [1.00, 1.17]$ and the intercept is $0.38\ [0.31, 0.46] 10^4$ atoms. The determined values depend on the chosen counting region. The slopes in the four regions are

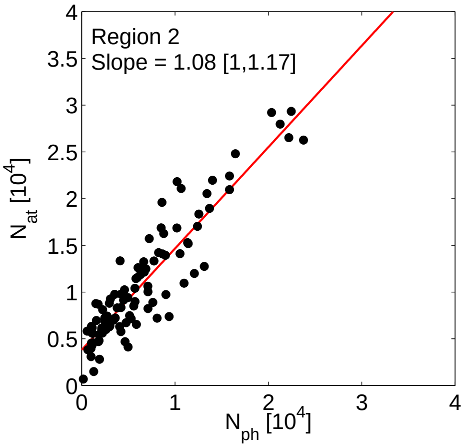

Figure 12.3: Correlation plot between atoms and photons for the atom counting region labeled as 'region 2' in Fig. 12.2. The slope of a linear fit is given with 95% confidence bounds.

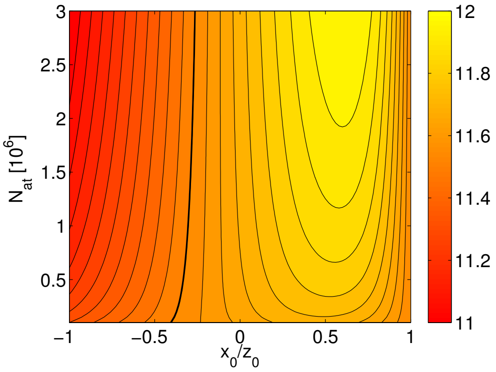

Figure 12.4: Simulation of the relative velocity of superradiantly scattered atoms as a function of the starting point within the cloud x_0 normalized to the long condensate axis z_0 and the total atom number within the condensate. The velocity is given in units of mm/s. The recoil velocity $v_r = 11.55\mathrm{mm/s}$, corresponding to the velocity with no interactions present between the atoms, is indicated by a thick contour line.

$[0.80, 1.08, 1.34, 1.62]$ and the intercepts are $[0.21, 0.38, 0.65, 1.12]$ atoms. A slope equal to 1 indicates that the same amount of atoms and photos were deduced from the images. A positive intercept indicates an offset in atom counting.

The halo of scattered atoms is unavoidable when using dense atomic clouds. A way to reduce the number of atoms in the halo is to probe after a short time of flight, such that the density is reduced. Additionally the calibrations of both cameras need to be well determined in order to see a perfect correlation. For the absorption imaging system the value of the scattering cross section needs to be well known to faithfully determine atom numbers.

Comparing the variance of the number difference to the number difference variance of two independent coherent states, we find $\mathrm{Var}(N_A - N_P)/(N_A + N_P) = 370$, indicating that we are far away from the quantum limit as discussed in Sec. 7.2.

12.2 Mean-Field Slow-Down of Superradiantly Scattered Atoms

When light enters the BEC and superradiant scattering sets in, it is the atoms at the front end of the cloud that scatter photons first. This has been observed in Maxwell-Bloch simulations [Hil08]. As the atoms scatter the light into the backward direction, they recoil into the forward direction and need to cross a large part of the condensate. Since

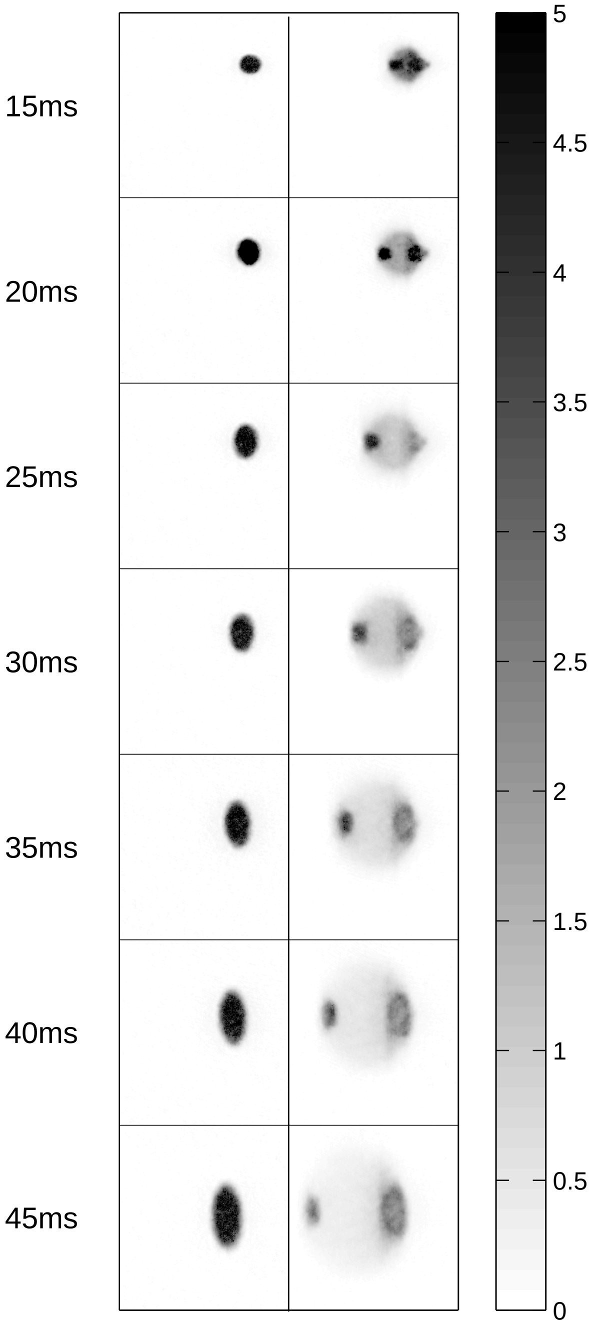

Figure 12.5: Absorption images showing the optical depth for several time of flight. Left column: condensate expansion. Right column: The atoms were probe inside the trap and scattered superradiantly. During the time of flight image series the scattered atoms move away from the condensate. The images are not magnification corrected.

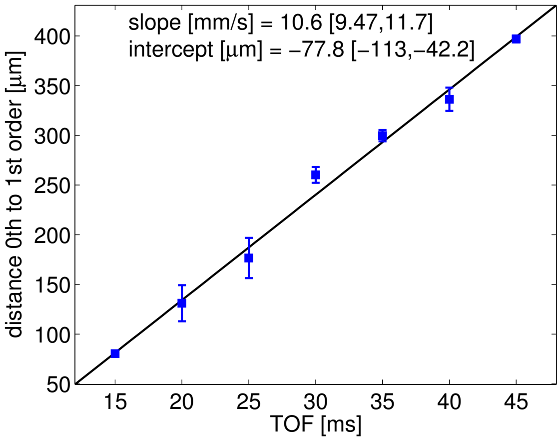

Figure 12.6: Plot of the distance between superradiantly scattered atoms and condensate atoms as determined from Fig. 12.5. Error bars indicate the standard deviation of 3 experimental runs. The determined velocity with the 95% confidence bounds was deduced from a linear fit.

the scattered atoms interact with the condensate atoms, the recoiling atoms need to cross an effective potential

$$U = 2\rho(\mathbf{r}, t)U_0, \tag{12.1}$$

where ρ is the atomic density and $U_0 = 4\pi\hbar^2 a/M$ is the atomic interaction energy. This means that the scattered atoms first loose energy as they climb the potential hill and are then accelerated after passing the peak of the density distribution. Depending on where the atoms started within the cloud a slow-down or speed-up of the scattered atoms compared to the initially transferred momentum by light scattering, $p = 2\hbar k = Mv_r$, where k is the wave vector of light and $v_r = 11.54\mathrm{mm/s}$ is two times the recoil velocity on the D1 line.

If the magnetic trapping potential is switched off immediately after the probe pulse, the scattered atoms cross an expanding density distribution. We can therefore solve the classical equations of motion

$$-\frac{\mathrm{d}U(\mathbf{r}, t)}{\mathrm{d}z} = M\frac{\mathrm{d}^2 z}{\mathrm{d}t^2} \tag{12.2}$$

for the velocity $v = \dot{z}$, taking into account the expansion of the density distribution and the time-dependent trap switch-off as a linear function $\max(1 - t/\tau, 0)$, with the experimentally determined time constant $\tau = 200\mu\mathrm{s}$. The trap switch-off alters the expansion of the Thomas-Fermi radii [CD96]. The resulting relative velocity of the superradiantly scattered atoms is plotted in Fig. 12.4 as a function of the normalized starting position x_0/z_0 along the long axis of the condensate and of the atom number inside the condensate. The recoil velocity v_r is marked as a thick contour line. A slow-down occurs for starting positions in the beginning of the condensate ($x_0/z_0 < 0$) and for high atom numbers. While the atoms are accelerated or decelerated as they interact with the condensate, their velocity is constant after they passed the condensate. The longest transit time occurs for the largest atom number and the starting point at the very beginning of the cloud. This time is 15ms.

In our experiments we determine the velocity of scattered atoms by probing the atoms inside the trap and then take absorption images after several time of flights as the scattered atoms move away from the main cloud. The shortest time of flight is 15ms and is equal to the longest determined transit time. We probe the atoms on the F=1, $m_F = -1$ to F'=2, $m_{F'} = -2$, σ^-, D1 line transition with a detuning of $\Delta_A = -2.73$GHz. The absorption image series is shown in Fig. 12.5 for non-probed atoms (left column) and probed atoms (right column). The BEC contains $N_{at,c} = 2.9 \cdot 10^5$ condensed atoms (determined from a bimodal fit) with a relative standard deviation over the full data set of $\sigma_N = 45\%$. The total atom number is $N_{at} = 4.7 \cdot 10^5$. The Thomas-Fermi radii were $z_0 = 55$µm with $\sigma_z = 4.8\%$ and $r_0 = 5.6$µm. The peak density is $\rho_c = 1 \cdot 10^{20}\text{m}^{-3}$. An interaction time of 100µs was used.

We use a numerical algorithm to determine the distance of the main cloud to the scattered atoms from absorption images, which is plotted in Fig. 12.6 and we use a linear fit to determine the relative velocity. We obtain a velocity of $v = 10.6\ [9.47, 11.7]\text{mm/s}$, with 95% confidence bounds and a starting point $x_0 = -77.8\ [-113, -42.2]$µm. While we do observe a reduction of the velocity mean value of 8% relative to v_r, the large statistical significance bounds of 10% do not allow for a definite claim of an observation of mean-field slow-down. We have additionally determined the distances by visually finding the center positions of resting to accelerated atoms, which led to a similar result. Since the determined atom numbers varied by 45% during the sequence the variation might explain the insufficient confidence bounds.

While the simple model presented above does predict a slow-down of atoms, it only reaches the velocity $v = 11\text{mm/s}$ for atoms that start at the very edge of the condensate $(x_0/z_0 = -1)$ in combination with very large atom numbers of $N_{at} = 3 \cdot 10^6$, which is much higher than the atom numbers observed in the experiment. If we determine atom numbers by using the Thomas-Fermi radii and trap frequencies we obtain $N_{at,cr} = 6.8 \cdot 10^5$. This value is still too low to account for the slow-down.

The relative velocity is also modified by magnetic fields. The force that a magnetic field exerts on the atoms is $F_x = \mu_B g_F m_F \nabla B_x$. For a field $B_x = B_0 + B_1 x + B_2 x^2$ it is only the quadratic part that can alter the relative velocity. A velocity reduction of 0.5mm/s after 45ms of TOF can be obtained with a field curvature of $B_2 = 18\text{G/m}^2$. The QUIC trap field curvature is $B_2^{QUIC} = \omega_z^2 \frac{M}{\mu_B g_F m_F} = 154\text{G/m}^2$, but the field is switched-off in 200µs and should therefore have no influence. The bias coils produce a field curvature of about $B_2^{bias} = 28\text{G/m}^2$ and are set up to compensate stray fields from the close by ion pumps at the position of the quadrupole field minimum. It is therefore possible that they have an influence on the motion of the atoms during time of flight.

The simple model presented above does not take into account the depletion of the condensate during superradiance. To account for this atom loss the coupled Maxwell-Bloch equations for the atomic density and the electric fields need to be solved [HKLT$^+$08, ZN06, ZN05].

Thirteen

Atom Loss Spectra

In this chapter the loss spectra of Bose condensed atomic ensembles are measured by monitoring the loss of atoms caused by a near resonant probe beam. The loss measurement is performed by absorption imaging after a time of flight of 45ms, while the probe beam is applied either while the atoms are inside the magnetic trap or after a short time of flight. In this way the influence of the atomic density on atom loss from the ensemble can be investigated.

The atoms are probed on the F=1, $m_F = -1$ to F'=2, $m_{F'} = -2$ transition on the D1 line, as indicated in the level scheme of Fig. 13.1. and the detuning is given relative to the F'=2 excited state manifold. The atoms are prepared in the F=1, $m_F = -1$ ground state. In order to investigate the influence of the density on line shapes we make use of the fact that the atomic cloud is expanding during a time of flight (TOF) after the trap is switched off. This leads to a decrease in density, which is plotted in the right panel of Fig. 13.1 as a function of time of flight. In the experiment the TOF duration is limited by the size of the probe beam, since the atoms fall perpendicular to the probe direction. The atoms are falling 90µm during 4.3ms of TOF, while the density reduces to 9% of the in-trap value. The light intensity reduces by a factor of about 4 as the atoms traverse the probe beam.

13.1 Atom-Loss Spectra for Various Densities

The measured atom loss spectra are shown in Fig. 13.2. We perform probe light detuning scans for atoms that are still inside the trap and for atoms that were freely falling for 1ms, 2ms and 4.3ms. The total atom number in the BEC is $N_{at} = 9.6 \cdot 10^5$ for the data sets with TOF of 1, 2 and 4.3ms, but lies 25% lower for the in-trap data set, with $N_{at} = 7.4cdot10^5$ (see figure caption). Therefore the spectra do not reach the same atom number at large detunings.

It is apparent that the width of the spectrum is largest for in-trap probing and reduces for the samples with lower density. The spectra are asymmetric and the observed resonance

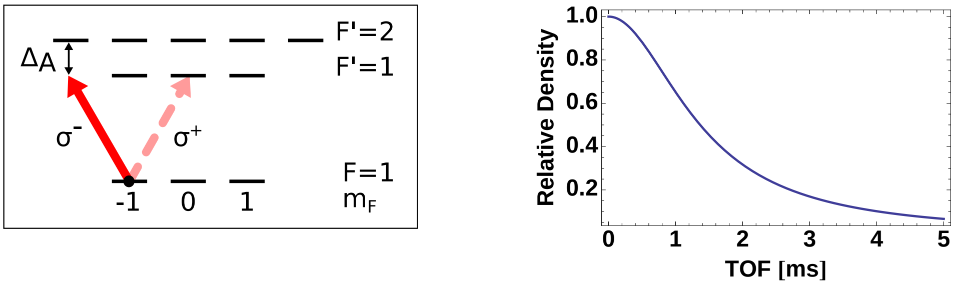

Figure 13.1: Left panel: D1 line level scheme with the σ^- probe light and the detuning relative to the F'=2 excited state. Right: Atomic density reduction as a function of time of flight (TOF).

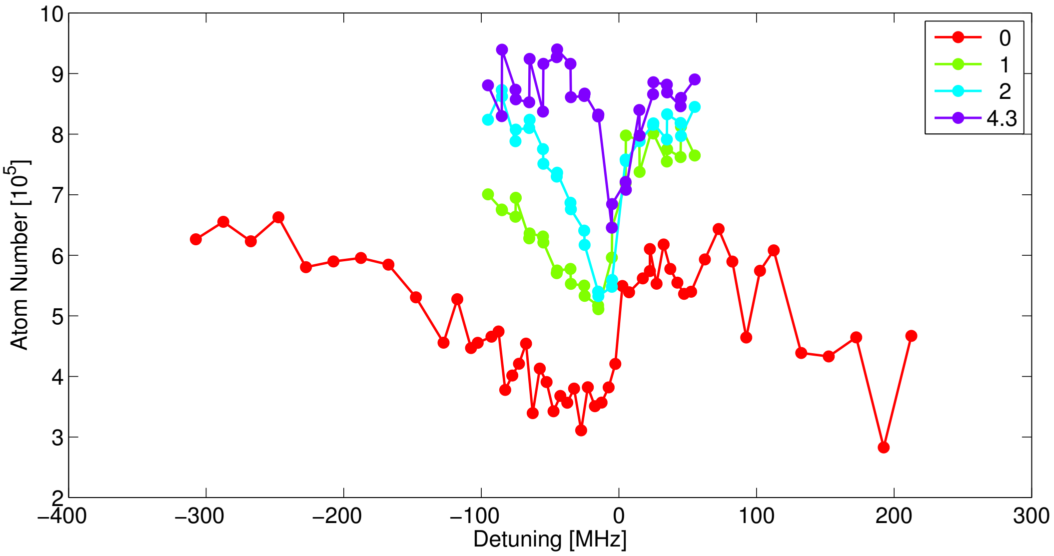

Figure 13.2: Atom loss spectrum of a BEC as determined from absorption images after 45ms TOF. The loss is induced by a probe beam, which is applied after various TOF with an intensity of $I = 0.42\text{W}/\text{m}^2$. The BEC has an in-trap density of $\rho = 1.4 \cdot 10^{20}\text{m}^{-3}$. The atom number without probe in the BEC is $N_{at} = 6.1\ 10^5$, the total atom number is $N_{at} = 9.6 \cdot 10^5$. The data set with 0ms TOF has slightly different parameters, The density is $\rho = 1.3 \cdot 10^{20}\text{m}^{-3}$, the BEC atom number is $N_{at} = 4.9\ 10^5$ and the total atom number is $N_{at} = 7.4 \cdot 10^5$.

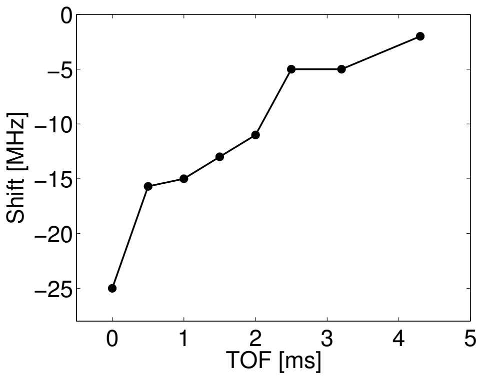

Figure 13.3: Detuning shift of the loss feature in Fig. 13.2 as a function of TOF, which is related to the atomic density.

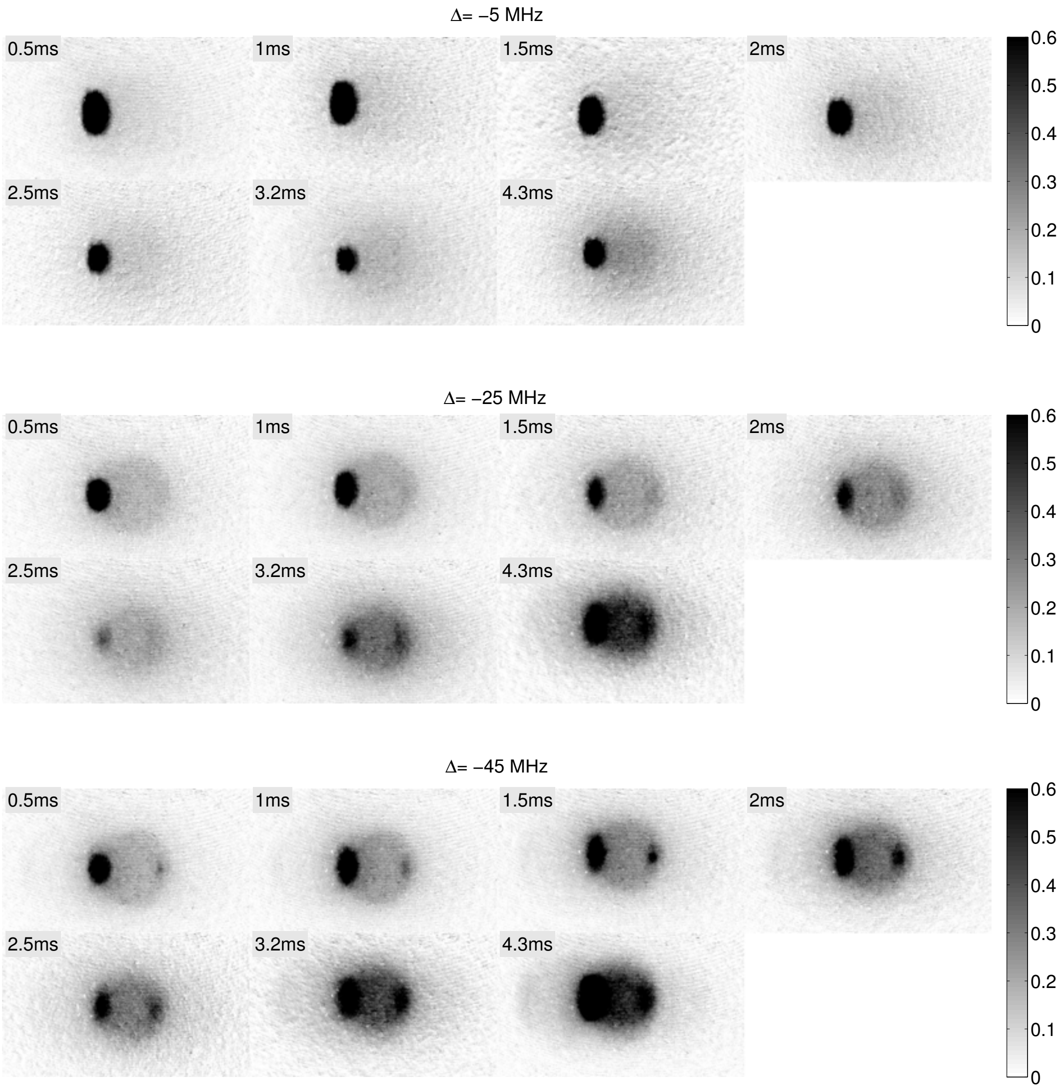

Figure 13.4: Absorption images taken after 45ms of TOF corresponding to the experiment of Fig. 13.2. Shown are three TOF scans. The probe light has a detuning of -5MHz for the first set, -25MHz for the second set and -45MHz for the third set. The OD is clipped at 0.6 to enhance low OD features on the images.

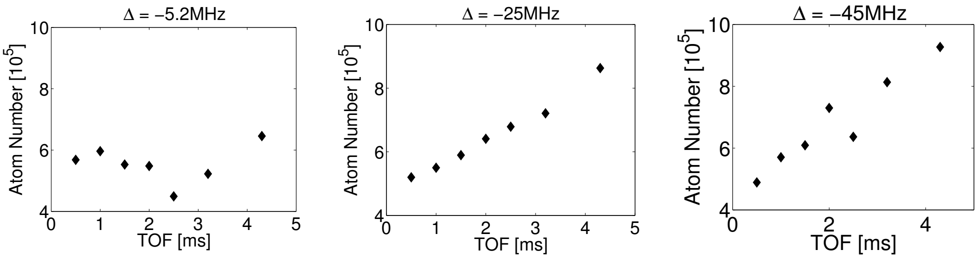

Figure 13.5: Atom number counts corresponding to the images of Fig. 13.4.

position shifts as plotted in Fig. 13.3. The in-trap data set also shows a loss feature at the +200MHz detuning.

In Fig. 13.4 the corresponding absorption images, taken after 45ms of TOF are shown. The upper set shows the $\Delta_A = -5$MHz probe detuning, the middle set shows the $\Delta_A = -25$MHz detuning and the bottom set the $\Delta_A = -45$MHz detuning. Each set shows several probe beam timings, corresponding to a reduced atomic density (0.5ms-4.3ms TOF).
It is striking that there is a halo for the detunings $\Delta_A = -25$MHz and $\Delta_A = -45$MHz, but not so for the $\Delta_A = -5$MHz detuning. The atom numbers on the $\Delta_A = -5$MHz images are low and stay constant with TOF, while they increase with TOF for the other two detunings. The atom number counts on these absorption images are shown in Figure 13.5.

A halo on the absorption images can be caused by several processes. Scattering photons from atoms transfers momentum to the atoms, which can be maximal $2\hbar k$ in a single scattering event, where k is the photon wave vector. Since absorption images are similar to the momentum distribution of the atoms, this process leads to a halo of radius $\hbar k$ on the images. If there is any superradiant scattering which leads to atoms with momentum $2\hbar k$, these atoms can in turn scatter from zero momentum atoms in the condensate mode, which leads to a similar halo. None of these processes leads to atom loss from the absorption image, since the atoms are still detectable as long as they are not hidden in the camera noise.
As is shown in Sec. 4.3, the refractive index in the self-consistent approach vanishes close to resonance for a density of $\rho = 1 \cdot 10^{20}\text{m}^{-3}$, which is comparable to the experimental in-trap density of $\rho = 1.4 \cdot 10^{20}\text{m}^{-3}$. This implies that the atoms at this density behave similar to a metal and light can not enter the high density center of the condensate for this detuning. A corresponding photon loss could not be extracted from the images taken with the dual-port imaging setup, since the probe beam is large and diffraction forces us to do photon counting over large areas.
The only mechanism that would remove atoms from the absorption images is an increase in kinetic energy, which would allow the atoms to leave the imaged area. An energy of $E \approx \hbar 2\pi$ 50kHz is sufficient for the atoms to leave the imaging region. A process that could provide this kinetic energy is the light-assisted collision model presented in Sec. 6. The positions of the resonances in this model do not depend on the density. The density only scales the strength of the interaction. Therefore an increase of the width of the loss spectrum after integrating the trap-loss rate over the whole cloud can not be obtained with this model. The loss rate also depends on light intensity. The intensity variation at the various TOF does not alter the lineshape appreciably.
At detunings close to the atomic resonance the Condon-radii become very large. When the Condon-radii become significantly larger than the mean particle distance it is likely that several atoms interact simultaneously forming trimers or bigger clusters of atoms. This might be a possible explanation for the loss features.
Especially for the $\Delta_A = -45$MHz detuning a halo in the backward direction is discernible. This is associated with Kapitza-Dirac scattering [STB$^+$03], which becomes energetically allowed for pulse durations shorter than 70µm.

13.2 Test of Polarization Mapping

The loss spectrum technique can also be used to analyze the degree of polarization of the light and of the atoms.
Since the atoms sag below the magnetic trap center, the atoms can be expected to be distributed over the F=1 ground state manifold if we choose the quantization axis along the propagation direction of the light. For the B-field angle of approximately 15° with respect to the propagation direction of light the $F = 1, m_F = -1$ population is reduced

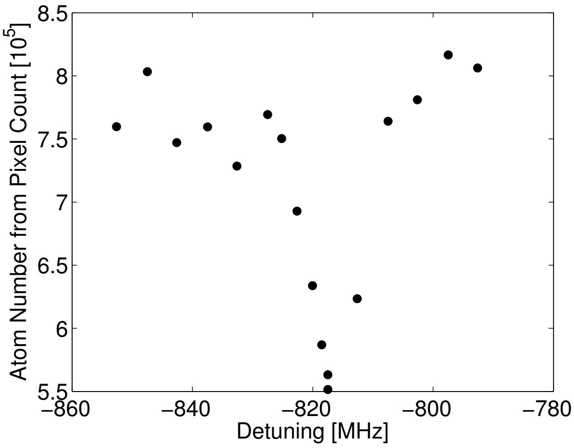

Figure 13.6: Atom loss from a BEC measured after 45ms of TOF. The probe beam drives the σ^- transition and was applied after 3ms of TOF. The detuning is given relative to the F'=2 manifold. The probe intensity is $I = 0.5\mathrm{W/m}^2$, the atomic density inside the trap is $\rho = 1.1 \cdot 10^{20}\mathrm{m}^{-3}$ and the atom number in the BEC is $N_{at} = 4.7 \cdot 10^5$ and the total atom number is $N_{at} = 8.1 \cdot 10^5$.

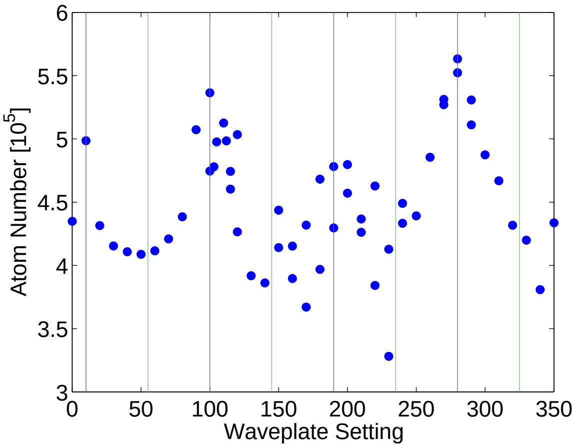

Figure 13.7: Atom loss as determined from absorption images after 45ms of TOF plotted against the setting of the quarter wave plate used to prepare the probe light polarization state. The atoms wered probed after 3ms TOF at a detuning of -817.5MHz (relative to F'=2). The BEC contained $N_{at} = 4.0 \cdot 10^5$ atoms and had an in-trap peak density of $\rho = 1.2 \cdot 10^{20}\mathrm{m}^{-3}$, the total atom number was $N_{at} = 7.1 \cdot 10^5$. The light intensity is $I = 0.45\mathrm{W/m}^2$.

to 96.63%, while the $m_F = 0$ state has a population of 3.34% and the $m_F = +1$ state contains 0.03% of the population. Moreover the quality of the polarization after a quarter wave plate, which is needed to prepare the circular polarized light that drives the σ^- transition, is not expected to be very good.

If the probe beam polarization is perfectly circular and the atomic ensemble is perfectly polarized in the $m_F = -1$ ground state no atomic loss should be observed when detuning the light by $\Delta_A = -814\mathrm{MHz}$ to be resonant with the F'=1 excited state manifold, since there is no resonant state for the probe light. The experimental result is shown in Fig. 13.6. The atoms were probed after a time of flight of 3ms to avoid line broadening and shifting. The atom loss is again deduced from absorption images after 45ms of TOF. There is a clear loss feature at the F'=1 resonance position which suggests that the polarizations are not ideal. About 30% of the atoms are lost at the F'=1 detuning.

In order to test if the polarization did indeed drive the σ^- transition we performed a wave plate scan at the F'=1 resonance position, $\Delta_A = -817.5\mathrm{MHz}$, again probing after 3ms TOF. The result is shown in Fig. 13.7. The plot shows that losses are smallest at the 100 and 280 positions of the wave plate. The initial wave plate setting was 103, suggesting that the polarization has been chosen correctly. The waveplate positions 10 and 190 correspond to σ^+ transitions and the losses are larger, since there is a resonant level. The largest losses, though, are observed for intermediate settings.

13.3 Conclusion

We have found a density dependent atom loss mechanism that produces asymmetric loss spectra around the atomic optical resonance. The width of these loss spectra increases as the density increases. While a light-assisted collision model can provide the kinetic energy to explain the atom loss, it can not explain the variation in the width of the spectra.

A loss spectrum as a function of light polarization revealed imperfections in either the quality of the polarization or the polarization of the atomic spins.

Fourteen

Conclusion

The motivation for this thesis was the prospect of using the large optical depth of ultracold atomic ensembles for the realization of high fidelity quantum memories that allow to store more than just a single light mode. The work presented in this thesis takes the first steps towards this goal.

Faraday rotation experiments were used to determine the atom-light interaction strength, which is the optical depth, and an extremely large peak optical depth of OD $= 680$ was determined for an ultracold thermal ensemble. This is about a factor of five higher than optical depths encountered in laser-cooled and room-temperature atomic ensembles. In Bose-condensed ensembles the optical depth is expected to be even larger. While the extreme coupling strength is desirable, it comes along with diffraction effects due to the inhomogeneity of the atomic density distribution, and with an increased atom-atom interaction, both van der Waals and light-mediated, because of the high density of evaporatively cooled samples.

The presented atom loss experiments showed that a rich set of physical effects are encountered when working with ultracold ensembles and there is much room for further investigation of these effects in order to get a better understanding of the underlying physical processes. In general, these effects tend to complicate experiments that aim at the investigation of spin properties at the quantum limit. An example for this is the recoil halo, observed in superradiant scattering. The effects of light-assisted collisions are expected to be introduce dephasing of the atomic collective excitations [**?**] and therefore decrease the lifetime of an atomic spinwave used for storage. The observed diffraction in the Faraday rotation experiments is not necessarily a limitation for a quantum memory, as diffraction has been recently included in quantum memory models [ZGGS11], as long as the imaging system does not distort the light mode and can resolve the finest structures of a given higher order light mode, for example a higher order Bessel mode. All the presented experiments are performed in a magnetic trap. Inhomogeneous magnetic fields also introduce dephasing of the atomic spins within the ensemble. For a quantum memory with long storage times a dipole trap is therefore essential.

A new dual-port polarization-contrast imaging technique was introduced in this thesis. While the alignment of this setup is more challenging than for standard polarization-contrast techniques, it has unique advantages. As has been shown in this thesis it has the ability to distinguish between diffraction and Faraday rotation. In ongoing work this imaging system is employed for spatially-resolved homodyne detection and it is a key component for a spatially-multimode quantum memory.

A model for the dispersive part of the interaction between two atoms and a photon, so-called light-assisted collisions, has been proposed in this thesis. The model predicts an enhancement of the interaction strength if the off-resonant contribution of the repulsive potentials is taken into account. This model can explain the enhancement of the determined Faraday angles as compared to a Maxwell-Bloch model. Any change in polarization of the atoms, i.e due to magnetic fields or light polarization imbalance, only leads to a decrease of rotation angles in our experimental configuration. A lensing effect of the atomic ensemble also leads to a reduction of the Faraday angle at the peak atomic density of the sample. Further insights to the validity of this collisional model could be gained with Faraday rotation experiments for various atomic densities, as this would scale the strength of this interaction.

The results of this thesis apply for any high density sample and could therefore also be observed in erbium doped crystals or nitrogen-vacancy centers in diamond. Diffraction effects can be avoided with atoms in an optical lattice or room-temperature gas cells, at the cost of a reduced interaction strength.

Part V

Appendix

One

Atomic Density Distributions

The theory of how to determine density distributions of ultracold gases was presented in Chap. 2. This appendix is focusing on the practical issues of how to deduce sample parameters from images and how to calculate optical depths. We use two different probing directions. In absorption imaging the samples are probed along the radial trap frequency direction. For in-trap images and probing the light travels along the axial trap direction.

To deduce parameters from absorption images we apply a fitting routine on the optical depth images. In order to determine the in-trap parameters the cloud radii need to be scaled accordingly.

When optical depth values are stated in this thesis, they are peak values. When Faraday rotation signals are obtained with a time-resolving detector, they are integrated over the density distribution. To make comparison of peak to mean optical depth values easily accessible, the ratios are given in this appendix.

A.1 BEC Density in Thomas-Fermi Approximation

The Thomas-Fermi density distribution in a cigar shaped harmonic oscillator trapping potential is [KDSK99]:

$$\rho(r,z) = \frac{15}{8\pi}\frac{N_{at}}{z_0 r_0^2}\max\left(1-\frac{r^2}{r_0^2}-\frac{z^2}{z_0^2},0\right). \tag{A.1}$$

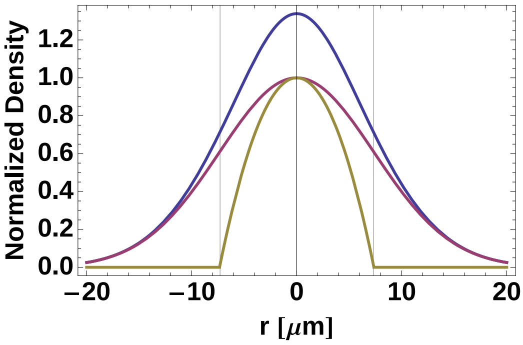

Figure A.1: Comparison of density distributions in a cigar shaped harmonic trap. The density distributions have identical radii indicated by black vertical lines, while the peak values are normalized. Yellow: Thomas-Fermi distribution of a condensed cloud normalized to its peak value. Red: Gaussian density distribution of a classical gas normalized to its peak value. Blue: Bose enhanced density distribution of a thermal gas with fugacity $\zeta = 0.6$ normalized to the Gaussian peak.

A plot can be seen in Fig. A.1. The column integrated density is for light propagating along the axial direction z (this is the case for our in-trap probing and imaging)

$$\tilde{\rho}(r) = \frac{5}{2\pi}\frac{N_{at}}{r_0^2}\max\left(1-\frac{r^2}{r_0^2},0\right)^{3/2}. \tag{A.2}$$

The ratio of peak column density to peak density is

$$\frac{\tilde{\rho}_0}{\rho_0} = \frac{4}{3}z_0. \tag{A.3}$$

The optical depth is then (assuming σ_0 is independent of position) $\mathrm{OD} = \sigma_0\tilde{\rho}$ and the peak value is

$$\mathrm{OD}^{\mathrm{peak}} = \sigma_0\frac{5}{2\pi}\frac{N_{at}}{r_0^2}. \tag{A.4}$$

The mean optical depth is found by integrating over the profile and normalizing by the integration area A

$$\overline{\mathrm{OD}}_A = \frac{1}{\iint_A r\mathrm{d}r\mathrm{d}\phi}\iint_A OD(r)r\mathrm{d}r\mathrm{d}\phi = \sigma_0\frac{N_{at}}{\pi r_0^2} = \sigma_0\frac{N_{at}}{A}. \tag{A.5}$$

Comparing this result to the peak optical depth gives a factor of

$$\frac{\overline{\mathrm{OD}}}{\mathrm{OD}^{\mathrm{peak}}} = \frac{2}{5}. \tag{A.6}$$

A.1.1 Deduction of Sample Parameters from Time-Of-Flight Images

This is an overview of the deduced parameters from absorption imaging. In absorption imaging the integration to obtain the optical depth is performed along one of the radial directions. The camera pixel area is A_{pix} and the imaging magnification is M_i.

Radial in-trap radius	$r_0(0) = \dfrac{r_0(t_{TOF})}{\sqrt{1+\omega_r^2 t_{TOF}^2}}$
Axial in-trap radius	$z_0(0) = r_0(0)\dfrac{\omega_r}{\omega_z}$
Chemical potential	$\mu = \dfrac{M}{2}\dfrac{\omega_r^2 r_0^2(t_{TOF})}{1+\omega_r^2 t_{TOF}^2}$
Temperature	$T = \dfrac{\mu}{k}$
Atom number from fit	$N_{at} = \mathrm{OD}^{\mathrm{peak}}\dfrac{2\pi}{5\sigma(\mathit{\Delta}_A)}z_0(t_{TOF})r_0(t_{TOF})$
Atom number from radii	$N_{at} = \dfrac{M^2}{15a\hbar^2}\dfrac{r_0^5(t_{TOF})}{\omega_z t_{TOF}^3}$
Atom number from pixel counting	$N_{at} = \dfrac{A_{pix}}{M_i^2\sigma(\mathit{\Delta}_A)}\sum_{(i,j)}\mathrm{OD}_{ij}^{pix}$
Peak density	$\rho(0,0) = \dfrac{15}{8\pi}\dfrac{N}{z_0 r_0^2}$

A.2 Thermal Cloud - Classical Limit

The density distribution of a thermal cloud in a cigar shaped harmonic oscillator trapping potential is a Gaussian

$$\rho(r,z) = \rho_0^G \exp\left(-\frac{r^2}{2w_r^2} - \frac{z^2}{2w_z^2}\right), \tag{A.7}$$

where the peak density is

$$\rho_0^G = \frac{N_{at}}{(2\pi)^{3/2} w_z w_r^2}. \tag{A.8}$$

A plot of the density can be seen in Fig. A.1. Then integrating along the z direction one obtains the column density along the axial in-trap axis

$$\tilde{\rho}(r) = \int_{-\infty}^{\infty} \rho(r,z)\mathrm{d}z = \tilde{\rho}_0^G \exp\left(-\frac{r^2}{2w_r^2}\right). \tag{A.9}$$

The ratio of peak column density $\tilde{\rho}_0^G$ to peak density ρ_0^G is

$$\frac{\tilde{\rho}_0^G}{\rho_0^G} = \sqrt{2\pi} w_0^z. \tag{A.10}$$

The mean column density, which is proportional to the optical depth, is found by integrating the column density over an area $A = \pi w'^2$ and normalizing by A

$$\widehat{\tilde{\rho}_{w'}^G} = \left(\pi w'^2\right)^{-1} \int_0^{2\pi} \int_0^{w'} \tilde{\rho}^G(r,\theta) r\mathrm{d}r\mathrm{d}\theta \tag{A.11}$$

$$= 2\left(\frac{w_r}{w'}\right)^2 \tilde{\rho}_0^G \left[1 - \exp\left(-\frac{1}{2}\left(\frac{w'}{w_r}\right)^2\right)\right]. \tag{A.12}$$

Note that only 63.2% of the atoms are contained within the waist w_r, compared to 86.5% for integrating over two times the waist.
In order to compare optical depth peak values to optical depth values that are calculated by averaging over the atomic cloud the following relations are useful

$$\frac{\widehat{\tilde{\rho}_{2w_0}^G}}{\tilde{\rho}_0^G} = \frac{1}{2}\left(1 - \exp(-2)\right) = 0.43 \tag{A.13}$$

$$\frac{\widehat{\tilde{\rho}_{w_r}^G}}{\tilde{\rho}_0^G} = 2\left(1 - \exp\left(-0.5\right)\right) = 0.79. \tag{A.14}$$

A.2.1 Deduction of Sample Parameters from Time-Of-Flight Images

This is an overview of how to deduce parameters of thermal samples from absorption imaging. In absorption imaging the integration to obtain the optical depth is along one of the radial directions. The camera pixel area is A_{pix} and the imaging magnification is M_i.

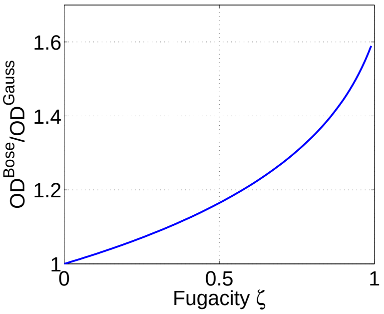

Figure A.2: Optical depth enhancement due to Bose statistics as compared to a classical gas, plotted against fugacity ζ. The critical point of the gas is reached at $\zeta = 1$.

Radial in-trap radius	$w_r(0) = \frac{w_r(t_{TOF})}{\sqrt{1+\omega_r^2 t_{TOF}^2}}$
Axial in-trap radius	$w_z(0) = \frac{w_z(t_{TOF})}{\sqrt{1+\omega_z^2 t_{TOF}^2}}$
Temperature	$T_r = \frac{M}{k}\omega_r^2 w_r^2(0)$
	$T_z = \frac{M}{k}\omega_z^2 w_z^2(0)$
Chemical potential	$\mu = kT\ln\left(\rho\lambda_{dB}^3\right)$
Atom number from fit	$N_{at} = \mathrm{OD}^{\mathrm{peak}}\frac{2\pi}{\sigma(\Delta_A)}w_z(t_{TOF})r_z(t_{TOF})$
Atom number from pixel counting	$N_{at} = \frac{A_{pix}}{M_i^2\sigma(\Delta_A)}\sum_{(i,j)}\mathrm{OD}_{ij}^{pix}$
Peak density	$\rho_0^G = \frac{N_{at}}{(2\pi)^{3/2}w_z w_r^2}$

A.3 Thermal Cloud - Bose Enhanced Density Distribution

The Bose enhanced density distribution is given by the equation of state of a Bose gas (Sec. 2.2.1) and becomes relevant for temperatures close to T_c. In the case of a cigar shaped harmonic oscillator potential it is

$$\rho(\mathbf{r}) = \sum_{n=1}^{\infty}\zeta^n\frac{1}{n^{3/2}\lambda_{dB}^3}\exp\left(-n\left(\frac{r^2}{2w_r^2}+\frac{z^2}{2w_z^2}\right)\right), \tag{A.15}$$

where the fugacity ζ is determined by the chemical potential. The Bose-enhanced column density is found in the same way as for the Gaussian density distribution, since it is a sum of Gaussians. Integrating along the y direction as in absorption imaging gives

$$\tilde{\rho}(x,z) = \frac{\sqrt{2\pi}w_r}{\lambda_{dB}^3}\sum_{n=1}^{\infty}\frac{\zeta^n}{n^2}\exp\left(-n\left(\frac{x^2}{2w_r^2}+\frac{z^2}{2w_z^2}\right)\right). \tag{A.16}$$

The Bose enhanced density distribution looks very similar to the simple Gaussian distribution and it is hard to decide on an absorption image if a thermal cloud is already in the Bose enhanced regime. Using a fitting routine that incorporates Bose enhancement failed, because compared to the Gaussian fit one has an additional fitting parameter, the fugacity. Therefore there are two fitting parameters, fugacity and $(\sqrt{2\pi}w_r)/(\lambda_{dB}^3)$, which form a product and fitting becomes infeasible at small fugacities, i.e. closer to the classical gas situation.

Figure A.2 shows the effect of the Bose enhancement on the optical depth plotted against fugacity ζ. Bose enhancement can be as large as 1.6 at the critical point. In Fig. A.1 a comparison of the Bose enhanced density and the Gaussian density for identical parameters and a fugacity of $\zeta = 0.6$ is presented.

Two

Light-Matter Interface

B.1 Spherical Basis

We define circular polarizations in terms of Cartesian polarization vectors [GSM06]

$$\vec{e}_{+} = -\frac{\vec{e}_x + i\vec{e}_y}{\sqrt{2}} \tag{B.1}$$

$$\vec{e}_{-} = \frac{\vec{e}_x - i\vec{e}_y}{\sqrt{2}} \tag{B.2}$$

$$\vec{e}_0 = \vec{e}_z. \tag{B.3}$$

We find the relations

$$\vec{e}_q^{\,*} = (-1)^q \vec{e}_{-q} \tag{B.4}$$

$$\vec{e}_q \vec{e}_{q'}^{\,*} = \delta_{qq'} \tag{B.5}$$

$$q \in \{-1, 0, 1\} \equiv \{-, 0, +\} \tag{B.6}$$

where $()^*$ denotes complex conjugation and δ is the Kronecker delta.

To write a vector $\vec{A}$ in the spherical basis one needs $A_q = \vec{e}_q \vec{A}$ and then any vector can be expressed in terms of its polarization components

$$\vec{A} = \sum_q A_q \vec{e}_q^{\,*} = \sum_q \vec{e}_q \vec{A} \vec{e}_q^{\,*} = \sum_q (-1)^q A_q \vec{e}_{-q}. \tag{B.7}$$

B.2 Collective Continuous Variables

Continuous variables describe the atomic and light operators as continuous in space instead of summing over single atom or photon contributions. While the continuous description is again discretized when implemented in a computational grid, the continuous description is interesting from a conceptual point of view. The section closely follows [Jul07], another good reference is [BLPS90].

B.2.1 Light

In SI units the electric field is

$$\hat{\mathbf{E}} = \sum_\lambda \sqrt{\frac{\hbar\omega_\lambda}{2\epsilon_0 V}} \left(\vec{\epsilon}_\lambda \hat{a}_\lambda e^{ik_\lambda z} + \vec{\epsilon}_\lambda^{\,*} \hat{a}_\lambda^\dagger e^{-ik_\lambda z} \right) \tag{B.8}$$

with V the quantization volume of the mode λ, ω_0 the frequency, $\vec{\epsilon}_\lambda$ the polarization vector and k_λ the wave vector. The creation/annihilation operators depend implicitly on time via $\dot{a} = i\omega_\lambda a$.

Now we define $\Delta k = 2\pi/L$ and let the length of the quantization domain diverge as for free space, $L \to \infty$, such that we can write $\sum \Delta k \to \int \mathrm{d}k$, i.e. the mode spacing becomes small. We define a new destruction operator

$$\hat{a}(k) = \frac{\hat{a}}{\sqrt{\Delta k}}$$

with units $[\hat{a}(k)] = \sqrt{\mathrm{m}}$ and can then rewrite the electric field as

$$\hat{\mathbf{E}}_\lambda = \sum \Delta k \sqrt{\frac{\hbar\omega_\lambda}{4\pi\epsilon_0 A}} \left(\vec{\epsilon}_\lambda \hat{a}(k) e^{ik_\lambda z} + \vec{\epsilon}^*_\lambda \hat{a}^\dagger(k) e^{-ik_\lambda z}\right) \tag{B.9}$$

$$\to \int \mathrm{d}k \sqrt{\frac{\hbar\omega_\lambda}{4\pi\epsilon_0 A}} \left(\vec{\epsilon}_\lambda \hat{a}(k) e^{ik_\lambda z} + \vec{\epsilon}^*_\lambda \hat{a}^\dagger(k) e^{-ik_\lambda z}\right). \tag{B.10}$$

Using a Fourier transform we can now get to the spatial domain

$$\hat{a}(z,t) = \frac{1}{\sqrt{2\pi}} \int_{-\infty}^{\infty} \hat{a}(k,t) e^{ikz} \mathrm{d}k \tag{B.11}$$

$$\hat{a}^\dagger(z,t) = \frac{1}{\sqrt{2\pi}} \int_{-\infty}^{\infty} \hat{a}^\dagger(k,t) e^{-ikz} \mathrm{d}k \tag{B.12}$$

where $[\hat{a}(z,t)] = 1/\sqrt{\mathrm{m}}$ and we have explicitly introduced the time dependence, therefore

$$\hat{\mathbf{E}}_\lambda(z,t) = \sqrt{\frac{\hbar\omega_\lambda}{2\epsilon_0 A}} \left(\vec{\epsilon}_\lambda \hat{a}(z,t) + \vec{\epsilon}^*_\lambda \hat{a}^\dagger(z,t)\right). \tag{B.13}$$

Note that A is the area of the mode perpendicular to the propagation direction z and is here assumed to have a flat profile. For i.e. Hermite-Gauss mode profiles corresponding mode functions need to be introduced [HSP10].

B.2.2 Atoms

In order to derive a collective representation of the atoms we need to sum single atom Hamiltonians over all atoms in the system. This is done by starting with the effective interaction Hamiltonian derived in (App. B.3). Equivalently one could start by summing the atomic Hamiltonians $\hat{\mathcal{H}}_\mathrm{A}$ and then pull through the adiabatic elimination which would give the same result.
Summing over all atoms N the collective Hamiltonian reads

$$\hat{\mathcal{H}}^{\mathrm{tot}} = \sum_{i=1}^{N} \hat{\mathcal{H}}_{\mathrm{int}}^{\mathrm{eff}(i)} = \sum_{i=1}^{N} \sum_{qq'} \hat{E}_q^{(-)} \hat{\alpha}_{qq'}^{(i)}(\Delta) \hat{E}_{q'}^{(+)}, \tag{B.14}$$

where the collective polarizability is $\sum_i \hat{\alpha}_{qq'}^{(i)}(\Delta)$.
Normalizing additionally to the number of atoms in a slab of thickness dz and density ρ we get to the collective polarizability in continuous variables

$$\hat{\alpha}_{qq'}(z,t,\Delta) = \frac{1}{\rho A \mathrm{d}z} \sum_{i=1}^{N} \hat{\alpha}_{qq'}^{(i)}(\Delta). \tag{B.15}$$

The effective interaction Hamiltonian then reads

$$\hat{\mathcal{H}} = \sum_{qq'} \int \rho A \mathrm{d}z \, \hat{E}_q^{(-)}(z,t) \hat{\alpha}_{qq'}(z,t,\Delta) \hat{E}_{q'}^{(+)}(z,t). \tag{B.16}$$

This is the final result, necessary for the light-atom dynamics.

B.2.3 Commutation Relations

The commutation relations in continuous variables read [HSP10, Kor09]

$$\left[\hat{S}_i(z,t), \hat{S}_j(z',t')\right] = i\hbar \sum_k \epsilon_{ijk} \hat{S}_k(z,t) \delta(z-z') \delta(t-t') \tag{B.17}$$

$$\left[\hat{f}_i(z,t), \hat{f}_j(z',t')\right] = \frac{i\hbar}{\rho A} \sum_k \epsilon_{ijk} \hat{f}_k(z,t) \delta(z-z') \delta(t-t'), \tag{B.18}$$

where ϵ_{ijk} is the Levi-Civita tensor. The relations allow to get rid of the integral in the equations of motion.

B.3 Derivation of the Effective Interaction Hamiltonian

In the first part we will derive the equation of motion for the continuous light operators in terms of the interaction Hamiltonian. We will see that finally we do not need the Hamiltonian for the radiative field. In the second part we will derive the effective interaction Hamiltonian between light and atoms. Here we will adiabatically eliminate the excited states to simplify the dynamics and introduce the polarizability of the atoms.

B.3.1 Space-Time Evolution of Light Field Operators

We will derive the coupled time and space evolution of continuous variable creation and annihilation operators. This section follows [Jul07].

We start by writing the time evolution:

$$\frac{\partial \hat{a}(z,t)}{\partial t} = \frac{1}{\sqrt{2\pi}} \int \frac{\partial}{\partial t} \hat{a}(k,t) e^{ikz} \mathrm{d}k \tag{B.19}$$

$$= \frac{1}{\sqrt{2\pi}} \int \left[\hat{a}(k,t), \hat{\mathcal{H}}_R + \hat{\mathcal{H}}_{AR}\right] e^{ikz} \mathrm{d}k, \tag{B.20}$$

where we have used the Fourier transform as above and have rewritten the time evolution of $\hat{a}(k)$ with Heisenberg type equation of motion. The radiation field Hamiltonian is

$$\hat{\mathcal{H}}_R = \sum_\lambda \hbar\omega_\lambda \left(\hat{a}_\lambda^\dagger \hat{a}_\lambda + \frac{1}{2}\right), \tag{B.21}$$

and we can write

$$\left[\hat{a}(k,t), \hat{\mathcal{H}}_R\right] = \int \mathrm{d}k' \, \hbar c k' \left[\hat{a}(k,t), \hat{a}^\dagger(k',t)\right] \hat{a}(k',t) = \hbar c k \hat{a}(k,t), \tag{B.22}$$

where we used $\left[\hat{a}(k,t), \hat{a}^\dagger(k',t)\right] = \delta(k-k')$. The Fourier transform of this simplifies to

$$\frac{1}{\sqrt{2\pi}} \int \left[\hat{a}(k,t), \hat{\mathcal{H}}_R\right] e^{ikz} \mathrm{d}k = \frac{1}{\sqrt{2\pi}} \int -icke^{ikz} \mathrm{d}k = -c \frac{\partial}{\partial z} \hat{a}(z,t), \tag{B.23}$$

and this results in the space-time evolution of the annihilation operator

$$\left(\frac{\partial}{\partial t}+c\frac{\partial}{\partial z}\right)\hat{a}(z,t)=\frac{1}{i\hbar}\left[\hat{a}(z,t),\hat{\mathcal{H}}_{AR}\right]. \tag{B.24}$$

This means we can write the electric field evolution in terms of the interaction Hamiltonian $\hat{\mathcal{H}}_{AR}$ only. The next section will simplify this Hamiltonian further.

B.3.2 Interaction Hamiltonian

In the following we will go through the steps to obtain the effective interaction Hamiltonian relevant for all dynamics of the coupled atom-light system. The final Hamiltonian will only include the ground states of the atoms, thereby simplifying calculations. This section closely follows [Kor09].

The dipolar interaction energy is [Jac62]

$$\hat{\mathcal{H}}_{\text{AR}}=-\hat{\mathbf{d}}\cdot\hat{\mathbf{E}},$$

where

$$\hat{\mathbf{E}}=\sum_{\lambda}\sqrt{\frac{\hbar\omega_\lambda}{2\epsilon_0 V}}\left(\vec{\epsilon}_\lambda\hat{a}e^{ik_\lambda z}+\vec{\epsilon}^{\,*}_\lambda\hat{a}^\dagger e^{-ik_\lambda z}\right)=\hat{\mathbf{E}}^{(+)}+\hat{\mathbf{E}}^{(-)} \tag{B.25}$$

is the electric field and

$$\hat{\mathbf{d}}=(P_g+P_e)\hat{\mathbf{d}}(P_g+P_e)=P_e\hat{\mathbf{d}}P_g+P_g\hat{\mathbf{d}}P_e=\hat{\mathbf{d}}^{(+)}+\hat{\mathbf{d}}^{(-)} \tag{B.26}$$

is the transition dipole operator with $\left(\hat{\mathbf{d}}^{(-)}\right)^\dagger=\hat{\mathbf{d}}^{(+)}$. Here we introduced the projectors $P_g=\sum_F P_F$ with $P_F=\sum_{m_F}|Fm_F\rangle\langle Fm_F|$ and accordingly for the excited states $|F'm'\rangle$ with $P_g+P_e=\mathbb{1}$.

With the rotating wave approximation (neglect fast rotating terms $\hat{\mathbf{d}}^{(+)}\hat{\mathbf{E}}^{(-)}$ and $\hat{\mathbf{d}}^{(-)}\hat{\mathbf{E}}^{(+)}$) the interaction Hamiltonian reads after inserting projectors for ground states $|F_i m_i\rangle$ and excited states

$$\hat{\mathcal{H}}_{\text{AR}}=-\sum_{F_iF'm_im'}\langle F_im_i|\hat{\mathbf{d}}^{(-)}|F'm'\rangle\hat{\sigma}_{F_im_iF'm'}\hat{\mathbf{E}}^{(-)}+\langle F'm'|\hat{\mathbf{d}}^{(+)}|F_im_i\rangle\hat{\sigma}_{F'm'F_im_i}\hat{\mathbf{E}}^{(+)} \tag{B.27}$$

and the atomic Hamiltonian is

$$\hat{\mathcal{H}}_{\text{A}}=\sum_{F'm'}\hbar(\varDelta_{F_iF'}+i\gamma)\hat{\sigma}_{F'm'F'm'}. \tag{B.28}$$

The time evolution of the atomic density matrix elements is

$$\frac{\mathrm{d}\hat{\sigma}_{F_im_iF'm'}}{\mathrm{d}t}=-\frac{i}{\hbar}[\hat{\sigma}_{F_im_iF'm'},\hat{\mathcal{H}}_{\text{AR}}+\hat{\mathcal{H}}_{\text{A}}] \tag{B.29}$$

$$=-\frac{i}{\hbar}\left(\sum_{F_fm_f}\langle F'm'|\hat{\mathbf{d}}^{(+)}|F_fm_f\rangle\hat{\mathbf{E}}^{(+)}\hat{\sigma}_{F_im_iF_fm_f}-\hbar(\varDelta_{F_iF'}+i\gamma)\hat{\sigma}_{F_im_iF'm'}\right). \tag{B.30}$$

$|F_im_i\rangle$ indicate initial and $|F_fm_f\rangle$ final ground states and $|F'm'\rangle$ are excited states.

The next step is to adiabatically eliminate excited states, i.e. assuming the excited state populations change on a time scale which is slow with respect to the ground state evolution and therefore the atomic dipoles follow the applied electric field adiabatically. This is true for low saturation parameters. We set

$$\frac{\mathrm{d}\sigma_{F'm'F'm'}}{\mathrm{d}t} = 0 \tag{B.31}$$

and obtain an expression for the coherences

$$\sigma_{F_im_iF'm'} = \frac{1}{\hbar(\varDelta_{F_iF'}+i\gamma)}\sum_{F_fm_f}\langle F'm'|\hat{\mathbf{d}}^{(+)}|F_fm_f\rangle\hat{\mathbf{E}}^{(+)}\sigma_{F_im_iF_fm_f}, \tag{B.32}$$

which we substitute in Eq. B.27 and B.28 for the interaction and atomic Hamiltonians to obtain

$$\hat{\mathcal{H}}_{\mathrm{AR}} = -2\sum_{F_fF'F_i}\hat{\mathbf{E}}^{(-)}\frac{P_{F_f}\hat{\mathbf{d}}^{(-)}P_{F'}\hat{\mathbf{d}}^{(+)}P_{F_i}}{\hbar(\varDelta_{F_iF'}+i\gamma)}\hat{\mathbf{E}}^{(+)} + h.c. = 2\hat{\mathbf{E}}^{(-)}\hat{\alpha}\hat{\mathbf{E}}^{(+)} \tag{B.33}$$

and by substituting $\sigma_{F'm'F'm'} = \sum_{F_gm_g}\sigma_{F'm'F_gm_g}\sigma_{F_gm_gF'm'}$ and replacing the coherences

$$\hat{\mathcal{H}}_{\mathrm{A}} = \hat{\mathbf{E}}^{(-)}\left(\sum_{F_fF'F_im_fm'm_i}\frac{\langle F_fm_f|\hat{\mathbf{d}}^{(-)}|F'm'\rangle\langle F'm'|\hat{\mathbf{d}}^{(+)}|F_im_i\rangle}{\hbar(\varDelta_{F_iF'}+i\gamma)}\hat{\sigma}_{F_im_iF_fm_f}\right)\hat{\mathbf{E}}^{(+)} \tag{B.34}$$

$$= -\hat{\mathbf{E}}^{(-)}\hat{\alpha}(\varDelta)\hat{\mathbf{E}}^{(+)}. \tag{B.35}$$

We defined the polarizability $\hat{\alpha}(\varDelta)$ as

$$\hat{\alpha}(\varDelta) = -\sum_{F_fF'F_i}\frac{P_{F_f}\hat{\mathbf{d}}^{(-)}P_{F'}\hat{\mathbf{d}}^{(+)}P_{F_i}}{\hbar(\varDelta_{F_iF'}+i\gamma)} = -\sum_{F_fF'F_i}\frac{\hat{\mathbf{d}}^{(-)}\hat{\mathbf{d}}^{(+)}}{\hbar(\varDelta_{F_iF'}+i\gamma)}. \tag{B.36}$$

Finally the effective interaction Hamiltonian is [Kor09]

$$\hat{\mathcal{H}}^{\mathrm{eff}}_{\mathrm{AR}} = \hat{\mathcal{H}}_{\mathrm{AR}} + \hat{\mathcal{H}}_{\mathrm{A}} = \hat{\mathbf{E}}^{(-)}\hat{\alpha}(\varDelta)\hat{\mathbf{E}}^{(+)} = \sum_{q_fq_i}\hat{E}^{(-)}_{q_f}\hat{\alpha}_{q_fq_i}(\varDelta)\hat{E}^{(+)}_{q_i}, \tag{B.37}$$

using the spherical polarization basis (App. B.1) in the last step

$$\hat{\alpha}_{q_fq_i}(\varDelta) = \vec{e}^{\,*}_{q_f}\hat{\alpha}(\varDelta)\vec{e}_{-q_i} \tag{B.38}$$

to map the polarizability onto the polarizations.

B.4 Atomic Electronic Structure

B.4.1 Angular Momentum

The total atomic angular momentum $\vec{\mathbf{F}} = (\hat{f}_x, \hat{f}_y, \hat{f}_z)$ is the sum of the electronic spin $\hat{\mathbf{S}}$, the electrons orbital angular momentum $\hat{\mathbf{L}}$ and the nuclear spin $\hat{\mathbf{I}}$

$$\hat{\mathbf{F}} = \hat{\mathbf{S}}\otimes\mathbb{1}_{L\otimes I} + \mathbb{1}_S\otimes\hat{\mathbf{L}}\otimes\mathbb{1}_I + \mathbb{1}_{S\otimes L}\otimes\hat{\mathbf{I}}. \tag{B.39}$$

The total angular momentum fulfills (in discrete variables) the typical commutation relations

$$[\hat{f}_i, \hat{f}_j] = i\hbar \sum_k \epsilon_{ijk} \hat{f}_k \tag{B.40}$$

where ϵ_{ijk} is the Levi-Civita tensor.

B.4.2 Transition Strengths

Projections of dipole operators $\hat{d}_q$ onto atomic hyperfine states $|f, m\rangle$ can be performed via the Wigner-Eckart theorem as

$$\langle F, m|\hat{d}_q|F', m'\rangle = \langle F, m|1, q; F', m-q\rangle\langle F||\mathbf{d}||F'\rangle \tag{B.41}$$

where $\langle F, m|1, q; F', m-q\rangle$ is a Clebsch-Gordan Coefficient. The nuclear spin degrees of freedom can be factored out, since they do not interact with the dipole operator

$$\langle F||\hat{\mathbf{d}}||F'\rangle = (-1)^{F'+J+I+1}\sqrt{(2F'+1)(2J+1)}\begin{Bmatrix} 1 & J & J' \\ I & F' & F \end{Bmatrix}\langle J||\hat{\mathbf{d}}_e||J'\rangle, \tag{B.42}$$

with I the nuclear spin quantum number, J and J' the ground and excited state fine structure quantum numbers and the curly brackets note 6j-symbols. The Clebsch-Gordan coefficients can be calculated via 3j-symbols and the Racah formula with the help of triangle coefficients [SM68, Mes62] and similarly for 6j-symbols.

The Clebsch-Gordan coefficient is

$$\langle J, M|j1, m1; j2, m2\rangle = (-1)^{M+j1-j2}\sqrt{2J+1}\begin{pmatrix} j1 & j2 & J \\ m1 & m2 & -M \end{pmatrix} \tag{B.43}$$

where the 3j-symbol is defined as

$$\begin{pmatrix} a & b & c \\ A & B & C \end{pmatrix} = (-1)^{a-b-C}\sqrt{D(a,b,c)}$$
$$\sqrt{(a+A)!(a-A)!(b+B)!(b-B)!(c+C)!(c-C)!}S_x(a,b,c,A,B,C). \tag{B.44}$$

The triangle coefficient is

$$D(a,b,c) = \frac{(a+b-c)!(b+c-a)!(c+a-b)!}{(a+b+c+1)!} \tag{B.45}$$

and

$$S_x(a,b,c,A,B,C) =$$
$$\sum_t \frac{(-1)^t}{t!(c-b+t+A)!(c-a+t-B)!(a+b-c-t)!(a-t-A)!(b-t+B)!}, \tag{B.46}$$

where t is chosen such that all factorials are non-negative. The 3j-symbols need to fulfill the triangular relations $(m1 + m2 - m) \equiv 0$, $|j1 - j2| \leq j$ and $j \leq j1 + j2$.

The 6j-symbols are given by

$$\begin{Bmatrix} j1 & j2 & j3 \\ J1 & J2 & J3 \end{Bmatrix} = \sqrt{D(j1, j2, j3)D(j1, J2, J3)D(J1, j2, J3)D(J1, J2, j3)} \\ S(j1, j2, j3, J1, J2, J3) \tag{B.47}$$

with

$$S(j1, j2, j3, J1, J2, J3) = \sum_t (-1)^t \frac{(t+1)!}{F(t, j1, j2, j3, J1, J2, J3)} \tag{B.48}$$

and

$$\begin{aligned} F(t, j1, j2, j3, J1, J2, J3) =& (t - j1 - j2 - j3)! \\ & (t - j1 - J2 - J3)!(t - J1 - j2 - J3)! \\ & (t - J1 - J2 - j3)!(j1 + j2 + J1 + J2 - t)! \\ & (j2 + j3 + J2 + J3 - t)!(j3 + j1 + J3 + J1 - t)!. \end{aligned} \tag{B.49}$$

The 6j-symbols need to fulfill the triangular relations $|j1 - j2| \leq j3$, $j3 \leq j1 + j2$, $|j1 - J2| \leq J3$, $J3 \leq j1 + J2$, $|J1 - j2| \leq J3$, $J3 \leq J1 + j2$, $|J1 - J2| \leq j3$, $j3 \leq J1 + J2$.

Some useful relations for Clebsch Gordan coefficients are

$$\langle j_1, m_1; j_2, m_2 | J, M \rangle = (-1)^{j_1 - m_1} \sqrt{\frac{2J+1}{2j_2+1}} \langle j_1, -m_1; J, M | j_2, m_2 \rangle \tag{B.50}$$

$$\langle j_1, m_1; j_2, m_2 | J, M \rangle = \langle J, M | j_1, m_1; j_2, m_2 \rangle \tag{B.51}$$

and for 6j-symbols

$$\begin{Bmatrix} 1 & J & J' \\ I & F' & F \end{Bmatrix} = \begin{Bmatrix} 1 & J' & J \\ I & F & F' \end{Bmatrix} = \begin{Bmatrix} J' & J & 1 \\ F & F' & I \end{Bmatrix}. \tag{B.52}$$

B.4.3 Tensor Operators

Here we state the general form of the polarizability in terms of the tensor operator matrices and the dependence on the polarization vectors [GSM06]:

$$\hat{\alpha}^{(0)} = \hat{T}_0^{(0)}\left(-\frac{1}{\sqrt{3}}\vec{e}_0^*\vec{e}_0^* + \frac{1}{\sqrt{3}}\vec{e}_+^*\vec{e}_-^* + \frac{1}{\sqrt{3}}\vec{e}_-^*\vec{e}_+^*\right) \tag{B.53}$$

$$\begin{aligned}\hat{\alpha}^{(1)} = {} & \hat{T}_0^{(1)}\left(\frac{1}{\sqrt{2}}\vec{e}_+^*\vec{e}_-^* - \frac{1}{\sqrt{2}}\vec{e}_-^*\vec{e}_+^*\right)\\ & + \hat{T}_{+1}^{(1)}\left(-\frac{1}{\sqrt{2}}\vec{e}_0^*\vec{e}_+^* + \frac{1}{\sqrt{2}}\vec{e}_+^*\vec{e}_0^*\right)\\ & + \hat{T}_{-1}^{(1)}\left(\frac{1}{\sqrt{2}}\vec{e}_0^*\vec{e}_-^* - \frac{1}{\sqrt{2}}\vec{e}_-^*\vec{e}_0^*\right)\end{aligned} \tag{B.54}$$

$$\begin{aligned}\hat{\alpha}^{(2)} = {} & \hat{T}_0^{(2)}\left(\sqrt{\frac{2}{3}}\vec{e}_0^*\vec{e}_0^* + \frac{1}{\sqrt{6}}\vec{e}_+^*\vec{e}_-^* + \frac{1}{\sqrt{6}}\vec{e}_-^*\vec{e}_+^*\right)\\ & + \hat{T}_{+1}^{(2)}\left(\frac{1}{\sqrt{2}}\vec{e}_0^*\vec{e}_+^* + \frac{1}{\sqrt{2}}\vec{e}_+^*\vec{e}_0^*\right)\\ & + \hat{T}_{-1}^{(2)}\left(\frac{1}{\sqrt{2}}\vec{e}_0^*\vec{e}_-^* + \frac{1}{\sqrt{2}}\vec{e}_-^*\vec{e}_0^*\right)\\ & + \hat{T}_{+2}^{(2)}\left(\vec{e}_+^*\vec{e}_+^*\right) + \hat{T}_{-2}^{(2)}\left(\vec{e}_-^*\vec{e}_-^*\right).\end{aligned} \tag{B.55}$$

The tensors $\hat{T}_m^{(j)}$ can be in general expressed in terms of dipole moment operators making use of Clebsch-Gordan coefficients which we state here explicitly as well as in terms of spin operators $\hat{F}$, here shown for the specific case of F=1:

$$\hat{T}_m^{(j)} = \sum_{q_f q_i}\hat{d}_{q_f}\hat{d}_{q_i}^{\dagger}\langle 1, q_f; 1, -q_i | j, m\rangle \tag{B.56}$$

$$\hat{T}_0^{(0)} = -\frac{1}{\sqrt{3}}\left(\hat{d}_0\hat{d}_0^{\dagger} - \hat{d}_+\hat{d}_-^{\dagger} - \hat{d}_-\hat{d}_+^{\dagger}\right) \qquad = -\,\alpha^{(0)}\mathbb{1}/\sqrt{3} \tag{B.57}$$

$$\hat{T}_0^{(1)} = \frac{1}{\sqrt{2}}\left(\hat{d}_+\hat{d}_-^{\dagger} - \hat{d}_-\hat{d}_+^{\dagger}\right) \qquad = +\,\alpha^{(1)}\hat{f}_z/\sqrt{2} \tag{B.58}$$

$$\hat{T}_{+1}^{(1)} = \frac{1}{\sqrt{2}}\left(-\hat{d}_0\hat{d}_+^{\dagger} + \hat{d}_+\hat{d}_0^{\dagger}\right) \qquad = +\,\alpha^{(1)}\hat{f}_+/\sqrt{2} \tag{B.59}$$

$$\hat{T}_{-1}^{(1)} = \frac{1}{\sqrt{2}}\left(\hat{d}_0\hat{d}_-^{\dagger} - \hat{d}_-\hat{d}_0^{\dagger}\right) \qquad = +\,\alpha^{(1)}\hat{f}_-/\sqrt{2} \tag{B.60}$$

$$\hat{T}_0^{(2)} = \frac{1}{\sqrt{6}}\left(\hat{d}_+\hat{d}_-^{\dagger} + 2\hat{d}_0\hat{d}_0^{\dagger} - \hat{d}_-\hat{d}_+^{\dagger}\right) \qquad = -\,\alpha^{(2)}\left[3\hat{f}_z^2 - F(F+1)\mathbb{1}\right]/\sqrt{6} \tag{B.61}$$

$$\hat{T}_1^{(2)} = \frac{1}{\sqrt{2}}\left(\hat{d}_0\hat{d}_+^{\dagger} + \hat{d}_+\hat{d}_0^{\dagger}\right) \qquad = -\,\alpha^{(2)}\sqrt{2}\hat{f}_+\left[\hat{f}_z + \mathbb{1}/2\right] \tag{B.62}$$

$$\hat{T}_{-1}^{(2)} = \frac{1}{\sqrt{2}}\left(\hat{d}_0\hat{d}_-^{\dagger} + \hat{d}_-\hat{d}_0^{\dagger}\right) \qquad = -\,\alpha^{(2)}\sqrt{2}\hat{f}_-\left[\hat{f}_z - \mathbb{1}/2\right] \tag{B.63}$$

$$\hat{T}_{+2}^{(2)} = \hat{d}_+\hat{d}_+^{\dagger} \qquad = -\,\alpha^{(2)}\hat{f}_+^2 \tag{B.64}$$

$$\hat{T}_{-2}^{(2)} = \hat{d}_-\hat{d}_-^{\dagger} \qquad = -\,\alpha^{(2)}\hat{f}_-^2. \tag{B.65}$$

More specifically for $F = 1/2$ the spin operators are related to the Pauli matrices as $\hat{f}_i = \frac{\hbar}{2}\hat{\sigma}_i$ with $i \in \{x, y, z, 0\}$ and for $F = 1$ the spin matrices $\hat{f}$ are given by [VMK88]

$$\hat{f}_{+1} = -\hbar\begin{pmatrix}0 & 1 & 0\\ 0 & 0 & 1\\ 0 & 0 & 0\end{pmatrix} \qquad \hat{f}_0 = \hbar\begin{pmatrix}1 & 0 & 0\\ 0 & 0 & 0\\ 0 & 0 & -1\end{pmatrix} \qquad \hat{f}_{-1} = \hbar\begin{pmatrix}0 & 0 & 0\\ 1 & 0 & 0\\ 0 & 1 & 0\end{pmatrix} \tag{B.66}$$

$$\hat{f}_x = \frac{1}{\sqrt{2}}\left(\hat{f}_{-1} - \hat{f}_{+1}\right) \qquad \hat{f}_y = \frac{i}{\sqrt{2}}\left(\hat{f}_{-1} + \hat{f}_{+1}\right) \qquad \hat{f}_z = \hat{f}_0 \tag{B.67}$$

$$\hat{f}_+ = -\frac{1}{\sqrt{2}}\left(\hat{f}_x + i\hat{f}_y\right) \qquad \hat{f}_- = \frac{1}{\sqrt{2}}\left(\hat{f}_x - i\hat{f}_y\right). \tag{B.68}$$

The commutation relation between discrete basis tensors and spin matrices is [VMK88]

$$\left[\hat{f}_\mu, \hat{T}_m^{(j)}(F)\right] = \hbar j(j+1)\langle j, m+\mu | j, m; 1, \mu\rangle \hat{T}_{m+\mu}^{(j)}(F), \tag{B.69}$$

where $\mu \in \{-1, 0, 1\}$.

The density operator can generally be decomposed into spin operators. In a two-level system the density operator reads

$$\hat{\sigma}_{F=1/2} = \frac{1}{2\hbar}\left(\hat{f}_0 + \hat{f}_x + \hat{f}_y + \hat{f}_z\right) = \frac{1}{2\hbar}\left(\hat{f}_0 + \hat{f}_z + \frac{1}{\sqrt{2}}\left((1+i)\hat{f}_- + (i-1)\hat{f}_+\right)\right). \tag{B.70}$$

in a F=1 system it looks more complicated:

$$\begin{aligned}\hat{\sigma}_{F=1} = \frac{1}{2\hbar}\Big(&\hat{f}_0 + \hat{f}_x + \hat{f}_y + \hat{f}_z + \left(\hat{f}_x^2 - \hat{f}_y^2\right) + \hat{f}_z^2 + \\ &\left(\hat{f}_x\hat{f}_y + \hat{f}_y\hat{f}_x\right) + \left(\hat{f}_x\hat{f}_z + \hat{f}_z\hat{f}_x\right) + \left(\hat{f}_y\hat{f}_z + \hat{f}_z\hat{f}_y\right)\Big).\end{aligned} \tag{B.71}$$

B.5 Light Stokes Operators

The quantized multimode light field [SZ97, GK05] in SI units and continuous variable notation, Eq. B.13, is

$$\hat{\mathbf{E}} = \sum_\lambda \sqrt{\frac{\hbar\omega_\lambda}{2\epsilon_0 A}}\left(\vec{\epsilon}_\lambda \hat{a}_\lambda + \vec{\epsilon}_\lambda^{\,*} \hat{a}_\lambda^\dagger\right) = \hat{\mathbf{E}}^{(+)} + \hat{\mathbf{E}}^{(-)} \tag{B.72}$$

and mapped on the spherical basis (App. B.1)

$$\hat{E}_q^{(-)} = \sqrt{\frac{\hbar\omega_\lambda}{2\epsilon_0 A}}\hat{a}_q^\dagger(z,t) \tag{B.73}$$

$$\hat{E}_q^{(+)} = \sqrt{\frac{\hbar\omega_\lambda}{2\epsilon_0 A}}\hat{a}_q(z,t). \tag{B.74}$$

The photon number in a mode λ is

$$N_{ph}^\lambda = \langle \hat{a}_\lambda^\dagger \hat{a}_\lambda \rangle. \tag{B.75}$$

In order to describe the polarization state of light we can define Stokes operators $\hat{S}_i$, which follow canononical Schwinger-Boson type commutation relations [Sak94] in the same way atomic angular momentum does. Written in discrete variables:

$$[\hat{S}_i, \hat{S}_j] = i\hbar\epsilon_{ijk}\hat{S}_k \tag{B.76}$$

and for the continuous variables:

$$\left[\hat{S}_i(z,t),\hat{S}_j(z,t)\right] = i\hbar\epsilon_{ijk}\hat{S}_k(z,t)\delta(z-z')\delta(t-t'). \tag{B.77}$$

They are defined as [Col05, CG08]

$$\hat{S}_1(z,t) = \frac{\hbar}{2}\left(\hat{a}_+^\dagger\hat{a}_- + \hat{a}_-^\dagger\hat{a}_+\right) = \frac{\hbar}{2}\left(\hat{a}_x^\dagger\hat{a}_x - \hat{a}_y^\dagger\hat{a}_y\right) \tag{B.78}$$

$$\hat{S}_2(z,t) = \frac{i\hbar}{2}\left(\hat{a}_-^\dagger\hat{a}_+ - \hat{a}_+^\dagger\hat{a}_-\right) = \frac{\hbar}{2}\left(\hat{a}_x^\dagger\hat{a}_y + \hat{a}_y^\dagger\hat{a}_x\right) \tag{B.79}$$

$$\hat{S}_3(z,t) = \frac{\hbar}{2}\left(\hat{a}_+^\dagger\hat{a}_+ - \hat{a}_-^\dagger\hat{a}_-\right) = \frac{\hbar}{2i}\left(\hat{a}_x^\dagger\hat{a}_y - \hat{a}_y^\dagger\hat{a}_x\right) \tag{B.80}$$

and can be understood as the photon number differences in the x-y basis, the 45° basis and the circular basis.
The total photon number is then given by

$$\hat{S}_0(z,t) = \frac{\hbar}{2}\left(\hat{a}_+^\dagger\hat{a}_+ + \hat{a}_-^\dagger\hat{a}_-\right) = \frac{\hbar}{2}\left(\hat{a}_x^\dagger\hat{a}_x + \hat{a}_y^\dagger\hat{a}_y\right) \tag{B.81}$$

Using the Stokes operators it is possible to define a second order coherence matrix for the polarization state of the photons [CG08] analogous to the atomic density matrix. Written in the circular basis:

$$\hat{\rho} = \frac{1}{\hbar}\left(\hat{S}_0 + \hat{S}_1 + \hat{S}_2 + \hat{S}_3\right) = \frac{1}{2}\left(S_0\hat{\sigma}_0 + S_1\hat{\sigma}_1 + S_2\hat{\sigma}_2 + S_3\hat{\sigma}_3\right) \tag{B.82}$$

$$= \frac{1}{2}\begin{pmatrix} S_0 + S_3 & S_1 - iS_2 \\ S_1 + iS_2 & S_0 - S_3 \end{pmatrix}, \tag{B.83}$$

where the Stokes parameters [LL80] are the expectation values of the Pauli matrices for the photonic polarization state $\hat{\rho}$ and give the photon number differences as stated above

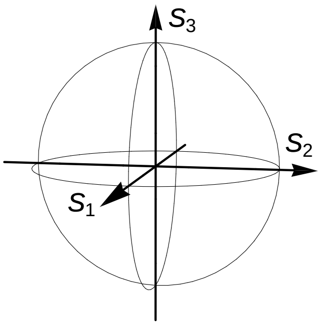

Figure B.1: The Poincaré sphere, a representation of the polarization state of light. The S_1-S_2 plane contains all linear polarizations, where S_1 is the x-y basis and S_2 is the ±45° basis. The S_3 is the basis of the circular polarizations.

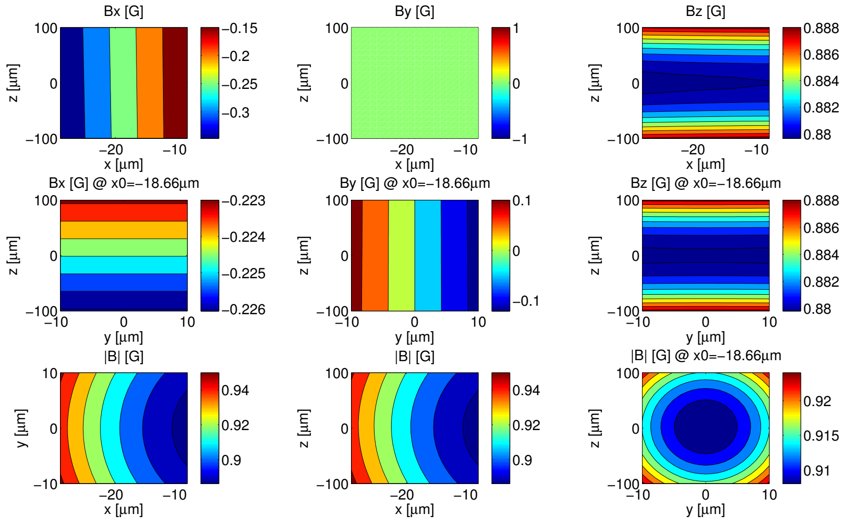

Figure B.2: Ioffe-Pritchard magnetic field configuration at the sagged position of the atomic ensemble $x_{sag} = -18\mu\text{m}$. The top row figure in the middle column

$$\langle \hat{S}_0 \rangle = \text{tr}(\hat{p} \cdot \hat{S}_0) = \frac{\hbar}{2} S_0 \tag{B.84}$$

$$\langle \hat{S}_1 \rangle = \text{tr}(\hat{p} \cdot \hat{S}_1) = \frac{\hbar}{2} S_1 \tag{B.85}$$

$$\langle \hat{S}_2 \rangle = \text{tr}(\hat{p} \cdot \hat{S}_2) = \frac{\hbar}{2} S_2 \tag{B.86}$$

$$\langle \hat{S}_3 \rangle = \text{tr}(\hat{p} \cdot \hat{S}_3) = \frac{\hbar}{2} S_3, \tag{B.87}$$

where $\text{tr}(\cdot)$ stands for the trace operation. The Stokes parameters can be visualized as the Poincaré sphere, which is shown in Fig. B.1. They have units $[S(z,t)] = [N_{ph}/(cT)] = m^{-1}$ defined by the number of photons per time T and speed of light c of per meter. They can be understood as components of a vector $\mathbf{S} = (S_1, S_2, S_3)/S_0$ defining the polarization state of light. Contrary to the Jones formalism the Stokes formalism can also describe depolarized light. The light is completely polarized if $S_0^2 = S_1^2 + S_2^2 + S_3^2$ and fully depolarized if $S_1 = S_2 = S_3 = 0$. The degree of polarization is $\Pi = \sqrt{S_1^2 + S_2^2 + S_3^2}/S_0$.
To calculate the photon flux at a detector we define $\hat{a}(t) = \sqrt{c}\hat{a}(z,t)$ and the photon flux is $\Phi(t) = \hat{a}^\dagger(t)\hat{a}(t)$.

B.6 Magnetic Fields

B.6.1 Ioffe-Pritchard Magnetic Field

In the QUIC [EBH98] trap the magnetic field is of the Ioffe-Pritchard type [Pri83]

$$\vec{\mathbf{B}} = B_0 \begin{pmatrix} 0 \\ 0 \\ 1 \end{pmatrix} + B'_\rho \begin{pmatrix} x \\ -y \\ 0 \end{pmatrix} + \frac{B''_z}{2} \begin{pmatrix} -xz \\ -yz \\ z^2 - (x^2 - y^2)/2 \end{pmatrix} \tag{B.88}$$

and the absolute value is

$$B(\vec{r}) = \sqrt{\left(B'_\rho x - \frac{B''_z}{2} xz\right)^2 + \left(B'_\rho y - \frac{B''_z}{2} yz\right)^2 + \left(B_0 + \frac{B''_z}{2} z^2 - \frac{B''_z}{4}(x^2 + y^2)\right)^2}. \tag{B.89}$$

For very cold temperatures, $k_B T \ll \mu B_0$, when the atoms reside only at the very bottom of the trap, the field is well approximated by a harmonic potential

$$V(\vec{r}) \approx \frac{M}{2}\left(\omega_r^2 r^2 + \omega_z^2 z^2\right) + \mu B_0 \tag{B.90}$$

with the frequencies given by

$$\omega_r^2 = \frac{\mu}{M}\left(\frac{B_r'^2}{B_{0z}} - \frac{B''_z}{2}\right) \qquad \text{and} \tag{B.91}$$

$$\omega_z^2 = \frac{\mu_B}{M} B''_z. \tag{B.92}$$

The atomic ensemble is dragged by gravity to a position below the trap center. The resulting sag position is given by the gravitational constant g and the trap frequency along the gravitation direction ω

$$x_{sag} = -\frac{g}{\omega^2}. \tag{B.93}$$

Figure B.2 shows the Ioffe-Pritchard magnetic field configuration at our sag position of $x_{sag} = -18\mu\text{m}$.

B.6.2 Time Evolution

For the time evolution of the density matrix we need the commutators of the magnetic field Hamiltonian with the total angular momentum operators. These are

$$\frac{\partial \hat{f}_x}{\partial t} = [\hat{H}_B, \hat{f}_x] = g_F \mu_B (\hat{f}_y B_z - \hat{f}_z B_y) \tag{B.94}$$

$$\frac{\partial \hat{f}_y}{\partial t} = [\hat{H}_B, \hat{f}_y] = g_F \mu_B (\hat{f}_z B_x - \hat{f}_x B_z) \tag{B.95}$$

$$\frac{\partial \hat{f}_z}{\partial t} = [\hat{H}_B, \hat{f}_z] = g_F \mu_B (\hat{f}_x B_y - \hat{f}_y B_x). \tag{B.96}$$

For the case of a $F = 1$ density matrix, Eq. B.71, also the following time evolutions are needed

$$\frac{i\hbar}{g_F\mu_B}\frac{\partial \hat{f}_z^2}{\partial t} = \big((\hat{f}_y\hat{f}_z + \hat{f}_z\hat{f}_y)B_x - (\hat{f}_x\hat{f}_z + \hat{f}_z\hat{f}_x)B_y\big) \tag{B.97}$$

$$\frac{i\hbar}{g_F\mu_B}\frac{\partial (\hat{f}_x^2 - \hat{f}_y^2)}{\partial t} = \big((\hat{f}_y\hat{f}_z + \hat{f}_z\hat{f}_y)B_x + (\hat{f}_x\hat{f}_z + \hat{f}_z\hat{f}_x)B_y - 2(\hat{f}_x\hat{f}_y + \hat{f}_y\hat{f}_x)B_z\big) \tag{B.98}$$

$$\frac{i\hbar}{g_F\mu_B}\frac{\partial (\hat{f}_x\hat{f}_y + \hat{f}_y\hat{f}_x)}{\partial t} = \big(-(\hat{f}_x\hat{f}_z + \hat{f}_z\hat{f}_x)B_x + (\hat{f}_y\hat{f}_z + \hat{f}_z\hat{f}_y)B_y + 2(\hat{f}_x^2 - \hat{f}_y^2)B_z\big) \tag{B.99}$$

$$\frac{i\hbar}{g_F\mu_B}\frac{\partial (\hat{f}_x\hat{f}_z + \hat{f}_z\hat{f}_x)}{\partial t} = \big((\hat{f}_x\hat{f}_y + \hat{f}_y\hat{f}_x)B_x + 2(\hat{f}_z^2 - \hat{f}_x^2)B_y - (\hat{f}_y\hat{f}_z + \hat{f}_z\hat{f}_y)B_z\big) \tag{B.100}$$

$$\frac{i\hbar}{g_F\mu_B}\frac{\partial (\hat{f}_y\hat{f}_z + \hat{f}_z\hat{f}_y)}{\partial t} = \big(2(\hat{f}_y^2 - \hat{f}_z^2)B_x - (\hat{f}_y\hat{f}_x + \hat{f}_x\hat{f}_y)B_y + (\hat{f}_x\hat{f}_z + \hat{f}_z\hat{f}_x)B_z\big). \tag{B.101}$$

B.6.3 Wigner D-Matrix

In ZYZ Euler angle convention a rotation operator can be written in terms of angular momentum operators $\hat{J}_k$ [VMK88]

$$\hat{\mathcal{R}}(\alpha,\beta,\gamma) = e^{-i\alpha\hat{J}_z}e^{-i\beta\hat{J}_y}e^{-i\gamma\hat{J}_z}. \tag{B.102}$$

Mapping the operator onto the states $|J,m\rangle$ we define the Wigner D-matrix

$$\begin{aligned} D^J_{m'm}(\alpha,\beta,\gamma) &= \langle J,m'|\hat{\mathcal{R}}(\alpha,\beta,\gamma)|J,m\rangle && \text{(B.103)}\\ &= e^{-im'\alpha}d^J_{m'm}(\beta)e^{-im\gamma}, && \text{(B.104)}\end{aligned}$$

where we used the Wigner small d matrices

$$\begin{aligned} d^J_{m'm}(\beta) =&\langle J,m'|e^{-i\beta\hat{J}_y}|J,m\rangle && \text{(B.105)}\\ =&\sqrt{(J+m')!(J-m')!(J+m)!(J-m)!}\times \\ &\sum_s \frac{(-1)^{m'-m+s}}{(J+m-s)!(s)!(m'-m+s)!(J-m'-s)!}\times \\ &\left(\cos\frac{\beta}{2}\right)^{2J-2s+m-m'}\left(\sin\frac{\beta}{2}\right)^{2s+m'-m}. && \text{(B.106)}\end{aligned}$$

Here s is chosen such that all factorials have non-negative arguments.

The rotation operators should be used on operators as $A' = \hat{\mathcal{R}}^{-1}A\hat{\mathcal{R}}$ and on states as $|b\rangle = \hat{\mathcal{R}}|c\rangle$.

Example For a $J = F = 1, m = m' = m_F = -1$ population of 100% and a B-field angle of $\beta = 30°$ with respect to the Hamiltonian quantization axis the D-matrix is

$$D^1(0,\beta,0) = \begin{pmatrix} \left(\cos\frac{\beta}{2}\right)^2 & \sqrt{2}\cos\frac{\beta}{2}\sin\frac{\beta}{2} & \left(\sin\frac{\beta}{2}\right)^2 \\ -\sqrt{2}\cos\frac{\beta}{2}\sin\frac{\beta}{2} & \left(\cos\frac{\beta}{2}\right)^2 - \left(\sin\frac{\beta}{2}\right)^2 & \sqrt{2}\cos\frac{\beta}{2}\sin\frac{\beta}{2} \\ \left(\sin\frac{\beta}{2}\right)^2 & -\sqrt{2}\cos\frac{\beta}{2}\sin\frac{\beta}{2} & \left(\cos\frac{\beta}{2}\right)^2 \end{pmatrix}, \tag{B.107}$$

resulting in a new density matrix $\hat{\sigma}^{QA} = (D^1(0,30°,0))^{-1}\,\hat{\sigma}^B\,D^1(0,30°,0)$, with a $m_F = -1$ population reduced to 87.05%.

B.6.4 Determining Euler Angles

Starting from the cartesian lab coordinate system in which the Hamiltonian quantization axis is $\vec{e}_{QA} = [0, 0, 1]$ we define a new system in which the B-field direction defines the z axis and the Hamiltonian quantization axis is used as a help to define the other axes:

$$\vec{e}_z^{\,\prime} = \frac{\vec{B}}{|\vec{B}|} \tag{B.108}$$

$$\vec{e}_y^{\,\prime} = \vec{e}_z^{\,\prime} \times \vec{e}_{QA} \tag{B.109}$$

$$\vec{e}_x^{\,\prime} = \vec{e}_y^{\,\prime} \times \vec{e}_z^{\,\prime}. \tag{B.110}$$

The inverse of the Euler rotation matrix is then given by using the new coordinate vectors as columns in it $\mathcal{R}^{-1} = [e_x', e_y', \vec{e}_z^{\,\prime}]$ and the Euler angles in ZYZ notation are then given by

$$\alpha = \mathrm{atan2}(\mathcal{R}_{23}, \mathcal{R}_{13}) \tag{B.111}$$

$$\beta = \mathrm{acos}(\mathcal{R}_{33}) \tag{B.112}$$

$$\gamma = -\mathrm{atan2}(\mathcal{R}_{32}, \mathcal{R}_{31}). \tag{B.113}$$

The Euler matrix then transforms a vector from the old system to the new as $\vec{x}^{\prime} = \mathcal{R}\vec{x}$ and for example the density matrix known in the B-field coordinate system σ^B to the quantization axis system σ^{QA} as $\sigma^{QA} = \mathcal{R}^{-1}\sigma^B\mathcal{R}$.

B.6.5 Arbitrary Magnetic Field – Light-Atom Dynamics

The problem at hand is that if we choose the quantization axis along the propagation direction of light, what we did when we derived the Hamiltonian, but the magnetic field is not aligned with this axis, the density matrix will have a different form than the simple form with only the $|F = 1, m_F = -1\rangle$ state populated. There will be coherences and populations among all the $F = 1$ states depending on the direction of the magnetic field.

By first calculating the Euler angles for the transformation from the B-field direction to the Hamiltonian quantization axis and then using those to calculate Wigner D-matrices which in turn can be used to transform the known density matrix with quantization axis along the B-field to the one along the Hamiltonian quantization axis.

Three

Light-Assisted Cold Collisions

This appendix gives all the details for the calculation of binary collisional loss rates. Additionally the topic of quantum statistics and the crucial step of including off-resonant effects of repulsive potentials will be explained.

C.1 Movre-Pichler Potentials

This section follows the original paper by Movre and Pichler [MP77]. First normalized variables are introduced

$$X = \frac{C}{9\varDelta_{FS} R^3} \quad \text{and} \qquad Y = \frac{E - E_{D1}}{\varDelta_{FS}}, \tag{C.1}$$

where $\varDelta_{FS}$ is the fine structure splitting, i.e. the energy difference between the D1 and D2 line expressed as a frequency and E_{D1} is the energy of the D1 line. The coefficient C is the square of the radial part of the dipole moment, where L is the orbital angular momentum quantum number $C = |\langle L = 0 || er || L' = 1 \rangle|^2$.
The relation to tabulated fine structure transition elements [Ste09] is

$$\langle J || er || J' \rangle = \langle L || er || L' \rangle (-1)^{J'+L+S+1} \sqrt{(2J'+1)(2L+1)} \begin{Bmatrix} L & L' & 1 \\ J' & J & S \end{Bmatrix}, \tag{C.2}$$

which relates the interaction strength C to the D1 Line fine structure transition strength via $C = 3 \cdot C(\mathrm{D1})$ and in atomic units (a.u.):

$$C(\mathrm{D1})\ [a.u.] = \frac{|\langle J = 1/2 | d | J' = 1/2 \rangle|^2}{(4\pi\epsilon_0)(E_H a_0^3)}, \tag{C.3}$$

where $E_H = 4.359\ 10^{-18}$J is the Hartree energy.

	^{87}Rb	^{23}Na
C (D1) [a.u.]	8.949	6.222
C [a.u.]	26.847	18.666
$\vert\langle J = 1/2 \vert d \vert J' = 1/2 \rangle\vert [10^{-29}\mathrm{Cm}]$	2.5377	2.1130

This implies that the C coefficients stated in i.e. [TJL$^+$05] and [JTLJ06] are for the D1 line and need to be multiplied by 3 to give the total dipole moment of both, D1 and D2 line, and reproduce specified maxima and minima of potential curves.

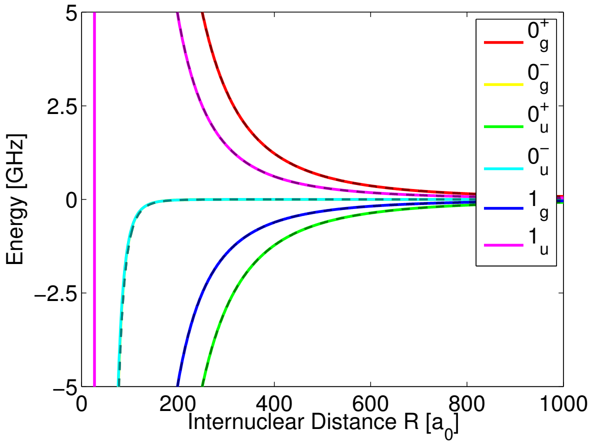

Figure C.1: D1 line Movre-Pichler (solid) and approximated c_3 or c_6 (dashed) potentials. For the relevant detunings the approximated potentials nicely match Movre-Pichler potentials.

The potential curves, parametrized as Y, are given by [MP77]:

$$Y(2_\sigma) = 1 + 3\sigma X \tag{C.4}$$

$$Y(0_\sigma^+) = \frac{1}{2}(1 + 9\sigma X \pm \sqrt{1 + 2\sigma X + 9X^2}) \tag{C.5}$$

$$Y(0_\sigma^-) = \frac{1}{2}(1 - 3\sigma X \pm \sqrt{1 - 6\sigma X + 81X^2}), \tag{C.6}$$

with $\sigma = g/u$, a symmetry property. For the 1_σ states the following equation needs to be solved, leading to somewhat longer expressions as solutions for Y:

$$\begin{aligned} Y^3 + (-2 + \sigma 6X)Y^2 + (1 - \sigma 8X - 9X^2)Y + \\ (\sigma 2X + 6X^2 - \sigma 54X^3) = 0, \end{aligned} \tag{1_σ}$$

and the secular equations for the $0_\sigma^\pm$ state solutions stated above are

$$Y^2 - (1 + \sigma 9X)Y + (\sigma 4X + 18X^2) = 0 \tag{0_σ^+}$$

$$Y^2 - (1 - \sigma 3X)Y - 18X^2 = 0. \tag{0_σ^-}$$

Figure C.1 shows the Movre-Pichler potentials of the ^{87}Rb D1 line for the detunings relevant in our experiment.

C.1.1 Oscillator Strengths

This section follows Movre and Pichler [MP80]. The oscillator strength of a molecular potential is given by

$$f_{osc}^{mol} = F(\Omega_\sigma^\pm) f_{osc}^{D2}, \tag{C.7}$$

where f_{osc}^{D2} is the D2 line oscillator strength and the $F(\Omega_\sigma^\pm)$ coefficients for each molecular potential $\Omega_\sigma^\pm$ are

$$F(2_g) = \frac{1}{2} \tag{C.8}$$

$$F(2_u) = 0 \tag{C.9}$$

$$F(1_g) = \frac{(A_p + 3B_p + 2C_p)^2 + 4(A_p - C_p)^2}{12(A_p^2 + 3B_p^2 + 2C_p^2)} \tag{C.10}$$

$$F(1_u) = \frac{(A_m - 3B_m + 2C_m)^2}{12(A_m^2 + 3B_m^2 + 2C_m^2)} \tag{C.11}$$

$$F(0_g^-) = \frac{1}{4} \tag{C.12}$$

$$F(0_u^-) = 0 \tag{C.13}$$

$$F(0_g^+) = \frac{(Y - 6X)^2}{12(Y^2 - 8XY + 18X^2} \tag{C.14}$$

$$F(0_u^+) = \frac{(Y + 3X)^2}{6(Y^2 + 8XY + 18X^2)} \tag{C.15}$$

with

$$A_p = (Y - 1)(Y + 2X) - 6X^2 \tag{C.16}$$

$$A_m = (Y - 1)(Y - 2X) - 6X^2 \tag{C.17}$$

$$B_p = 4X^2 + X(Y + 2X) \tag{C.18}$$

$$B_m = 4X^2 - X(Y - 2X) \tag{C.19}$$

$$C_p = 3X^2 + 2X(Y - 1) \tag{C.20}$$

$$C_m = 3X^2 - 2X(Y - 1). \tag{C.21}$$

The oscillator strengths can then be used to calculate the molecular potential interaction strength $V_{eg} = \hbar b_C \Omega_A$, where Ω_A is the atomic Rabi frequency and $b_C^2 = f_{osc}^{mol} / f_{osc}^{D1}$.

C.1.2 Approximated c_3 Potentials

In order to approximate Movre-Pichler potentials [SUP78] as $E = c_n(\Omega_\sigma^{(\pm)})/R^n$ potentials the expressions above need to be simplified by assuming X to be small (large R), therefore neglecting powers of 2 and higher and choosing $Z = Y$ or $Z = Y - 1$ for the D1 and D2 lines respectively and then assuming Z to be small as well.

Assuming all potentials following n=3 type potentials we obtain c_3 coefficients

$$c_3(0_\sigma^+, D1) = \sigma \frac{4}{9} C \tag{C.22}$$

$$c_3(0_\sigma^+, D2) = \sigma \frac{5}{9} C \tag{C.23}$$

$$c_3(0_\sigma^-, D1) = -\sigma \frac{1}{6} C \tag{C.24}$$

$$c_3(0_\sigma^-, D2) = -\sigma \frac{1}{3} C \tag{C.25}$$

$$c_3(1_\sigma, D1) = -\sigma \frac{2}{9} C \tag{C.26}$$

$$c_3(1_\sigma, D2) = \frac{-2\sigma \pm \sqrt{7}}{9} C \tag{C.27}$$

$$c_3(2_\sigma, D2) = \sigma \frac{1}{3} C. \tag{C.28}$$

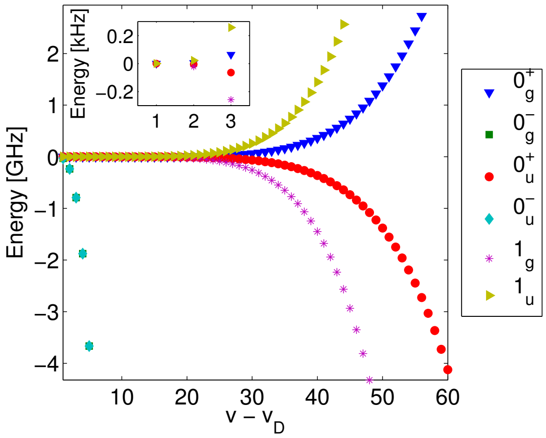

Figure C.2: LeRoy-Bernstein energies of the D1 line potentials relevant for our experiments. The inset shows the energies close to the dissociation limit.

The $0_\sigma^-(D1)$ potentials, though, turn out to be better resembled by a n=6 type potential, with $E = c_6/R^6$. The resulting c_6 coefficient is

$$c_6(0_\sigma^-, D1) = -\frac{1}{4}\frac{C^2}{\Delta_{FS}}. \tag{C.29}$$

The transition to the 0_u^- potential is a forbidden transition (oscillator strength is zero) and therefore won't play a role in our analysis. The approximated potentials are plotted in Fig. C.1 as dotted lines together with the Movre-Pichler potentials.

C.2 LeRoy-Bernstein Formula

The LeRoy-Bernstein formula [LeR70, JTLJ06, WBZJ99] estimates the energies of vibrational resonances $E_{LeRoy}(\mathrm{v})$ in a $E = \frac{c_n}{R^n}$ potential. With a scaling energy

$$E_n = \left(\sqrt{\frac{\pi}{2\mu}}\frac{\hbar(n-2)}{c_n^{1/n}}\frac{\Gamma(1+\frac{1}{n})}{\Gamma(\frac{1}{2}+\frac{1}{n})}\right)^{\frac{2n}{n-2}} \tag{C.30}$$

where $\Gamma(\cdot)$ refers to the Gamma function one can write the LeRoy-Bernstein formula as

$$\mathrm{v}_D - \mathrm{v} = \left(\frac{E_{LeRoy}(\mathrm{v})}{E_n}\right)^{\frac{n-2}{2n}}, \tag{C.31}$$

where v_D is the non-integer number ([0 1)) corresponding to the dissociation limit and v is an integer number labeling the levels starting with '1' closest to the dissociation level and counting up towards deeper bound states. The LeRoy-Bernstein energies are plotted in Fig. C.2 for all the relevant D1 line potentials.

C.3 Discussion of Quantum Statistics

The prefactor of the loss rate coefficient K_e, introduced in Eq. 6.8, $g^{(2)}(0) = (2-x)/2$, was taken from [BJS96], but originates from [SJKV89], where the second-order correlation function is given as $g^{(2)}(0) = (2-x^2)/2$. Since condensate fractions x of either 0 or 1 are the only ones used in this thesis, the difference is unimportant. The prefactor accounts for the coherence properties of the condensate and the resulting reduction in the $g^{(2)}(\mathbf{r})$ function [NG99]. What is not accounted for is the hard-core potential of the mean-field by the Gross-Pitaevskii equation [NG99].

Corrections to the refractive index due to quantum statistics are treated in [MCD95] by summing over all dipoles in a sample, truncating the induced dipole responses at two-particle interactions. Their result contains the second-order correlation function, taking into account the quantum mechanical statistical distribution of particle positions. These statistical positions are included in the presented light-assisted collision model by the ground state wavefunction. The model therefore contains the quantum statistical particle position distribution. Since only dimers are accounted for the result should be very similar to the on presented in [MCD95].

C.4 Argument for Introducing Discrete Resonances to Repulsive Potentials

The aim is to show why it is feasible to assign artificial vibrational resonances to repulsive potentials by comparing the resulting interaction strengths.

LeRoy resonances can be easily assigned to the repulsive potentials, by using the corresponding C_n values. As long as the resulting total interaction strength is conserved, this is at least formally justified.

To compare interaction strengths we start by integrating the attractive potential rate coefficient over the full frequency space

$$\int_{-\infty}^{\infty} \mathrm{d}\varDelta_{\mathrm{v}} K_e(\mathrm{v}) \frac{\nu_{\mathrm{v}}\gamma_{\mathrm{v}}}{\varDelta_{\mathrm{v}}^2 + (\gamma_{\mathrm{v}}/2)^2} = K_e(\mathrm{v}) 2\pi\nu_{\mathrm{v}}. \tag{C.32}$$

This result needs to be compared with the integration of the rate coefficient of repulsive potentials. The correct integration region should be chosen to lie around the LeRoy energy of the attractive potential, covering half the distance to the next bound levels on each side. The integral is then

$$\begin{aligned} &\int_{\varDelta_A(\mathrm{v}) - \frac{E_{\mathrm{v}} - E_{\mathrm{v}-1}}{2\hbar}}^{\varDelta_A(\mathrm{v}) + \frac{E_{\mathrm{v}+1} - E_{\mathrm{v}}}{2\hbar}} K_e(\varDelta_A) \mathrm{d}\varDelta_A \approx \\ &K_e(\mathrm{v}) \frac{E_{\mathrm{v}+1} - E_{\mathrm{v}-1}}{2\hbar} = K_e(\mathrm{v}) 2\pi\nu_{\mathrm{v}}. \end{aligned} \tag{C.33}$$

It is apparent that the same interaction strength is recovered. Therefore it is permissible to formally use a resonance line description even for repulsive potentials. This does not represent the actual structure of repulsive resonances, but if the detuning is chosen to be far away from resonance with any repulsive potential, the treatment can be used to introduce dispersive wings to these potentials.

Four

Technical Documentation

D.1 Water Flow Control

The quadrupole coils, the Ioffe coil and the magnetic field switch box are water cooled. The water is stored in a large 180L tank and cooled by a chiller (Neslab M33 PD1, 5L/min), which also pumps the water into the system. We can manually stop the water flow for each coil and the switch box individually. The coils are driven by a power supply (Agilent E4356A, 0-30 A, 0-80 V, maximum power 2100 W).

There are two experimental situations: 1) normal operation - power supply is on, coils have to be cooled and 2) flushing coils - this is done to remove bubbles inside the tubes and coil holders by closing the flow through all but one coil, the power supply has to be off to avoid overheating.

An emergency situation occurs when there is a water leak and water spills into the lab or even onto the optical table. To account for this situation we only used to have a flow wheel (McMillan 101) in the switch box arm. It gives an analog signal V_{flow} corresponding to the flow. If the flow was unusual a comparator circuit would turn off the power supply and the chiller. This meant that we had to overrule the security circuit in order to flush the coils. In that case it was possible to turn on the power supply while water would flow through only one coil.

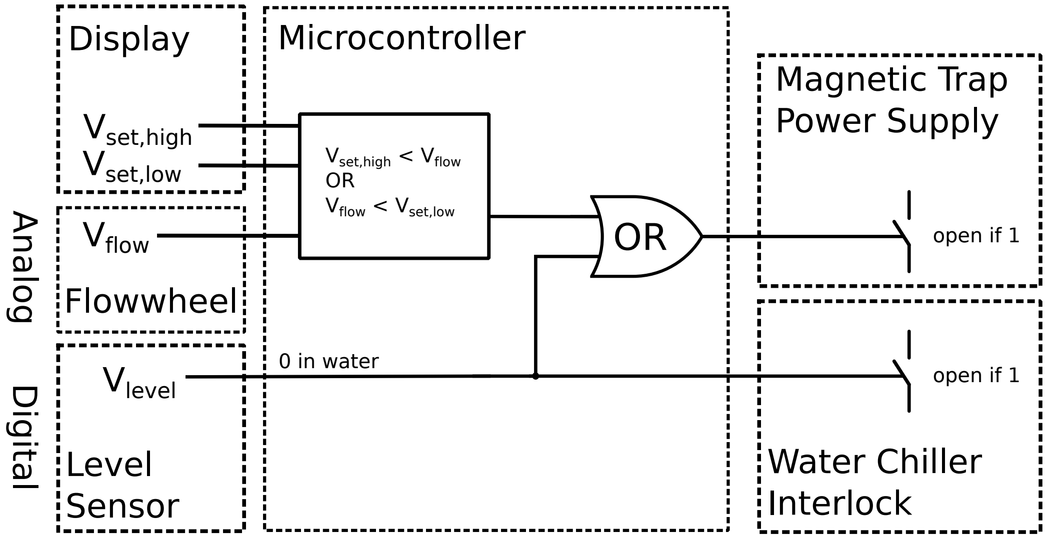

Figure D.1: Logic scheme of the water flow control system. A microcontroller gets the sensor information on water tank level V_{level} (digital) and flow wheel signal V_{flow} (analog) as well as set values specified by the user via the display, $V_{set,high}$ and $V_{set,low}$. Depending on the programmed logic the magnetic trap power supply and the chiller can be switched off.

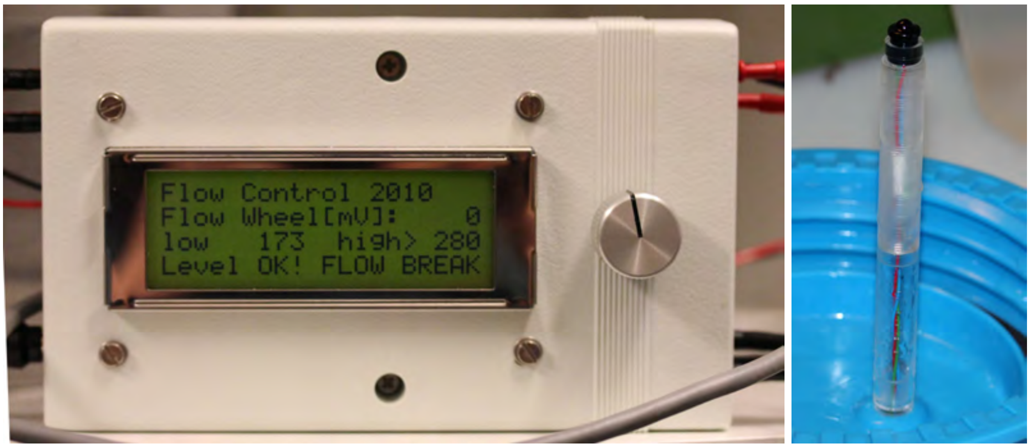

Figure D.2: Pictures of the final device. Left: the display showing the low and high setting points, the flow wheel signal and if there is a flow break or a problem with the water level. Right: the water tank level sensor as mounted on the inner side of the water tank lid.

To avoid this situation we came up with a new security circuit (see Fig. D.1) with a second sensor, an optical water level sensor (Honeywell LLE105000), that gives a digital signal V_{level} depending on if it is being submerged in water or not (low in water). Now the chiller can be switched off if the water level in the tank is reduced. The power supply is switched off if either the water level is low or the flow is outside of set bounds $V_{set,high}$ and $V_{set,low}$. This means that in the case of coil flushing (2) the power supply is automatically turned off, while the chiller keeps running. In the emergency case of a water leak, both the chiller and the power supply are turned off.

The circuit was realized with a microcontroller (ATMEGA168PA). A digital display and a rotateable knob (Fig. D.2) is used as an interface to set the upper and lower flow levels and to reset the logic after a flow break or low level in the water tank. The programming was done using a USB UART interface (FT232RL). The switches for the power supply and the chiller are external as well as the sensors. The electronic circuit, Fig. D.3, contains therefore mainly the microcontroller and the USB interface for programming. There are also two LEDs indicating data transmission and flow break. The circuit was designed in cooperation with Henrik Bertelsen from our electronic workshop.

D.2 Cameras

Andor Cam Superradiance Settings	
Read-Out Rate	50kHz
Temperature	-60°C
Exposure Time	100ms
Shift Speed	0.875µs
Preamplifier Gain	4x

Table D.1

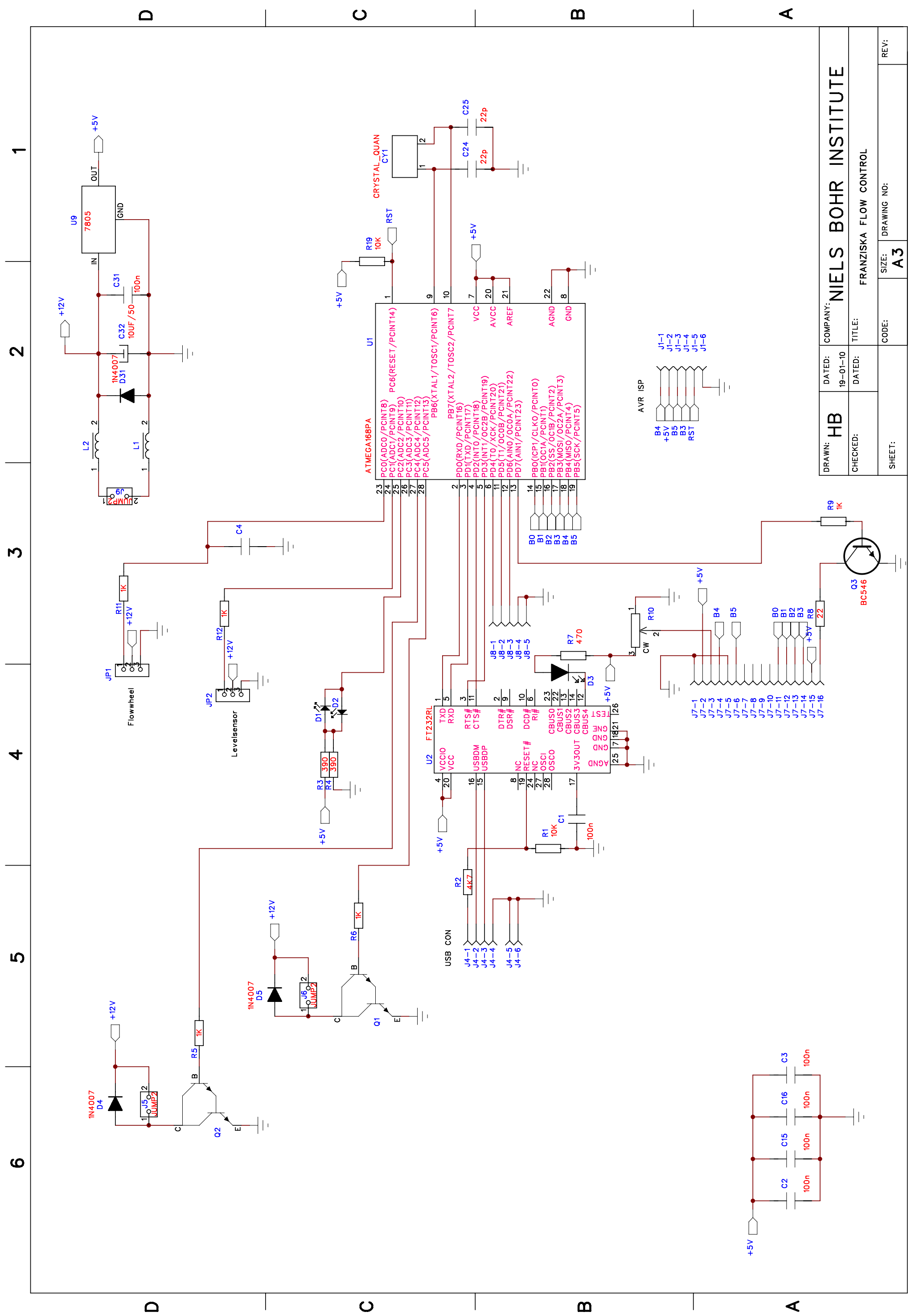

Figure D.3: Schematic drawing of the electronic circuit containing the microcontroller for the water flow control system.

Andor Cam Faraday Settings	
Read-Out Rate	1MHz
Temperature	-60°C
Exposure Time	12ms
Shift Speed	0.875µs
Preamplifier Gain	4x

Table D.2

DTA Cam Data Sheet Specifications	
Pixel Size	6.8µm
Quantum Efficiency	0.6
Read-Out Noise	14.7 eles
Gain/Sensitivity	1.6 eles/ADU
Dark Current	0.06 eles/s/pix
Shot Noise Limit	360 photons

Table D.3

Andor Cam Data Sheet Specifications		
Read-Out Rate	50kHz	1MHz
Pixel Size [µm]	13	
Quantum Efficiency	0.95	
Read-Out Noise [eles]	2.7	7
Gain/Sensitivity [eles/ADU]	1.4	1.3
Dark Current @ $-60°$ [eles/s/pix]	1	
Base Level [counts]	3751	3585
Shot Noise Limit [photons]	7	47

Table D.4

Bibliography

[AEM$^+$95] M H Anderson, J R Ensher, M R Matthews, C E Wieman, and E A Cornell. Observation of Bose-Einstein Condensation in a Dilute Atomic Vapor. *Science*, 269:198, July 1995.

[Al09] J Appel et Al. A versatile digital GHz phase lock for external cavity diode lasers. pages 1–5, April 2009.

[AMvD$^+$96] M R Andrews, M O Mewes, N J van Druten, D S Durfee, D M Kurn, and W Ketterle. Direct, Nondestructive Observation of a Bose Condensate. *Science*, 273(5271):84–87, July 1996.

[Bay66] Gordon Baym. *Lectures on Quantum Mechanics*. Benjamin, New York, September 1966.

[BBKS06] Pawel Berczynski, Konstantin Yu Bliokh, Yuri A Kravtsov, and Andrzej Stateczny. Diffraction of a Gaussian beam in a three-dimensional smoothly inhomogeneous medium: an eikonal-based complex geometrical-optics approach. *Journal of the Optical Society of America A*, 23:1442, June 2006.

[BGP$^+$09] Waseem S Bakr, Jonathon I Gillen, Amy Peng, Simon Fölling, and Markus Greiner. A quantum gas microscope for detecting single atoms in a Hubbard-regime optical lattice. *Nature*, 462(7269):74–77, November 2009.

[BJS96] K Burnett, P Julienne, and K A Suominen. Laser-Driven Collisions between Atoms in a Bose-Einstein Condensed Gas. *Physical Review Letters*, 77(8):1416–1419, August 1996.

[BKŻ08] Paweł Berczyński, Yury A Kravtsov, and Grzegorz Żeglinski. Gaussian beam diffraction in inhomogeneous and nonlinear media: analytical and numerical solutions by complex geometrical optics. *Central European Journal of Physics*, 6:603, September 2008.

[BLPS90] K J Blow, Rodney Loudon, Simon J D Phoenix, and T J Shepherd. Continuum fields in quantum optics. *Physical Review A (ISSN 1050-2947)*, 42:4102, October 1990.

[BPM$^+$09] R Bücker, A Perrin, S Manz, T Betz, C Koller, T Plisson, J Rottmann, T Schumm, and J Schmiedmayer. Single-particle-sensitive imaging of freely propagating ultracold atoms. *New Journal of Physics*, 11:103039, 2009.

[BSH97] C C Bradley, C A Sackett, and R G Hulet. Bose-Einstein Condensation of Lithium: Observation of Limited Condensate Number. *Physical Review Letters*, 78(6):985–989, February 1997.

[BW05] M Born and E Wolf. *Principles of Optics - M.Born, E. Wolf.* January 2005.

[CD96] Y Castin and R Dum. Bose-Einstein condensates in time dependent traps. *Physical Review Letters*, 77(27):5315–5319, 1996.

[CG08] Raymond Chiao and John Garrison. *Quantum Optics (Oxford Graduate Texts).* Oxford University Press, USA, August 2008.

[CK77] T CVITAS and N Kallay. EQUATIONS OF ELECTROMAGNETISM FROM CGS TO SI. Journal Of Chemical Education, January 1977.

[Col05] Edward Collett. *Field Guide to Polarization (SPIE Vol. FG05).* SPIE Publications, September 2005.

[DGPS99] F Dalfovo, S Giorgini, LP Pitaevskii, and S Stringari. Theory of Bose-Einstein condensation in trapped gases. *Reviews Of Modern Physics*, 71(3):463–512, 1999.

[Dic54] R H Dicke. Coherence in Spontaneous Radiation Processes. *Physical Review*, 93:99, January 1954.

[DLCZ01] LM Duan, MD Lukin, JI Cirac, and P Zoller. Long-distance quantum communication with atomic ensembles and linear optics. *Nature*, 414(6862):413–418, January 2001.

[EBH98] T Esslinger, I Bloch, and TW Hänsch. Bose-Einstein condensation in a quadrupole-Ioffe-configuration trap. *Physical Review A*, 58(4):2664–2667, 1998.

[EGW$^+$08] J Esteve, C Gross, A Weller, S Giovanazzi, and MK Oberthaler. Squeezing and entanglement in a Bose–Einstein condensate. *Nature*, 455(7217):1216–1219, 2008.

[GGZS11] Anna Grodecka-Grad, Emil Zeuthen, and Anders S Sørensen. High capacity spatial multimode quantum memories based on atomic ensembles. *arXiv:1110.6771v1*, October 2011.

[GK05] Christopher C Gerry and Peter L Knight. *Introductory quantum optics.* Cambridge Univ Pr, 2005.

[Goo06] Joseph W. Goodman. *Introduction to Fourier Optics.* January 2006.

[GSM06] J Geremia, John Stockton, and Hideo Mabuchi. Tensor polarizability and dispersive quantum measurement of multilevel atoms. *Physical Review A*, 73(4):042112, April 2006.

[GTR$^+$04] F Gerbier, J Thywissen, S Richard, M Hugbart, P Bouyer, and A Aspect. Critical Temperature of a Trapped, Weakly Interacting Bose Gas. *Physical Review Letters*, 92(3):030405, January 2004.

[Ham06] K Hammerer. *Quantum Information Processing with Atomic Ensembles and Light.* PhD thesis, 2006.

[Hil08] Andrew Hilliard. *Collective Rayleigh scattering in a Bose Einstein condensate.* PhD thesis, November 2008.

[HKLT$^+$08] A Hilliard, F Kaminski, R Le Targat, C Olausson, E Polzik, and J Müller. Rayleigh superradiance and dynamic Bragg gratings in an end-pumped Bose-Einstein condensate. *Physical Review A*, 78(5), November 2008.

[HSI+05] J Higbie, L Sadler, S Inouye, A Chikkatur, S Leslie, K Moore, V Savalli, and D Stamper-Kurn. Direct Nondestructive Imaging of Magnetization in a Spin-1 Bose-Einstein Gas. *Physical Review Letters*, 95(5):050401, July 2005.

[HSP10] K Hammerer, AS Sørensen, and ES Polzik. Quantum interface between light and atomic ensembles. *Reviews Of Modern Physics*, 82(2):1041–1093, 2010.

[Hua01] Kerson Huang. *Introduction to Statistical Physics*. CRC Press, January 2001.

[ICSK+99] S Inouye, AP Chikkatur, DM Stamper-Kurn, J Stenger, DE Pritchard, and W Ketterle. Superradiant Rayleigh scattering from a Bose-Einstein condensate. *Science*, 285(5427):571–574, January 1999.

[Jac62] J. D. Jackson. *Classical Electrodynamics*. January 1962.

[JSC+04] Brian Julsgaard, Jacob Sherson, J Ignacio Cirac, Jaromír Fiurášek, and Eugene S Polzik. Experimental demonstration of quantum memory for light. *Nature*, 432:482, November 2004.

[JTLJ06] Kevin Jones, Eite Tiesinga, Paul Lett, and Paul Julienne. Ultracold photoassociation spectroscopy: Long-range molecules and atomic scattering. *Reviews Of Modern Physics*, 78(2):483–535, May 2006.

[Jul96] PS Julienne. Cold binary atomic collisions in a light field. *Journal Of Research Of The National Institute Of Standards And Technology*, 101(4):487–503, 1996.

[Jul07] Brian Julsgaard. *Entanglement and Quantum Interactions with Macroscopic Gas Samples*. PhD thesis, April 2007.

[KDSK99] W Ketterle, D S Durfee, and D M Stamper-Kurn. Making, probing and understanding Bose-Einstein condensates. *arXiv*, cond-mat, April 1999.

[KFC+09] M Karski, L Förster, J Choi, W Alt, A Widera, and D Meschede. Nearest-Neighbor Detection of Atoms in a 1D Optical Lattice by Fluorescence Imaging. *Physical Review Letters*, 102(5), February 2009.

[Kim08] H J Kimble. The quantum internet. *Nature*, 453(7198):1023–1030, June 2008.

[KKN+09] M Kubasik, M Koschorreck, M Napolitano, S de Echaniz, H Crepaz, J Eschner, E Polzik, and M Mitchell. Polarization-based light-atom quantum interface with an all-optical trap. *Physical Review A*, 79(4):043815, April 2009.

[KM09] M Koschorreck and M W Mitchell. Unified description of inhomogeneities, dissipation and transport in quantum light-atom interfaces. *Journal of Physics B-Atomic Molecular and Optical Physics*, 42(19):–, 2009.

[KMN+04] M Kemmann, I Mistrik, S Nussmann, H Helm, C Williams, and P Julienne. Near-threshold photoassociation of 87Rb_2. *Physical Review A*, 69(2), February 2004.

[KMS+05] DV Kupriyanov, OS Mishina, IM Sokolov, B Julsgaard, and ES Polzik. Multimode entanglement of light and atomic ensembles via off-resonant coherent forward scattering. *Physical Review A*, 71(3):–, 2005.

[Kor09] Nikolaj Korolev. Spontaneous emission in light-atom interactions for atomic ensembles. Master's thesis, December 2009.

[KV96] W Ketterle and NJ VanDruten. Evaporative cooling of trapped atoms. *Advances in Atomic, Molecular, and Optical Physics, Vol 37*, 37:181–236, 1996.

[LeR70] Robert J LeRoy. Dissociation Energy and Long-Range Potential of Diatomic Molecules from Vibrational Spacings of Higher Levels. *The Journal of Chemical Physics*, 52(8):3869, 1970.

[LJM$^+$09] Y Liu, S Jung, S Maxwell, L Turner, E Tiesinga, and P Lett. Quantum Phase Transitions and Continuous Observation of Spinor Dynamics in an Antiferromagnetic Condensate. *Physical Review Letters*, 102(12):125301, March 2009.

[LL80] L. D. Landau and E M Lifshitz. *The Classical Theory of Fields*. Butterworth-Heinemann, January 1980.

[Mar03] Andreas Marte. *Feshbach-Resonanzen bei Stößen ultrakalter Rubidiumatome*. PhD thesis, August 2003.

[MCD95] Olivier Morice, Yvan Castin, and Jean Dalibard. Refractive index of a dilute Bose gas. *Physical Review A*, 51:3896, May 1995.

[Mes62] Albert Messiah. *Quantum Mechanics 2*. North Holland, September 1962.

[MP77] M Movre and G Pichler. Resonance Interaction and Self-Broadening of Alkali Resonance Lines .1. Adiabatic Potential Curves. *Journal of Physics B-Atomic Molecular and Optical Physics*, 10(13):2631–2638, 1977.

[MP80] M Movre and G Pichler. Resonance Interaction and Self-Broadening of Alkali Resonance Lines .2. Quasi-Static Wing Profiles. *Journal of Physics B-Atomic Molecular and Optical Physics*, 13(4):697–707, 1980.

[MPO$^+$05] J H Müller, P Petrov, D Oblak, C L Garrido Alzar, S R de Echaniz, and E S Polzik. Diffraction effects on light–atomic-ensemble quantum interface. *Physical Review A*, 71(3):033803, March 2005.

[MRK$^+$10] R Meppelink, R A Rozendaal, S B Koller, J M Vogels, and P van der Straten. Thermodynamics of Bose-Einstein-condensed clouds using phase-contrast imaging. *Physical Review A*, 81(5):053632, 2010.

[NG99] M Naraschewski and R J Glauber. Spatial coherence and density correlations of trapped Bose gases. *Physical Review A (Atomic*, 59:4595, June 1999.

[NLW07] Karl D Nelson, Xiao Li, and David S Weiss. Imaging single atoms in a three-dimensional array. *Nature Physics*, 3(8):556–560, June 2007.

[Ola07] Christina Olausson. A Rubidium Bose-Einstein Condensate. Master's thesis, August 2007.

[Pri83] David Pritchard. Cooling Neutral Atoms in a Magnetic Trap for Precision Spectroscopy. *Physical Review Letters*, 51(15):1336–1339, October 1983.

[PS01] Chris Pethick and Henrik Smith. *Bose-Einstein condensation in dilute gases - Pethick C.J., Smith H.* September 2001.

[RLWGO07] G Reinaudi, T Lahaye, Z Wang, and D Guéry-Odelin. Strong saturation absorption imaging of dense clouds of ultracold atoms. *Optics Letters*, 32(21):3143–3145, 2007.

[RWE$^+$95] L Ricci, M Weidemüller, T Esslinger, A Hemmerich, C Zimmermann, V Vuletic, W König, and TW Hänsch. A compact grating-stabilized diode laser system for atomic physics. *Optics Communications*, 117(5-6):541–549, 1995.

[RYG$^+$10] Steffen Rath, Tarik Yefsah, Kenneth Günter, Marc Cheneau, Rémi Desbuquois, Markus Holzmann, Werner Krauth, and Jean Dalibard. Equilibrium state of a trapped two-dimensional Bose gas. *Physical Review A*, 82(1):013609, July 2010.

[SAA$^+$10] C Simon, M Afzelius, J Appel, A. Boyer de la Giroday, S J Dewhurst, N Gisin, C Y Hu, F Jelezko, S Kröll, J H Müller, J Nunn, E S Polzik, J G Rarity, H de Riedmatten, W Rosenfeld, A J Shields, N. Skoeld, R M Stevenson, R Thew, I A Walmsley, M C Weber, H Weinfurter, J Wrachtrup, and R J Young. Quantum memories. *The European Physical Journal D*, 58(1):1–22, 2010.

[Sak94] J. J. Sakurai. *Modern Quantum Mechanics*. Addison-Wesley, revised edition, January 1994.

[SCJ03] GA Smith, S Chaudhury, and PS Jessen. Faraday spectroscopy in an optical lattice: a continuous probe of atom dynamics. *Journal Of Optics B-Quantum And Semiclassical Optics*, 5:323, 2003.

[SJKV89] H T C Stoof, A M L Janssen, J M V A Koelman, and B J Verhaar. Decay of spin-polarized atomic hydrogen in the presence of a Bose condensate. *Physical Review A*, 39(6):3157–3169, March 1989.

[SKKH09] I Sokolov, M Kupriyanova, D Kupriyanov, and M Havey. Light scattering from a dense and ultracold atomic gas. *Physical Review A*, 79(5):053405, May 2009.

[SM68] Bruce W Shore and Donald Howard Menzel. *Principles of atomic spectra*. John Wiley & Sons Inc, 1968.

[STB$^+$03] D Schneble, Y Torii, M Boyd, EW Streed, DE Pritchard, and W Ketterle. The onset of matter-wave amplification in a superradiant Bose-Einstein condensate. *Science*, 300(5618):475, 2003.

[Ste09] Daniel A Steck. Rb 87 D Line Data, August 2009.

[SUP78] William Stwalley, Yea-Hwang Uang, and Goran Pichler. Pure Long-Range Molecules. *Physical Review Letters*, 41(17):1164–1167, October 1978.

[SZ97] Marlan Orvil Scully and Muhammad Suhail Zubairy. *Quantum optics*. Cambridge Univ Pr, 1997.

[TBF08] Matthew Terraciano, Mark Bashkansky, and Fredrik Fatemi. Faraday spectroscopy of atoms confined in a dark optical trap. *Physical Review A*, 77(6):063417, June 2008.

[TDS05] L Turner, K Domen, and R Scholten. Diffraction-contrast imaging of cold atoms. *Physical Review A*, 72(3):031403, September 2005.

[THT$^+$99] Y Takahashi, K Honda, N Tanaka, K Toyoda, K Ishikawa, and T Yabuzaki. Quantum nondemolition measurement of spin via the paramagnetic Faraday rotation. *Physical Review A*, 60(6):4974–4979, 1999.

[TJL$^+$05] Eite Tiesinga, Kevin Jones, Paul Lett, Udo Volz, Carl Williams, and Paul Julienne. Measurement and modeling of hyperfine- and rotation-induced state mixing in large weakly bound sodium dimers. *Physical Review A*, 71(5), May 2005.

[VGL$^+$10] M Vengalattore, J Guzman, S R Leslie, F Serwane, and D M Stamper-Kurn. Periodic spin textures in a degenerate F=1 87Rb spinor Bose gas. *Physical Review A*, 81(5):053612, May 2010.

[VMK88] D. A. Varshalovich, A. N. Moskalev, and V. K. Khersonskii. *Quantum Theory of Angular Momentum.* World Scientific, September 1988.

[VSP10] Denis V Vasilyev, Ivan V Sokolov, and Eugene S Polzik. Quantum volume hologram. *Physical Review A*, 81(2):020302(R), February 2010.

[WBIH94] D J Wineland, J J Bollinger, W M Itano, and D J Heinzen. Squeezed atomic states and projection noise in spectroscopy. *Physical Review A*, 50:67, July 1994.

[WBZJ99] John Weiner, Vanderlei S Bagnato, Sergio Zilio, and Paul S Julienne. Experiments and theory in cold and ultracold collisions. *Reviews Of Modern Physics*, 71:1, January 1999.

[ZGGS11] Emil Zeuthen, Anna Grodecka-Grad, and Anders Sørensen. Three-dimensional theory of quantum memories based on Lambda-type atomic ensembles. *Physical Review A*, 84(4):043838, October 2011.

[ZGH09] Rui Zhang, Sean R Garner, and Lene Vestergaard Hau. Creation of Long-Term Coherent Optical Memory via Controlled Nonlinear Interactions in Bose-Einstein Condensates. *Physical Review Letters*, 103(23):233602, December 2009.

[ZN05] O Zobay and Georgios M Nikolopoulos. Dynamics of matter-wave and optical fields in superradiant scattering from Bose-Einstein condensates. *arXiv:1110.6771v1*, cond-mat.other, November 2005.

[ZN06] O Zobay and Georgios M Nikolopoulos. Spatial effects in superradiant Rayleigh scattering from Bose-Einstein condensates. *arXiv:1110.6771v1*, cond-mat.other, January 2006.

Scientific Contributions

Journals

Peer Reviewed

- Franziska Kaminski, Nir S. Kampel, Mads P. H. Steenstrup, Axel Griesmaier, Eugene S. Polzik, and Jörg H. Müller, *In-Situ Dual-Port Polarization Contrast Imaging of Faraday Rotation in a High Optical Depth Ultracold 87Rb Atomic Ensemble*, to be published in EPJ D HIDEAS special issue

- F. Kaminski, N. Kampel, A. Griesmaier, E. Polzik, and Jörg H. Müller, *Dispersive Effects in Light-Assisted Cold Collisions of Homonuclear Diatomic Molecules*, in preparation

- N. S. Kampel, A. Griesmaier, M.P. Hornbak Steenstrup, F. Kaminski, E. S. Polzik and J. H. Müller, *The effect of light assisted collisions on matter wave coherence in superradiant Bose-Einstein condensates*, Phys. Rev. Lett. **108**, 090401(2012)

- Mohammadi, A; Kaminski, F; Sandoghdar, V; Agio, M, *Fluorescence Enhancement with the Optical (Bi-) Conical Antenna* , J. Phys. Chem. C, **114**, Issue 16, 7372-7377 (2010)

- Mohammadi, A; Kaminski, F; Sandoghdar, V; Agio, M;, *Spheroidal nanoparticles as nanoantennas for fluorescence enhancement*, Int. J. Nanotechnol., **6**, Issue 10-11, 902-914 (2009)

- A. Hilliard, F. Kaminski, R. le Targat, C. Olausson, E. S. Polzik, and J. H. Müller, *Rayleigh superradiance and dynamic Bragg gratings in an end-pumped Bose-Einstein condensate*, Physical Review A **78**, 051403(R) (2008)

- Lavinia Rogobete, Franziska Kaminski, Mario Agio, and Vahid Sandoghdar, *Design of plasmonic nanoantennae for enhancing spontaneous emission*, Opt. Lett., **32**, Issue 12, pp. 1623-1625 (2007)

- F. Kaminski, V. Sandoghdar, M. Agio, *Finite-Difference Time-Domain Modeling of Decay Rates in the Near Field of Metal Nanostructures*, J. Comput. Theor. Nanosci. **4**, 635-643 (2007)

Conference Proceedings

- Mario Agio, Giorgio Mori, Franziska Kaminski, Lavinia Rogobete, and Sergei Kühn, Victor Callegari and Philipp M. Nellen, Franck Robin, Yasin Ekinci, Urs Sennhauser, Heinz Jäckel, Harun H. Solak, Vahid Sandoghdar, *Engineering gold nano-antennae to enhance the emission of quantum emitters*, Proc. SPIE, Vol. **6717**, 67170R (2007)

- Mario Agio, Franziska Kaminski, Lavinia Rogobete, Sergei Kühn, Giorgio Mori, and Vahid Sandoghdar, *Engineering the Decay Rates and Quantum Efficiency of Emitters Coupled to Gold Nanoantennae*, Quantum Electronics and Laser Science Conference (QELS), BalRmore, Maryland, May 6, 2007, Plasmonics I (QThB)

Meeting and Conference Contributions

Talks

- EMALI Final Conference, *Spatially Resolved Faraday Rotation in High Optical Depth Atomic Ensembles*, September 2010, Barcelona, Spain
- EMALI Annual Meeting, *An Ultra-Cold Light-Matter Interface - Bose-Einstein Condensates and Quantum Information*, September 2009, Pisa, Italy
- QNLO Meeting, *An Ultra-Cold Light-Matter Interface - Bose-Einstein Condensates and Quantum Information*, August 2009, Copenhagen, Denmark
- EMALI - Young Researchers Meeting and Annual Meeting, *Ultracold Atoms as a Storage Medium for Quantum Information*, April 2009, Oxford, Great Britain
- QAP Meeting, *Experiments on Superradiant Light Scattering by a ^{87}Rb Bose-Einstein-Condensate*, July 2008, Copenhagen, Denmark
- QUANTOP Meeting, *Experiments on Superradiant Light Scattering by a ^{87}Rb Bose-Einstein-Condensate*, June 2008, Copenhagen, Denmark
- EMALI - Young Researchers Meeting, *Experiments on Superradiant Light Scattering by a ^{87}Rb Bose-Einstein-Condensate*, May 2008, Vienna, Austria

Poster Presentations

- Conference on ultracold Atoms, *Collective Atom-Light-Scattering in Ultracold ^{87}Rb*, May 2009, ICTP, Trieste, Italy
- EMALI - Young Researchers Meeting and Annual Meeting, *An Ultracold Gas as a Storage Medium for Quantum Information*, April 2009, Oxford, Great Britain
- Bits, Quanta and Complex Systems, *Atom-Light Correlations: Rayleigh Superradiance in a ^{87}Rb BEC*, May 2008, Brussels, Belgium
- EMALI - Annual Meeting, *Superradiance in a ^{87}Rb Bose Einstein Condensate*, October 2007, Heraklion, Greece